University of Alberta

Baroclinic Frontal Dynamics in the Presence of Continuous Stratification and Topography

by

Mateusz K. Reszka ©

A thesis submitted to the Faculty of Graduate Studies and Research in partial fulfillment of the requirements for the degree of **Doctor of Philosophy**

in

Applied Mathematics

Department of Mathematical and Statistical Sciences

Edmonton, Alberta

Spring 2003

National Library
of Canada

Acquisitions and
Bibliographic Services

395 Wellington Street
Ottawa ON K1A 0N4
Canada

Bibliothèque nationale
du Canada

Acquisisitons et
services bibliographiques

395, rue Wellington
Ottawa ON K1A 0N4
Canada

Your file Votre référence
ISBN: 0-612-82160-9
Our file Notre référence
ISBN: 0-612-82160-9

The author has granted a non-exclusive licence allowing the National Library of Canada to reproduce, loan, distribute or sell copies of this thesis in microform, paper or electronic formats.

The author retains ownership of the copyright in this thesis. Neither the thesis nor substantial extracts from it may be printed or otherwise reproduced without the author's permission.

L'auteur a accordé une licence non exclusive permettant à la Bibliothèque nationale du Canada de reproduire, prêter, distribuer ou vendre des copies de cette thèse sous la forme de microfiche/film, de reproduction sur papier ou sur format électronique.

L'auteur conserve la propriété du droit d'auteur qui protège cette thèse. Ni la thèse ni des extraits substantiels de celle-ci ne doivent être imprimés ou aturement reproduits sans son autorisation.

Canada

University of Alberta

Library Release Form

Name of Author: Mateusz Krzysztof Reszka

Title of Thesis: Baroclinic Frontal Dynamics in the Presence of Continuous Stratification and Topography

Degree: Doctor of Philosophy

Year this Degree Granted: 2003

Permission is hereby granted to the University of Alberta Library to reproduce single copies of this thesis and to lend or sell such copies for private, scholarly or scientific research purposes only.

The author reserves all other publication and other rights in association with the copyright in the thesis, and except as herein before provided, neither the thesis nor any substantial portion thereof may be printed or otherwise reproduced in any material form whatever without the author's prior written permission.

Mateusz K. Reszka
Dept. of Mathematical
and Statistical Sciences
University of Alberta
Edmonton, Alberta, Canada
T6G 2G1

Date: Dec 13, 2002

University of Alberta

Faculty of Graduate Studies and Research

The undersigned certify that they have read, and recommend to the Faculty of Graduate Studies and Research for acceptance, a thesis entitled **Baroclinic Frontal Dynamics in the Presence of Continuous Stratification and Topography** submitted by Mateusz K. Reszka in partial fulfillment of the requirements for the degree of **Doctor of Philosophy** in **Applied Mathematics**.

Gordon E. Swaters (Supervisor)

T. Bryant Moodie (Committee chair)

John C Bowman

John C. Bowman

Bruce R. Sutherland

Andrew B. G. Bush

Paul Glen Myers

Paul G. Myers (External to Department)

Michael A. Spall (External to University)

Date: Dec 13/02

Abstract

An investigation of subinertial dynamics involving oceanic fronts is presented in the context of layered models, which allow for vanishing thickness in the frontal layer and continuous stratification in the ambient fluid. The focus of the study is the baroclinic destabilization and subsequent evolution of surface-trapped, bottom-trapped and intermediate-depth currents, as well as their interaction with topography. Two new theories are derived that include the effect of ambient stratification, and a previous theory is generalized. Reduction of all three models to simpler governing equations in the limit of no stratification is demonstrated and basic analytical results are established with respect to boundary conditions, flow invariants and linear stability criteria.

The linear stability problems for an abyssal current and a surface current in the presence of sloping topography are solved for physically-relevant configurations. It is shown that growth rates increase and dominant lengthscales decrease with the relative current thickness or ambient stratification. Predicted instability characteristics and results of fully nonlinear numerical simulations are compared with several oceanographic phenomena of interest, in particular the Denmark Strait Overflow. It is argued that the models presented provide a superior description of baroclinic dynamics than traditional quasigeostrophic theory, in that the assumed lengthscales are larger than the Rossby radius and variations in the frontal layer thickness scale with the layer thickness itself. The resulting balances still allow reasonably straightfor-

ward interpretation of the physical mechanisms involved but are appropriate in many situations where quasigeostrophic models are not.

Acknowledgements

First and foremost, I would like to thank my supervisor and mentor, Dr. Gordon Swaters, without whose guidance and inspiration this work would not have come to fruition. I have learned much from Gordon about fluid dynamics, and about being a scientist. I am indebted to Dr. Bruce Sutherland for helpful discussions regarding this research, as well as for his special attention to graduate student enrichment within the fluids group. I gratefully acknowledge my instructors for fluid dynamics related courses, especially Dr. Bryant Moodie, Dr. Andrew Bush and Dr. John Bowman. Many thanks go to my friends and colleagues, Paul Choboter, Francis Poulin, Richard Karsten, Kathleen Dohan and Morris Flynn, whose insights and encouragement have been invaluable. Mr. Edmund Sumbar and Mr. Adrian Driga of CNS provided some much-needed help in implementing the MUDPACK routines. Finally, I wish to thank my parents, who have been for me a constant source of strength and wisdom.

Contents

1 Introduction **1**
- 1.1 Motivation 1
- 1.2 Model Classification 3
- 1.3 Case studies discussed in this thesis 8
  - 1.3.1 Strait of Georgia deep water replacement 8
  - 1.3.2 Denmark Strait Overflow 9
  - 1.3.3 Instability in the California Current 11
  - 1.3.4 Axisymmetric surface currents 12
  - 1.3.5 Mediterranean outflow and Meddies 13

2 CS-PG Model **15**
- 2.1 Model Equations 15
  - 2.1.1 The Nof velocity 15
  - 2.1.2 Model Derivation 18
  - 2.1.3 Governing Equations 25
  - 2.1.4 Boundary conditions at incroppings 27
  - 2.1.5 Reduction to SW-PG 28
  - 2.1.6 Mass Conservation 29
- 2.2 Preliminary Results 32
  - 2.2.1 Instability Mechanism 32
  - 2.2.2 Application to Strait of Georgia 38
- 2.3 Linear Stability Analysis 47
  - 2.3.1 Analysis of a Wedge Front 51
- 2.4 Parabolic Front 59
  - 2.4.1 The Dispersion Relation 62
  - 2.4.2 Primary Mode of Instability 67
  - 2.4.3 Secondary Modes of Instability 71
  - 2.4.4 Dependence on μ 75
- 2.5 Numerical confirmation 76

3 Denmark Strait Overflow **81**
- 3.1 Source flow simulations 81

3.2 Cyclogenesis 92
3.3 Discussion 101

4 FG-CS Model **104**
4.1 Model Equations 104
  4.1.1 Model Derivation 105
  4.1.2 Governing Equations 110
  4.1.3 Boundary conditions at outcroppings 114
  4.1.4 Reduction to FG-SW 116
  4.1.5 An invariant of the equations 117
  4.1.6 Mass Conservation 119
4.2 Linear Stability Analysis 121
  4.2.1 Homogeneous limit 124
  4.2.2 Normal modes 125
  4.2.3 Necessary Condition for Instability 127
  4.2.4 Gently sloping wedge front 129
4.3 The nonseparable problem 137
  4.3.1 General wedge front 139
  4.3.2 Exponential front 143
4.4 Axisymmetric currents 152
  4.4.1 Linear Stability 152
  4.4.2 Numerical details 155
  4.4.3 Description of the instability 158
  4.4.4 Some diagnostics 162
  4.4.5 Source flow simulations 166
  4.4.6 Eddy transports 168
  4.4.7 Discussion of topographic effects 170

5 CS-FG-CS Model **173**
5.1 Model Equations 173
  5.1.1 Model Derivation 174
  5.1.2 Governing Equations 181
  5.1.3 Boundary conditions at incroppings 183
  5.1.4 Reduction to SW-FG-SW 184
5.2 Meddy Simulation 185

6 Conclusions **192**
6.1 Summary 192
6.2 Avenues for further research 197

A SW-FG-SW Model **199**

B Numerical Scheme **205**

List of Tables

1.1 Models discussed in this thesis, and previous work 4
1.2 Acronyms used throughout this thesis 7

2.1 Dimensional instability characteristics for parabolic front 66

3.1 Dimensional overflow properties for simulations EXP1 86
3.2 Dimensional instability characteristics relevant for series EXP1 87

4.1 Instability characteristics for O(1) wedge resulting from spectral technique and from direct simulation 141
4.2 Instability characteristics for exponential profile predicted by linear theory 145
4.3 Instability characteristics for exponential profile resulting from direct simulation 145
4.4 Configuration and observed wavelength for simulations of axisymmetric currents 157

List of Figures

1.1 Dynamic topography southwest of Denmark Strait 10

2.1 Diagram which elucidates origin of Nof speed 16
2.2 CS-PG model geometry 18
2.3 Lower-layer thickness in abyssal current simulation 35
2.4 Diagnostics for abyssal current simulation 36
2.5 Cross-sections of topography and abyssal current 39
2.6 Lower-layer thickness for SOG simulation using S91 model 40
2.7 Upper-layer pressure for SOG simulation using S91 model 41
2.8 Lower-layer thickness for SOG simulation using PSa model 43
2.9 Upper-layer pressure for SOG simulation using PSa model 44
2.10 Vertical sections of upper-layer pressure in SOG simulation 45
2.11 Range of unstable wavenumbers for wedge front 52
2.12 Maximum growth rates vs. μ and s 54
2.13 Instability characteristics for wedge front 55
2.14 Perturbation solution for wedge front at $z = -1$ 56
2.15 Growth rate vs. time for wedge front simulations 57
2.16 Perturbation vertical section for wedge front 58
2.17 Instability characteristics for parabolic front with $\mu = 1, 2, 3$ 63
2.18 Instability characteristics for parabolic front with $N^2 = 0.5, 1.0, 1.5$. 64
2.19 Instability characteristics for parabolic front with $a = 0.5, 1.0, 1.5$ . . 65
2.20 Upper-layer perturbation solution at $z = -1$ 67
2.21 Upper-layer perturbation solution at $z = 0$ 68
2.22 Vertical section of upper-layer perturbation solution 68
2.23 Perturbed lower-layer thickness 69
2.24 Lower-layer geostrophic pressure 70
2.25 Growth rate curves for secondary modes 71
2.26 Phase speeds for secondary modes 72
2.27 Spatial structure of secondary modes 73
2.28 Maximum growth rate vs. μ for parabolic front 74
2.29 Upper-layer streamfunction at $z = -1$ in simulation of parabolic front 76
2.30 Upper-layer streamfuction at $z = 0$ in simulation of parabolic front . 77
2.31 Perturbation growth rate vs. time in simulation of parabolic front . . 78

3.1 Lower layer thickness in plume simulation 83
3.2 Upper layer pressure in plume simulation 84
3.3 Average velocity 50 km downstream from inflow 85
3.4 Plume penetration distance for series EXP1 90
3.5 Lower layer thickness in simulation EXP2 95
3.6 Upper layer pressure in simulation EXP2 96
3.7 Close-up of eddy in simulation EXP2 97
3.8 Eddy formation period vs. μ 100

4.1 FG-CS model geometry 105
4.2 Marginal stability curves for gently sloping wedge front, $N = 0$ 130
4.3 Marginal stability curves for gently sloping wedge front, $N > 0$ 132
4.4 Instability characteristics for gently sloping wedge with $N = 0.5$ . . . 133
4.5 Instability characteristics for gently sloping wedge with $N = 1.0$ . . . 134
4.6 Marginal stability curves for FG-SW model and QG model 135
4.7 Instability characteristics for gently sloping wedge predicted by linear theory 140
4.8 Lower layer perturbation vertical section predicted by linear theory . 142
4.9 Instability characteristics for exponential front predicted by linear theory 144
4.10 Lower layer pressure perturbation obtained with spectral technique . 146
4.11 Upper layer thickness perturbation obtained with spectral technique . 147
4.12 Lower layer pressure perturbation resulting from direct simulation . . 148
4.13 Upper layer thickness perturbation resulting from direct simulation . 149
4.14 Streamfunctions during nonlinear stage of growth 150
4.15 Upper layer thickness in simulation step1-I 159
4.16 Lower layer pressure in simulation step1-I 160
4.17 Streamfunction plots for simulation step1-O 162
4.18 Diagnostics for axisymmetric current simulations 164
4.19 Streamfunction plots for simulation flat2 167
4.20 Azimuthal eddy transports 168

5.1 CS-FG-CS model geometry 174
5.2 Middle layer thickness in Meddy simulation 186
5.3 Upper layer pressure in Meddy simulation 188
5.4 Trajectories of Meddies and centroid 190

A.1 SW-FG-SW model geometry 200

Chapter 1

Introduction

1.1 Motivation

Density-driven currents occur throughout the world's oceans, and are characterized by a balance between the pressure force due to sloping isopycnals and the Coriolis force. They are often associated with sharp horizontal and vertical density gradients that separate water masses with different physical, chemical and biological properties. Distinct, relatively fast-flowing currents may be found at all depths in the ocean. Surface currents typically develop due to buoyancy inputs and wind stress. They generally fall into two categories, western boundary currents and eastern coastal currents. Dense, bottom waters form through atmospheric cooling and brine rejection from sea ice, and subsequent open-ocean convection or descent along sloping topography. They tend to migrate equatorward as concentrated currents, flowing along continental shelves and oceanic ridges.

Outflows from marginal seas often equilibrate at intermediate depths, the most prominent example being the Mediterranean salt tongue, which extends far into the interior of the North Atlantic. Dynamically, the effects of these flows, and the associated mesoscale phenomena, are crucial for the general circulation of the global ocean. *Via* the thermohaline circulation, the oceans play an important role in natural climate variability, and account for approximately 10%–20% of the total meridional heat transport (Trenberth and Caron 2001).

Many fronts intersect the sea surface or the bottom topography. In order to describe these flows correctly using the multi-layer approach, it is necessary to allow the thickness of the frontal layer(s) to vanish. This is in contrast to quasigeostrophic layered models, which only permit small deformations of the interface(s). In quasigeostrophic theory the leading order mass conservation equation reduces to the statement that the velocity is divergence-free. In frontal models, on the other hand, the frontal layer is governed by a fully nonlinear mass conservation equation, allowing for O(1) thickness variation.

The governing equations in such models are still geostrophic to leading order however, reflecting that most oceanic currents are roughly in geostrophic balance. A small Rossby number, ε, results not from the requirement of small velocities, as in quasigeostrophic theory, but from the condition that the dynamic lengthscale L is much larger than the internal deformation radius R. Since $\varepsilon = (R/L)^2$, we only require that $L^2 \gg R^2$, not $L \gg R$. Consequently, (adopting the notion that a factor of 10 corresponds to an "order of magnitude") flows for which $L > \sqrt{10}R$ may already fall in this regime (Cushman-Roisin 1986). These are the flows on which we will focus in this study.

Reduced models are often advantageous in that they demonstrate more clearly than primitive equation models the physical processes and dynamical balances operative in particular phenomena. This is certainly true of QG theory, however the models we present here offer a more accurate representation of frontal dynamics (e.g. Cushman-Roisin and Tang 1989). Furthermore, by introducing appropriate scalings and approximations (e.g. subinertial scalings) it is possible to filter out processes (such as inertia-gravity waves) which are unlikely to affect the overall flow evolution. This allows larger timesteps in numerical integrations and eliminates potential sources of error.

A practical motivation for developing simplified theories is that general circulation models (GCMs) are presently unable to resolve mesoscale phenomena associated with boundary currents, bottom water spreading and topographic interactions (Griffies *et al.* 2000). This leads to significant inaccuracies in overall heat and salinity transports as well as mixing rates. Process studies can suggest ways of improving parameterizations within GCMs, and simple models could be nested, in principle, within GCMs at particularly under-resolved locations.

1.2 Model Classification

Layer models derived and discussed in this thesis are classified as follows. Each layer is designated by one of four two-letter codes, such that the order of codes in a model name starts with the uppermost layer and continues with deeper layers. Each code is based on the dynamical property that most clearly differentiates a given layer from the other layers. The codes FG and PG refer to the Frontal Geostrophic and Planetary Geostrophic scalings (see below), respectively. Layers designated by these codes are always homogeneous, and governed by a reduced form of shallow water theory.

Layers which are not FG or PG are governed by quasigeostrophic dynamics. The codes SW and CS differentiate between the Shallow-Water and Continuously-Stratified versions of the quasigeostrophic formalism, respectively. Table 1.1 lists the six models we discuss, and references most of the relevant contributions to the development of each model. As the table suggests, the present work may be viewed as a continuation and extension of the general theory of baroclinic dynamics in the context of oceanic fronts, with a special focus on the model of Poulin and Swaters (1999a).

The goal in developing reduced theories, rather than dealing with the primitive equations themselves, is to arrive at an optimal description of a given phenomenon. It is hoped that the physical mechanisms retained are the ones that determine the

model	derivation	linear analysis	numerical simulations
SW-PG	SF, S91	S91	KST, S98, **chapter 2**
CS-PG	PSa	PSa, **chapter 2**	**chapters 2, 3**
FG-SW	S93	R97, RS99a	RS99a, RS99b, **chapter 4**
FG-CS	**chapter 4**	**chapter 4**	**chapter 4**
SW-FG-SW	**appendix A**	future	**chapter 5**
CS-FG-CS	**chapter 5**	future	future

Table 1.1: Models discussed in this thesis, and previous relevant work. The dynamical limits SW (Shallow-Water), CS (Continuously-Stratified), PG (Planetary Geostrophic) and FG (Frontal Geostrophic) are discussed in the text. For an explanation of reference acronyms, see table 1.2.

qualitative (and to some degree, quantitative) properties of the process. In the oceanographic context, the multi-layer approximation can often illuminate the physics with just two or three layers (Pedlosky 1996). All the models we describe have two or three layers, where the frontal layer is homogeneous. The latter assumption is reasonable in situations where the density variations are relatively small outside the frontal region, and are not likely to influence significantly the evolution of the front.

The water mass associated with the current may be more homogenous than the ambient ocean for the following reasons. Surface waters are typically subject to wind action, which tends to aid mixing. Also, before geostrophic adjustment, intrusions at depth often form from dense water cascades across steep topography, a process which, again, induces mixing. The ambient layer in our models, as is often the case in the real ocean, comprises most of the fluid column, and is allowed to be continuously-stratified. The stratification is assumed to be relatively weak, as we want to focus on the baroclinic dynamics associated with the deforming layer interface. As it turns out, in oceanographic applications of interest here, this assumption is not unreasonable. Nevertheless, we find that even modest stratification has a significant effect on observed instability characteristics.

The CS-PG model is an extension of a two-layer model that was introduced, in the context of abyssal currents, in Swaters (1991). It includes stratification in the upper layer, but uses similar scalings as Swaters and Flierl (1991) and Swaters (1991). In particular, the lower layer velocity is scaled such that the only contribution to the final balance from the momentum equations is the geostrophic relation. However, time derivative and nonlinear advective terms in the continuity equation for the abyssal current are retained at leading order. This approximation is termed planetary geostrophic (PG). An important aspect of the CS-PG scaling is that the abyssal current is buoyancy-driven and topographically-steered.

Upper layer dynamics is governed by quasigeostrophic theory, and upper layer velocities are driven by deformations of the interface through vortex stretching, in the presence of a topographically-induced potential vorticity gradient. While geostrophic flow is purely along sloping topography, ageostrophic effects permit down-slope motion, which results in release of gravitational potential energy. Our derivation of CS-PG is slightly more general than in Poulin and Swaters (1999a), as we have introduced source/sink terms, the beta effect and a simple bottom drag parameterization.

We present a new theory for surface-intensified currents, here called FG-CS. The governing equations are a generalization of the model presented in Swaters (1993) (see also Cushman-Roisin, Sutyrin, and Tang 1992). We have introduced stratification in the lower layer, as well as source/sink terms and the beta effect. As pointed out in Swaters (1993), the dynamics of buoyancy-driven currents is fundamentally different from that of abyssal currents in that potential energy can be released only by spreading outward. In this model the scaling for the frontal layer velocities is such that the advective terms from the momentum equation enter the first nontrivial balance. As with CS-PG, the mass conservation equation for the current is fully nonlinear. This dynamic regime is traditionally called frontal geostrophic (FG). Previous linear, weakly-nonlinear and numerical studies demonstrated that the Swaters (1993) equations exhibit explosive growth in some parameter regimes, leading to development of prominent warm core and cold core eddies (Reszka and Swaters 1999a; Karsten and Swaters 2000b). Here we investigate the effect of a stratified lower layer. An assumption of the FG-CS and FG-SW models is that the surface current is buoyancy-driven and is influenced by topography only through interaction with the lower layer.

A three layer model, CS-FG-CS, is derived in which the middle layer is FG, while the outer layers are continuously-stratified and quasigeostrophic. The analogous model with three homogeneous layers, SW-FG-SW, is obtained as a limiting case and also derived from the primitive equations. These two models are expected to prove useful in studying aspects of the Mediterranean outflow and Meddy dynamics (see section 1.3). Destabilization of intermediate-depth boundary currents has been studied, so far, mainly in the laboratory. Analytical theories that elucidate baroclinic dynamics at mid-depth are lacking in the literature. While the FG-CS, SW-FG-SW and CS-FG-CS governing equations are based on the scaling in Swaters (1993), to our knowledge they have not been derived before. We have not analyzed the three-layer models in detail, however a preliminary simulation is presented.

It must be remembered that we have made a number of simplifying assumptions and have neglected various physical processes, which may or may not play a role in the dynamics. Our derivations assume Cartesian coordinates, with a Coriolis parameter that varies only linearly in the meridional direction (the β-plane). The latter assumption is justified for domains of a few hundred kilometers, however Karsten and Swaters (1999) demonstrated that metric terms associated with approximating a spherical geometry by rectangular coordinates may be important, especially at high latitudes. These metric terms are neglected in our study, to allow more straightforward comparison with previous investigations. A very general derivation and analysis of two-layer reduced models can be found in Karsten and Swaters (1999, 2000a, 2000b). This series of papers includes a discussion of the SW-PG and FG-SW dynamical limits. A linear analysis and numerical simulations of axisymmetric currents in the context of the SW-PG model appeared in Choboter and Swaters (2000). Other investigations will be introduced as needed.

acronym	explanation
CL	Cenedese and Linden (2002)
DSO	Denmark Strait Overflow
IDBC	Intermediate-Depth Boundary Current
KS99, KS00a, KS00b	Karsten and Swaters (1999, 2000a, 2000b)
KST	Karsten, Swaters, and Thomson (1995)
PSa,b	Poulin and Swaters (1999a, 1999b)
R97	Reszka (1997)
RS99a,b	Reszka and Swaters (1999a, 1999b)
RS01	Reszka and Swaters (2001)
RSS	Reszka, Swaters, and Sutherland (2002)
S91, S93	Swaters (1991, 1993)
SOG	Strait of Georgia

Table 1.2: Some acronyms used throughout this thesis.

The thesis is organized as follows. The rest of this chapter is devoted to a description of specific situations where our models will be applied. In chapter 2 we derive the CS-PG model, develop the linear instability analysis, present numerical simulations applicable to the SOG and also a simulation that corroborates the linear theory results. In chapter 3 the linear theory is applied to the Denmark Strait Overflow, and numerical simulations of dense plumes are discussed. Chapter 4 consists of a derivation of the FG-CS model, and the corresponding linear instability calculation. Simulations of unstable axisymmetric currents are also presented.

In chapter 5 we derive the CS-FG-CS model and briefly discuss numerical simulations of a mid-depth lens. Appendix A contains a derivation of the SW-FG-SW model, while details of our numerical scheme are given in Appendix B. Much of the work described herein has been published already. In particular, chapters 1, 2 and 3 contain text and figures that appear in Reszka and Swaters (2001) and Reszka *et al.* (2002). We will also refer to a number of other papers, which are highly relevant to this study. For greater readability, acronyms will be used for references and proper names that appear frequently in the text. An alphabetized list of these acronyms is provided in Table 1.2.

1.3 Case studies discussed in this thesis

1.3.1 Strait of Georgia deep water replacement

The evolution of deep water is important in the local dynamics of marginal seas, estuaries and other coastal areas (Price and Baringer 1994). Episodic intrusions of bottom water off the coast of British Columbia, Canada are often characterized by considerable spatial and temporal fluctuations (LeBlond, Ma, Doherty, and Pond 1991). In particular, the dynamics of deep water replacement in the Strait of Georgia (henceforth SOG) received a great deal of attention when it became apparent that the deep current variability is associated with the development of small, bottom-intensified vortical anomalies.

The SOG is a long, narrow channel between Vancouver Island and mainland British Columbia, with dimensions of roughly 40 km by 280 km. Typical depths for the central part of the strait are 300–400 m, although there are shallow sills at the northern end, which inhibit free exchange with continental shelf waters. Estuarine circulation is primarily driven by freshwater discharge from the Fraser River. Tidal currents, formation of fronts, and deep water renewal are all known to occur in the SOG (LeBlond *et al.* 1991, and references therein).

A detailed as well as intriguing data set was obtained by Stacey, Pond, LeBlond, Freeland, and Farmer (1987) regarding the low-frequency dynamics of a dense, bottom-trapped current in the SOG. This survey employed a high-resolution array of cyclosonde and current-meter moorings which gathered data from June, 1984 to January, 1985 in one region of the strait. The moorings were placed close enough together that small scale features on the order of a few kilometers could be resolved. Subsequent analyses (Stacey, Pond, and LeBlond 1988, 1991) revealed highly-nonlinear flowfields with relatively short time scales. There was clear evidence of bottom-intensified cyclonic and anticyclonic eddies, with length scales on the order of 10 km. It was suggested that the high degree of spatial and temporal variability within the strait was, at least sometimes, the result of baroclinic instability.

1.3.2 Denmark Strait Overflow

Considerable interest has been generated in the past few years by observations of deep current fluctuations and intense vortices south of the Denmark Strait Overflow (henceforth DSO). Located between Greenland and Iceland, Denmark Strait is approximately 480 km long and 290 km wide. This relatively shallow strait (500 m depth) opens up into the much deeper Irminger Basin (maximum depth 4000 m). Observations show a vein of dense water flowing south through the Denmark Strait and along the western slope of the Irminger Basin. The dense fluid often appears as discrete plumes, or boluses (Cooper 1955), and exhibits a high degree of time variability with a dominant period of 2–3 days (Dickson and Brown 1994). Concurrently, strong eddies roughly 30 km in diameter are generated in the ambient ocean, which travel along isobaths at an average of 27 cm/s, with a small but detectable velocity component away from the shore (Bruce 1995).

Since the period of these eddies could not be correlated with atmospheric or tidal forcing, it is likely that they owe their existence to the intrinsic dynamics of the deep and/or intermediate flow. While the sense of rotation associated with the observed vortices is predominantly cyclonic (Bruce 1995), recent hydrographic surveys also indicate the presence of anticyclones. Fig. 1.1 (reproduced from Krauss and Käse 1998) is a plot of dynamic topography southwest of Denmark Strait, based on a

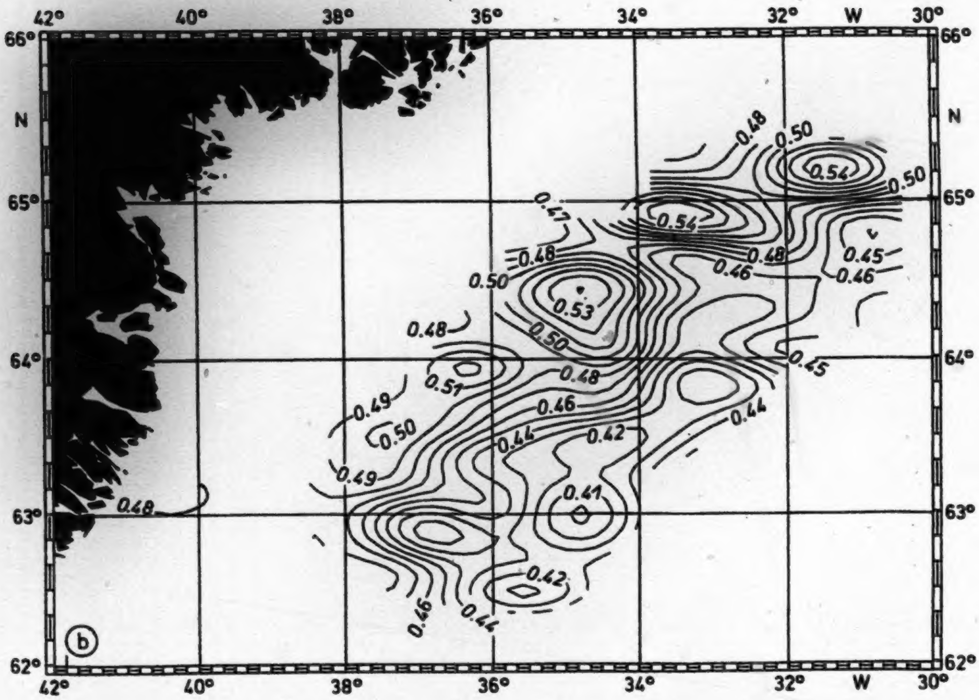

Figure 1.1: Plot of the dynamic topography southwest of the Denmark Strait, based on hydrographic data from the 1996 survey of R/V Poseidon. Closed contours indicate vortical motion, where local maxima and minima correspond to anticyclonic and cyclonic flow, respectively. Anticyclones are found closer to shore than cyclones. Plot reproduced from fig. 1 in Krauss and Käse (1998).

1996 hydrographic survey. Subtracting the mean (about 0.47), the contours mark positive and negative anomalies, which indicate anticyclonic and cyclonic motion, respectively[1]. The presence of anticyclones and their relative location (closer to shore than cyclones) will be an important aspect of our discussion in chapter 3.

The numerical investigation of Jiang and Garwood Jr. (1996) showed that the descent of a dense plume over linearly sloping topography results in the formation of subplumes through baroclinic instability, with an accompanying eddy field in the ambient ocean. Employing a 3-layer shallow water model, Spall and Price (1998) proposed that the development of strong cyclones is mainly caused by vortex stretching of the intermediate outflow layer, which is drawn offshore due to the thermal wind relation. In their theory, the thermal wind arises from a drag-induced descent of dense water, without the need for instability in the overflow layer. The recent numerical study of Jungclaus, Hauser, and Käse (2001) indicates that the above two mechanisms are not mutually exclusive, and that the instability regime depends on the local value of the Rossby number.

---

[1] We point out that the interpretation of Fig. 1.1 is not entirely straightforward, since the plot is based on near-bottom velocity measurements relative to those at 1000 m depth, where eddy kinetic energies are known to be significant (Spall and Price 1998).

In their computational study of DSO dynamics, Jungclaus *et al.* (2001) considered a bottom-trapped flow in a periodic channel domain. After geostrophic adjustment, the current was found to deform through baroclinic instability, with accompanying cyclonic and anticyclonic eddies in the overlying fluid. The authors argued that subsequent intensification of the cyclones was the result of nonlinear vorticity advection. Other relevant computational efforts include Jiang and Garwood Jr. (1995), Gawarkiewicz and Chapman (1995) and Shi, Røed, and Hackett (2001). The effect of steep topography on offshore transport was numerically investigated by Kikuchi, Wakatsuchi, and Ikeda (1999), Gawarkiewicz (2000) and Tanaka and Akitomo (2001).

1.3.3 Instability in the California Current

The California Current, flowing along the west coast of North America as far north as British Columbia, Canada, is a good example of an upwelling front, and has been studied both observationally and theoretically. Isopycnals tend to slope downward in the offshore direction, and geostrophic balance induces an equatorward flow throughout most of the year (Ikeda and Emery 1984). Cold, nutrient-rich water upwells near the coast, with beneficial effects on the ecosystem. Meanders, long filaments and eddies have all been observed in association with the surface-intensified current (Ikeda and Emery 1984; Ikeda, Emery, and Mysak 1984). Filaments and cyclonic eddies are of particular significance ecologically, as they transport the upwelled water toward the interior of the ocean (Haidvogel, Beckmann, and Hedström 1991).

Observed meanders typically have wavelengths on the order of 100 km and phase speeds close to 10 cm/s. The instability responsible for deforming the front is believed to be baroclinic, or mixed, baroclinic-barotropic (Shi and Røed 1999). Barth (1989b) solved the linear problem in a two-layer shallow water model, and found that the unstable wave motions were dominant in the upper layer and frontally trapped. The propagation speed was in the direction of the mean flow. Topography that sloped in the same sense as the front served to decrease growth rates. As noted by Ikeda *et al.* (1984) however, deep stratification, even if it is weak, supports a surface intensified mode that should not be neglected in modelling studies of the California Current. Barth (1994) conducted a similar study as Barth (1989b), but using the Boussinesq equations. He found the conventional baroclinic mode that was surface intensified but present throughout the fluid column, as well as a short-wave frontal mode trapped near the surface.

1.3.4 Axisymmetric surface currents

Among the many recent investigations of frontal instabilities at the shelf break is the laboratory study of Cenedese and Linden (2002, henceforth, CL). They conducted experiments on buoyant axisymmetric currents in a rotating frame, in order to assess the role of different topographic configurations. A ring source at the inner wall of an annular tank provided a constant supply of buoyant fluid, which formed a geostrophically-balanced azimuthal current. The interface between the buoyant current and the ambient fluid sloped upward in the radial direction, forming an outcropping front. In addition to flat topography, three configurations were employed for the tank bottom, whose radial profiles were: a step, a linear slope, and a step adjacent to a slope. The variable topographies all became deeper in the radial direction so that, in analogy with a coastal shelf, the inner annulus boundary played the role of a coastline. Roughly speaking, then, the front always sloped in the opposite sense to the topography.

After the width of the current reached several Rossby radii, a wavelike instability was always observed at the outcropping. The instability was believed to be largely baroclinic in nature. The dominant wavelength was inversely related to the Froude number, and was several times the Rossby radius. Typically, growth of these waves lead to the development of anticyclonic eddies, which sometimes pinched off, while at other times they remained attached to the main body of the current. Often the vortices were reabsorbed establishing a new axisymmetric front, which outcropped farther from the center than the original one. The new, wider current was subject to the same kind of instability as before. It was found that step topography inhibits the spreading of buoyant fluid, thus temporarily trapping it near the coast. Linearly sloping topography trapped the fluid on the shelf to a lesser degree, but was also found to significantly impede the instability process. The latter result, while not inconsistent with the usual QG stability criteria, does seem counterintuitive in the QG context (see section 4.4.7).

1.3.5 Mediterranean outflow and Meddies

Intermediate water masses can be found at a number of locations in the world ocean, and contribute significantly to inter-basin exchange. They often form boundary currents and isolated lenses. Such intermediate depth eddies have been associated with, for example, Levantine Intermediate Water (Leddies) and the Mediterranean outflow (Meddies) (Baey, Renouard, and D'Hieres 1995). Warm, salty Mediterranean water spills over the sill of the Strait of Gibraltar, cascades down the continental slope, and finds its equilibrium at depths of 500–1500 m (Richardson, Bower, and Zenk 2000). Following the coast of the Iberian Peninsula, it flows westward and then northward as the Mediterranean Undercurrent (Price and Baringer 1994).

Large portions of this current separate and form anticyclonic lenses, called Meddies, which then migrate into the interior of the North Atlantic. The processes of

Meddy detachment are not well understood at this point, although baroclinic instability and interaction with the Cape of St. Vincent are likely to play a role. Intermediate Depth Boundary Currents were studied numerically by Jungclaus (1999), and in the laboratory setting by Davies, Fernando, Besley, and Simpson (1991), Baey *et al.* (1995), Sadoux, Baey, Fincham, and Renouard (2000), Folkard and Davies (2001) and others.

The term Meddy was coined by McDowell and Rossby (1978), who observed a subsurface eddy composed of warm, salty water north of Hispañola. Their conclusion that the eddy contained Mediterranean water, and must have therefore traversed at least 6000 km, initiated a wave of intense investigation within the observational and theoretical oceanography communities. Surprisingly, Prater and Rossby (1999) argue that the eddy observed in the Bahamas was not a Meddy, but in fact originated near Newfoundland, and was advected southward by Gulf Stream recirculations. Nevertheless, Meddies are ubiquitous in the North Atlantic and are important in the transport of heat and salinity. They range in diameter from 40 to 150 km, and their cores are typically found at depths of 800–1400 m (Richardson *et al.* 2000). Azimuthal velocities of 30 cm/s are not uncommon, and are often measured over the entire water column. Approximately 17 Meddies are produced every year, and their average lifespan is about 1.5 years. Mesoscale lenses almost invariably exhibit a gradual southwestward drift, a topic that was investigated analytically and numerically by, among others, Killworth (1983), Flierl (1984) and Cushman-Roisin, Chassignet, and Tang (1990).

Chapter 2

CS-PG Model

2.1 Model Equations

The original derivation of the CS-PG model on an f-plane may be found in PSa. Here we derive a somewhat more general set of equations, which includes the beta effect, as well as a mass source and simple bottom drag. The model employs a two-layer configuration, in which the interface is allowed to intersect the topography and upper-layer motions are driven by vortex tube stretching associated with deformations of the interface, in the presence of a topographically-induced background vorticity gradient. An important aspect of the theory is the scaling for the abyssal current velocity, which we discuss presently.

2.1.1 The Nof velocity

In geostrophic equilibrium, a bottom-trapped mass of dense fluid tends to follow topographic contours, with little or no cross-slope motion. Consider topography $z = s^*y$, such that x points along the slope and y points across the slope. Neglecting processes such as instability, interaction with the ambient ocean and Ekman draining,

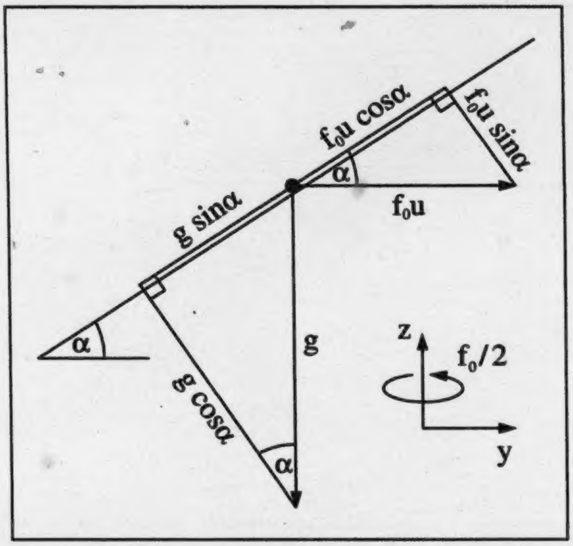

Figure 2.1: Simple diagram showing the force balance for a point mass in geostrophic equilibrium, situated on linearly sloping topography. Here the x coordinate points out of the page.

the steady along-slope velocity of an isolated patch of dense fluid is then given by

$$\mathbf{u}_{\text{Nof}} = \left(\frac{-g' s^*}{f}, 0 \right), \tag{2.1.1}$$

where g' is the reduced gravity and f is the local Coriolis parameter (Nof 1983). While the original derivation of the Nof velocity (2.1.1) referred explicitly to an isolated dome of fluid in the context of one-layer shallow water theory, a simple force balance shows that (2.1.1) holds for each fluid parcel individually. Fig. 2.1 shows a unit point mass situated on a frictionless incline with slope $s^* = \tan(\alpha)$, acted on by gravity and the Coriolis force. Here we denote the along-slope (perpendicular to the page) component of velocity by u. If there is no cross-slope motion, then the projections of the gravitational and Coriolis forces onto the incline must be equal in magnitude and opposite in direction, i.e. $fu\cos(\alpha) = -g\sin(\alpha)$. Solving for u, we obtain

$$u = -\frac{g}{f}\tan(\alpha) = -\frac{gs^*}{f}, \tag{2.1.2}$$

in agreement with (2.1.1). In this coordinate system, if f and s^* are both positive, then $u < 0$ (i.e. the flow is into the page).

This force balance is also applicable, in an average sense, to bottom-trapped currents. Given a homogeneous current with height $h(y)$, the average geostrophic along-slope speed is simply

$$u_{\mathrm{avg}} = -\frac{g'}{f(b-a)} \int_a^b \left(s^* + \frac{\mathrm{d}h}{\mathrm{d}y} \right) dy, \tag{2.1.3}$$

if the cross-slope extent of the current is given by $a < y < b$. Simplifying,

$$u_{\mathrm{avg}} = -\frac{g'}{f} \left(s^* + \frac{1}{b-a} h(y)\Big|_a^b \right), \tag{2.1.4}$$

we see that whenever $h(a) = h(b)$ the contribution from the current height vanishes, and we are left with the Nof speed. Many geostrophic bottom-dwelling flows are isolated in the cross-slope coordinate, such that $h(a) = h(b) = 0$ (Meacham and Stephens 2001). Because the dense plumes south of Denmark Strait also seem to exhibit this property, we feel that the Nof velocity is highly relevant to that case. The above argument may be extended to include bottom friction, which results in a reduced along-slope component of the Nof velocity and a non-zero cross-slope component in the down-hill direction.

Given conditions favorable to instability, such a water mass will gradually give up its gravitational potential energy as it slowly descends down the incline. This mechanism is somewhat different from potential energy release due to the flattening of isopycnals, since an isolated patch of lower-layer fluid can, at least conceptually, migrate into deeper water without any flattening of the interface. This process cannot be described by traditional quasigeostrophic (QG) theory, and is frequently under-resolved in GCMs (Griffies *et al.* 2000). The governing equations introduced in PSa are more general than those in S91 in that they allow the ambient layer to be continuously-stratified and can describe the vertical structure of the evolving flow fields.

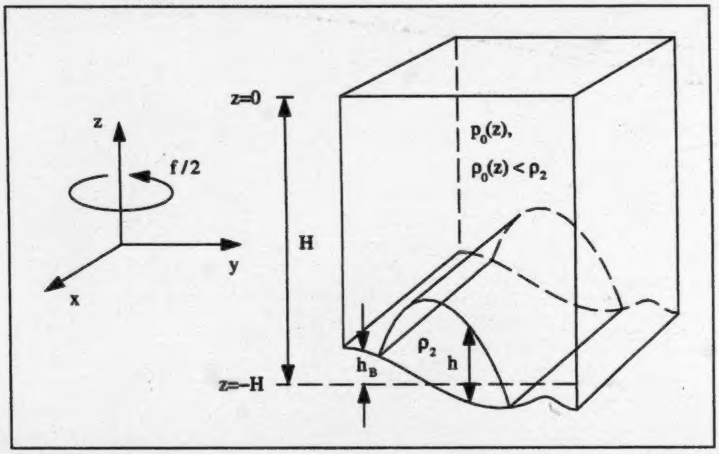

Figure 2.2: CS-PG model geometry. A deep but finite continuously-stratified layer overlies a thin, homogeneous layer situated on sloping, or otherwise varying, topography. The interface is allowed to intersect the topography, thus forming true fronts.

2.1.2 Model Derivation

A schematic of the model geometry is shown in Fig. 2.2. Analyses of oceanographic observations imply that bottom waters often take the form of coherent, isolated patches of fluid. As mentioned previously, it is a key feature of the present model that it permits O(1) variations of the interface. We assume that the density of the upper layer (layer 1) consists of a z-dependent background density $\rho_0(z)$, plus a density fluctuation $\rho(x, y, z, t)$ that is in hydrostatic balance with the upper-layer dynamic pressure (the part of the total pressure independent of z). The lower layer (layer 2) has a constant density, $\rho_2 > \rho_0(z)$, and its dimensional thickness scale h_* is given by δH, where H is the total fluid depth and $\delta < 1$.

In what follows, unscaled quantities will typically have a superscript asterisk, to differentiate them from their nondimensional counterparts. We begin by considering the lower layer. A term, $Q_2^*(x^*, y^*)$, corresponding to a constant mass flux of dense fluid, will appear in the mass conservation equation. In this formulation, Q_2^* has the dimensions of velocity and represents an imposed time rate of change in lower-layer thickness at a given point (x^*, y^*). Introduction of dense fluid is of interest in regional studies of, for example, dense overflows, such as the ones we discuss later in this chapter and in chapter 3.

Derivation of the lower-layer equation begins with shallow water theory on a β-plane, where the right-hand side of the momentum equation includes a simple parameterization for bottom drag in the form of Rayleigh damping,

$$\mathbf{u}^*_{2t^*} + (\mathbf{u}^*_2 \cdot \nabla^*)\mathbf{u}^*_2 + (f_0 + \beta_0 y^*)\mathbf{e}_3 \times \mathbf{u}^*_2 = -\frac{1}{\rho_2}\nabla^* p^* - C^*_d \mathbf{u}^*_2, \tag{2.1.5}$$

$$h^*_{t^*} + \nabla^* \cdot (\mathbf{u}^*_2 h^*) = Q^*_2. \tag{2.1.6}$$

Here $\mathbf{u}^*_2 = (u^*_2, v^*_2)$, $\nabla^* = (\partial_{x^*}, \partial_{y^*})$, p^* and h^* are the lower-layer horizontal velocity, horizontal gradient operator, dynamic pressure and layer thickness, respectively.

Bottom drag will play a minor role in this dynamic regime, and in practice the drag coefficient, C^*_d will be relatively small. A similar drag parameterization was used in Samelson and Vallis (1997), Samelson (1998) and Choboter and Swaters (2002). Although it is simple, this form of drag nevertheless allows down-pressure-gradient flow, while it still allows us to utilize a streamfunction-vorticity formulation in the final equations. The parameterization captures the essential feature of Ekman layer dynamics for a homogeneous quasigeostrophic fluid, in which bottom friction due to the presence of an Ekman layer results in a damping term in the potential vorticity equation that is (negatively) proportional to the relative vorticity (Pedlosky 1987). This is clear upon taking the curl of (2.1.5).

The Boussinesq system for the upper layer (layer 1) may be written

$$\mathbf{u}^*_{1t^*} + (\mathbf{u}^*_1 \cdot \nabla^*)\mathbf{u}^*_1 + w^* \mathbf{u}^*_{1z^*} + (f_0 + \beta_0 y^*)\mathbf{e}_3 \times \mathbf{u}^*_1 = -\frac{1}{\rho_*}\nabla^* p^*_1, \tag{2.1.7}$$

$$\rho_*(w^*_{t^*} + (\mathbf{u}^*_1 \cdot \nabla^*)w^* + w^* w^*_{z^*}) = -p^*_{1z^*} - g\rho^*, \tag{2.1.8}$$

$$\rho^*_{t^*} + (\mathbf{u}^*_1 \cdot \nabla^*)\rho^* + w^* \rho^*_{z^*} = 0, \tag{2.1.9}$$

$$\nabla^* \cdot \mathbf{u}^*_1 + w^*_{z^*} = -\frac{Q^*_1}{H - h^*_B - h^*}, \tag{2.1.10}$$

where $\mathbf{u}^*_1 = (u^*_1,\ v^*_1)$, w^*, ρ_*, p^*_1 and ρ^* are, respectively, the upper-layer horizontal velocity, vertical velocity, constant reference density, total pressure and dynamic density field (the part of the density that is in balance with the dynamic pressure). To facilitate conservation of total volume for the two-layer system, a negative flux, $Q_1^*(x^*, y^*)$, has been introduced in the upper-layer mass conservation equation, distributed uniformly over the depth of the ambient fluid. Uniform vertical distribution of the sink was assumed mainly for simplicity, and more realistic choices are possible. Here h_B^* is the topographic height above $z^* = -H$, so that $H - h_B^* - h^*$ is the dimensional thickness of the upper layer. The motivation for introducing a sink in this manner will be made more clear in subsection 2.1.6. At this point we simply mention that $Q_1^* \equiv Q_2^* > 0$ corresponds to conversion of upper-layer fluid into lower-layer fluid (or vice versa, if $Q_1^* \equiv Q_2^* < 0$).

Assuming a rigid lid and no flow normal to the bottom topography or fluid interface, the dimensional vertical boundary conditions for the upper layer are

$$w^* = 0, \qquad z^* = 0, \tag{2.1.11}$$

$$w^* = h_{t^*}^* + \mathbf{u}_1^* \cdot \nabla^*(h_B^* + h^*), \qquad z^* = -H + h_B^* + h^*. \tag{2.1.12}$$

The total pressures in the upper and lower layer can be written as, respectively,

$$p_1^*(x^*, y^*, z^*, t^*) = g \int_{z^*}^{0} \rho_0(\xi) d\xi + \varphi^*(x^*, y^*, z^*, t^*), \tag{2.1.13}$$

$$\begin{aligned} p_2^*(x^*, y^*, z^*, t^*) = g \int_{-H+h_B^*+h^*}^{-H} \rho_0(\xi) d\xi + g \int_{-H}^{0} \rho_0(\xi) d\xi \\ + \varphi^*(x^*, y^*, -H + h_B^* + h^*, t^*) + g\rho_2(-H + h_B^* + h^* - z^*), \end{aligned} \tag{2.1.14}$$

where $\rho_0(z^*)$ is the upper-layer hydrostatic density (as mentioned previously) and φ^* is the upper-layer dynamic pressure.

Before expressing the lower-layer pressure as the sum of a hydrostatic part (independent of x and y) and a dynamic part (independent of z), we Taylor expand the 1st and 3rd terms in (2.1.14) about $z^* = -H$, exploiting the fact that $|h^*| \ll H$ and $|h_B^*| \ll H$. We point out that the last assumption only limits variations in topography height over distances comparable to the dynamic lengthscale L_*. An equivalent condition is that topographic gradients are much smaller than the aspect ratio, H/L_*. This is a reasonable assumption for our purposes (see section 2.2 and chapter 3).

The Boussinesq reference density is taken to be that of the lower layer, $\rho_* = \rho_2$. The reduced gravity based on the density difference across the interface is then

$$g' = g\frac{\Delta\rho}{\rho_2}, \quad \text{with} \quad \Delta\rho = \rho_2 - \rho_0(-H). \tag{2.1.15}$$

To leading order, we have

$$p_2^*(x^*, y^*, z^*, t^*) = g\int_{-H}^{0} \rho_0(\xi)d\xi - g\rho_2(H + z^*) + p^*(x^*, y^*, t^*), \tag{2.1.16}$$

where the lower-layer dynamic pressure is given by

$$p^* = \varphi^*|_{z^*=-H} + g'\rho_2(h_B^* + h^*). \tag{2.1.17}$$

We introduce generic scalings for the spatial coordinates,

$$(x^*, y^*) = L_*(x, y), \qquad z^* = Hz, \tag{2.1.18}$$

and remind the reader that

$$h^* = \delta H h, \tag{2.1.19}$$

where $\delta = h_*/H$. The relevant length scale for subinertial baroclinic processes in this regime is the upper-layer internal deformation radius,

$$L_* = \frac{\sqrt{g'H}}{f_0}. \tag{2.1.20}$$

A full discussion of possible dynamical limits for a two-layer fluid may be found in Karsten and Swaters (1999). Roughly speaking however, given our other assumptions, other choices for the lengthscale would lead to an O(1) Rossby number, or topographic steering.

Upper-layer horizontal velocities are assumed to be principally driven by vortex-tube stretching, i.e.

$$\mathbf{e}_3 \cdot (\boldsymbol{\nabla}^* \times \mathbf{u}_1^*) = O(fh_*/H). \tag{2.1.21}$$

Likewise, the upper-layer vertical velocity is scaled according to the vertical motion of the interface,

$$w^* = O(h^*_{t^*}), \tag{2.1.22}$$

and the lower-layer velocity is scaled with the Nof speed,

$$\mathbf{u}_2^* = \frac{g's^*}{f_0}\mathbf{u}_2, \tag{2.1.23}$$

where s^* is a typical topographic slope.

We choose the time scale to be the advective time scale of the lower layer,

$$t^* = \frac{f_0 L_*}{g's^*}t, \tag{2.1.24}$$

while the pressures are scaled geostrophically,

$$p_1^* = g\int_{z^*}^{0} \rho_0(\xi)d\xi + \rho_2\delta(f_0L_*)^2\varphi(x,y,z,t), \qquad p^* = \rho_2 g's^*L_*p, \tag{2.1.25}$$

and the upper-layer dynamic density is scaled hydrostatically with the geostrophic pressure,

$$\rho^* = \rho_0(z^*) + \frac{\rho_2\delta(f_0L_*)^2}{gH}\rho. \tag{2.1.26}$$

Consistent scalings for the bottom topography, sink/source fluxes and drag coefficient are then

$$h_B^* = s^*L_*h_B, \qquad (Q_1^*, Q_2^*) = \delta s f_0 H(Q_1, Q_2), \qquad C_{\mathrm{d}}^* = f_0 C_{\mathrm{d}}. \tag{2.1.27}$$

The beta parameter is scaled according to traditional QG theory, using δ (since this will turn out to be the Rossby number of the ambient fluid),

$$\beta_0 = \delta f_0 \beta / L_*. \tag{2.1.28}$$

At this point we define the topographic parameter, s, by

$$s^* = \frac{H}{L_*}s, \tag{2.1.29}$$

which is typically small for the oceanographic settings in which we are interested. We also introduce the Swaters interaction parameter, μ,

$$\mu \doteq \frac{\delta}{s} \equiv \frac{h_*}{h_B^*}, \tag{2.1.30}$$

which measures the effects of baroclinicity (relative size of h_*) versus topographic effects (relative size of h_B^*) (Swaters 1991). We formally take this ratio to be an O(1) quantity, since δ and s are often of the same magnitude in oceanographic settings of interest (see section 2.2 and chapter 3). This assumption implies that the bottom-trapped flow is both buoyancy-driven and topographically-steered. The regime where δ and s are of similar magnitude is one of a few possible limits that leads to non-trivial dynamics in the two-layer context, assuming a relatively thin but vanishing frontal layer (Karsten and Swaters 1999). We are interested in the dynamics arising from an interplay between buoyancy and topographic effects; however, we note that this assumption is not appropriate for many important oceanic phenomena, such as regimes where the lower-layer velocity is much higher than that in the ambient fluid.

The velocity scalings for layers 1 and 2, respectively, may be related to the gravity wave speed, $\sqrt{g'H}$, as follows,

$$U_1 = \delta\sqrt{g'H} \text{ and } U_2 = s\sqrt{g'H}. \tag{2.1.31}$$

Because we want to focus on subinertial processes and filter out internal gravity wave modes, U_1 and U_2 should be small compared to the typical gravity wave speed, i.e. we must have that $\delta, s \ll 1$. (Surface gravity waves are filtered out by the rigid lid approximation.) One can easily show that δ and s are equivalent to the Rossby numbers for the upper and lower layer, respectively,

$$\delta = \varepsilon_1 \equiv \frac{U_1}{fL_*} \text{ and } s = \varepsilon_2 \equiv \frac{U_2}{fL_*}, \tag{2.1.32}$$

so that μ may be interpreted as a ratio of Rossby numbers. Again, ε_1 and ε_2 are small, and the pressure in each layer is scaled so that geostrophic balance is achieved at leading order.

Substitution of the scalings into the dimensional equations results in

$$s(\mathbf{u}_{1t} + \mu\mathbf{u}_1\cdot\nabla\mathbf{u}_1 + \delta w\mathbf{u}_{1z}) + (1+\delta\beta y)\mathbf{e}_3\times\mathbf{u}_1 = -\nabla\varphi, \tag{2.1.33}$$

$$\left(\frac{sH}{L}\right)^2 (w_t + \mu\mathbf{u}_1\cdot\nabla w + \delta w w_z) = -\rho - \varphi_z, \tag{2.1.34}$$

$$\rho_t + \mu\mathbf{u}_1\cdot\nabla\rho + \delta w\rho_z = N^2(z)w, \tag{2.1.35}$$

$$\nabla\cdot\mathbf{u}_1 + sw_z = -\frac{sQ_1}{1 - sh_B - \delta h}, \tag{2.1.36}$$

$$s(\mathbf{u}_{2t} + \mathbf{u}_2\cdot\nabla\mathbf{u}_2) + (1+\delta\beta y)\mathbf{e}_3\times\mathbf{u}_2 = -\nabla p - C_{\mathrm{d}}\mathbf{u}_2, \tag{2.1.37}$$

$$h_t + \nabla\cdot(\mathbf{u}_2 h) = Q_2, \tag{2.1.38}$$

where the lower-layer pressure is given by

$$p = h_B + \mu(\varphi + h) + O(s), \qquad z = -1. \tag{2.1.39}$$

Since we wish to focus on the baroclinic evolution of the lower layer, we will assume that the effects of ambient stratification are not more significant than those associated with the density jump across the interface. Then, using g' and H, the buoyancy frequency N_* is scaled as follows,

$$N_* = \sqrt{\frac{g'}{H}}N, \qquad \text{where} \qquad N_*^2 \equiv -\frac{g}{\rho_2}\frac{\mathrm{d}\rho_0(z^*)}{\mathrm{d}z^*}, \tag{2.1.40}$$

and where the nondimensional buoyancy frequency N is assumed to be O(1). Equivalently, we may think of N^2 as the Burger number for the upper layer,

$$B \equiv \frac{N_*^2 H^2}{f_0^2 L_*^2}, \tag{2.1.41}$$

which is evident upon substitution of (2.1.20) and (2.1.40) in (2.1.41). Numerical values of B appropriate for oceanographic settings of interest will be discussed later in this chapter and in chapter 3.

The nondimensional boundary conditions become

$$w = 0, \qquad z = 0, \tag{2.1.42}$$

$$w = h_t + \mathbf{u}_1 \cdot \boldsymbol{\nabla}(h_B + \mu h), \qquad z = -1 + s h_B + \delta h. \tag{2.1.43}$$

The second of these is Taylor expanded about $z = -1$, so that to leading order in s,

$$w = h_t + \mathbf{u}_1 \cdot \boldsymbol{\nabla}(h_B + \mu h), \qquad z = -1. \tag{2.1.44}$$

2.1.3 Governing Equations

Next, we expand all variables in the small parameter s (or, equivalently, in δ),

$$(\mathbf{u}_1, \varphi, \rho, w, \mathbf{u}_2, p, h) = (\mathbf{u}_1, \varphi, \rho, w, \mathbf{u}_2, p, h)^{(0)} + s(\mathbf{u}_1, \varphi, \rho, w, \mathbf{u}_2, p, h)^{(1)} + \ldots \tag{2.1.45}$$

The O(1) problem is

$$\mathbf{u}_1^{(0)} = \mathbf{e}_3 \times \boldsymbol{\nabla}\varphi^{(0)}, \qquad \boldsymbol{\nabla} \cdot \mathbf{u}_1^{(0)} = 0, \tag{2.1.46}$$

$$\rho_t^{(0)} + \mu \mathbf{u}_1^{(0)} \cdot \boldsymbol{\nabla}\rho^{(0)} = -N^2 w^{(0)}, \qquad \rho^{(0)} = -\varphi_z^{(0)}, \tag{2.1.47}$$

$$\mathbf{u}_2^{(0)} = \frac{1}{C_\mathrm{d}^2 + 1}(\mathbf{e}_3 \times \boldsymbol{\nabla} p^{(0)} - C_\mathrm{d} \boldsymbol{\nabla} p^{(0)}), \qquad p^{(0)} = h_B + \mu(\varphi^{(0)}|_{z=-1} + h^{(0)}), \tag{2.1.48}$$

$$h_t^{(0)} + \frac{1}{C_\mathrm{d}^2 + 1} \boldsymbol{\nabla} \cdot [h^{(0)}(\mathbf{e}_3 \times \boldsymbol{\nabla} p^{(0)} - C_\mathrm{d} \boldsymbol{\nabla} p^{(0)})] = Q_2, \tag{2.1.49}$$

with boundary conditions

$$w^{(0)} = 0, \qquad z = 0, \tag{2.1.50}$$

$$w^{(0)} = h_t^{(0)} + \mathbf{u}_1^{(0)} \cdot \boldsymbol{\nabla}(h_B + \mu h^{(0)}), \qquad z = -1. \tag{2.1.51}$$

Taking the curl of the O(s) momentum equation and introducing the leading-order relative vorticity, $\zeta_1 = \mathbf{e}_3 \cdot \boldsymbol{\nabla} \times \mathbf{u}_1^{(0)}$, we have

$$\zeta_{1t} + \mu \mathbf{u}_1^{(0)} \cdot \boldsymbol{\nabla}\zeta_1 + \boldsymbol{\nabla} \cdot \mathbf{u}_1^{(1)} = 0, \tag{2.1.52}$$

where the pressure term no longer appears since the curl of the gradient of any twice-differentiable function is zero. The divergence term can be eliminated using the O(s) continuity equation,

$$\boldsymbol{\nabla} \cdot \mathbf{u}_1^{(1)} = -w_z^{(0)} - Q_1, \tag{2.1.53}$$

where $w^{(0)}$ is eliminated by using equations (2.1.47). Dropping the superscripts, the leading-order balance may then be written

$$(\Delta\varphi + (N^{-2}\varphi_z)_z)_t + \mu J(\varphi, \Delta\varphi + (N^{-2}\varphi_z)_z + \beta y) = Q_1, \tag{2.1.54}$$

$$\varphi_{zt} + \mu J(\varphi, \varphi_z) = 0, \qquad \text{on } z = 0, \tag{2.1.55}$$

$$(\varphi_z + N^2 h)_t + \mu J(\varphi, \varphi_z + N^2 h) + N^2 J(\varphi, h_B) = 0, \qquad \text{on } z = -1, \tag{2.1.56}$$

$$h_t + \frac{1}{C_\mathrm{d}^2 + 1} J(p, h) = \frac{C_\mathrm{d}}{C_\mathrm{d}^2 + 1} \boldsymbol{\nabla}\cdot(h\boldsymbol{\nabla} p) + Q_2, \qquad \text{on } z = -1, \tag{2.1.57}$$

where the lower-layer geostrophic pressure is given by

$$p = h_B + \mu(\varphi|_{z=-1} + h). \tag{2.1.58}$$

Here it was convenient to use the Jacobian, $J(A, B) = A_x B_y - B_x A_y$ and subscripts refer to derivatives unless otherwise specified. The nondimensional upper-layer horizontal velocity, vertical velocity and density fluctuation are determined from the auxiliary diagnostic relations

$$\mathbf{u}_1 = \mathbf{e}_3 \times \boldsymbol{\nabla}\varphi, \qquad w = -N^{-2}[\varphi_{zt} + \mu J(\varphi, \varphi_z)], \qquad \rho = -\varphi_z, \tag{2.1.59}$$

respectively. The lower-layer velocity is given by

$$\mathbf{u}_2 = \frac{1}{C_\mathrm{d}^2 + 1}(\mathbf{e}_3 \times \boldsymbol{\nabla} p - C_\mathrm{d}\boldsymbol{\nabla} p), \tag{2.1.60}$$

where p is determined from (2.1.58).

The upper-layer equation (2.1.54) is essentially a statement of QG potential vorticity (PV) conservation for a stratified fluid, where the parameter μ controls the size of the nonlinear terms (cf. Pedlosky 1987). The time-dependent boundary conditions (2.1.55) and (2.1.56) arise from the no-normal-flow condition at the rigid surface and at the fluid interface. The lower-layer equation (2.1.57) expresses the conservation of mass, but equivalently, determines the evolution of the leading-order lower-layer PV, $1/h$. This model has the unsatisfying property that the leading-order PV of the dense layer becomes infinite at incroppings, where h vanishes. However, it does allow description of a wide variety of frontal profiles with spatially-varying PV. We do not make the assumption of a zero PV front, as has been done in some other studies (e.g. Meacham and Stephens 2001). The coupling of equations (2.1.56) and (2.1.57) determines the baroclinic nature of the system as a whole.

If $C_d = 0$ then it is convenient to replace (2.1.56), (2.1.57) with

$$\varphi_{zt} + \mu J(\varphi, \varphi_z) + N^2 J(\varphi + h, h_B) = -N^2 Q_2, \qquad \text{on } z = -1, \tag{2.1.61}$$

$$h_t + J(h_B + \mu\varphi, h) = Q_2, \qquad \text{on } z = -1, \tag{2.1.62}$$

where h was eliminated from (2.1.56) *via* (2.1.62).

2.1.4 Boundary conditions at incroppings

Following Swaters and Flierl (1991), boundary conditions at an incropping are derived as follows, starting with dimensional variables and setting $Q_1 \equiv Q_2 \equiv 0$, $C_d = 0$. In dimensional terms, assume that the projection onto $z^* = 0$ of an incropping is given by $y^* = \xi^*(x^*, t^*)$. We require

$$\left.\begin{aligned} \xi^*_{t^*} + \mathbf{u}^*_2 \cdot \nabla^*(\xi^* - y^*) &= 0 \\ h^* &= 0 \end{aligned}\right\} \text{on } y^* = \xi^*(x^*, t^*). \tag{2.1.63}$$

Scaling h^* as before and employing $\xi^* = L_* \xi$,

$$\xi_t + \mathbf{u}_2 \cdot \nabla(\xi - y) = 0, \tag{2.1.64}$$

$$h = 0, \tag{2.1.65}$$

on $y = \xi(x,t)$. After expanding the variables as in (2.1.45), with

$$\xi = \xi^{(0)} + s\xi^{(1)} + ... \tag{2.1.66}$$

the leading-order quantities must still satisfy conditions (2.1.64), (2.1.65). Since the lower-layer balance is determined at leading order, there is no need to consider higher order corrections to this condition, and we drop the superscript (0).

It must be stressed that evolution of the governing equations forward in time does not require us to compute explicitly the location incroppings. Below we demonstrate that (2.1.62) and (2.1.65) imply (2.1.64). Taking the x derivative and y derivative of (2.1.65) we obtain, respectively,

$$h_x + h_y \xi_x = 0, \tag{2.1.67}$$

$$h_t + h_y \xi_t = 0, \tag{2.1.68}$$

on $y = \xi(x,t)$. Eliminating h_t and h_x from (2.1.62) *via* (2.1.67) and (2.1.68), respectively, and dividing through by h_y yields

$$\xi_t - \mu([\varphi_x]_{z=-1} + \xi_x[\varphi_y]_{z=-1}) - (h_{Bx} + h_{By}\xi_x) = 0. \tag{2.1.69}$$

If we add this to $-\mu\times$(2.1.67), then the result can be written as

$$\xi_t + J(h_B + \mu h + \mu\varphi|_{z=-1}, \xi - y) = 0, \tag{2.1.70}$$

and upon elimination of $h_B + \mu h + \mu\varphi_{z=-1}$ *via* (2.1.60), we recover (2.1.64). Since h vanishes on any incropping by definition, the incropping boundary conditions are automatically satisfied when h_t is determined by (2.1.62). A similar result was obtained for the FG-SW model in Swaters (1993).

2.1.5 Reduction to SW-PG

Here we show that the CS-PG model is an extension of the theory presented in Swaters (1991, henceforth S91), in which both layers were assumed homogeneous. Equations (2.1.54)–(2.1.58) reduce to the S91 theory in the limit of no upper-layer stratification (see RS01). Thus, in the following sections, results for $N = 0$ correspond to the S91 case and, as expected, are consistent with the S91 instability analysis. For simplicity, we set $C_{\rm d} = 0$, although we retain Q_1, Q_2 and β.

To show that the PSa model reduces to the S91 theory in the limit of vanishing z-dependence, we first integrate (2.1.54) in z,

$$\int_{-1}^{0} \left[(\Delta\varphi + (N^{-2}\varphi_z)_z)_t + \mu J(\varphi, \Delta\varphi + (N^{-2}\varphi_z)_z + \beta y)\right] dz = Q_1. \tag{2.1.71}$$

Simplifying, we obtain

$$\begin{aligned}\frac{\partial}{\partial t}\Delta\int_{-1}^{0}\varphi dz + N^{-2}\varphi_{zt}\big|_{z=-1}^{z=0} + \mu\int_{-1}^{0}J(\varphi,\Delta\varphi)dz \\ + \mu N^{-2}J(\varphi,\varphi_z)\big|_{z=-1}^{z=0} - \mu\int_{-1}^{0}N^{-2}J(\varphi_z,\varphi_z) + \mu\beta\int_{-1}^{0}\varphi_x dz = Q_1,\end{aligned} \tag{2.1.72}$$

where the fourth and fifth terms are a result of integration by parts. Rearranging, and realizing that $J(A,A)\equiv 0$ for any differentiable function A, we find

$$\begin{aligned}\frac{\partial}{\partial t}\Delta\int_{-1}^{0}\varphi dz + N^{-2}\left[\varphi_{zt} + \mu J(\varphi,\varphi_z)\right]_{z=0} - N^{-2}\left[\varphi_{zt} + \mu J(\varphi,\varphi_z)\right]_{z=-1} \\ +\mu\int_{-1}^{0}J(\varphi,\Delta\varphi)dz + \mu\beta\int_{-1}^{0}\varphi_x dz = Q_1.\end{aligned} \tag{2.1.73}$$

Substituting the vertical boundary conditions (2.1.55) and (2.1.61) in the second and third terms respectively, the result is

$$\frac{\partial}{\partial t}\Delta\int_{-1}^{0}\varphi dz + J(\varphi|_{z=-1} + h, h_B) + \mu\int_{-1}^{0}J(\varphi,\Delta\varphi)dz + \mu\beta\int_{-1}^{0}\varphi_x dz = Q_1 - Q_2. \tag{2.1.74}$$

Taking the limit $\frac{\partial\varphi}{\partial z}\to 0$, we may write the upper- and lower-layer equations as

$$\Delta\varphi_t + \mu J(\varphi, \Delta\varphi + \beta y) + J(\varphi + h, h_B) = Q_1 - Q_2, \tag{2.1.75}$$

$$h_t + J(\mu\eta + h_B, h) = Q_2, \tag{2.1.76}$$

where $\varphi = \varphi(x,y,t)$,

$$p = h_B + \mu(\varphi + h), \tag{2.1.77}$$

and the velocities are geostrophic as before. Equations (2.1.75)–(2.1.77) represent the same dynamical limit as those presented in Swaters and Flierl (1991) and Swaters (1991) (see also Karsten and Swaters 1999). In terms of our nomenclature, (2.1.75)–(2.1.76) will henceforth be referred to as the SW-PG model. The same equations with $Q_1 \equiv Q_2 \equiv 0$ and $\beta = 0$ will be called the "S91 model".

2.1.6 Mass Conservation

We would like to verify that mass is conserved for the system as a whole, if the sink and source fluxes are equal, $Q_2^* = Q_1^*$. First, we integrate the dimensional upper-layer continuity equation (2.1.10) over the depth of the layer,

$$\int_{-H+h_B^*+h^*}^{0} \nabla^*\cdot\mathbf{u}_1^* + w_{z^*}^* \; dz^* = -Q_1^*. \tag{2.1.78}$$

At this point we need Leibniz's Theorem, which, for differentiable functions $a(x,y)$, $b(x,y)$ and $\mathbf{F}(x,y,z) = (F_x, F_y)$ may be stated as (Kundu 1990),

$$\begin{aligned}\nabla\cdot\int_{a(x,y)}^{b(x,y)} \mathbf{F}(x,y,z)\; dz &= \int_a^b \nabla\cdot\mathbf{F}(x,y,z)\; dz \\ &\quad +\mathbf{F}(x,y,b)\cdot\nabla b - \mathbf{F}(x,y,a)\cdot\nabla a,\end{aligned} \tag{2.1.79}$$

where $\nabla = (\partial_x, \partial_y)$. In the present case, $a = -H + h_B^* + h^*$, $b \equiv 0$ and $\mathbf{F} = \mathbf{u}_1^*$. Then

$$\nabla^*\cdot\int_{-H+h_B^*+h^*}^{0} \mathbf{u}_1^*\; dz^* + \mathbf{u}_1^*|_{-H+h_B^*+h^*}\cdot\nabla^*(h_B^* + h^*) + w^*|_{-H+h_B^*+h^*}^{0} = -Q_1^*. \tag{2.1.80}$$

Substitute in the vertical boundary conditions (2.1.11) and (2.1.12) to obtain

$$\nabla^*\cdot\int_{-H+h_B^*+h^*}^{0} \mathbf{u}_1^*\; dz^* - h_{t^*}^* = -Q_1^*. \tag{2.1.81}$$

Eliminating $h_{t^*}^*$ *via* (2.1.6) and using that $Q_2^* = Q_1^*$,

$$\nabla^*\cdot\int_{-H+h_B^*+h^*}^{0} \mathbf{u}_1^*\; dz^* + \nabla^*\cdot(\mathbf{u}_2^* h^*) = 0. \tag{2.1.82}$$

Since $\mathbf{u}_2$ is z-independent, this may also be written as

$$\nabla^*\cdot\left[\int_{-H+h_B^*+h^*}^{0} \mathbf{u}_1^*\; dz^* + \int_{-H+h_B^*}^{-H+h_B^*+h^*} \mathbf{u}_2^*\; dz^*\right] = 0. \tag{2.1.83}$$

Thus we see that the vertically integrated horizontal mass flux is divergence-free. This as a statement of mass conservation for the fluid.

We now demonstrate that the above balance holds to $O(s^2)$ for the leading-order fields under the governing equations (2.1.54)–(2.1.57). Defining D^* to be the left-hand side of (2.1.83) and nondimensionalizing according to $D^* = \delta f_0 H D$, we have

$$D = \nabla\cdot\left[\int_{-1+sh_B+\delta h}^{0} \mathbf{u}_1\; dz + s\mathbf{u}_2 h\right]. \tag{2.1.84}$$

Taylor expanding the integral about $z = -1$ and truncating the expansion with error $O(s^2)$, we may write

$$D = \nabla\cdot\left[\int_{-1}^{0} \mathbf{u}_1\ dz - \mathbf{u}_1|_{z=-1}(sh_B + \delta h) + s\mathbf{u}_2 h\right] + O(s^2). \tag{2.1.85}$$

Introducing the expansion (2.1.45) and retaining terms up to $O(s)$,

$$\begin{aligned} D &= \nabla\cdot\left[\int_{-1}^{0} (\mathbf{u}_1^{(0)} + s\mathbf{u}_1^{(1)})\ dz - s\mathbf{u}_1^{(0)}|_{z=-1}(h_B + \mu h^{(0)}) + s\mathbf{u}_2^{(0)} h^{(0)}\right] + O(s^2) \\ &= \int_{-1}^{0} (\nabla\cdot\mathbf{u}_1^{(0)} + s\nabla\cdot\mathbf{u}_1^{(1)})\ dz - s\mathbf{u}_1^{(0)}|_{z=-1}\cdot\nabla(h_B + \mu h^{(0)}) + s\nabla\cdot(\mathbf{u}_2^{(0)} h^{(0)}) + O(s^2) \\ &= s\left[\int_{-1}^{0} \nabla\cdot\mathbf{u}_1^{(1)}\ dz - \mathbf{u}_1^{(0)}|_{z=-1}\cdot\nabla(h_B + \mu h^{(0)}) + \nabla\cdot(\mathbf{u}_2^{(0)} h^{(0)})\right] + O(s^2), \end{aligned} \tag{2.1.86}$$

where we have applied the divergence operator to each term individually, and used the fact that the leading-order upper-layer velocity is divergence-free. After substituting $-w_z^{(0)} - Q_1$ for the integrand, by employing (2.1.53), we integrate to obtain

$$\begin{aligned} D = s\Big[-w^{(0)}|_{z=-1}^{0} - Q_1 - \mathbf{u}_1^{(0)}|_{z=-1}\cdot\nabla(h_B + \mu h^{(0)}) \\ + \nabla\cdot(\mathbf{u}_2^{(0)} h^{(0)})\Big] + O(s^2). \end{aligned} \tag{2.1.87}$$

Using the leading-order boundary conditions (2.1.50) and (2.1.51) we have

$$\begin{aligned} D = s\Big[h_t^{(0)} + \mathbf{u}_1^{(0)}|_{z=-1}\cdot\nabla(h_B + \mu h^{(0)}) - Q_1 \\ - \mathbf{u}_1^{(0)}|_{z=-1}\cdot\nabla(h_B + \mu h^{(0)}) + \nabla\cdot(\mathbf{u}_2^{(0)} h^{(0)})\Big] + O(s^2). \end{aligned} \tag{2.1.88}$$

Finally, using the leading-order problem associated with (2.1.38) to eliminate $h_t^{(0)}$,

$$D = s\left[Q_2 - \nabla\cdot(\mathbf{u}_2^{(0)} h^{(0)}) - Q_1 + \nabla\cdot(\mathbf{u}_2^{(0)} h^{(0)})\right] + O(s^2). \tag{2.1.89}$$

Since $Q_1 = Q_2$ by assumption, we obtain

$$D = O(s^2). \tag{2.1.90}$$

Although we did not explicitly use the governing equations, the above result holds under the leading-order balance expressed by the model equations (2.1.54)–(2.1.58).

2.2 Preliminary Results

In this section we present simulations that elucidate the energetics of the baroclinic process and its relevance to deep water dynamics in the Strait of Georgia (SOG). Dynamics at depth in the SOG are briefly described in chapter 1. Here, the conversion of potential energy to kinetic energy as dense fluid slumps down-hill is discussed in the context of a highly idealized, linearly sloping topography. Application of the model to deep water processes in the SOG employs a more realistic "valley" topography.

In both cases we will make the f-plane approximation due to the relatively small meridional extent of the strait. Generally, the beta term cannot be neglected on meridional scales L_* such that $\beta_0 L_*/f_0 \ll 1$ no longer holds (Gill 1982). At the latitude of the SOG, for example, $\beta_0 L_*/f_0 = O(1)$ for lengthscales of about 7000 km. If L_* is much less than this value, as it is in all of our simulations, it is safe to set $\beta = 0$. We also set $C_d = 0$ and $Q_1 \equiv Q_2 \equiv 0$ in order to focus on the energy exchanges associated with a perturbed along-slope current. Our preliminary results concern the fully nonlinear evolution of the flow. A rigorous theory for the linear regime of instability will be presented in the next two sections. We discuss the domain size and resolution for each simulation as necessary; however, the reader is referred to appendix B for all other details of the numerical scheme.

2.2.1 Instability Mechanism

To facilitate discussion of the energetics we describe, nondimensionally, the energy budget for this model. The upper-layer total energy,

$$E(t) = \frac{1}{2} \iiint_\Omega |\nabla\varphi|^2 + N^{-2}(\varphi_z)^2 dxdydz, \tag{2.2.1}$$

is composed of the kinetic energy (1st term) and the potential energy associated with sloping upper-layer isopycnals (2nd term). There are two types of potential energy associated with the lower layer,

$$PE_1(t) = \frac{1}{\mu} \int\!\!\int_{\Omega_H} h_B h \, dx dy \tag{2.2.2}$$

and

$$PE_2(t) = \frac{1}{2} \int\!\!\int_{\Omega_H} h^2 \, dx dy. \tag{2.2.3}$$

PE_1 is the energy released as the dense fluid descends down the sloping topography, and is the only source of energy for perturbation growth in this model. One may easily show that, without a source of lower-layer fluid, PE_2 is an invariant of the system (Poulin and Swaters 1999a). Likewise, the total system energy,

$$E_{\text{tot}} = E + PE_1 + PE_2, \tag{2.2.4}$$

is invariant in time.

In order to appreciate the instability characteristics in dimensional terms, we will use scalings appropriate for the Strait of Georgia, as presented in Karsten *et al.* (1995, henceforth KST). Of particular interest here is the low-frequency variability of the deep currents, as reported by Stacey *et al.* (1987). The thickness of the gravity current was $h_* = 65$ m, with a nominal total fluid depth $H = 300$ m. This determines the depth ratio, $\delta \approx 0.2$. The upper-layer Rossby radius (i.e. the dynamic lengthscale) was 7 km. The simulation was performed in an x-periodic channel with dimensions $0 \leq x \leq 28$ km and $0 \leq y \leq 56$ km. The width of the domain was large compared to the width of the current in order to minimize the effects of the boundaries on the upper layer. The channel length was chosen to accommodate roughly two wavelengths of the most unstable mode. We note that for a simulation where the channel was twice as long (not shown), twice as many waves developed, but the dynamics was otherwise similar. The horizontal and vertical resolutions are then 290 m and 19 m, respectively.

For simplicity, we employ a linearly sloping bottom, nondimensionally given by

$$h_B = y, \tag{2.2.5}$$

which yields an unscaled slope of 9×10^{-3}. In keeping with KST we let $s = \delta$, so that $\mu = 1.0$. The bottom-trapped current is modelled as an x-invariant parabolic front with two incroppings, and is described by

$$h_0(y) = \max[1 - (y - b)^2, 0]. \tag{2.2.6}$$

Here we set $b = 5.75$ so that, dimensionally, the current axis lies approximately 40 km away from the down-slope lateral boundary. Constant stratification is assumed in the upper layer ($B = 0.6$), such that the buoyancy frequency has a value of 1.5×10^{-3} s^{-1}, roughly consistent with σ_t sections in the northern part of the strait (LeBlond *et al.* 1991).

The evolution of the lower-layer thickness, h, for this simulation is given in Figs. 2.3a–d, corresponding to days 0, 7.4, 10.1 and 12.2 respectively. The undisturbed gravity current appears in Fig. 2.3a. The instability is first manifested as a wavelike deformation of the incroppings. Deformation of the down-slope incropping is much more pronounced, as Fig. 2.3b demonstrates. This asymmetry is consistent with the argument that dense water is more likely to slump down-hill than flow uphill, thus releasing its potential energy (Swaters 1991). The asymmetric evolution of the flow can also be explained in terms of a necessary condition for instability, which we describe in section 2.3.

The initial wavelength is 14 km, however, the instability then saturates and a shift to larger scales occurs between days 7.4 and 10.1. The perturbed incropping is dominated by a single large deformation in Fig. 2.3c. Further growth occurs at the larger lengthscales, leading to destruction of the mean flow and the development of a single spiral-like feature, rotating anticyclonically (Fig. 2.3d). This is not unlike results obtained numerically by Swaters (1998) for the S91 model.

During the course of the instability, a row of alternating high- and low-pressure cells develops in the upper layer, close to the down-slope incropping. These features are, in fact, topographic Rossby waves induced by deformations of the interface. After the initial stage of intensification, the pressure anomalies merge into a single dipole,

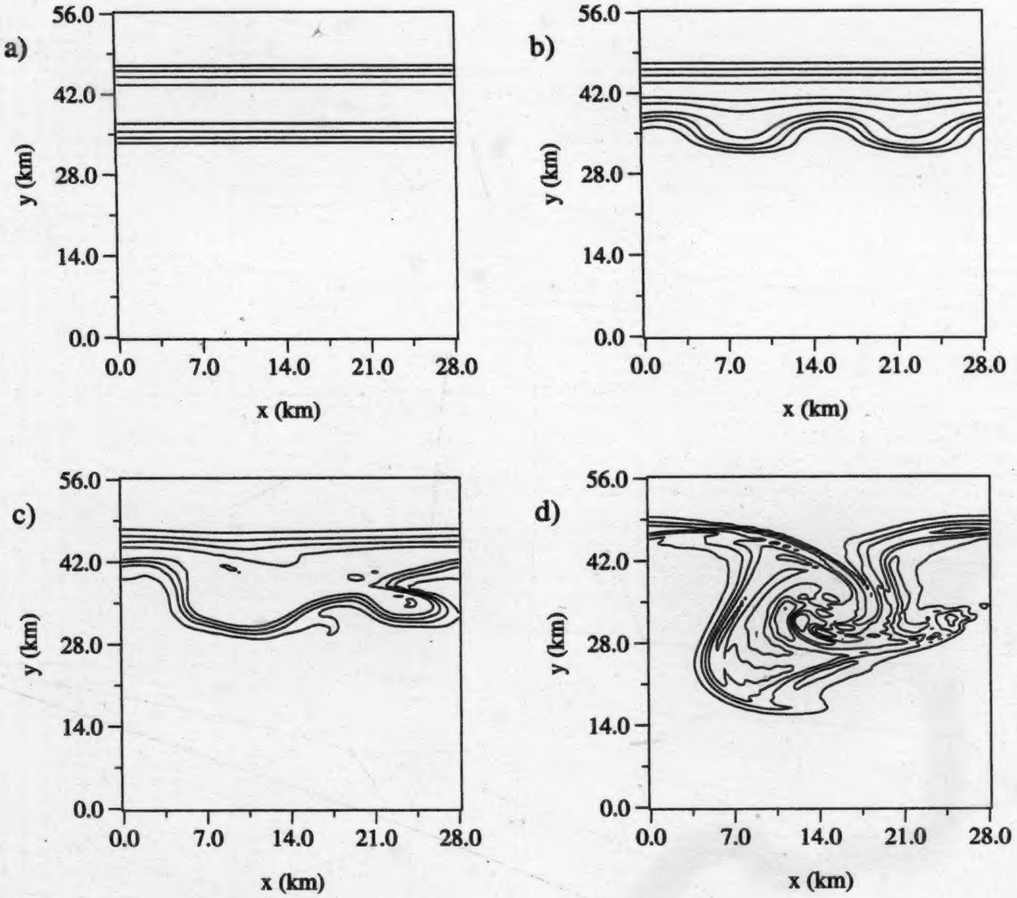

Figure 2.3: Contour plots of dimensional lower-layer thickness $h^*(x, y, t)$ for the simulation using the PSa model, with linearly-sloping topography. The frames correspond to a) 0, b) 7.4, c) 10.1 and d) 12.2 days. The contour range is 0 to 60 m. The contour interval is 15 m in all four plots.

which then grows to O(1) amplitude. Evolution of the upper layer will further be discussed in the next subsection, where we also provide plots of the streamfunction. The shift in dominant lengthscale evident in this simulation is a result of the so-called red energy cascade, a well-documented behavior of quasi-two-dimensional rotating systems, (e.g. Rhines 1977; Ikeda *et al.* 1984; Samelson and Chapman 1995). Since the ambient ocean in our models is always governed by QG theory (homogeneous

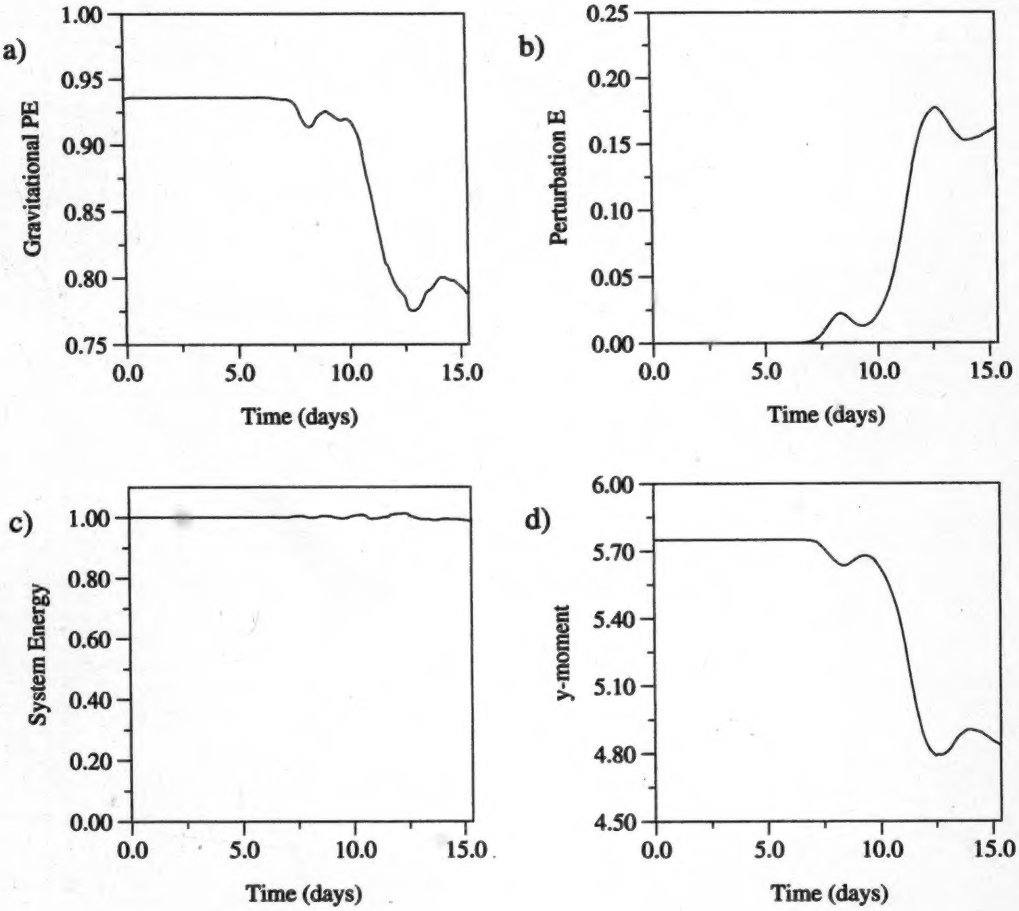

Figure 2.4: Diagnostics for the simulation with linearly sloped topography: a) normalized gravitational potential energy of the lower layer, b) normalized perturbation energy (i.e. total energy of the upper layer), c) normalized total system energy, and d) nondimensional y moment of the lower layer. All quantities are defined in the text.

or continuously-stratified), this nonlinear cascade will be a recurring theme in our simulations. We emphasize that, in this model, no along-front topographic variation is needed to destabilize the flow.

The growth of perturbations in the CS-PG model (as in the SW-PG model) relies on the release of gravitational potential energy associated with the dense fluid descending down the slope. The time evolution of the lower-layer gravitational potential energy PE_1 is plotted in Fig. 2.4a while in Fig. 2.4b we plot the time evolution of the perturbation energy, that is, the upper-layer total energy E. Both energies have been normalized by the total system energy, E_{tot}. The perturbation energy clearly grows by many orders of magnitude. The two peaks visible in Fig. 2.4b correspond to the two successive episodes of instability at approximately 8 and 12 days, as described above.

Comparison of Figs. 2.4a and b shows the close correlation between increases in $E(t)$ and the decreases in $PE_1(t)$. This is to be expected, given that $PE_1(t)$ is the only source of energy available for the growth of perturbations. Indeed, in Fig. 2.4c we plot the computed total system energy E versus time, normalized by its initial value. While a small amount of fluctuation, due to numerical effects, is evident at late times in the simulation, the system energy is conserved with reasonable accuracy during the entire instability process. Although higher spatial and temporal resolution can improve the accuracy of the scheme, the elimination of negative values of h (see Appendix B) does introduce some error into the simulations. However, the observed deviation of the total energy is no more than 3% of its initial value over the duration of the run, and in general we have not found the flow evolution to be very sensitive to the resolution or the elimination of negative thickness.

Fig. 2.4d shows the time evolution of the nondimensional y coordinate of the lower-layer center of mass. The initial coordinate value is $y = 5.75$, i.e. the initial location of the current axis. As the instability progresses, the y moment of the dense fluid decreases, indicating a gradual descent of the evolving gravity current into deeper water. Again, we see the two local maxima that correspond to temporary saturation of the instability. The location of these extrema and the overall shape of the curve are in good agreement with Fig. 2.4b (as well as Fig. 2.4a), further emphasizing the direct link between the cross-shelf migration of the dense fluid and the growth of perturbations.

2.2.2 Application to Strait of Georgia

To investigate the role of baroclinic instability in the observed SOG fluctuations (see chapter 1), KST performed a linear instability calculation, employing the S91 model in a configuration appropriate for the central part of the strait. The cross-channel shape of the bathymetry was approximated by a piecewise-linear trough (with its minimum in the interior of the channel), as shown in Fig. 2.5a. The deep current was assumed to have a parabolic profile, and was initially situated entirely on one (linear) slope of the topography. Data from Stacey *et al.* (1987) clearly indicate that the most intense pulses of deep water intruding into the SOG basin were detected on its eastern side, consistent with the supposition that the bottom-trapped flow travels along sloping topography with the shallow water on its right.

As part of their analysis, KST found that the instability takes the form of wavelike undulations of the incroppings, which are greater on the down-slope side than the up-slope side. The most unstable mode was found to be $k = 1.1$, which corresponds to a dimensional wavelength of about 40 km. It was thought that these undulations may grow into eddies, whose diameter would be 20 km (half of 40 km), or about twice as large as the observational record indicates.

We integrated the S91 equations numerically, using the same basic state and parameter values as those suggested in KST. The channel dimensions were 4.0×11.4 for a dimensional width and length of 28 km and 80 km, respectively. The lower layer was initialized as (2.2.6) with $b = 2.25$, which corresponds to a 14 km wide current, with a maximum thickness of 65 m and its axis 15.75 km away from the down-slope lateral boundary. Given this profile, the average initial velocity is 18 cm/s, typical of deep flows in the region. As in all other simulations, the only velocity structure imposed on the ambient layer was that associated with a small random perturbation. In this case, the maximum initial speed in the upper layer was about 4.5×10^{-5} cm/s. In a trial simulation, we employed the nondimensional piecewise-linear topography

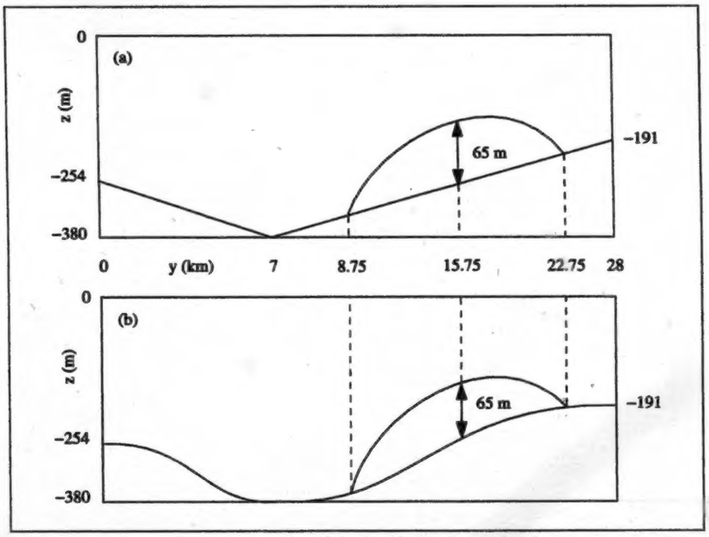

Figure 2.5: Cross-channel sections of the topography and bottom-trapped current used in our SOG simulations showing a) piecewise-linear topography and b) smooth topography.

given by,

$$h_B(y) = \begin{cases} 2(1-y), & 0 \le y \le 1, \\ y-1, & 1 < y \le 4. \end{cases} \tag{2.2.7}$$

The instability initially progressed according to the KST linear theory, producing undulations of the incroppings, especially on the down-slope side. We found, however, that lower-layer fluid which reached the discontinuity in the topographic gradient at $y = 7$ km immediately developed an along-slope velocity in the opposite direction. This is not surprising, given that the lower-layer flow is essentially topographically steered when φ and h are small (see (2.1.77)). The abrupt change in bathymetry effectively acts as a barrier and inhibits the gradual evolution of the growing plumes. Since this topography is somewhat unrealistic, it will not be considered further.

The S91 model was then integrated numerically using the following smooth topography (in nondimensional units)

$$h_B(y) = \begin{cases} 1.0 + \cos(\pi y), & 0 \le y \le 1, \\ \frac{3}{2}\left[1.0 + \cos\left(\frac{\pi}{3}(y-4)\right)\right], & 1 < y \le 4. \end{cases} \tag{2.2.8}$$

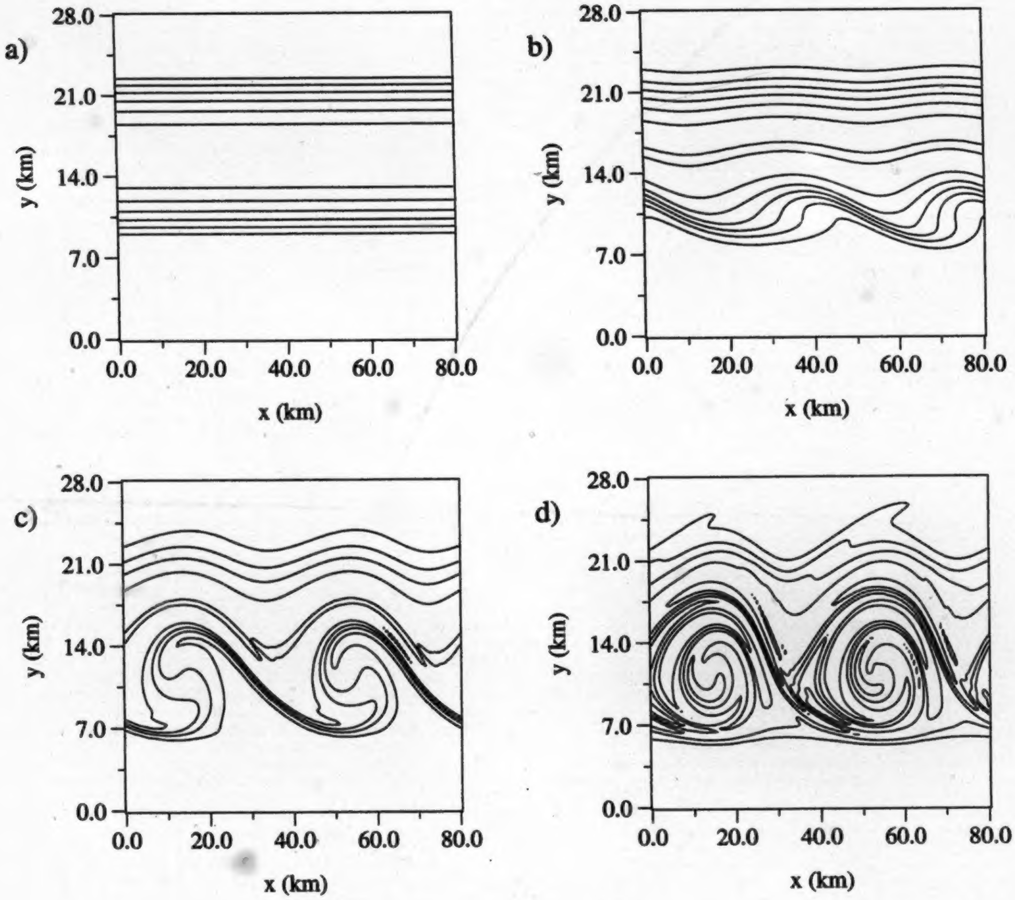

Figure 2.6: Contour plots of h for the S91 model SOG simulation using the smooth topography, at a) 0, b) 17.5, c) 19.3 and d) 23.0 days. The contour range is 0 to 60 m. The contour interval is 10 m in a) and b), and 15 m in c) and d).

This function approximates the SOG bathymetry in the region of interest and corresponds to the same fluid depths at $y = 0$, 7 and 28 km as (2.2.7). Unlike the piecewise-linear topography, (2.2.8) is continuously differentiable (see Fig. 2.5b). Fig. 2.6 depicts four contour plots of the lower-layer thickness for this simulation at 0, 17.5, 19.3 and 23.0 days. In Fig. 2.6a we see the undisturbed parabolic front, which at this stage, rests entirely on one slope of the trough. The down-slope incropping has deformed in Fig. 2.6b yielding 2 waves of the most unstable mode.

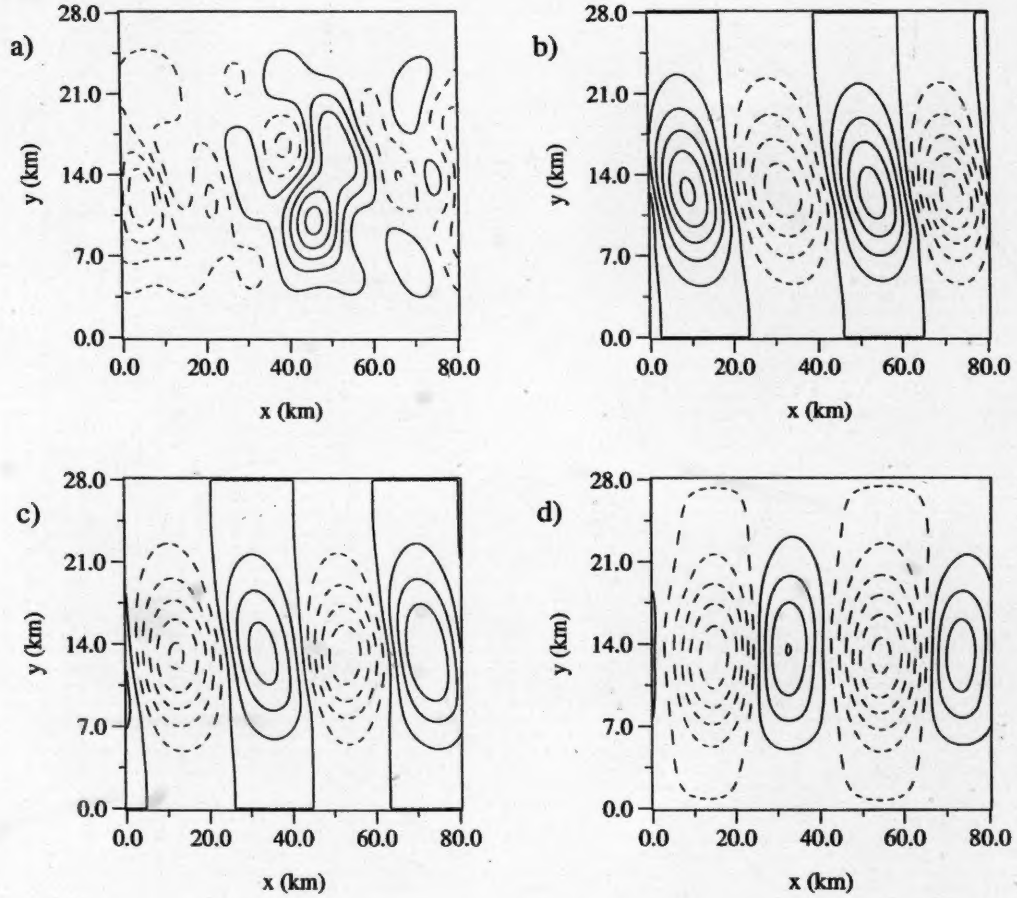

Figure 2.7: Contour plots of p for the simulation corresponding to Fig. 2.6. The contour range and interval are, respectively, a) 2.0×10^{-6}, 2.0×10^{-7}, b) 0.2, 0.02, c) 0.7, 0.08 and d) 0.9, 0.1. Dashed contours correspond to negative values.

The wavelike perturbation moves with the current (i.e. in the negative x direction) at a speed of roughly 12 cm/s, in agreement with KST. As these protrusions grow, they subsequently encounter the opposite face of the valley and begin to roll up on themselves in a spiral-like pattern (Fig. 2.6c). This process continues and the flow eventually reaches a quasi-steady state in Fig. 2.6d. For the initial phase of growth, we estimate e-folding times of approximately 15 h. In the end, the spiral structures have a wavelength of 40 km, though individual filaments exhibit much smaller lengthscales.

In Figs. 2.7a–d we plot the upper-layer pressure corresponding to the same times as Figs. 2.6a–d. Fig. 2.7a shows the initial random perturbation with small amplitude (about 10^{-6}). The upper-layer streamfunction quickly organizes itself into 2 pairs of high/low pressure cells (Fig. 2.7b) which intensify as the gravity current gives up its available gravitational energy (Figs. 2.7c and d). These pressure cells clearly indicate strong cyclonic and anticyclonic circulations in the upper layer, and their along-slope wavelength is about 40 km, as predicted by KST.

A number of factors may account for the discrepancy between this wavelength and the Stacey *et al.* (1988) estimate (see chapter 1), such as the simplifying assumption of x-invariant topography. However the eddies in Figs. 2.6b–d extend over the entire width of the channel, and are therefore qualitatively different from the localized vortices described in Stacey *et al.* (1988). Lengthscales associated with the PSa model tend to be smaller than in the S91 model, and therefore the nonlinear evolution of a double front in the continuously-stratified context is of interest.

In a series of simulations we employed the PSa model with the same configuration (2.2.6) and (2.2.8), in order to determine the effects of ambient stratification on the instability process. We remark that the actual fluid density does not appear as a parameter in any of the models presented here. The dynamics is determined solely by the relative density difference across any given interface, as measured by g', and background stratification, if present. However, it is assumed that g'/g is small, and that stratification in any continuously-stratified layer is no more important than the density contrast between layers (see section 2.1.2). The width of the channel was 28 km as in the S91 simulation and the channel length was reduced to 28 km. Contour plots of the lower-layer thickness at 8.7, 10.6, 12.4 and 14.3 days are depicted in Fig. 2.8.

The initial lower-layer profile was the same as in the S91 case, and is thus not shown. The dominant along-channel wavenumber which emerges is 3.1, about three times the value obtained for the S91 model. This gives a dimensional wavelength of

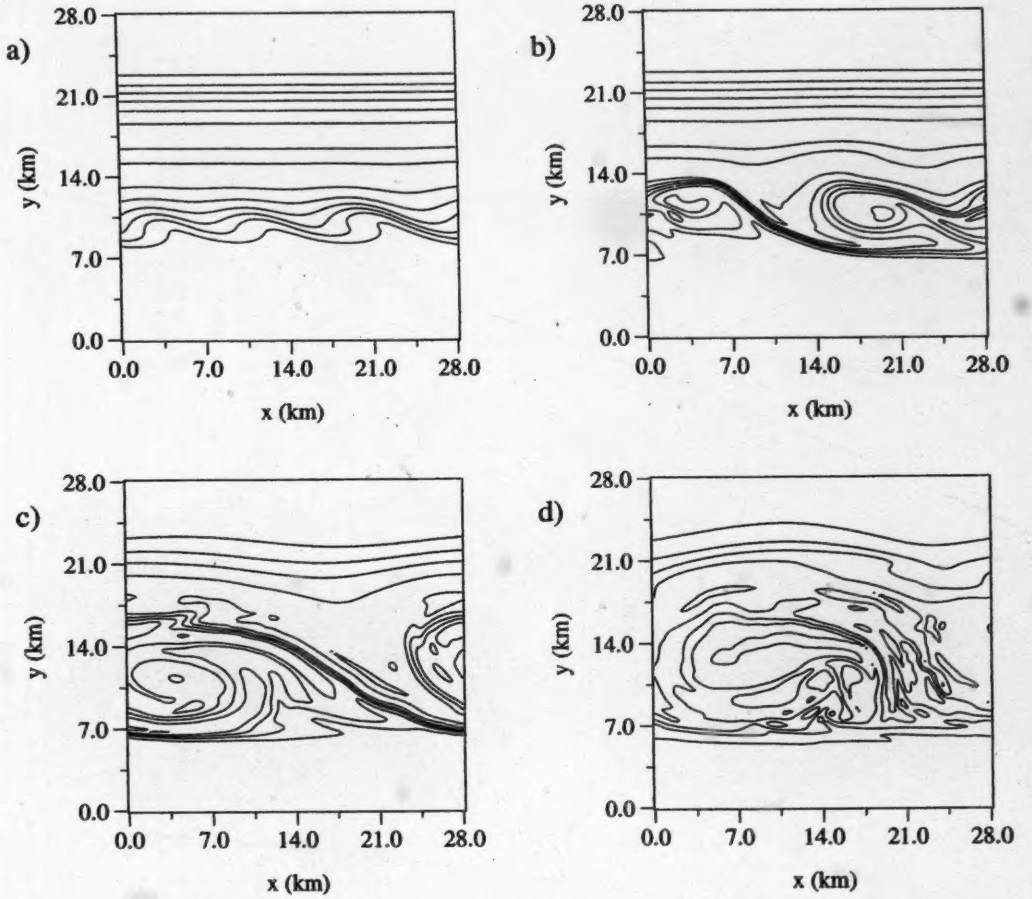

Figure 2.8: Contour plots of h for the SOG simulation using the PSa model with smooth topography, at a) 8.7, b) 10.6, c) 12.4 and d) 14.3 days. Contour range is 0 to 60 m. Contour intervals are 8.5 m in a) and b), and 12 m in c) and d).

approximately 9 km (Fig. 2.8a). We point out that this lengthscale is smaller than the one obtained in the linearly-sloping topography case, because the most unstable wavenumber is highly influenced by the topographic gradient near the down-slope incropping. The nondimensional slope of (2.2.8) near the lower-incropping is smaller than 1, thus giving rise to a higher along-front wavenumber.

As in previous simulations, the down-slope deformations can be seen to grow and break backwards in relation to the direction of flow. Between 8.7 and 10.6 days the

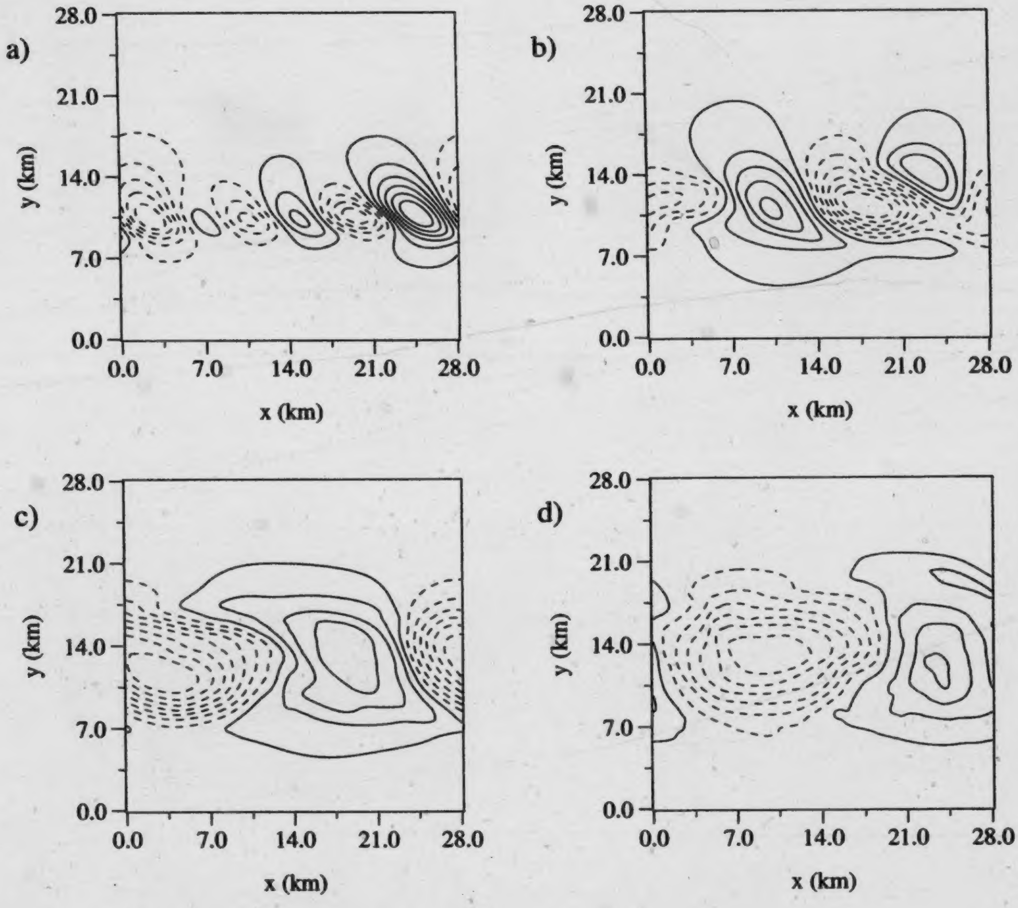

Figure 2.9: Contour plots of upper-layer pressure at the bottom of the upper layer for times corresponding to Fig. 2.8. The contour range and interval are, respectively, a) 0.12, 0.01, b) 0.44, 0.04, c) 0.92, 0.08 and d) 1.01, 0.1. Dashed contours correspond to negative values.

instability is temporarily saturated and the wavelike perturbations merge, increasing the dominant wavelength (Fig. 2.8b). As cyclonic vorticity is concentrated behind the wave crests, the roll-up process continues in Fig. 2.8c and eventually destroys the mean flow, giving rise to a single irregular gyre (Fig. 2.8d).

The evolution of the upper-layer pressure at $z = -1$ (dimensionally, $z^* = -H$) is depicted in Fig. 2.9. We note that the lower layer does not appear in these cross-

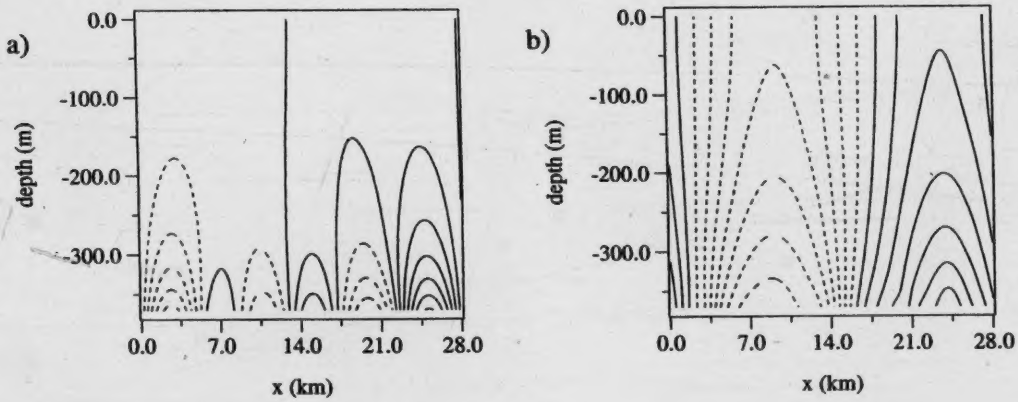

Figure 2.10: Vertical cross-sections of upper-layer pressure corresponding to Fig. 2.9 at $y = 14$ km. Plot a) corresponds to Fig. 2.9a while plot b) corresponds to Fig. 2.9d.

sections due to the Taylor expansion introduced in (2.1.44) so that, to leading order, the bottom boundary of the upper layer is at $z = -1$. The initial random wave field first develops into a train of alternating high and low pressure cells (Fig. 2.9a) at $y \approx 10$ km. These propagate in the negative x direction at around 7 cm/s. We have found that this stage of the instability is very rapid, with e-folding times of 7 hours, about half that predicted by the S91 model. The vortices are highly localized, unlike the ones in Figs. 2.7c–d. The formation of small eddies at the onset of the instability is in good agreement with the Stacey *et al.* (1988) analysis. The eddies merge in Fig. 2.9b and again in Fig. 2.9c while they continue to intensify.

The resulting eddy dipole persists for the next several days without significant change (Fig. 2.9d). Growth at the larger lengthscales was found to be an order of magnitude slower than the initial instability. Analysis of the current meter data (Stacey *et al.* 1987) does indicate a basin-wide gyre at mid-depth, as well as a clockwise/counterclockwise oscillation of the mean velocity field, which may be related to the slowly-propagating, domain-scale dipole evident at late times in our simulations. We hasten to add however that, in reality, wind stress and tides (as well as their nonlinear interactions) constantly inject energy into high frequency/wavenumber motions. Because our model neglects such external forcing, we are inclined to focus mainly on the initial and intermediate stages of the simulations.

Based on their observational data, Stacey *et al.* (1991) estimated the *e*-folding times of barotropic and baroclinic transfers to be about 1–4 days. However, it must be stressed that their baroclinic growth rate calculation was based entirely on density and velocity correlations. The baroclinic process we are modelling here, and which we believe is operative in the SOG, is the release of gravitational potential energy by a dense fluid mass that descends down a topographic slope. The growth rates associated with this mechanism may indeed be higher than the Stacey *et al.* (1991) estimate suggests. Given that the deep current fluctuations in the SOG exhibit a highly nonlinear, almost turbulent character (Stacey *et al.* 1987), we believe that *e*-folding times of less than a day are not unreasonable. The first phase of instability is very rapid (*e*-folding times of less than 10 hours) which increases the likelihood that vortices can form before external forces, such as tides, alter the flowfield.

We found that in a narrow channel such as the SOG, the topography tends to decrease growth rates in the second stage of instability. This is because the reversal in slope effectively arrests the downward propagation of dense plumes, and therefore the release of gravitational potential energy. Stacey *et al.* (1991) also suggested that baroclinic processes may be inhibited by the small size of the strait relative to the deformation radius (about 5–8 km). The assumption of a periodic channel domain is also likely to influence quantitative aspects of flow evolution at late times. A similar study of SOG dynamics employing a source flow and actual SOG topography would be of interest.

The emergent vortices in the stratified layer are clearly bottom-intensified. For example, the maximum dimensional velocity in Fig. 2.9d is 36 cm/s and occurs at the bottom of the upper layer, while the velocities for the same time frame at the top of the fluid column are only half as large. Vertical cross-sections of the upper-layer pressure corresponding 8.7 and 14.3 days are given in Figs. 2.10a and b. The observed tapered structure highly resembles analytical eddy solutions for the PSa model found by Poulin and Swaters (1999b). Indeed, numerous bottom-intensified vortices were reported by Stacey *et al.* (1988). The ability to describe this vertical structure is a strength of the PSa model.

None of our simulations resulted in a turbulent eddy field, which the analysis of Stacey *et al.* (1988) seems to imply. It is plausible that along-channel topographic variations, which we have neglected in this study, could introduce eddy motions that are more turbulent in character. The assumption of along-channel periodicity may also be too restrictive, since deep water replacement in the SOG tends to be episodic rather than continual. Simulations involving a source flow (in a somewhat different setting) will be discussed in chapter 3.

2.3 Linear Stability Analysis

In this section and the rest of the chapter, it is assumed that $Q_1 \equiv Q_2 \equiv 0$ and $C_\mathrm{d} = 0$. We choose an x-periodic channel domain such that $-L \leq y \leq L$, and an x-invariant topography,

$$h_B = h_B(y). \tag{2.3.1}$$

The lower layer is assumed to have two time-dependent incroppings, implicitly defined by

$$y = \xi_i(x,t), \qquad \text{for } i = 1, 2, \tag{2.3.2}$$

where $i = 1, 2$ refers to the particular incropping. We impose boundary conditions on the upper-layer cross-channel velocity,

$$v_1 = 0, \qquad \text{on } y = -L, L, \tag{2.3.3}$$

and the lower-layer incroppings,

$$\left.\begin{aligned} h &= 0, \\ \partial_t \xi_i + \mathbf{u}_2 \cdot \nabla(\xi_i - y) &= 0 \end{aligned}\right\} \qquad \text{on } y = \xi_i, \;\; i = 1, 2, \tag{2.3.4}$$

where $v_1 = \varphi_x$ by (2.1.59) and $\mathbf{u}_2$ is given by (2.1.58), (2.1.60).

Perturbed flow fields of the form

$$\varphi(x,y,z,t) = \varphi'(x,y,z,t),$$

$$h(x,y,t) = h_0(y) + h'(x,y,t),$$

$$\xi_i = a_i + \xi_i'(x,t), \;\; i = 1,2, \tag{2.3.5}$$

are introduced, where $h_0(y)$ is a known, prescribed frontal profile such that $h_0(y) > 0$ on $a_1 < y < a_2$. The prescribed constants a_1, a_2 satisfy $-L \leq a_1 < a_2 \leq L$, and the perturbation fields satisfy $|\varphi'|, |h'|, |\xi_i'| \ll 1$. We note that, in order to focus on the baroclinic aspect of the instability, there is no prescribed mean flow in the upper layer. A non-zero but depth-independent buoyancy frequency, $N =$ const, is also assumed since we would like to retain stratification while keeping the problem somewhat more tractable.

Substituting (2.3.1) and (2.3.5) into the governing equations (2.1.54)–(2.1.57) and boundary conditions (2.3.3), (2.3.4) and immediately dropping the primes, the linearized equations are given by

$$(\Delta\varphi + N^{-2}\varphi_{zz})_t = 0, \tag{2.3.6}$$

$$\varphi_{zt} = 0 \qquad \text{on } z = 0, \tag{2.3.7}$$

$$\varphi_{zt} + N^2 h_{By}(\varphi + h)_x = 0 \qquad \text{on } z = -1, \tag{2.3.8}$$

$$h_t + \mu h_{0y}\varphi_x - h_{By}h_x = 0 \qquad \text{on } z = -1, \tag{2.3.9}$$

with linearized boundary conditions

$$\varphi_x = 0, \qquad \text{on } y = \pm L$$

$$\left.\begin{aligned} h + h_{0y}\xi_i &= 0, \\ \xi_{it} - (\mu h_{0y} + h_{By})\xi_{ix} &= \mu(\varphi + h)_x \end{aligned}\right\} \quad \text{on } y = a_i, z = -1, \tag{2.3.10}$$

for $i = 1,2$, where $h_{0y} = \dfrac{\mathrm{d}h_0}{\mathrm{d}y}$ and $h_{By} = \dfrac{\mathrm{d}h_B}{\mathrm{d}y}$.

A brief discussion of system energetics is appropriate here. The upper-layer perturbation energy equation was derived and discussed in Poulin (1997). The main result of that derivation was that

$$h_{By}h_{0y} > 0 \qquad \text{for some } y \in (-L, L), \tag{2.3.11}$$

is a necessary condition for instability. Conversely, the system is stable if $h_{By}h_{0y} \leq 0$ for all y. It is instructive to rephrase this condition in terms of the absolute interfacial height,

$$h_A \equiv h_B + h_0. \tag{2.3.12}$$

An assumption of the model derivation was that $h_{By} \neq 0$ and, without loss of generality, we assume that $h_{By} > 0$. Then (2.3.11) implies that

$$h_{Ay} > h_{By} \qquad \text{for some } y \in (-L, L), \tag{2.3.13}$$

is necessary for instability. The situation here is similar to the stability model presented by Blumsack and Gierasch (1972), in which a continuously-stratified QG atmosphere was stabilized by sloping topography when the slope of the isentropes was smaller than the topographic gradient, but was destabilized when the isentropic slope was larger than the bottom slope.

It is noteworthy that, for a parabolic front, the frontal and topographic gradients are always of the same sign on the down-slope incropping, but not on the up-slope incropping. Although (2.3.11) is only a necessary (not sufficient) condition for instability, heuristically, we could expect that such a basic state is more likely to become unstable on the down-slope side, thus leading to the asymmetry already mentioned in section 2.2.

Presently, we focus on the lower-layer equation. It is assumed that the flow is periodic in x and that the domain is a periodic channel with $0 \leq x < x_R$. For convenience, we introduce the along-channel integration operator

$$\langle (*) \rangle = \int_0^{x_R} (*) dx. \tag{2.3.14}$$

This can be replaced by integration over a wavelength, without loss of generality.

Multiplying (2.3.9) by h and integrating over the horizontal extent of the domain,

$$\frac{\mathrm{d}}{\mathrm{d}t}\int_{-L}^{L}\left\langle \tfrac{1}{2}h^2\right\rangle dy = \int_{-L}^{L}\left\langle \tfrac{1}{2}h_{By}(h^2)_x - \mu h_{0y} h \varphi_x\right\rangle dy. \tag{2.3.15}$$

The first term in the integrand on the right-hand side vanishes due to periodicity in x, so that we may write

$$\frac{\mathrm{d}}{\mathrm{d}t}\int_{-L}^{L}\left\langle h^2\right\rangle dy = -2\mu\int_{-L}^{L}\left\langle h_{0y} v_1 h\right\rangle dy. \tag{2.3.16}$$

The interpretation for this equation is analogous to that presented in PSa. For simplicity we assume that the continental shelf topography and fluid interface are both linearly sloping. If the topographic gradient is negative (so that y points offshore) then we must also have $h_{0y} < 0$ by (2.3.11). For perturbation growth (i.e. positive left-hand side), the average cross-shore transport of thickness anomalies, $\int_{-L}^{L}\langle hv_1\rangle\, dy$, must be positive, since $\mu > 0$ by construction. Thinking of positive h anomalies as cold anomalies, we see that there must be a net on-shore transport of heat. This is consistent with the idea that instability in this model is associated with down-slope slumping of dense bottom waters. The argument in the case where $h_{By} > 0$ is similar.

Carrying on with the analysis, we assume normal mode solutions for the perturbations,

$$(\varphi, h, \xi_i) = (\widetilde{\varphi}(y,z), \widetilde{h}(y), \widetilde{\xi}_i)\exp[ik(x-ct)] + \text{c.c.}, \tag{2.3.17}$$

(where c.c. refers to the complex conjugate) as well as simple, linear topography,

$$h_B(y) = \nu y, \tag{2.3.18}$$

with $\nu = \pm 1$. Here ν plays the role of a scaled slope, however it would be inconsistent to allow $|\nu| \neq 1$ since the relative amplitude of the topographic slope is already accounted for by the parameter s. The parameter ν controls only the sign of the slope. The along-channel wavenumber k is assumed to be real, which precludes spatially growing instabilities (see Hogg 1976; Sutherland and Peltier 1992).

Substitution of (2.3.17) and (2.3.18) into (2.3.6)–(2.3.10) before dropping the tildes yields a Helmholtz equation,

$$-k^2\varphi + \varphi_{yy} + N^{-2}\varphi_{zz} = 0, \tag{2.3.19}$$

with the boundary conditions

$$\varphi_z = 0, \qquad \text{on } z = 0, \tag{2.3.20}$$

$$\varphi_z = F(c,y)\varphi, \qquad \text{on } z = -1, \tag{2.3.21}$$

$$\varphi = 0, \qquad \text{on } y = \pm L, \tag{2.3.22}$$

where

$$F(c,y) = \nu N^2 \frac{c + \mu h_{0y} + \nu}{c(c+\nu)}. \tag{2.3.23}$$

The lower-layer thickness and incroppings are now determined diagnostically by

$$h = \frac{\mu h_{0y}}{c+\nu}\varphi(y,-1) \qquad \text{and} \qquad \xi_i = -\frac{\mu}{c+\nu}\varphi(a_i,-1), \qquad i = 1,2. \tag{2.3.24}$$

Since the bottom boundary condition (2.3.21) involves a function of y, this system is, in general, non-separable. This difficulty is avoided if h_0 is linear in y, that is, if the lower layer forms a wedge front without actual incroppings. In this special case F is independent of y and separation of variables may be employed. While the resulting dispersion relation and corresponding solutions have been discussed in PSa, here we provide a few further details and describe a relevant numerical simulation.

2.3.1 Analysis of a Wedge Front

We consider an idealized flow where the lower-layer thickness has the x-invariant form,

$$h_0(y) = 1 - \gamma y, \tag{2.3.25}$$

for constant γ. As was shown by Poulin and Swaters (1999a) for the linear stability problem associated with this wedge-like frontal profile and zero initial upper-layer

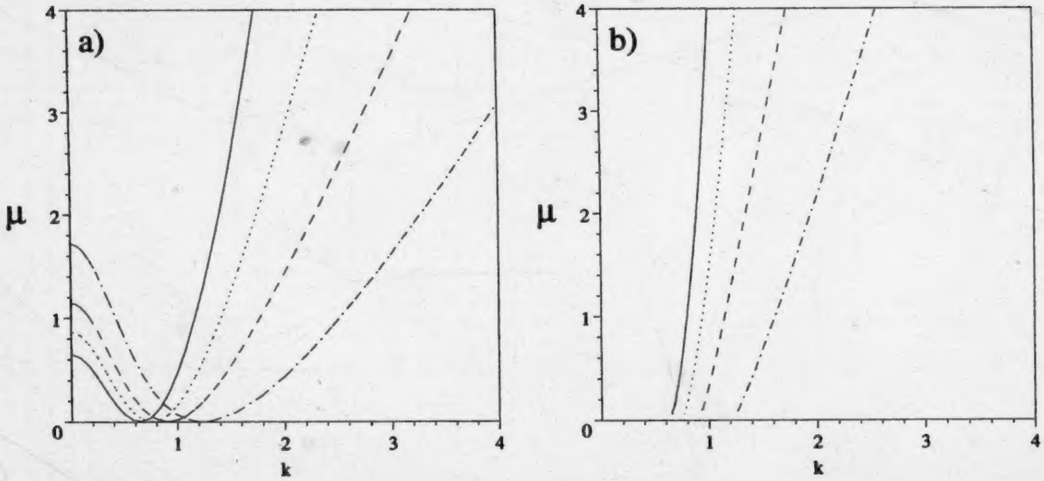

Figure 2.11: a) Range of unstable wavenumbers k for a given μ, b) most unstable k for a given μ. These curves correspond to $\nu = -1.0$, $\gamma = 0.1$ and $L = 2.0$, with $N^2 = 0.1$ (continuous lines), 0.5 (dotted lines), 1.0 (dashed lines) and 2.0 (dot-dash lines).

mean flow, the perturbation quantities, φ' and h', have the exact normal mode solutions,

$$\varphi' = A \sin \frac{n\pi(y+L)}{2L} \cosh(\lambda z) \exp[ik(x-ct)] + \text{c.c.}, \tag{2.3.26}$$

$$h' = \frac{-A\gamma\mu}{c+\nu} \sin \frac{n\pi(y+L)}{2L} \cosh(\lambda) \exp[ik(x-ct)] + \text{c.c.}, \tag{2.3.27}$$

where A is an arbitrary constant,

$$\lambda = N \left[k^2 + \left(\frac{n\pi}{2L} \right)^2 \right]^{\frac{1}{2}}, \tag{2.3.28}$$

is the vertical wavenumber and $c = c_R + ic_I$ is the complex phase speed. Here k is the along-channel wavenumber and $\frac{n\pi}{2L}$ is the quantized cross-channel wavenumber ($n = 1, 2, 3, \ldots$). The corresponding dispersion relation is given by

$$c = \frac{-\nu(T+N^2) \pm \sqrt{(T-N^2)^2 + 4\nu\gamma\mu N^2 T}}{2T}, \tag{2.3.29}$$

where $T = \lambda \tanh \lambda > 0$.

Although the assumed basic profile (2.3.25) does not actually intersect the bottom, it nevertheless demonstrates several important characteristics of the model. For instability to occur ($c_I > 0$), the product of ν and γ must be negative, so that the bottom topography must slope in the same sense as the interface (in agreement with the necessary condition for instability (2.3.11). This is in contrast to instability of surface currents, where a positive correlation between the interfacial and topographic gradients is a stabilizing influence (e.g. Reszka and Swaters 1999a). We note that, if the interface is parallel to the topography (i.e. $\gamma = 0$), (2.3.29) predicts stability, for any nonzero bottom slope [1] (Mooney and Swaters 1996).

If we set the discriminant in (2.3.29) equal to zero and solve for μ, we obtain

$$\mu = \frac{-\nu(T - N^2)^2}{4\gamma N^2 T}, \tag{2.3.30}$$

a plot of which, as a function of k, is shown in Fig. 2.11a. Curves for four different values of the Burger number are plotted, with ν, γ and L fixed. For a given μ and N, the graph shows the range of unstable wavenumbers k. This range decreases as μ decreases, which is consistent with the idea that decreasing δ stabilizes the flow. However, for any μ, there are always some wavenumbers that are unstable. For a given μ, the range of unstable wavenumbers also increases with the stratification in the ambient layer. Contours showing the most unstable wavenumber in $\mu - k$ space are plotted in Fig. 2.11b for the same values of ν, γ, L and N as in Fig. 2.11a. It is evident that the dominant wavenumber increases more or less linearly with μ (equivalently, as δ increases or s decreases), and the rate of increase is greater for higher values of N.

The dependence of the maximum growth rate $\sigma_{\max} = \max\limits_{k}\{kc_I\}$ on the interaction parameter is shown in Fig. 2.12a. The growth rate vanishes as μ approaches zero. Associating a decrease in μ with a decrease in δ, it is clear that decreasing the depth fraction stabilizes the system. A stable region is of interest physically, since in

---

[1] Flat topography cannot be considered within the framework of this model since, for $\delta > 0$, we require that $s > 0$ (see section 2.1.2).

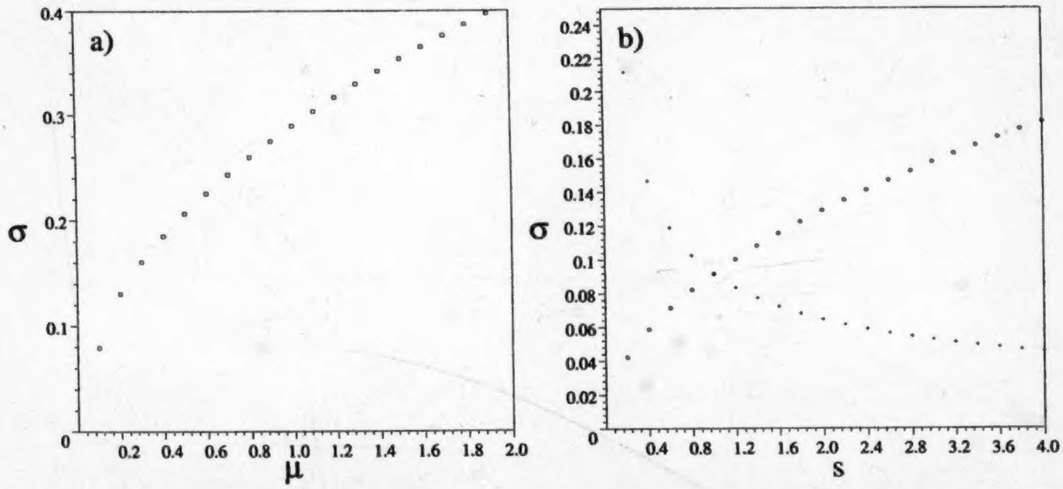

Figure 2.12: Growth rates determined from the wedge front dispersion relation. a) Nondimensional maximum growth rate, $\sigma_{\max} = kc_I$ versus μ, with $s = 0.1$, b) $\sigma_{\max}$ (crosses) and scaled maximum growth rate $s\sigma_{\max}$ (circles) versus s with $\delta = 0.1$. In both plots we used $\nu = -1.0$, $\gamma = 0.1$, $N^2 = 1.0$ and $L = 2.0$.

real oceanographic settings, bottom-trapped flows are known to propagate significant distances before undergoing instability. With respect to the baroclinic processes we are describing then, the above analysis suggests that a relatively deep ambient layer can serve to maintain the stability of such a current.

As seen in Fig. 2.12a or the dispersion relation (2.3.29), we may expect smaller growth rates for lower values of μ. However, it turns out that dimensional growth rates actually increase with s. This is because the temporal scaling in the CS-PG model is $(sf_0)^{-1}$, so that nondimensional growth rates must be multiplied by sf_0 in order to obtain dimensional values. In Fig. 2.12b we plot the maximum nondimensional growth rate $\sigma_{\max}$ and a scaled growth rate $s\sigma_{\max}$ versus s. The factor f_0 was neglected since it has no effect on the trend with respect s. We see from the figure that, dimensionally, we should expect more vigorous growth for higher slopes, which is consistent with most laboratory studies (e.g. Lane-Serff and Baines 1998).

The wedge-front linear stability analysis for the S91 model was presented in Mooney and Swaters (1996). As $N \to 0$ in the above dispersion relation, we re-

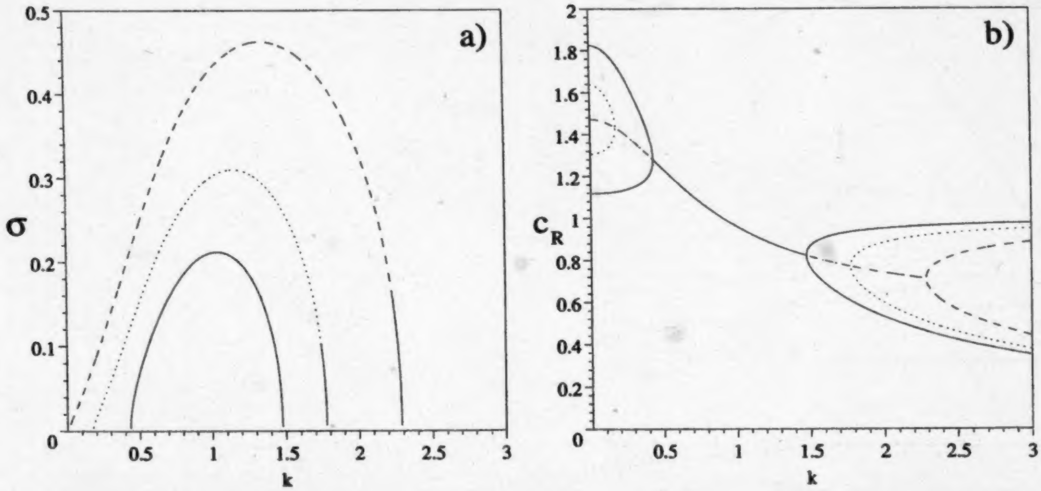

Figure 2.13: a) Growth rate curves and b) phase speed curves versus k of the gravest mode, obtained from the wedge front dispersion relation (2.3.29) for $\gamma = 0.05$ (solid lines), 0.1 (dotted lines) and 0.2 (dashed lines). Here we used $\nu = -1.0$, $\mu = N^2 = 1.0$ and $L = 2.0$.

cover the Mooney and Swaters (1996) result, which is to be expected, given that the PSa model reduces to the S91 model in this limit. As was shown by Poulin and Swaters (1999a), the two main effects of allowing stratification (or increasing it) in the upper layer are to increase the along-channel wavenumber of the most unstable mode, as well as to increase the growth rate of that mode. Because stratification inhibits vertical motions, increasing the stratification focuses the effects of vortex tube stretching/compression closer to the interface, thus leading to a more intense, localized instability (Lane-Serff and Baines 2000, see also section 2.4.1).

Typical growth rate and phase speed curves of the gravest (i.e. $n = 1$) mode, as predicted by (2.3.29), are shown in Fig. 2.13. The frontal slope parameter is varied, which demonstrates that higher growth rates result from steeper wedge profiles. The low-wavenumber cutoff decreases, while the high-wavenumber cutoff are increases as γ is increased. Thus, larger available potential energy of the mean flow leads to shorter timescales and a larger range of unstable along-shelf wavenumbers. However, increas-

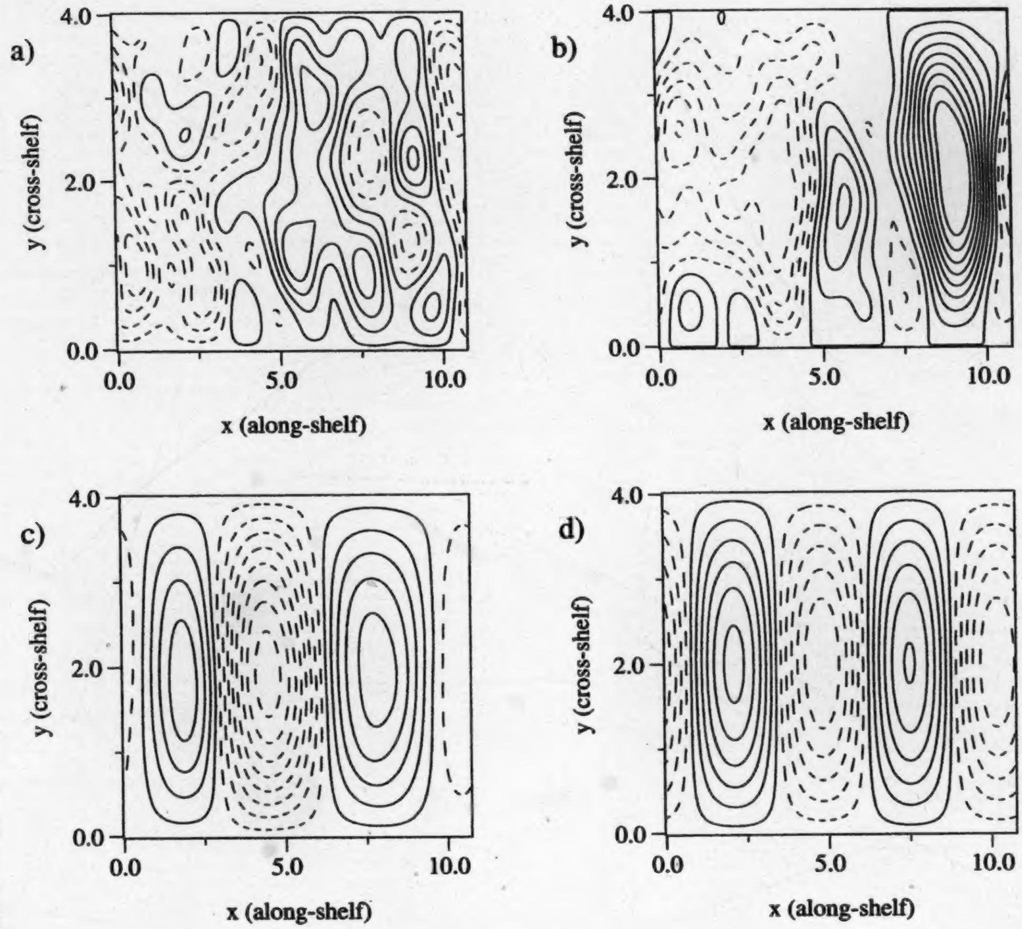

Figure 2.14: Contour plots of upper-layer pressure (i.e. the growing perturbation) at $z = -1$ for a wedge front simulation, using the PSa model, at nondimensional times a) 0, b) 10, c) 20 and d) 50. The contour range and interval are, respectively, a) 3.0×10^{-10}, 4.0×10^{-11}, b) 1.1×10^{-9}, 8.0×10^{-11}, c) 1.0×10^{-8}, 8.0×10^{-10} and d) 9.1×10^{-5}, 8.0×10^{-6}. Dashed contours correspond to negative values.

ing γ has practically no effect on phase speeds in the unstable regime (Fig. 2.13b). We remark that the low cut-off for the total wavenumber λ is strictly positive, since n is always non-zero. However, the low-wavenumber cut-off for k does in fact vanish for γ large enough (e.g. $\gamma = 0.2$ in Fig. 2.13a).

By numerically integrating the PSa governing equations (2.1.54)–(2.1.57) forward

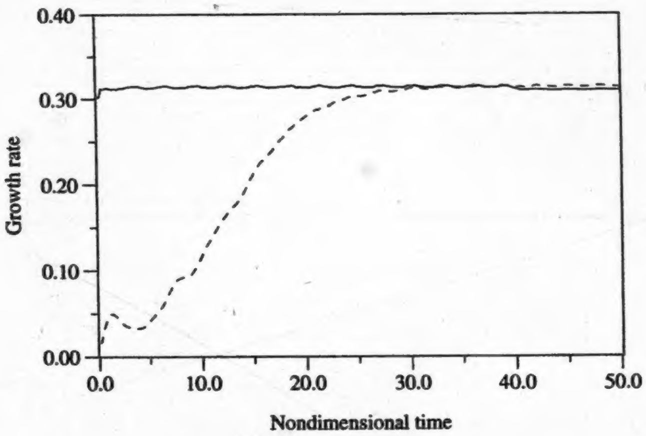

Figure 2.15: Perturbation growth rate versus nondimensional time for two wedge-front simulations. Dashed line corresponds to the simulation in Fig. 2.14. Solid line corresponds to a simulation where the initial condition was the analytical solution (2.3.26), (2.3.27).

in time, we have verified that the structure of the perturbation which emerges from a random wavefield of negligible amplitude is in fact described by (2.3.26) and (2.3.27). The development of upper-layer pressure at $z = -1$ is shown for nondimensional times 0, 10, 20 and 50 in Fig. 2.14. Here the nondimensional channel width and length are 4.0 and 10.7, respectively, with $\mu = 1.0$, $\gamma = 0.1$, $\nu = -1.0$ and $N^2 = 1.0$. By $t = 50$, the normal mode solution (2.3.26) has emerged, with an along-channel wavenumber of approximately 1.2, which is the theoretical most-unstable wavenumber, as Fig. 2.13 shows (dotted line). The dominant cross-channel structure is clearly the gravest ($n = 1$) mode.

We determined the corresponding growth rate by computing, at each time step, the finite-difference analogue of

$$\overline{\sigma} = \frac{\mathrm{d}}{\mathrm{d}t} \ln \left(\sqrt{\frac{E(t)}{E(0)}} \right), \tag{2.3.31}$$

where the volume-averaged upper-layer perturbation energy, $E(t)$, is given by (2.2.1).

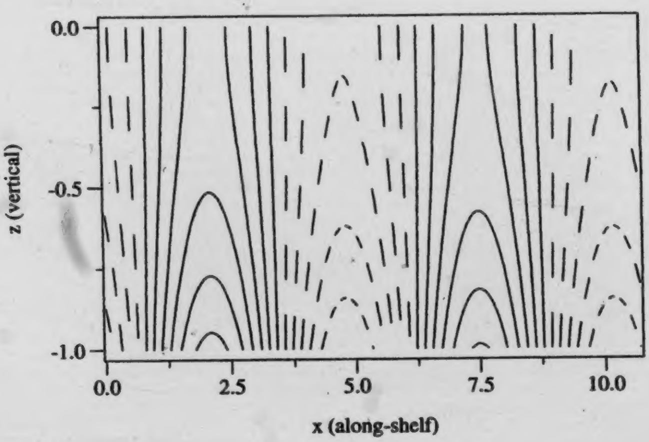

Figure 2.16: Vertical cross-section of upper-layer pressure corresponding to Fig. 2.14d at $y = 2.0$. Dashed lines correspond to negative values. The bottom-intensified structure of the upper-layer pressure cells is clearly visible.

The growth rate, $\overline{\sigma}$, is plotted versus time in Fig. 2.15 (dashed line). It starts near zero, then increases and levels off at $t = 25$, with a final value of approximately 0.32. This is quite close to the analytical value of 0.31, resulting from the dispersion relation (2.3.29). Moreover, the high/low pressure cells seen in Fig. 2.14 propagate in the positive x direction at a nondimensional speed of 0.91, which compares favorably with the analytical value, 0.87.

If we start the simulation using the exact solution (2.3.26) and (2.3.27) with the most unstable wavenumber, $k = 1.2$, then the growth rate during the linear stage of growth is almost exactly 0.31, as predicted by the dispersion relation (2.3.29). The growth rate for this simulation is also included in Fig. 2.15 for comparison (solid line). As with the SOG solutions in the previous section, the upper-layer perturbation preferentially amplifies at the bottom of the layer, thus giving the developing high/low pressure cells a somewhat conical appearance. A vertical cross-section at $y = 2.0$, $t = 50.0$ of the upper-layer streamfunction is plotted in Fig. 2.16. This tapered vertical structure is also ubiquitous in the source flow simulations, described in the next chapter.

2.4 Parabolic Front

While a wedge-type basic state illustrates some of the features of instability in this model, hydrographic measurements suggest that a parabolic current profile is highly relevant for oceanographic applications (e.g. Bruce 1995). A double front, i.e. one bounded by two incroppings, has been observed in association with the southwestward-flowing DSO water, northward-flowing Antarctic Bottom Water, and other abyssal currents (Paldor and Ghil 1990; Sandoval and Weatherly 2001). We consider a basic state of the form

$$h_0(y) = \max\left[1 - (y/a)^2, 0\right], \tag{2.4.1}$$

where $a > 0$ measures the half-width of the undisturbed current, so that the undisturbed incroppings are located at $y = a_1 = -a$ and $y = a_2 = a$. The cross-channel gradient of the current thickness is then given by

$$h_{0y} = \begin{cases} -2y/a^2 & \text{if } |y| < a, \\ 0 & \text{otherwise,} \end{cases} \tag{2.4.2}$$

so that F retains its y dependence, making the problem non-separable. At this point we utilize a Galerkin-type method similar to that used in Sutherland and Peltier (1994). We first expand φ in an orthonormal basis, such that each of the modes individually satisfies (2.3.19), (2.3.20) and (2.3.22),

$$\varphi(y, z) = \frac{1}{\sqrt{L}} \sum_{n=1}^{\infty} b_n \sin Y_n \cosh(\lambda_n z), \tag{2.4.3}$$

where

$$Y_n = \frac{n\pi(y+L)}{2L} \qquad \text{and} \qquad \lambda_n^2 = N^2\left[k^2 + \left(\frac{n\pi}{2L}\right)^2\right]. \tag{2.4.4}$$

We note that k, $\dfrac{n\pi}{2L}$ and λ_n are the along-channel, cross-channel and vertical wavenumbers, respectively. Physically, the expansion eigenfunctions represent topographic Rossby wave modes (see PSa).

Substituting the assumed solution (2.4.3) into (2.3.21), multiplying through by $\sin Y_m$ and integrating over $y \in (-L, L)$, yields the following infinite system of equations in the unknowns b_n,

$$\sum_{n=1}^{\infty}\left[(c+\nu)(c\lambda_n \sinh\lambda_n + \nu N^2 \cosh\lambda_n)I_1^{mn} - 2\frac{\mu\nu N^2\cosh\lambda_n}{a^2}I_2^{mn}\right]b_n = 0, \tag{2.4.5}$$

for $m = 1, 2, 3, \ldots$, where

$$I_1^{mn} = \int_{-L}^{L} \sin Y_m \sin Y_n dy \qquad \text{and} \qquad I_2^{mn} = \int_{-a}^{a} y \sin Y_n \sin Y_m dy. \tag{2.4.6}$$

The above linear system may be written more compactly as

$$(c^2\mathbf{A} + c\mathbf{B} + \mathbf{D})\mathbf{b} = \mathbf{0}, \tag{2.4.7}$$

for appropriate coefficient matrices **A**, **B**, **D**, where the elements of the vector **b** are the expansion coefficients b_n.

Because the (unknown) complex phase speed appears quadratically in (2.4.7), the equation is referred to as a quadratic eigenvalue problem. Such problems arise in a wide variety of applications, including structural mechanics, acoustics and signal processing. For an excellent survey of their applications and mathematical properties as well as relevant solution techniques, we refer the reader to Tisseur and Meerbergen (2001). Here we follow the approach of Wilkinson (1965). Since **A** is diagonal with non-zero diagonal entries we can multiply through by $\mathbf{A}^{-1}$ and, defining the auxiliary vector $\widetilde{\mathbf{b}} = c\mathbf{b}$, we obtain the doubly-infinite, but otherwise standard, eigenvalue problem,

$$\mathbf{PV} = c\mathbf{V}, \tag{2.4.8}$$

where

$$\mathbf{P} = \begin{bmatrix} \mathbf{O} & \mathbf{I} \\ \mathbf{P}_{21} & \mathbf{P}_{22} \end{bmatrix} \qquad \text{and} \qquad \mathbf{V} = \begin{bmatrix} \mathbf{b} \\ \widetilde{\mathbf{b}} \end{bmatrix}. \tag{2.4.9}$$

Here **O** denotes the zero matrix, **I** is the identity matrix, while P_{21} and P_{22} are defined below.

For nontrivial solutions, c will be an eigenvalue of the system, in which case (2.4.8) implicitly defines a dispersion relation of the form

$$c = \widehat{c}(k, \mu, \nu, N, a, L). \tag{2.4.10}$$

The normal mode analog of the energy equation associated with (2.1.54)–(2.1.57) imposes a constraint on the allowed solutions. This constraint has the form of a semicircle theorem (PSa) and may be written

$$\left(c_R + \nu + \frac{2\mu}{a}\right)^2 + c_I^2 \leq \frac{2\mu}{a}\left(\frac{2\mu}{a} + \nu\right). \tag{2.4.11}$$

Aphysical modes, which do not satisfy the above condition, are filtered out. For completeness, we write down the explicit expressions for the necessary integrals,

$$I_1^{mn} = \delta_{mn} L, \tag{2.4.12}$$

$$I_2^{mn} = \begin{cases} \left(\frac{L}{m\pi}\right)^2 \sin(m\pi)\sin\left(\frac{m\pi a}{L}\right) - \frac{La}{m\pi}\sin(m\pi)\cos\left(\frac{m\pi a}{L}\right) & m = n, \\ \left[\frac{2La}{\pi(m-n)}\cos\left(\frac{\pi(m-n)a}{2L}\right) - \left(\frac{2L}{\pi(m-n)}\right)^2 \sin\left(\frac{\pi(m-n)a}{2L}\right)\right]\sin\left(\frac{\pi(m-n)}{2}\right) & \\ -\left[\frac{2La}{\pi(m+n)}\cos\left(\frac{\pi(m+n)a}{2L}\right) - \left(\frac{2L}{\pi(m+n)}\right)^2 \sin\left(\frac{\pi(m+n)a}{2L}\right)\right]\sin\left(\frac{\pi(m+n)}{2}\right) & m \neq n \end{cases} \tag{2.4.13}$$

and coefficient matrices,

$$\mathbf{P}_{21}^{mn} = (-\mathbf{A}^{-1}\mathbf{D})^{mn} = \frac{2\mu\nu N^2 \cosh\lambda_n}{a^2 L \lambda_m \sinh\lambda_m} I_2^{mn} - \delta_{mn}\frac{\nu^2 N^2}{\lambda_m}\coth\lambda_m, \tag{2.4.14}$$

$$\mathbf{P}_{22}^{mn} = (-\mathbf{A}^{-1}\mathbf{B})^{mn} = -\delta_{mn}\nu\left(1 + \frac{N^2}{\lambda_m}\coth\lambda_m\right). \tag{2.4.15}$$

Truncating the expansion (2.4.3) at a finite number of modes M, i.e. $1 \leq m \leq M$, allows the system (2.4.8) to be solved using one of several standard numerical routines. We have verified that as the number of modes is increased, there is clear convergence to a set of distinct solutions. The results presented here were all obtained using 120 modes, which we found to be adequate for our purposes. For example, the change in maximum growth rate or the high-wavenumber cutoff was less than 1% when M

was doubled to 240. Our tests, for a variety of parameter values, seem to suggest that a truncation of $M = 120$ offers a reasonable balance between accuracy and computational cost. The system (2.4.8) was solved employing the routine DEIGV from the NSWC Library of Mathematics Subroutines (Morris 1993).

Before we characterize the initial stages of instability with respect to various regimes of parameter space, two remarks should be made. First, we point out that the truncated eigenproblem (2.4.8) admits several modes of instability. The class of solutions described in the next two subsections is that which corresponds to the highest growth rates for a given set of parameter values. This family of solutions also exhibits a single extremum in the cross-channel direction. We refer to these modes as primary modes of the instability. Secondary modes, with smaller growth rates and a more complicated cross-channel structure, are discussed in subsection 2.4.3. Secondly, we note that in the rest of this chapter it is assumed that $L = 3.0$. We have found that the instability characteristics are not significantly affected by varying the channel width, $2L$, as long as the channel is wide enough to allow deformation of the incroppings. In the results that follow, the distance between an incropping and the closest boundary is at least as large as the current half-width. In general, however, we find that there is a weak tendency for lengthscales and timescales to increase with increasing L.

2.4.1 The Dispersion Relation

Setting $N^2 = \nu = a = 1.0$, (2.4.8) was solved with three different values of the interaction parameter, μ. In Fig. 2.17a, we plot primary mode perturbation growth rates, $\sigma = kc_I$, versus along-channel wavenumber k, for $\mu = 1.0$, 2.0 and 3.0. While there is no low-wavenumber cutoff, there is a high-wavenumber cutoff in all three cases. As μ increases, so do the maximum growth rate, the value of the most unstable wavenumber and the range of unstable wavenumbers. This is consistent with the analysis of S91 for parabolic coupled fronts. Physically, the trend may be interpreted

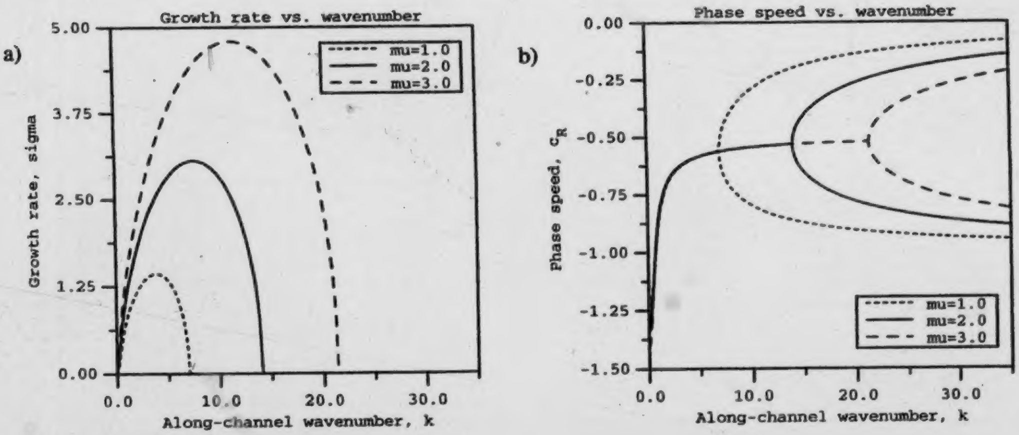

Figure 2.17: a) Growth rates $\sigma = kc_I$, and b) phase speeds c_R, versus along-channel wavenumber k, corresponding to the most unstable mode found for $\mu = 1.0$ (dotted lines), $\mu = 2.0$ (solid lines) and $\mu = 3.0$ (dashed lines). In both plots, $\nu = a = N^2 = 1.0$.

as follows. Increasing μ is equivalent to increasing δ, while keeping s fixed. As the depth fraction is increased, the fluid becomes more baroclinic, leading to larger growth rates and shorter wavelengths. Similarly, if we interpret δ as the upper-layer Rossby number (see (2.1.32)), we see that growth rates increase when the upper-layer inertial terms become more important.

As was alluded to previously, the most unstable wavenumbers are larger in the present model, for nonzero N, than those obtained for the S91 model with the same parameter values. This trend is discussed further below. Phase speed curves corresponding to Fig. 2.17a are displayed in Fig. 2.17b. The speeds are all negative, i.e. moving in the direction of the mean flow in the present channel geometry. Also, the phase speed curves show very little change in the unstable range of wavenumbers as μ is increased. They are however, fairly dispersive. Fig. 2.17b also suggests that this mode of instability results from a coalescence of two Rossby wave modes.

Increasing N, the nondimensional buoyancy frequency, has a similar effect to that of increasing μ, as Fig. 2.18a demonstrates. Setting $\mu = 2.0$ and $\nu = a = 1.0$, we solved (2.4.8) for $N^2 = 0.5$, 1.0 and 1.5. Again, with increasing N, the growth rate

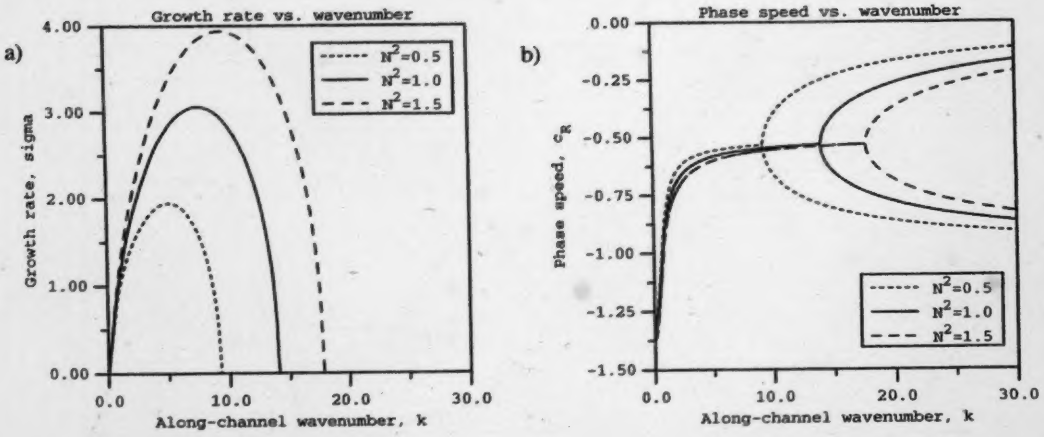

Figure 2.18: a) Growth rates $\sigma = kc_I$, and b) phase speeds c_R, versus along-channel wavenumber k, corresponding to the most unstable mode found for $N^2 = 0.5$ (dotted lines), $N^2 = 1.0$ (solid lines) and $N^2 = 1.5$ (dashed lines). In both plots, $\mu = 2.0$, and $\nu = a = 1.0$.

for any given wavenumber is increased, as is the high-wavenumber cutoff. This is reasonable on physical grounds, since increasing the stratification inhibits vertical motions. A density stratified fluid disturbed from below may be characterized by an effective depth (see Lane-Serff and Baines 2000) above which perturbations are damped out and isopycnal departures become negligible. This depth, where it is smaller than the actual depth, will determine the qualitative behavior of the fluid. Thus, in the present model, increasing N corresponds to decreasing the effective thickness of the upper layer, which, in essence, makes the system more baroclinic without increasing μ.

As in the case of the wedge front, the increased baroclinicity is manifested in a more vigorous, localized instability. While not shown, the analogous σ curve for $N = 0$ (i.e. the S91 case) is smaller than all three curves in Fig. 2.18a, with a maximum of 0.7 at $k = 1.2$ (see Table 2.1). Fig. 2.18b contains a plot of the phase speed curves corresponding to Fig. 2.18a. We can see that c_R becomes more dispersive at low wavenumbers as N is decreased.

Next, the half-width, a, of the current was varied while the other parameters were

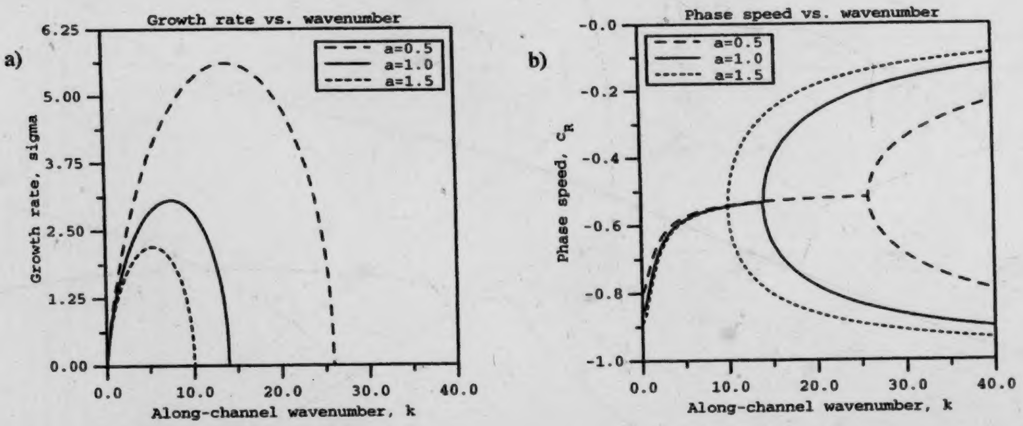

Figure 2.19: a) Growth rates, $\sigma = kc_I$, and b) phase speeds, c_R, versus along-channel wavenumber, k, corresponding to the most unstable mode found for $a = 0.5$ (dashed lines), $a = 1.0$ (solid lines) and $a = 1.5$ (dotted lines). In both plots, $\mu = 2.0$ and $\nu = N = 1.0$.

held fixed, i.e. $\mu = 2.0$, $\nu = N^2 = 1.0$. Fig. 2.19a demonstrates growth rate curves for $a = 0.5$, 1.0 and 1.5. The opposite trend from the previous two cases is apparent, in the sense that both the growth rates and range of unstable wavenumbers decrease with increasing a. Similarly, as the current width becomes smaller, the dominant wavelength of the instability increases. This result is consistent with the findings of S91. We plot the corresponding phase speed curves in Fig. 2.19b.

For easy reference, Table 2.1 contains selected quantitative results which characterize the instability, with $a = \nu = 1.0$. For the most-unstable wavenumber $\widehat{k}$, we have tabulated the corresponding lengthscale λ, phase speed $\widehat{c}_R$ and growth rate $\sigma_{\max} = \sigma(\widehat{k})$. It is useful at this point to cast the same quantities in terms of dimensional variables. We choose scaling parameters applicable to the SOG, as discussed in section 2.2.1. Based on available data, the case $\mu = N^2 = 1.0$ is most closely applicable to dynamics at depth in the SOG. The other entries are provided for comparison purposes, where an increase in μ may be interpreted as a thicker lower layer, and a higher value of N corresponds to a larger Burger number for the ambient ocean.

Vertical density profiles in the northern part of the strait suggest $0.5 < N^2 < 1.0$

μ	N^2	$\widehat{k}$	λ	$\widehat{c}_R$	$\sigma_{\max}$	λ^*(km)	c_R^*(cm/s)	T_e^*(h)
1.0	1.0	3.9	1.61	-0.61	1.42	11.8	-10.0	8.5
2.0	1.0	7.6	0.83	-0.56	3.06	6.0	-9.2	3.9
3.0	1.0	11.4	0.55	-0.54	4.79	4.0	-8.8	2.5
2.0	0.0	1.2	5.20	-0.50	0.70	38.2	-8.2	17
2.0	0.5	5.1	1.23	-0.56	1.95	9.0	-9.2	6.2
2.0	1.5	9.6	0.65	-0.56	3.94	4.8	-9.2	3.1

Table 2.1: Dispersion characteristics for various values of μ and N^2. We define $\widehat{k}$, λ and $\sigma_{\max}$ to be the most-unstable wavenumber, dominant wavelength and maximum growth rate, respectively. The asterisked quantities λ^*, c_R^* and T_e^* are the dimensional dominant wavelength, phase speed and e-folding time, respectively. The symbols μ, N and $\widehat{c}_R$ are defined in the text.

as a reasonable estimate (LeBlond *et al.* 1991). While a linearly sloping topography is a poor approximation of the SOG bathymetry, KST utilized a piecewise-linear topography in their calculation, such that the current was initially located on one linearly-sloping surface. It is not unreasonable therefore, to compare our results with those of KST in a quantitative way. Table 2.1 also contains the dimensional quantities λ^*, c_R^* and T_e^*, i.e. the dominant wavelength, phase speed and e-folding time, respectively.

The relatively short lengthscales and timescales predicted for the SOG seem to be consistent with the observational analyses of Stacey *et al.* (1991). In the case $\mu = N^2 = a = 1.0$, Table 2.1 shows that the dominant along-channel wavelength is about 11 km and the e-folding time is several hours. This is in good agreement with the results of Stacey *et al.* (1991), in which the flow field is highly variable, with eddy diameters on the order of 10 km. The linear analysis of KST predicted lengthscales of about 40 km in this parameter regime. We believe it is noteworthy that for the present model we obtain lengthscales much more in agreement with the SOG observations.

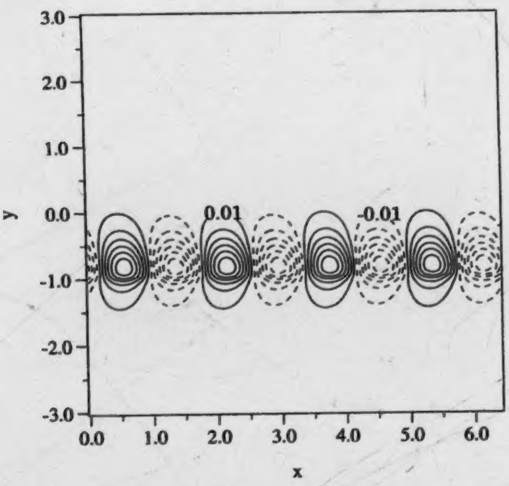

Figure 2.20: Upper-layer perturbation solution at $z = -1$, corresponding to the most unstable mode found for $\mu = N^2 = \nu = a = 1.0$, plotted at the most unstable wavenumber, $k = 3.9$ (see dotted curve in Fig. 2.17a). Four along-channel wavelengths are shown. Dashed lines correspond to negative values. The contour interval is 4×10^{-3}.

2.4.2 Primary Mode of Instability

In this section we describe the spatial structure of the primary mode of instability. Figs. 2.20, 2.21 and 2.22 are cross-sections of the upper-layer streamfunction, φ, for $\mu = N^2 = \nu = a = 1.0$. The along-channel wavenumber is $k = 3.9$, which corresponds to the highest growth rate in Fig. 2.17a (dotted curve). Physically, if the parabolic-front current is perturbed by a superposition of small waves with random wavelengths, then for these values of the parameters, the wavelength expected to dominate the flow is $2\pi/3.9 \approx 1.61$, at least until nonlinear effects become important. Using our SOG scalings, Table 2.1 suggests a dimensional wavelength of about 12 km. The instability manifests itself in the upper layer as high- and low-pressure anomalies aligned along the down-slope edge of the current in an alternating pattern. The contour plots in Figs. 2.20, 2.21 and 2.22 represent upper-layer sections at $z = -1$, $z = 0$ and $y = -0.84$, respectively.

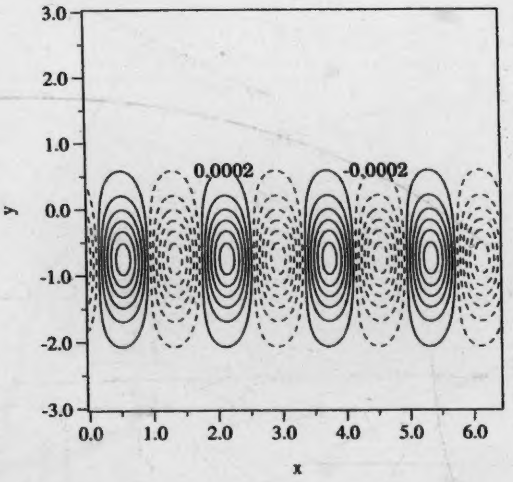

Figure 2.21: Upper-layer perturbation solution at $z = 0$, corresponding to the most unstable mode found for $\mu = N^2 = \nu = a = 1.0$, plotted at the most unstable wavenumber, $k = 3.9$ (see dotted curve in Fig. 2.17a). Four along-channel wavelengths are shown. Dashed lines correspond to negative values. The contour interval is 4×10^{-5}

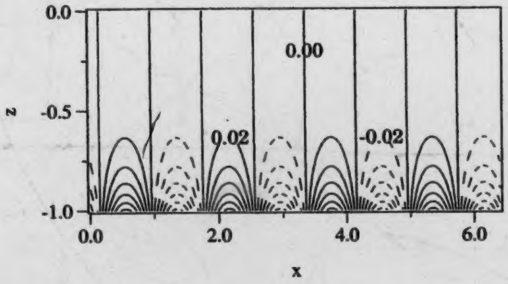

Figure 2.22: Vertical cross-section of the perturbation solution at y = -0.84, corresponding to the most unstable mode found for $\mu = N^2 = \nu = a = 1.0$, plotted at the most unstable wavenumber, $k = 3.9$ (see dotted curve in Fig. 2.17a). Four along-channel wavelengths are shown. Dashed lines correspond to negative values. The contour interval is 4×10^{-3}.

We can see from Figs. 2.20 and 2.21 that the perturbation is bottom-intensified, as its amplitude at the surface, $z = 0$, is about 50 times smaller than at the bottom, $z = -1$. The vertical section in Fig. 2.22 was taken at $y = -0.84$ since this is

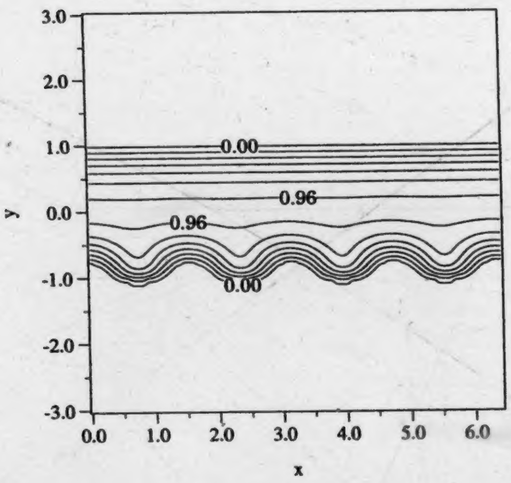

Figure 2.23: Lower-layer thickness corresponding to the most unstable mode found for $\mu = N^2 = \nu = a = 1.0$, plotted at the most unstable wavenumber, $k = 3.9$ (see dotted curve in Fig. 2.17a). Four along-channel wavelengths are shown. The contour interval is 0.12.

where the pressure anomalies were most intense. Again, the bottom-intensified nature of upper-layer flow is evident. We interpret these pressure anomalies as vertically-tapered eddies, not unlike bottom-intensified structures which are often associated with coherent, bottom-trapped features propagating along continental shelves. It is also important to point out that the anomalies in Figs. 2.20 and 2.21 are highly localized in the cross-channel direction, which is consistent with the Stacey *et al.* (1991) survey. The S91 solutions, on the other hand, exhibit upper-layer vortices which extend over the entire width of the channel. Retaining ambient stratification in the two-layer frontal-geostrophic formalism seems to result in more realistic eddy features, whose vertical and horizontal structure is more consistent with observations.

In Fig. 2.23 we plot the perturbed lower-layer thickness (i.e. $h_0(y) + h'(x, y, t_0)$), corresponding to the upper-layer plots in Figs. 2.20, 2.21, and 2.22. The down-slope front has been deformed by the wave-like perturbation. While a similar deformation of the up-slope front also exists, it is much weaker and cannot be discerned from

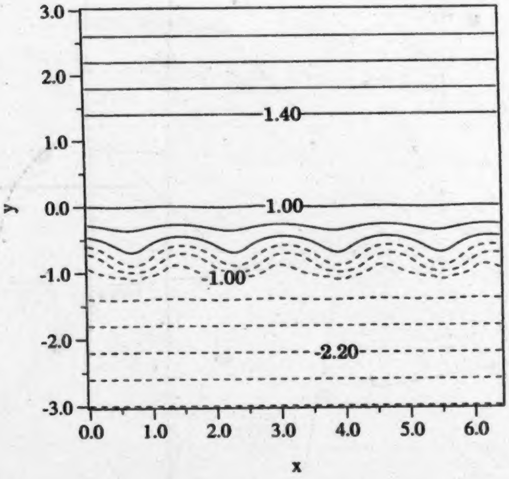

Figure 2.24: Lower-layer geostrophic pressure corresponding to the most unstable mode found for $\mu = N^2 = \nu = a = 1.0$, plotted at the most unstable wavenumber, $k = 3.9$ (see dotted curve in Fig. 2.17a). Four along-channel wavelengths are shown. The contour interval is 0.4.

the contour plots. This asymmetry is not surprising, since it clearly takes energy for fluid parcels to move up the slope, while moving down the slope releases energy. As the perturbation grows, dense plumes of lower-layer fluid descend into deeper water. Qualitatively, the plumes resemble the initial stages of bottom water spreading seen in numerical simulations of Gawarkiewicz and Chapman (1995) as well as Jiang and Garwood Jr. (1996).

It must be noted that the amplifying upper-layer Rossby waves are shifted slightly upstream of the corresponding lower-layer anomalies (compare Figs. 2.20 and 2.23). We interpret this as a vertical tilt of the unstable wave into the mean flow, which is the configuration favored by baroclinic energy release Pedlosky (1987). A contour plot of the lower-layer geostrophic pressure (2.1.58) is plotted in Fig. 2.24. Although the pressure, i.e. the streamfunction, is defined everywhere in the domain, it is only appropriate to consider lower-layer velocities in the region where the layer thickness is nonzero, as shown in Fig. 2.23. The pressure is a monotonically increasing function

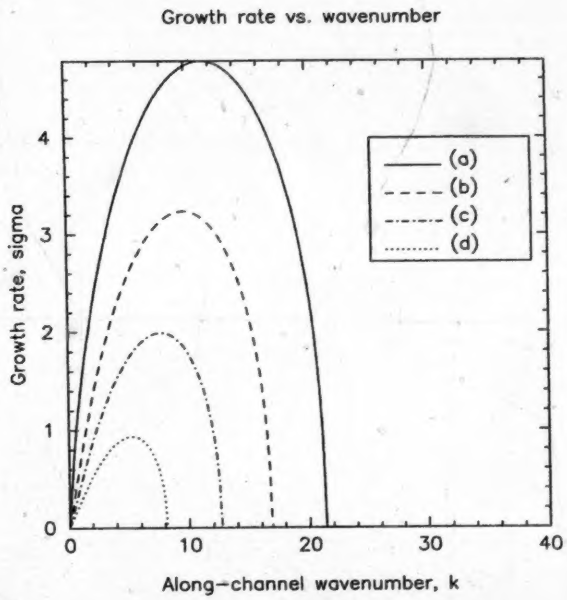

Figure 2.25: Growth rates, $\sigma = kc_I$, for four distinct solutions of (2.4.8) versus along-channel wavenumber, k, for $\mu = 3.0$ and $N^2 = \nu = a = 1.0$. The solid line (a) reflects the highest growth rates, and is the same curve as the dashed line in Fig. 2.17a. The curves (b), (c) and (d) are associated with successively weaker modes of instability and also exhibit successively smaller high-wavenumber cut-offs.

of y, indicating that the velocity is everywhere negative.

Our discussion in this chapter has been in the context of an x-periodic channel and x-invariant initial basic state. While this was done in order to facilitate comparison with the earlier studies of S91 and KST, the restrictions of periodicity and a continuous current are rather unphysical. As we show in chapter 3, however, the linear instability characteristics derived here remain valid, to a reasonable degree, for unsteady, propagating plumes. We shall discuss the relevance of our numerical integrations for other abyssal flows, such as the DSO.

2.4.3 Secondary Modes of Instability

The solutions we have discussed up to this point represent only the family of fastest-growing solutions to (2.4.8). Other solutions exist, however, whose instability char-

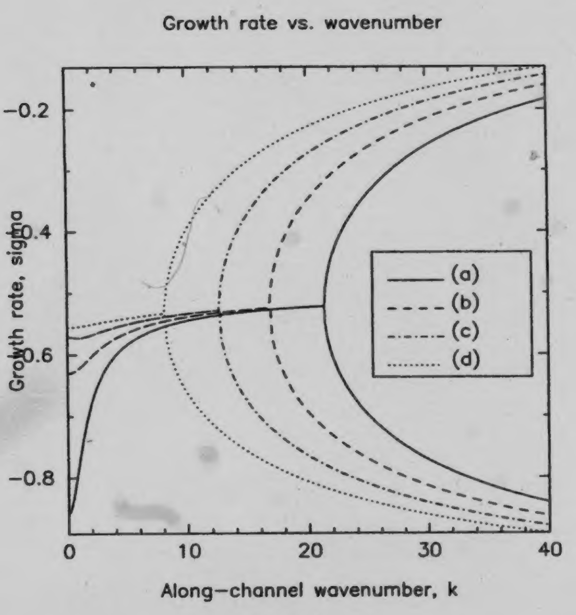

Figure 2.26: Phase speed curves corresponding to Fig. 2.25. Curve (a) is the same curve as the dashed line in Fig. 2.17b.

acteristics we now describe. As an example, for $\mu = 3.0$, $N = \nu = a = 1.0$, we have found four distinct solutions, whose growth rates and phase speeds are plotted in Figs. 2.25 and 2.26, respectively. Growth rate curve (a) in Fig. 2.25 is the same curve as the dashed line in Fig. 2.17a. (Similarly, phase speed curve (a) in Fig. 2.26 is the dashed line in Fig. 2.17b). The secondary modes (b), (c) and (d) are characterized by smaller growth rates, for any given unstable wavenumber k. Thus the σ curves in Fig. 2.25 and the c_R curves in Fig. 2.26 have been given the labels (a), (b), (c) and (d), in order of decreasing maximum growth rate, $\sigma_{\max}$, over all unstable k.

While these secondary solutions are unlikely to be realized physically starting from an infinitesimal disturbance, they may still emerge if a perturbation with the right wavenumber is of sufficient amplitude to push the system close to the nonlinear regime. The linear analysis of S91 identified a second distinct mode of instability for parabolic fronts, with smaller growth rates than the primary mode. This mode only existed beyond $\mu \approx 3.5$, whereas in the continuously-stratified case, the first

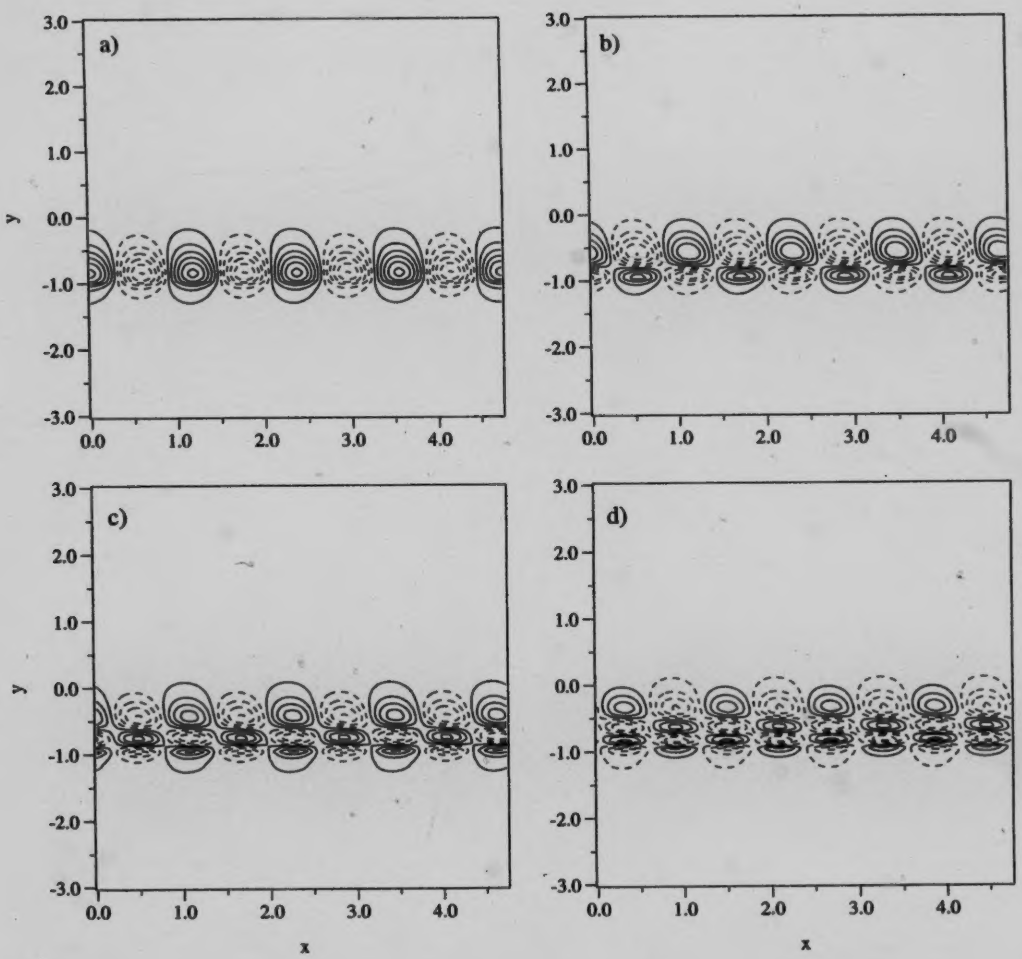

Figure 2.27: Contour plots of the upper-layer perturbation at z=-1 with $\mu = 2.0$ and $N^2 = \nu = a = 1.0$ at $k = 5.3$. The plots a), b) c) and d) correspond to the curves (a), (b), (c) and (d) in Fig. 2.25. The wavenumber, $k = 5.3$, is the most unstable wavenumber for the dotted-line curve, Fig. 2.25, i.e. the smallest growth rate curve found for these parameter values.

secondary mode already appears at $\mu \approx 0.1$.

The connection with the S91 theory becomes even more apparent when we consider the perturbation spatial structure. The solutions discussed in the previous subsection have a single extremum in the cross-channel direction (see Figs. 2.20 and 2.21), and

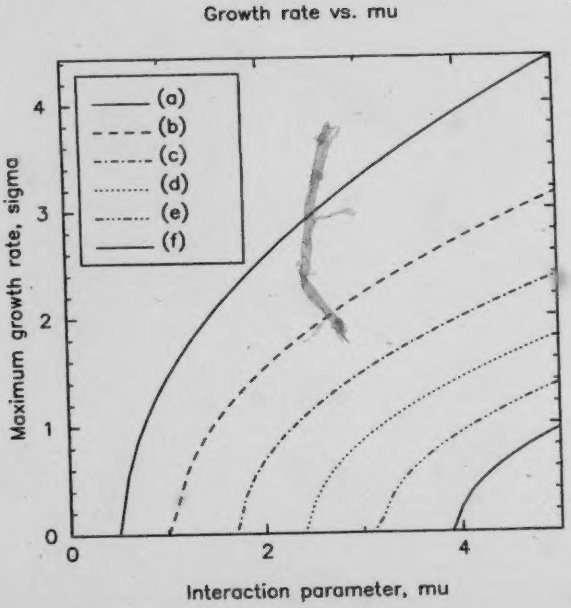

Figure 2.28: Growth rate at $k = 3.9$ versus μ. All existing unstable modes are shown, where the designations (a) through (f) refer to successively weaker modes. $k = 3.9$ is the most unstable wavenumber for $\mu = N^2 = \nu = a = 1.0$ (see dotted line curve in Fig. 2.17a). All curves in this plot correspond to $N^2 = \nu = a = 1.0$.

correspond to the "monopole" solutions in S91. The secondary mode in S91 was called a "dipole", as it exhibited two extrema in y. In the present model we can find solutions whose cross-channel structure exhibits two, three or more extrema, depending on the size of the solution set for a given choice of parameter values.

In Figs. 2.27a–d we plot the upper-layer perturbation at $z = -1$, corresponding to the four growth rate curves in Figs. 2.25a–d, respectively. Clearly, the contour plot in Fig. 2.27a (i.e. the solution with the highest growth rate) shows anomalies with a single extremum in the y direction, such as those in Fig. 2.20a. Fig. 2.27b is the "dipole" mode, similar to the secondary mode in S91. Finally Figs. 2.27c and 2.26d demonstrate the existence of solutions with 3 and 4 extrema in the cross-channel direction, respectively.

2.4.4 Dependence on μ

As was already mentioned, our analysis shows that the number of solutions to the dispersion relation is dependent on μ. In Fig. 2.28 we graph $\max_k[\sigma]$ for all existing solutions to (2.4.8) at $k = 3.9$ versus μ, where again, $N = \nu = a = 1.0$. We have chosen $k = 3.9$ since this is the fastest-growing wavenumber for the slowest-growing primary mode we have discussed. It is found that the system is stable to perturbations with this wavenumber for $0 < \mu < 0.6$, and a single solution mode appears at $\mu = 0.6$. Thereafter, with increasing μ, additional solution modes appear at $\mu \approx 1.1, 1.8, 2.5, 3.2$ and 4.0 so that a total of six solutions are found at $\mu = 5.0$. Presumably, the trend continues for higher values of μ, however we remind the reader that, formally, μ is required to be $O(1)$ in order for the leading-order balance (2.1.54)–(2.1.57) to hold. Finally, we note that increasing the buoyancy frequency N has a similar effect as increasing μ, in that the number of solutions to (2.4.8) also increases. This is again consistent with the idea that upper-layer stratification decreases the effective depth of the ambient fluid.

2.5 Numerical confirmation

The present simulation deals with the destabilization of a current such that its initial configuration exactly corresponds to our linear theory. Agreement between direct simulation and the spectral technique will serve as a check on the accuracy of both methods. The simulation employs the fully nonlinear CS-PG governing equations, and is performed in a periodic channel. Again, details of the computational method are contained in appendix B. The length of the channel is chosen such that it allows four wavelengths of the most unstable mode (as in Fig. 2.20), i.e. $\Omega_h = \{(x,y) | 0 < x < 0.644, -3.0 < y < 3.0\}$. The topography is linearly sloping as in (2.3.18) and we use the parameter values $\mu = \nu = N = 1.0$.

The current profile is given by (2.4.1) with $a = 1.0$. Initially the upper layer pressure is seeded with a random superposition of waves such that the range of along-channel wavenumbers is centered on the most unstable one, $k = 3.9$. The initial perturbation has no vertical variation, and the structure which later develops is purely

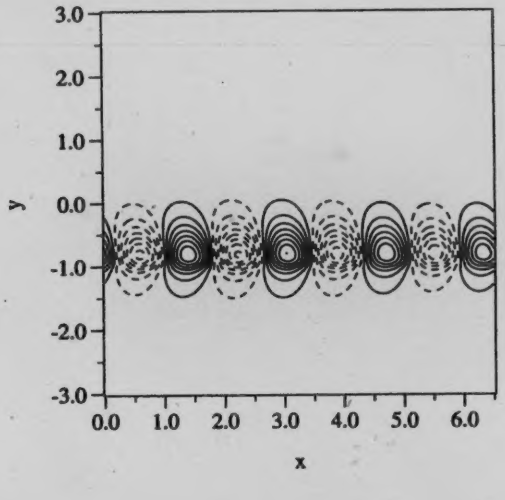

Figure 2.29: Contour plot of the upper-layer streamfunction at z=-1 obtained from the numerical simulation at $t = 15.0$. This plot should be compared with Fig. 2.20. The contour range is -1.05×10^{-2} to 1.05×10^{-2} and the contour interval is 1.4×10^{-3}. Dashed contours correspond to negative values.

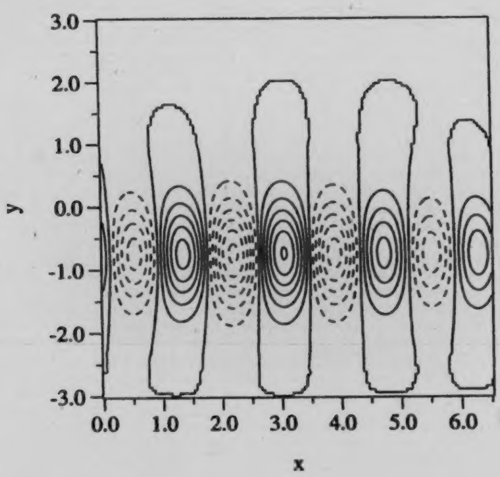

Figure 2.30: Contour plot of the upper-layer streamfunction at z=0 obtained from the numerical simulation at $t = 15.0$. This plot should be compared with Fig. 2.21. The contour range is -2.4×10^{-4} to 2.4×10^{-4} and the contour interval is 4.0×10^{-5}. Dashed contours correspond to negative values.

due to the baroclinic dynamics of the instability. The initial perturbation amplitude is adjusted so that its energy is small compared to the lower-layer gravitational energy, that is $E(0) = 10^{-30}PE_1(0)$. This ensures that the dominant mode emerges before the flow leaves the linear regime. The grid resolution is $138 \times 128 \times 16$ in the x, y and z coordinates, respectively. There is no friction or bottom drag in this simulation.

The instability is found to proceed according to our linear theory. Localized cyclonic/anticyclonic upper-layer pressure anomalies develop over the down-slope incropping, and the incroppings themselves become deformed. Figs. 2.29 and 2.30 show the $z = -1$ and $z = 0$ cross-sections of the upper-layer streamfunction at $t = 15.0$, which is well within the linear regime (see Fig. 2.31). Comparing the contour plots in Figs. 2.29 and Fig. 2.20, it is clear that the horizontal structure of the perturbation is well described by our theory. While not shown, the vertical structure of upper-layer anomalies, which are in effect amplifying topographic Rossby waves, is found to be vertically tapered, as in Fig. 2.22. Deformation of the up-slope incropping is very

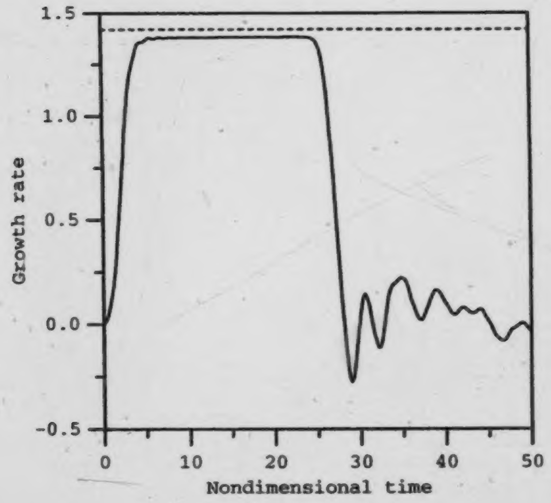

Figure 2.31: Perturbation growth rate versus time obtained from the numerical simulation, with parameter values same as in Figs. 2.20–2.24. Growth rate is based on the upper-layer total energy (i.e. the perturbation energy). The flat portion of the curve between $t \approx 5.0$ and $t \approx 25.0$ corresponds to the regime of linear growth, where our analysis applies.

small, whereas on the down-slope side the current clearly exhibits the initial stages of plume formation, in agreement with Fig. 2.23.

Heuristically, local increases in lower-layer thickness lead to compression of upper-layer fluid columns, causing anticyclonic anomalies. Similarly, regions of decreasing lower-layer thickness correspond to cyclonic upper-layer anomalies. The along-channel phase speed of the disturbance was approximately -0.61, which is consistent with the linear prediction (see Table 2.1). The initial flow evolution is similar to that observed in numerical simulations of Jungclaus *et al.* (2001). In their study of DSO dynamics using a primitive equation model, they found that anticyclones form closer to shore than cyclones. This behavior does not occur in the linear stage of growth we are describing, however it does become apparent later in the simulation. The staggered vortex pattern also develops early in our source-flow simulations, described in the next chapter.

In Fig. 2.31 we plot the growth rate $\overline{\sigma}$ vs. nondimensional time, where $\overline{\sigma}$ was calculated at each time step according to the finite difference equivalent of (2.3.31). After an initial adjustment period, the growth rate levels off at a value of 1.36, which is reasonably close to the predicted growth rate of 1.42 (see Table 2.1). The instability is in the linear regime for $5 \lesssim t \lesssim 25$, after which nonlinear effects become important. At this point the extent of lower-layer plumes is on the order of a, the current half-width, and the current is still mostly intact. The instability is nonlinearly saturated, temporarily halting the growth, and the growth rate remains close to zero for $30 \lesssim t \lesssim 50$.

Further nonlinear evolution of the flow has been described earlier in chapter 2 (see also Reszka and Swaters 2001; Swaters 1998), however a few remarks are appropriate here. As previously mentioned, the upper layer in this model is governed by QG dynamics, and is therefore subject to the red energy cascade (Pedlosky 1987). Typically, we find that after the initial saturation, upper-layer anomalies begin to merge, and the dominant along-channel wavenumber of the instability decreases. A similar drift toward larger lengthscales is then induced in the lower layer, and growth resumes at the lower wavenumber.

By contrast, no such shift in wavelength is evident in simulations of propagating plumes, described in chapter 3. In that scenario, mushroom-shaped subplumes form at a frequency roughly consistent with our linear theory, and the original plume disintegrates before any shift in lengthscale is observed. We believe that the source-flow configuration is more relevant for DSO dynamics than that of a continuous filament. Finally, we note that the long-term behavior we observed in the present simulation is somewhat different from that presented in (Swaters 1998). As the linear regime in the limit of a homogeneous upper layer is characterized by longer lengthscales in both the along-slope and cross-slope directions, developing pressure anomalies typically extend over the entire width of the current. This results in fairly prominent deformations of both incroppings (the sinuous mode; see S91) and sustained growth at the original wavenumber, which breaks up the mean flow into discrete spiral features.

Instability of rotationally constrained filaments in periodic domains was studied analytically by Griffiths, Killworth, and Stern (1982), Paldor and Killworth (1987), Paldor and Ghil (1990), S91, KST, Meacham and Stephens (2001) and others. The first three investigations do not include topographic effects and therefore cannot describe the baroclinic process which we are considering. All the above authors assume that the fluid surrounding the filament is homogeneous. Analogous numerical studies include Krauss and Käse (1998) and Jungclaus *et al.* (2001), who applied their primitive equation models to the DSO. These studies showed a similar initial flow evolution to the one we described in this section. Both cyclones and anticyclones were produced in the ambient fluid, although the anticyclones formed closer to the shore than cyclones.

Etling *et al.* (2000) investigated overflow dynamics and vortex formation in the laboratory setting, for a wide range of Rossby numbers. Their data suggest that for O(1) Rossby number, strong upper-layer cyclones are formed at regular intervals without baroclinic instability, possibly through the mechanism of Spall and Price (1998). They called this the "vortex regime". On the other hand for small Rossby number, the lower layer formed plumes similar to those reported by Jiang and Garwood Jr. (1996), with accompanying cyclonic vortices in the upper layer. We investigate the latter scenario, called the "plume regime", in the next chapter.

Chapter 3

Denmark Strait Overflow

3.1 Source flow simulations

An x invariant dense filament in a periodic channel is obviously a convenient steady state solution for the purposes of linear analysis. Our discussion of instability in this context also facilitated comparison with earlier studies. However, dense water intrusions tend to be pulse-like or episodic, rather than continuous (Dickson and Brown 1994). Moreover, laboratory experiments of bottom water spreading usually involve source flows with no imposed periodic structure (e.g. Whitehead, Stern, Flierl, and Klinger 1990; Lane-Serff and Baines 2000). Nevertheless, we find that the linear instability characteristics found in chapter 2 remain valid, to a reasonable degree, for unsteady, propagating plumes. In this chapter we describe two different numerical experiments, called EXP1 and EXP2, for easy reference. EXP1 describes the evolution of a dense plume that flows into the domain through one of the boundaries. Section 3.2 discusses simulation EXP2, which elucidates the role of realistic bottom topography in cyclogenesis.

In EXP1 the domain is closed, and the dense fluid enters from a source region along one of the boundaries. As part of EXP1, we will also investigate the effect of varying the interaction parameter, μ. The standard experiment is EXP1A, with $\mu = 1.0$.

Cases EXP1B ($\mu = 0.5$), EXP1C ($\mu = 0.25$) and EXP1D ($\mu = 0.1$) will be described below. For application to the DSO, we introduce the following scalings, where the notation is the same as in chapter 2: $H = 900$ m, $s^* = 2 \times 10^{-2}$, $g' = 2.0 \times 10^{-3}$ m/s^2, $f_0 = 1.3 \times 10^{-4}$ s^{-1} and $N_* = 1.5 \times 10^{-3}$ s^{-1}. This determines the stratification number, $N^2 = 1.0$, and slope parameter, $s = 0.22$. These environmental parameter values are consistent with those used in other numerical modelling studies of the DSO (e.g. Jiang and Garwood Jr. 1996; Spall and Price 1998). In particular, we assume the same value for the unscaled bottom slope s^* as Spall and Price (1998).

Next, we compute the dynamic lengthscale, $L^* = 10$ km, lower-layer velocity scale, $U_2 = 30$ cm/s, and with $\delta = 0.22$ (as in the standard experiment), an upper-layer velocity scale of $U_1 = 30$ cm/s. Dimensionally, the computational domain covers an area of 320 km×192 km, with a grid resolution of 1 km. Employing 16 vertical levels, the upper-layer vertical resolution is 60 m. The time scaling is 10 hours and the dimensional time step is 5.5 minutes. In order to damp out grid-scale noise, Laplacian and bi-harmonic numerical friction are introduced into the lower-layer equation, with coefficients 5.0×10^{-3} and 5.0×10^{-4}, respectively. We note that Laplacian friction is likely to damp out most of the noise occurring on spatial scales that would normally be damped by biharmonic friction.

A source of dense water is maintained on the right-hand boundary at $y = 144$ km for the duration of the experiment, by imposing a fixed, parabolic profile on h, the lower-layer thickness. This is the same profile as the basic state (2.4.1) with $a = 2.5$, but is shifted in the y coordinate and applied at the boundary only. Leading-order geostrophy then induces a velocity in the negative x direction, forcing fluid into the domain at a constant rate. The current is 50 km wide and has a thickness of 200 m in the standard experiment (see Table 3.1). We note that there is no up-slope counter-current associated with this thickness profile. The dimensional volume transport, $\overline{Q}^*$, into the domain is then 2.0 Sv, which is a reasonable approximation for the DSO (Price and Baringer 1994).

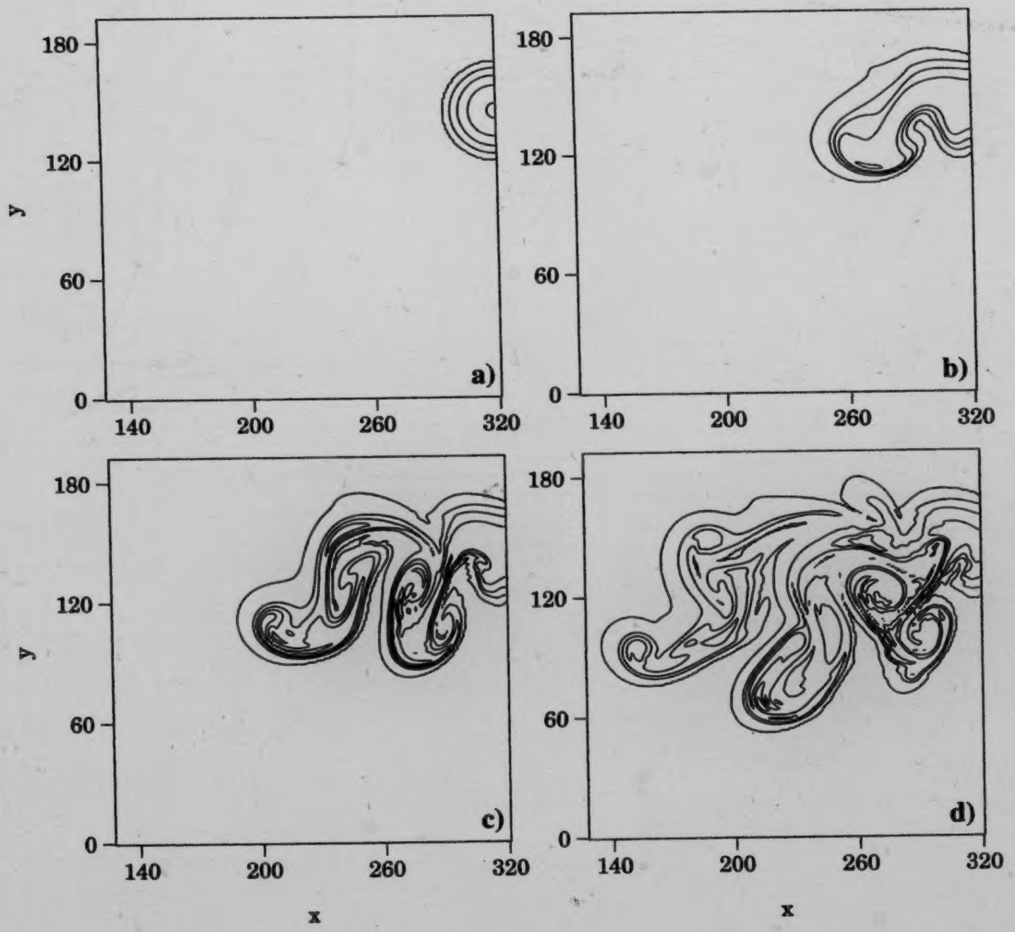

Figure 3.1: Contour plots of the dimensional lower-layer thickness at a) 0, b) 1.6, c) 3.2 and d) 4.8 days in simulation EXP1A. The contour extrema and intervals are a) 0 m, 200 m, 50 m, b) 0 m, 200 m, 50 m, c) 0 m, 240 m, 60 m, and d) 0 m, 240 m, 60 m, respectively.

In order to avoid steep spatial gradients at the head of the current, a surface in the shape of a quarter-sphere is also initially imposed adjacent to the source region, as shown in Fig. 3.1a. However, this *ad hoc* measure plays a minor role in subsequent dynamics, and its presence or neglect does not significantly alter the results. We initialize the upper-layer streamfunction to be identically zero, and prescribe no-

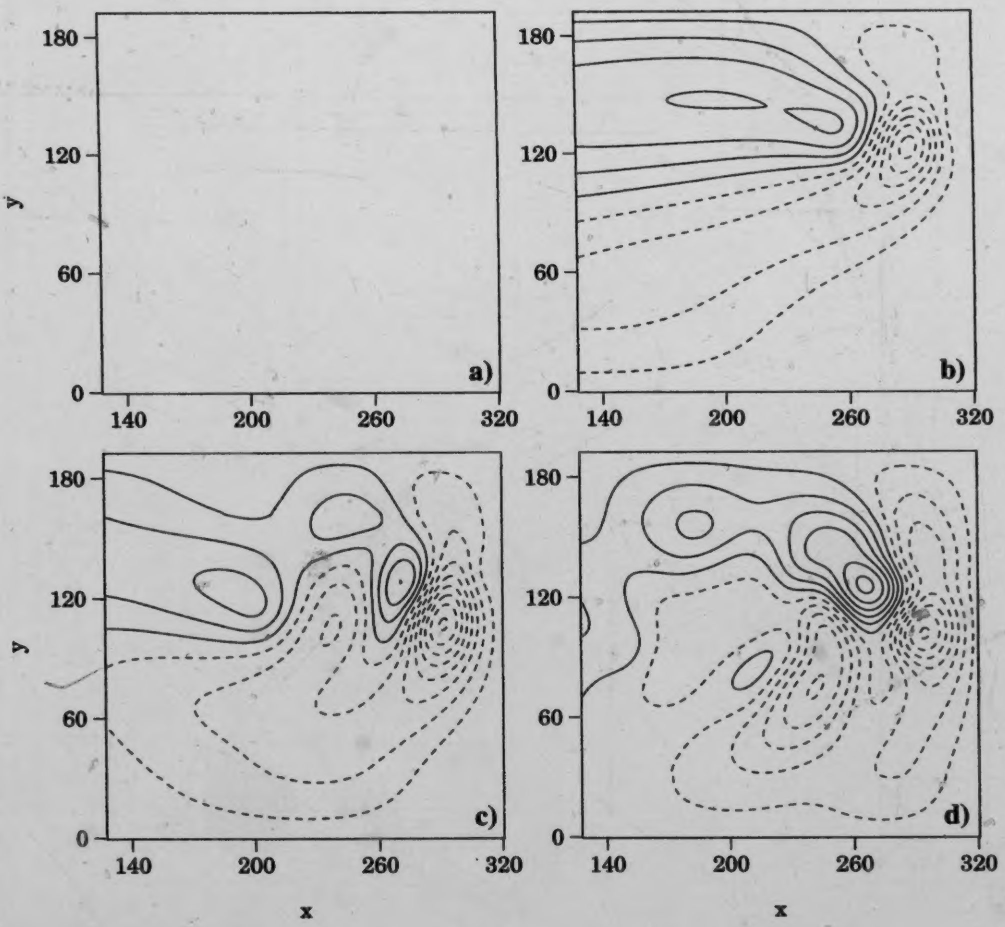

Figure 3.2: Contour plots of the nondimensional upper-layer streamfunction at $z = 0$ corresponding to the plots in Fig. 3.1. Dashed contours correspond to negative values. The initial condition, plot a), is zero everywhere. The contour extrema and intervals for the other plots are, respectively, b) -1.1, 0.7, 0.2, c) -2.3, 1.0, 0.3, and d) -2.6, 2.2, 0.4. Dashed lines correspond to negative values.

normal-flow conditions on all the horizontal boundaries.

Because the source is located at a boundary, mass conservation is implemented somewhat differently from the approach presented in chapter 2. In the context of the DSO, as pulses of dense water flow into the Irminger basin, presumably they cause some compression of the ambient fluid near the sill, while overall volume is conserved

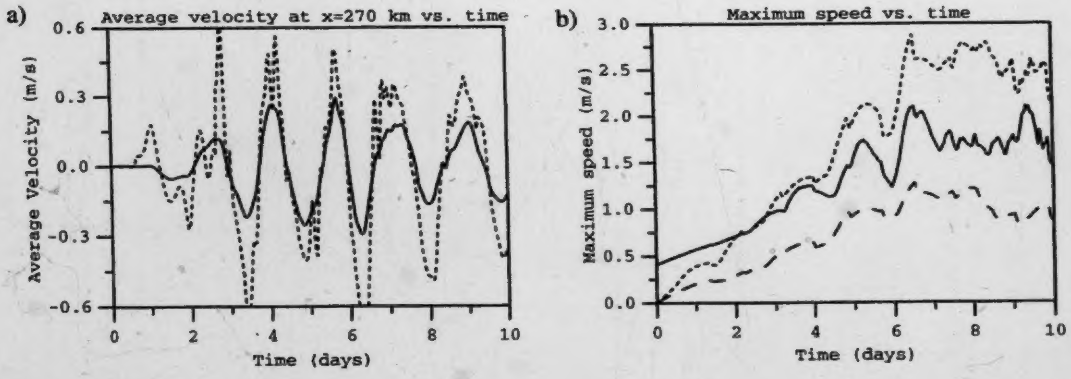

Figure 3.3: a) Cross-slope average of cross-slope velocity (m/s) versus time (days) measured 50 km downstream from the inflow in simulation EXP1A. Continuous line refers to the lower layer, dotted line refers to the upper layer at $z = -1$. b) Maximum flow speed (m/s) over the domain versus time (days) in simulation EXP1B. Speeds for the lower layer (solid line), upper layer at $z = -1$ (dotted line) and upper layer at $z = 0$ (dashed line) are shown.

through a diffuse mean flow of ambient fluid out of the basin. Our simulations do not include an outflow condition, nor do we wish to model conversion of upper-layer fluid to lower-layer fluid. Thus, the mass sink in the upper layer is distributed uniformly in the horizontal, such that the total rate of upper-layer fluid loss exactly compensates for the lower-layer source flux. Given the idealized nature of our numerical study, this choice seemed reasonable. Also, in order to avoid reflection of Rossby waves, a smoothing operator is successively applied to the upper-layer streamfunction at the sidewalls and downstream boundary. This crude sponge effectively removes energy from the system and allows us to focus on dynamics in the interior of the domain.

The evolution of the lower-layer height, $h(x, y, t)$, in simulation EXP1A is shown in Fig. 3.1 at 0, 1.6, 3.2 and 4.8 days. Corresponding plots of the upper-layer streamfunction at the surface, $\varphi(x, y, 0, t)$, are shown in Fig. 3.2. The computational domain in EXP1 and EXP2 was quite long to ensure that instability near the source region was not influenced by the downstream boundary. In order to focus on the unstable plumes, the panels in Fig. 3.1 and Fig. 3.2 only show the rightmost 192 km segment

Case	μ	h_* (m)	$\overline{Q}^*$ (Sv)	u_u (cm/s)	u_d (cm/s)
EXP1A	1.0	200	2.0	-6.0	-54.0
EXP1B	0.50	100	1.0	-18.0	-42.0
EXP1C	0.25	50	0.5	-24.0	-36.0
EXP1D	0.10	20	0.2	-28.0	-32.0

Table 3.1: Dimensional overflow properties for simulation series EXP1. Here u_u and u_d refer to the inflow velocity at the up-slope and down-slope incropping, respectively.

of the domain. The current becomes unstable immediately after entering the domain and a descending, mushroom-shaped plume has formed at 1.6 days. It continues to deform as it propagates along and down the slope, while two more plumes appear in the next two plots, at day 3.2 and 4.8 respectively.

For a parabolic current with $a = 2.5$, our linear analysis suggests a frequency of 1.57. This yields a dimensional period of roughly 1.6 days, which is indeed the period between successive subplumes in this simulation. The agreement in plume frequency, and therefore eddy size, seems to be a robust phenomenon with regard to parameter space. Thus, we feel that the linear results of chapter 2 are useful in characterizing the development of source flows in this regime. Good correlation between the predicted and actual frequencies of instability events is, to some degree, a result of the simplified physics we have assumed. To illustrate, as μ is decreased and the instability becomes weaker, the geostrophically balanced plume travels along the slope and acts similarly to the periodic gravity currents our linear theory considers. Table 3.2 lists some characteristics of the instability in dimensional units, as predicted by the analysis of section 2.4.1. The period, T^*, increases as μ (equivalently, the current height) decreases.

As part of the baroclinic process, strong eddies of both signs develop in the upper layer, and migrate away from the source region as seen in Figs. 3.2b–d. These vortices are bottom-intensified, although their surface signature is reasonably strong. Typical

Case	λ^* (km)	T^* (days)	T^*_e
EXP1A	29	1.6	11 hours
EXP1B	42	1.9	18 hours
EXP1C	48	2.1	1.2 days
EXP1D	52	2.1	2.1 days

Table 3.2: Dimensional instability characteristics predicted by the linear theory for the same configuration as simulation series EXP1, with $\nu = N^2 = 1.0$ and $a = 2.5$. Scalings appropriate for the DSO are discussed in text. Here λ^* is the dominant along-front wavelength, T^* is the period between successive instability events and T^*_e is the e-folding time. These values are consistent with the results of the nonlinear source-flow simulations in EXP1.

velocities are 120 cm/s at the bottom and 50 cm/s at the top of the layer. Overall, we did not find cyclones to be stronger than anticyclones in our simulations. At times, we observed domes of dense fluid coupled to strong low-pressure anomalies in the ambient layer, not unlike the vortices described by Whitehead *et al.* (1990) and Lane-Serff and Baines (1998, 2000). However, these baroclinic pairs did not form with any regularity and were not very long-lived (but see the discussion in section 3.2). As the above authors have noted, there are several potential processes by which a plume wraps up into a coherent, domed anomaly, and at the same time becomes coupled to a strong cyclone in the overlying fluid. Mechanisms such as Ekman draining and geostrophic adjustment, suggested by Lane-Serff and Baines (1998), are absent in our model. Krauss and Käse (1998) argue that ageostrophic advection of positive vorticity into the core of the eddy plays an important role in cyclogenesis.

In the PSa formalism, the only contribution from the lower-layer momentum equation is the geostrophic relation (the PG approximation), while the upper layer is governed by the conservation of QG PV. Upper- and lower-layer relative vorticity is advected solely by the geostrophic velocity field, which may explain the scarcity of baroclinic vortex pairs in our tests. However, coherent structures of this sort do appear regularly in EXP2, where the topography is no longer linear. It must also be remembered that we have chosen very simple boundary conditions, with no inflow or outflow imposed on the upper-layer velocity. Nevertheless, we found a definite asymmetry in the location of the eddies, in that cyclones tended to form on the offshore side of the current, while anticyclones appeared closer to shore. While this behavior is not described by our linear theory, it is entirely consistent with the numerical findings of Krauss and Käse (1998) and Jungclaus *et al.* (2001), as well as the observational data presented in Krauss and Käse (1998) (see chapter 1, Fig. 1.1).

The propagation of subplumes along and down the slope is associated with very regular velocity fluctuations in both layers. In Fig. 3.3a, for instance, we plot the cross-slope average of the cross-slope velocity versus time, measured at $x = 270$ km, i.e. 50 km downstream of the source. Both the upper and lower layer exhibit roughly sinusoidal velocity variations with an average period of 1.6 days. Similar fluctuations exist in the along-slope velocities (not shown). Near-bottom velocity fluctuations with timescales of 1.5–2.5 days downstream of the Denmark Strait have been reported by several authors on the basis of current meter measurements (Dickson and Brown 1994). A good example is the dataset from the Anmagssalik array off the east coast of Greenland (Dickson and Brown 1994, Fig. 6). As μ decreases, we find that velocities in the lower layer tend to be weaker than those at intermediate depths. In Fig. 3.3b we plot the evolving maximum lower-layer speed, $\sqrt{u_2^2 + v_2^2}$, for $\mu = 0.5$. The same figure also contains the upper-layer maximum speed at $z = -1$ and $z = 0$ as a function of time.

Velocities increase up to about 5 days, and thereafter the system remains in a quasi-steady state until the plume reaches the downstream boundary at 10 days. As Fig. 3.3b suggests, the upper-layer velocity structure is bottom-intensified, with speeds reaching 200 cm/s at the fluid interface during the first 3 instability events. However, lower-layer velocities during this time period rarely exceed 170 cm/s. Thus, in actual oceanographic applications, the highest velocities may occur not in the overflow waters, but at some depth above the bottom. We note that these velocities are somewhat higher than those typically observed in the DSO, however, these are the maximum speeds, and are limited to localized regions of the domain. During a typical instability event, we observe the following trend in the along-shore velocity. Initially the velocity of a nascent plume is close to the Nof velocity, with little cross-slope motion. During instability the along-slope component significantly decreases and the cross-slope component increases. After saturation the newly-formed plume resumes along-slope motion at the Nof speed.

The dynamics of the instability is highly dependent on the parameter μ, which measures the relative size of the upper- and lower-layer Rossby numbers. This parameter was recently used by Etling *et al.* (2000) to characterize the regime of instability in the DSO[1]. Here we present three additional simulations, which demonstrate the influence of μ on plume penetration and maximum velocities. The simulations are the same as EXP1A in every respect, except for the value of μ. Lower values of the interaction parameter may be interpreted as a smaller current height.

Near-bottom velocities south of Denmark Strait exhibit large fluctuations in velocity (and presumably volume flux) on periods as long as 12 days, quite apart from the variability associated with passing eddies (Dickson and Brown 1994). Thus, we believe the effect of varying the source strength is of interest. For reference, table 3.1 lists the four cases, along with the corresponding current height, h_*, source strength, $\overline{Q}^*$, as well as the minimum and maximum velocity at the source. As discussed in the Appendix, the mean current velocity at the inflow is 30 cm/s, i.e. the Nof speed. The theoretical wavelength, λ^*, period between instability events, T^*, and e-folding time, T_e^* relevant to these simulations are given in table 3.2. Qualitatively, the trend in T_e^* and T^* implies that the instability should be faster and more intense for higher

---

[1] Etling *et al.* (2000) estimate that $\mu = 0.6$ in the DSO, which is in the transition region between the vortex regime (lower μ, weak rotation) and plume regime (higher μ, strong rotation). Note, however, that this does not imply that our simulations describe the vortex regime since our derivation of the governing equations assumed that the fluid is geostrophic to leading order.

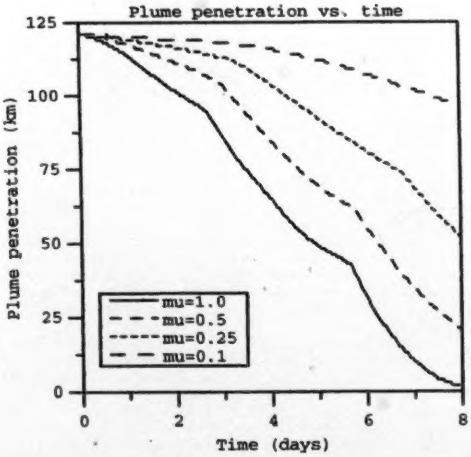

Figure 3.4: Plume penetration (km) versus time for the simulations in EXP1. Plume penetration refers to the smallest y coordinate for which $h(x, y, t) > 0$. Initially, the down-slope edge of the plume is at $y = 119$ km in all four cases. The cross-slope extent of the plume decreases with μ since the instability becomes progressively weaker.

values of μ. This is indeed the case in our simulations.

Fig. 3.4 is a plot of plume penetration distance versus time for the four different values of μ. We define this distance as the smallest y coordinate over the domain, for which h is nonzero. Initially, the down-slope incropping is located at $y = 119$ km for all four cases. In EXP1A, some subplumes reach the down-slope boundary, $y = 0$, at 8 days. As we would expect, smaller values of μ induce a weaker instability, allowing the plume to propagate farther along the topography as a coherent current. Conversely, more vigorous plume formation events resulting from higher values of the interaction parameter lead to increased cross-slope (and therefore down-slope) motion. Kinks in the curves, most visible in the $\mu = 1.0$ case, correspond to temporary saturation of growing subplumes. It should be noted that, once formed, some of the subplumes deform and subsequently undergo further baroclinic instability.

Eddy formation in the DSO has been the focus of many recent modelling efforts. Spall and Price (1998) propose the following mechanism by which strong cyclones are produced at regular intervals south of the strait. In their theory, dense fluid descends into the deeper ocean due to bottom drag, without the need for instability. Their simulations suggest that, as the overflow water migrates along and across the topographic slope, the result is an along-slope density gradient, which then induces midlevel water to migrate offshore as required by the thermal wind relation. The intense stretching of the upper Arctic Intermediate Water then leads to pronounced cyclonic eddies. However, Krauss and Käse (1998) point out that observations do not seem to support the presence of this intermediate layer farther than 150 km from the sill, or its stretching to any significant degree[2].

Jungclaus *et al.* (2001) suggest that the mechanism of Spall and Price (1998) may be operative if the local Rossby number is O(1), while for smaller Rossby numbers baroclinic instability of the deep layer induces eddies of both signs to form in the ambient ocean. Indeed, observations from the R/V *Poseidon* cruise in 1996 do confirm the existence of anticyclones in the DSO region (Krauss and Käse 1998). On theoretical grounds, Etling *et al.* (2000) argue that the dynamics of the DSO lies somewhere between these two regimes. It is possible therefore, that both of the mechanisms described above are operative to some degree in the DSO and other overflows.

Since the PSa model is derived assuming geostrophy to leading order, our simulations are relevant for the small Rossby number regime, and are in that respect similar to the numerical results of Jiang and Garwood Jr. (1996) and the second series of laboratory experiments in Etling *et al.* (2000). We would also like to make a general remark regarding cyclone intensification. Given that the Denmark Strait outflow encounters increasingly deeper topography upon entering the Irminger Basin, we should expect that fluid columns tend to be stretched, rather than compressed. It seems reasonable that, on average, this trend leads to a net gain in positive relative vorticity, which may then be manifested in subsequent instability processes.

---

[2] On the other hand, some observations do show midlevel water in the cores of the cyclonic eddies (e.g. Fig. 2 in Spall and Price 1998) downstream of the sill. Midlevel fluid in the surrounding ocean could be difficult to detect due to intense mixing associated with eddy formation (M. Spall, personal communication).

Fig. in Bruce (1995) suggests that DSO water is geostrophically balanced (flows along the slope with the coast on its right) and is constrained in the cross-slope directions (i.e. has two incroppings) (see also Paldor and Ghil 1990). However, the isopycnals may assume other configurations (M. Spall, personal communication). The dynamics we have described are not significantly sensitive to the exact initial shape of the abyssal layer, in the sense that any profile with a down-slope incropping gives rise to descending plume-like structures, with accompanying bottom-intensified, localized vortical waves in the ambient fluid. More gently sloping interfaces result in longer along-slope deformations of the incropping and broader vortex features in the overlying fluid. Instability characteristics for wedge-type fronts with no incroppings have been described in PSa and section 2.3.1. In that case, instability may be inhibited altogether in this model, if the necessary condition for instability (2.3.11) is not satisfied.

3.2 Cyclogenesis

While eddies of both signs have been reported in association with the DSO, observations and numerical results suggest that intense cyclones dominate the ambient flow field (Bruce 1995; Jungclaus *et al.* 2001). Baroclinic vortex pairs with a strong cyclonic component were observed in the laboratory by Whitehead *et al.* (1990), Lane-Serff and Baines (1998) and others. Such vortices exhibit a coherent dome of dense fluid, coupled to a low pressure anomaly in the overlying water, often detected as a well-defined surface depression (Whitehead *et al.* 1990).

A coupled vortex travels along the slope as a unit, often for a significant distance. Poulin and Swaters (1999b) found analytical eddy solutions to (2.1.54)–(2.1.57) with exactly these characteristics. For a radially-symmetric lower-layer anomaly with a parabolic cross-section, the upper-layer streamfunction could be described in terms of a superposition of Bessel functions. It was found that these eddies were bottom-intensified, and could transport fluid parcels for physically relevant values of the parameter μ, due to closed streamlines at some depths. In addition, the cyclonic circulation in the upper layer was typically strong enough to reverse the natural anticyclonic flow in the core of the dome anomaly.

We believe this property to be an important factor in the coupling of the two layers. Simulations in series EXP1, which employed linearly sloping topography, did not give rise to such eddy pairs with any regularity. On the other hand, we have found that topography which is convex does allow for the formation of these features at regular intervals. (Here and in the rest of the thesis, convex refers to a function whose second derivative is positive, while concave will refer to functions with negative second derivative.) Coastal topography, such as the western boundary of the Irminger Basin, is often steeper near the coast than offshore (e.g. Bruce 1995). Indeed, we can expect the bathymetry of any oceanic subbasin to flatten out in its interior. Therefore, we feel that a discussion of the effects of curvature in the topography is relevant here.

Let us consider a geostrophically balanced abyssal current with thickness $h(y)$, situated on topography given by $z = h_B(y)$. For simplicity, let $\mu = 1.0$, in the language of chapter 2. Assuming that the overlying fluid is initially quiescent, the lower-layer pressure (2.1.59) simplifies to

$$p = h_B + h. \tag{3.2.1}$$

Given that $p(y)$ is a streamfunction and the velocity is geostrophic, the lower-layer relative vorticity ζ will be

$$\zeta = (h_B + h)_{yy}. \tag{3.2.2}$$

If h_B is linear in y, the topographic term vanishes.

Moreover, for any $h(y)$ that is concave (e.g. a parabolic profile), we can see that the current possesses anticyclonic shear since $\zeta < 0$. This inherent anticyclonic vorticity must be overcome by an upper-layer cyclone if the dense fluid is to wrap up into a coherent dome. However, if h_{By} is an increasing function of y, then the topographic term can compensate to some degree, decreasing the anticyclonic shear. In that situation, upper-layer cyclones that form as a result of the initial instability are more likely to be strong enough to advect growing plumes in a cyclonic fashion, thus leading to the baroclinic vortex pairs described above. This is the process we see occurring in EXP2.

The boundary source is placed with its center at $y = 115$ km, in the same domain as EXP1. We introduce nondimensional topography of the form

$$h_B = A \ln(\exp(y - y_0) + 1.0), \tag{3.2.3}$$

which has the property that its gradient vanishes for decreasing y (away from the shore) and approaches a positive constant for increasing y (close to shore). We choose $A = 1.1$ and $y_0 = 9.2$ so that the topographic slope is 2×10^{-2} (as in EXP1) at the plume center. The topography flattens out considerably just below the down-slope incropping, where we expect plume development. Rayleigh damping was introduced in this simulation, with $C_d = 2.5 \times 10^{-2}$. While the diffusion-type term on the right-hand side of (2.1.57) is conducive to the development of prominent domed features, we stress that curvature in the topography plays the dominant role in this process. The simulation is the same as series EXP1 in all other respects.

Initial flow fields are similar to Figs. 3.1a and 3.2a, and are not shown. Contour plots of the evolving plume for $t = 2.8$, 4.7, 6.7 and 8.6 days are displayed in Figs. 3.5a–d. Plots of the upper-layer streamfunction at $z = 0$ are displayed in Fig. 3.6a–d. We remind the reader that, as before, each panel only shows the rightmost 192 km segment of the computational domain. While the initial instability proceeds similarly to the previous experiments, at 2.8 days the plume begins to wrap up on itself in a cyclonic sense (Fig. 3.5a), due to an intense low pressure cell in the overlying fluid (Fig. 3.6a). Retardation of lower-layer velocity due to smaller topographic gradients at the down-slope incropping aids in this process. A dome-like feature begins to emerge in the overflow layer at 4.7 days (Fig. 3.5b).

A coherent, steadily travelling dome of dense fluid is seen on the left-hand side

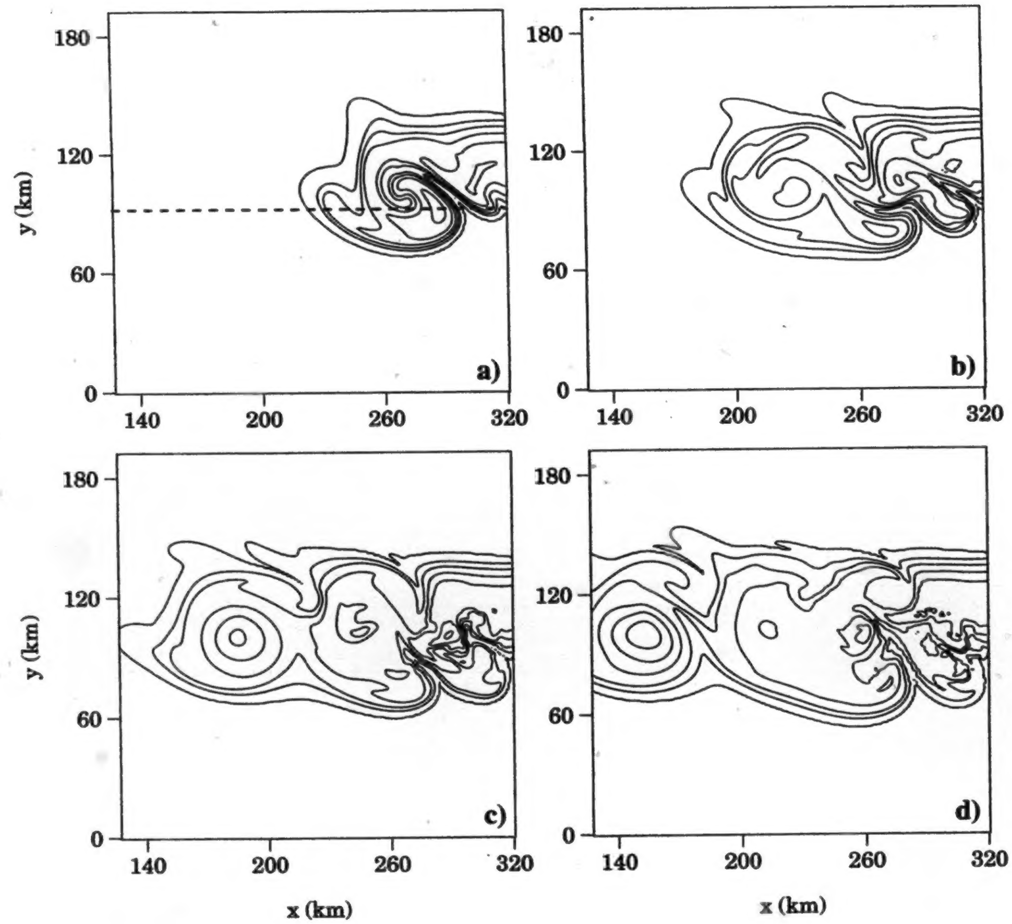

Figure 3.5: Dimensional lower-layer thickness at a) 2.8, b) 4.7, c) 6.7 and d) 8.6 days in simulation EXP2. The contour extrema and intervals are, respectively, a) 0 m, 200 m, 40 m, b) 0 m, 200 m, 40 m, c) 0 m, 240 m, 40 m, d) 0 m, 240 m, 30 m. The dashed line marks the dimensional coordinate $y^* = 92$ km, which corresponds to $y_0 = 9.2$ in the topographic profile (3.2.3).

of Figs. 3.5c and d. It is coupled to the cyclonic eddy visible in the same positions in Figs. 3.6c and d. This dome/cyclone pair was observed to propagate in unison for a much greater distance than any anomaly in the previous simulations. As soon as the original dome had formed and moved away from the source, another one began to develop in a similar fashion, induced by another strong upper-layer cyclone. This

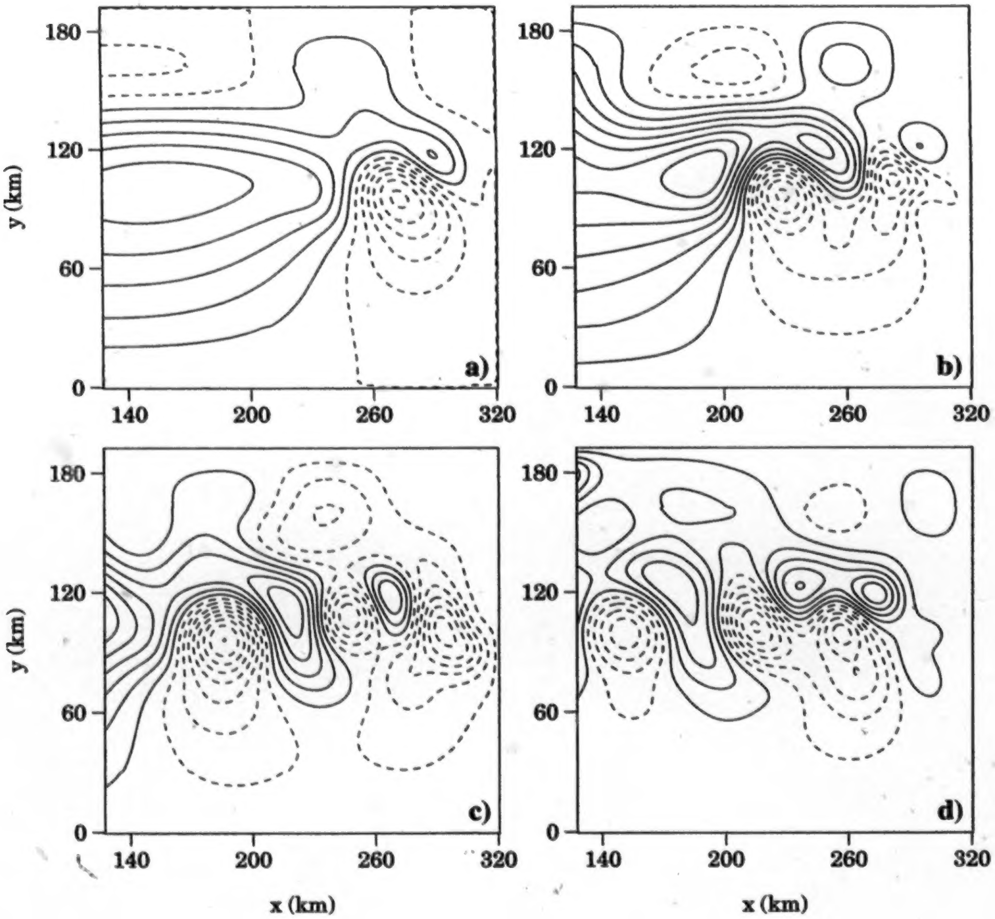

Figure 3.6: Upper layer pressure at $z = 0$ at a) 2.8, b) 4.7, c) 6.7 and d) 8.6 days in simulation EXP2. The contour extrema and intervals are, respectively, a) -0.5, 0.5, 0.1, b) -0.35, 0.18, 0.05, c) -0.31, 0.29, 0.05, and d) -0.32, 0.27, 0.06. Dashed contours correspond to negative values.

pair, though less well defined, appears in the middle of Figs. 3.5d and 3.6d. The along-slope speed of the baroclinic vortices was approximately 22 cm/s, somewhat slower than the average speed of 27 cm/s exhibited by DSO eddies (Bruce 1995). A small but non-negligible downhill component was also consistently present in our tests. We note that the theoretical Nof speed of 30 cm/s for a slope, $s^* = 2 \times 10^{-2}$,

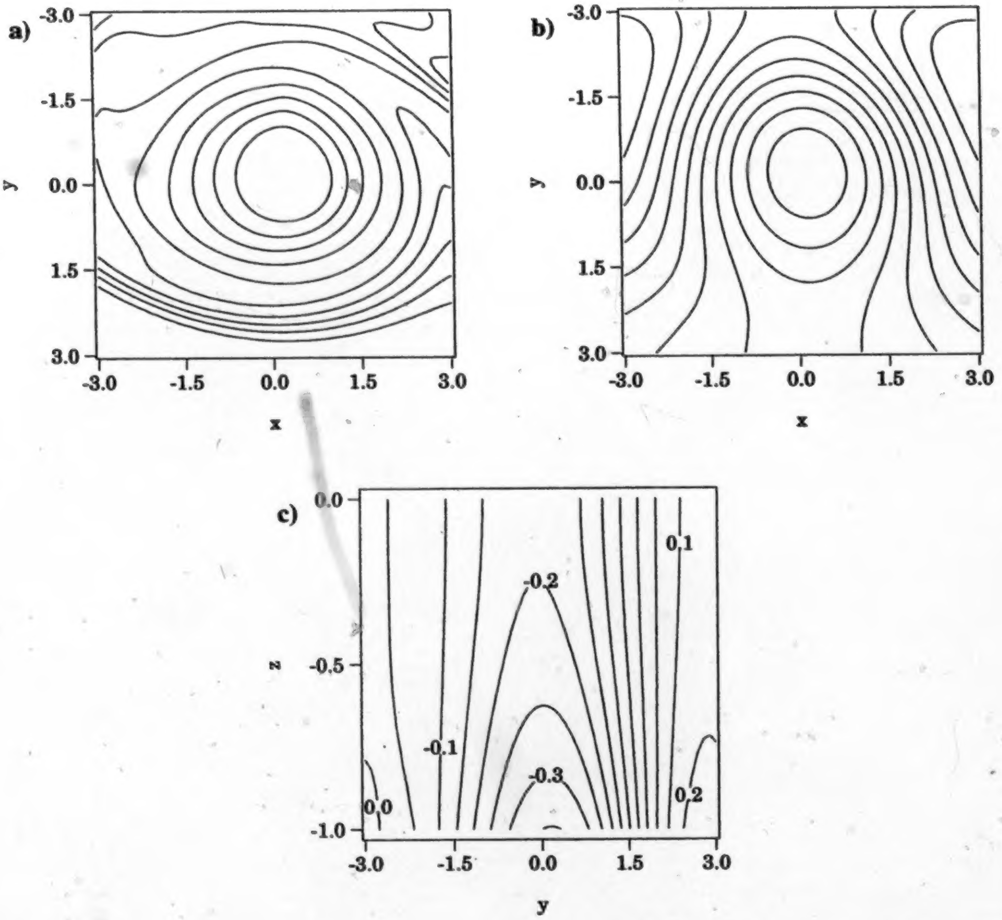

Figure 3.7: Close-up of nondimensional eddy structure in simulation EXP2: a) lower-layer thickness b) upper-layer pressure at $z = -1$ c) upper-layer pressure vertical cross-section.

is not inconsistent with available data on cyclone propagation in the DSO.

The dome-cyclone coupling is more clear from a movie of the simulation than from Figs. 3.5 and 3.6. Obviously, the instability gives rise to other positive and negative pressure anomalies, however we find these to be more elongated and transient, and usually weaker than cyclones that are coupled to lower-layer domes. We are able to discern a third baroclinic vortex at 8.6 days (Figs. 3.5d and 3.6d), roughly at $x = 260$

km. However by this time the flow at the source is highly irregular. The reason for this is that the flow is geostrophic and unstable as soon as it enters the domain. As noted previously, each baroclinic event is associated with a local decrease in the along-slope speed, with the result that dense fluid temporarily piles up behind each developing dome, with no clear outlet.

This behavior is a consequence of the simplifying assumptions made in deriving the governing equations. In contrast, the primitive equation numerical model of Jiang and Garwood Jr. (1996) allowed for down-slope motion before geostrophic adjustment took place, and their source was located at the top of the slope, providing a buffer zone between the source and the unstable region. Naturally, laboratory experiments, such as those of Lane-Serff and Baines (1998) or Etling *et al.* (2000), allow for several types of sinks for the dense fluid, including Ekman draining and turbulent entrainment. Nevertheless, the formation of the first dome as we have described it is a robust process with respect to the parameters A, y_0 and C_d. The only crucial ingredient is topography whose gradient increases with y.

The topography in EXP2 was similar enough to the linearly sloping bottom used previously, that the frequency of instability events did not change significantly. On average, the separation between cold dome anomalies was about 60 km, which is not unreasonable compared to eddies in the DSO. Each upper-layer cyclone had a diameter of roughly 35 km, which agrees well with observational estimates of 30 km (e.g. Bruce 1995). Undoubtedly, the dynamics we have presented reflect only some aspects of instability in abyssal currents. Nevertheless, the basic mechanisms we described should be relevant for the DSO and other rotationally dominated overflows. We are not claiming that the topographic effect can, by itself, account for the particular intensity of cyclogenesis in the DSO, compared to other overflows. The western slope of the Irminger Basin does not seem to be significantly different from the bathymetry south of the Iceland–Faroe Ridge, for example. A detailed comparison of the topography in several overflow regions, together with knowledge of the exact overflow paths, could certainly shed light on this issue.

As the analytical nonlinear eddy solutions of Poulin and Swaters (1999b) imply, the upper-layer low pressure cell is often strong enough to induce cyclonic vorticity in the core of the cold dome. A close-up of the first eddy in EXP2 is shown in Fig. 3.7. Numerical simulations of Jungclaus *et al.* (2001) indicate that roll-up of cyclonic vorticity into coherent vortices occurs mainly due to ageostrophic terms. In our model, the ageostrophic terms are neglected in the lower layer, so that the cyclonic spin-up of lower-layer domes is achieved entirely by upper-layer cyclones. However, in the upper layer, ageostrophic advection is only as strong as QG theory allows, so that the spin-up and coupling process is not as robust as in Jungclaus *et al.* (2001).

By introducing curved topography, which is more consistent with typical coastal bathymetry than a linear bottom, some of the anticyclonic shear is removed from the lower layer. No cyclonic shear is initially present (this would require a decrease in slope with y) however it seems that a small amount of curvature in the topography has a significant effect on the roll-up process. We believe therefore, that this mechanism may indeed be operative in cyclogenesis, ageostrophic influences notwithstanding.

Assuming that the instability we have described above leads to coherent vortex pairs of the sort described by Lane-Serff and Baines (2000), it is interesting to use our linear theory of the previous chapter to determine the relationship between the period of eddy formation and μ. Fig. 3.8 is a plot that shows our predicted period values as well as those obtained experimentally by Lane-Serff and Baines (2000). The expected relation is

$$2s\frac{T_{\text{int}}}{T} \approx \frac{1}{kc_R}, \tag{3.2.4}$$

where s is the topographic parameter as before, T_{int} is the time interval between successive eddies observed by Lane-Serff and Baines (2000) scaled by the rotation period T, and kc_R is the frequency predicted by (2.4.8). There is disagreement for small values of μ, i.e. $\delta \ll s$. It is possible that in an experimental setting, for very small δ the current thickness is similar to the Ekman layer depth, which would

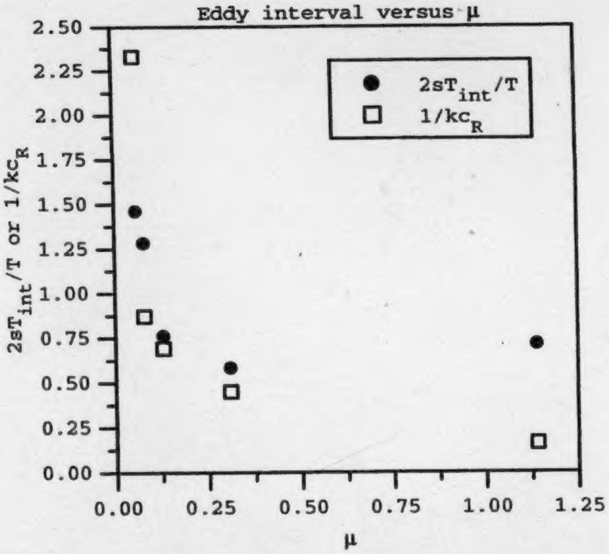

Figure 3.8: Period of eddy formation predicted by the linear theory (open boxes) and that observed by LSB (filled circles) versus μ. All quantities are defined in text.

significantly modify the observed dynamics.

There is also some disagreement at $\mu \approx 1.13$, at which point the observed eddy generation period seems to indicate an increasing trend with μ. However, we suspect that this data point may be spurious, since it is inconsistent with the monotonically decreasing trend associated with the experiments in Lane-Serff and Baines (1998) (see Choboter and Swaters 2000). Although Fig. 3.8 is not convincing in itself, it does suggest that further investigation is in order. The agreement between the experimental evidence of Lane-Serff and Baines (1998) and the theoretical prediction of Choboter and Swaters (2000) with respect to (3.2.4) was quite reasonable (i.e. a monotonic trend in both cases), except for small μ. It seems unlikely that the introduction of upper-layer stratification would result in entirely new dynamics at $\mu \sim 1$. Still, it is hard to make a judgment with only five data points. More observations should shed light on the issue.

3.3 Discussion

There is much debate in the literature as to the dominant mechanism of eddy formation associated with the DSO. We have taken the view, proposed in several pioneering studies (e.g. Smith 1976), that intense variability and vortex generation are the result of baroclinic instability of the deep layer. (Sandoval and Weatherly (2001) also proposed that this mechanism is responsible for observed velocity fluctuations of the Deep Western Boundary Current in the Brazil Basin.) Several recent observational and numerical studies of the DSO also support this viewpoint (Jiang and Garwood Jr. 1995; Krauss and Käse 1998; Jungclaus *et al.* 2001). Moreover, the laboratory experiments of Etling *et al.* (2000) clearly demonstrate that, in principle, cyclogenesis through instability, plume formation and subsequent coupling of the bottom-trapped and ambient layers is a viable process for flows where buoyancy and Coriolis effects are strong.

However, the baroclinic mechanism does not explain certain features of DSO dynamics, and we should point out that there are several important differences between our simulation results and the observational record. In particular, it would be inappropriate to state that convex topography is necessary for cyclone generation, since the topography near the sill does not seem to possess a significant amount of curvature, and indeed, in some locations it is actually concave. What we are claiming is that development of strong coupled vortices is likely to be enhanced by convex topography, where it does exist. Since the positive curvature of Irminger Basin topography is only clear on fairly large lengthscales, our arguments do not explain the unique intensity of DSO variability. However, flow through other openings in the Iceland-Scotland Ridge is quite complicated and has not been studied in as much detail as the DSO. We do not believe this mechanism can be completely discounted at this point.

Cyclonic eddies in our simulations typically appear on the down-slope side of the current, whereas the observed eddy kinetic energy maximum south of Denmark Strait lies over the core of the bottom-trapped flow (Dickson and Brown 1994). The cause is likely to be the neglect of the advective terms in the lower-layer momentum equation, since this discrepancy does not appear in the primitive equation results of Jungclaus *et al.* (2001). Furthermore, there is observational evidence of relatively fresh water over the sloping shelf at large distances downstream from the sill, suggesting an active role played by the (low salinity) intermediate layer (Spall and Price 1998). This supports the idea that strong cyclones are formed due to significant stretching of mid-depth water, and since this water mass is a unique feature of the DSO, the mechanism also explains why cyclones are not observed at other overflows. Thus, providing that the DSO is in the "vortex regime", it may well be governed by the dynamics outlined in Spall and Price (1998).

The contribution of this study can be summarized as follows. We have shown that the governing equations (2.1.54)–(2.1.58) can describe the temporal and spatial evolution of an overflow plume into smaller subplumes, with an accompanying Rossby wave field in the ambient fluid. Many characteristics of this instability are consistent qualitatively and quantitatively with measurements in the DSO region and results of numerical simulations using primitive equations models (e.g. Jiang and Garwood Jr. 1996; Krauss and Käse 1998; Jungclaus *et al.* 2001). In itself, the present model is almost certainly too simple to fully capture the complex dynamics of unstable overflows. However, it demonstrates the mechanism responsible for gross features seen in previous simulations, especially those of Jiang and Garwood Jr. (1996) and Jungclaus *et al.* (2001).

In addition, we have elucidated the role of convex topography in cyclogenesis. We believe this process should be generic in regions where topography has the correct sign of curvature, and may be valuable in assessing future observational and simulation data. Finally, the present study shows that weak vorticity advection tends to result in cyclones and anticyclones of equal strength, with cyclones predominantly on the offshore side of the abyssal current. If DSO cyclones are produced, at least sometimes, through baroclinic instability of the deep flow, then stronger nonlinearity in the momentum equations is probably required for an accurate description.

Chapter 4

FG-CS Model

4.1 Model Equations

Here we derive a generalization of the S93 model, where the lower layer is continuously-stratified, while the upper layer is frontal geostrophic. Additionally we include a β-plane term, as well as source/sink fluxes, $Q_1(x, y)$ and $Q_2(x, y)$. We present some basic analytical results, which are again extensions of S93. A linear instability calculation and numerical simulations are also described. Instability characteristics are compared with those obtained by Barth (1994) as part of their investigation of instabilities associated with the California Current. We also apply the FG-SW model, in a numerical setting, to instabilities on an axisymmetric current, as observed by CL in their laboratory study. We describe volume-conserving simulations where $Q_1 \equiv Q_2$, as well as simulations in which upper layer fluid is added without a compensating sink in the ambient layer, i.e. $Q_1 > 0$, $Q_2 \equiv 0$. Because many details of the model derivation are similar to chapter 2, our explanations are more brief.

Although the applications we describe in this chapter do not require the use of the β-plane approximation, we nevertheless retain β in the model derivation, as we feel it is instructive to observe the location of the β term in the final governing equations. Specifically, a β term will appear in the QG equation in the traditional manner. However, due to the relative importance of thickness deformations, the frontal layer will not be affected by the presence of a β-plane at leading order. Furthermore, we wish to emphasize that the FG class of models can be used in studies of larger-scale phenomena, where variations of the Coriolis parameter cannot be neglected. This regime was investigated, in the limit of a homogeneous ambient layer, by Tang and Cushman-Roisin (1992), Karsten and Swaters (2000a), Karsten and Swaters (2000b) and others.

4.1.1 Model Derivation

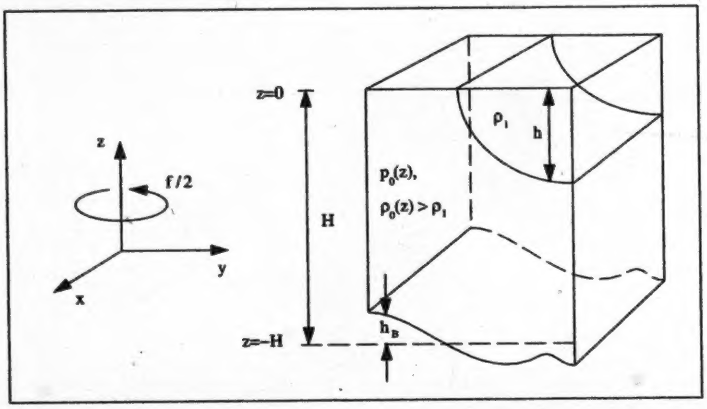

Figure 4.1: FG-CS model geometry. A thin, homogeneous layer overlies a continuously-stratified layer that is relatively deep, but finite. The fluid interface is allowed to intersect the surface, thus forming true fronts. The topography may be flat or spatially varying.

A diagram of the prototypical model configuration is given in Fig. 4.1. We begin with the Shallow Water equations for the upper layer,

$$\mathbf{u}^*_{1t^*} + (\mathbf{u}^*_1 \cdot \boldsymbol{\nabla}^*)\mathbf{u}^*_1 + (f_0 + \beta_0 y^*)\mathbf{e}_3 \times \mathbf{u}^*_1 = -\frac{1}{\rho_1}\boldsymbol{\nabla}^* p^*_1, \tag{4.1.1}$$

$$(h^* + \eta^*)_{t^*} + \boldsymbol{\nabla}^* \cdot (\mathbf{u}^*_1(h^* + \eta^*)) = Q^*_1, \tag{4.1.2}$$

where h^* is the distance of the interface below $z^* = 0$ and η^* is the surface deformation above $z^* = 0$. However, below we invoke the rigid lid approximation, and henceforth

η^* will be interpreted as a pressure term. The Boussinesq system comprises the primitive equations for the lower layer,

$$\mathbf{u}_{2t^*}^* + (\mathbf{u}_2^* \cdot \nabla^*)\mathbf{u}_2^* + w^* \mathbf{u}_{2z^*}^* + (f_0 + \beta_0 y^*)\mathbf{e}_3 \times \mathbf{u}_2^* = -\frac{1}{\rho_*}\nabla^* p_2^*, \tag{4.1.3}$$

$$\rho_*(w_{t^*}^* + (\mathbf{u}_2^* \cdot \nabla^*)w^* + w^* w_{z^*}^*) = -p_{2z^*}^* - g\rho^*, \tag{4.1.4}$$

$$\rho_{t^*}^* + \mathbf{u}_2^* \cdot \nabla^* \rho^* + w^* \rho_{z^*}^* = 0, \tag{4.1.5}$$

$$\nabla^* \cdot \mathbf{u}_2^* + w_{z^*}^* = -\frac{Q_2^*}{H - h_B^* - h^*}. \tag{4.1.6}$$

The notation is similar to that used in chapter 2, where the subscripts 1 and 2 refer to the upper and lower layer, respectively. All quantities are dimensional (i.e. unscaled) at this point. Variables with superscript asterisks will be appropriately scaled below. Here, $Q_1^* > 0$, $Q_2^* > 0$ corresponds to a source in the upper layer and a sink in the lower layer. As before, the sink in the ambient fluid is distributed uniformly over the vertical extent of the layer, $H - h_B^* - h^*$, where H is the total fluid depth above some reference level, h_B^* is the height of the topography and h^* is the thickness of the upper layer.

The boundary conditions for the vertical velocity in the ambient fluid are

$$w^* = -h_{t^*}^* - \mathbf{u}_2^* \cdot \nabla^* h^* \qquad z^* = -h^*, \tag{4.1.7}$$

$$w^* = \mathbf{u}_2^* \cdot \nabla^* h_B^* \qquad z^* = -H + h_B^*, \tag{4.1.8}$$

at the interface and bottom, respectively. The total pressures in the upper and lower layer may be written, respectively,

$$p_1^*(x^*, y^*, z^*, t^*) = -\rho_1 g z^* + \rho_1 g \eta^*(x^*, y^*, t^*), \tag{4.1.9}$$

$$p_2^*(x^*, y^*, z^*, t^*) = g\int_{z^*}^{0} \rho_0(\xi)d\xi + \varphi^*(x^*, y^*, z^*, t^*), \tag{4.1.10}$$

where η^* and φ^* are reduced pressures in the upper and lower layers, respectively.

We require pressure continuity at the interface, $z^* = -h^*$,

$$g\int_{-h^*}^{0} \rho_0(\xi)d\xi + \varphi^*(x^*, y^*, -h^*, t^*) = g\rho_1(h^* + \eta^*). \tag{4.1.11}$$

Using the fact that the upper layer scale depth h_* is much less than H, we Taylor expand about $z^* = 0$,

$$\begin{aligned} \varphi^*(x^*, y^*, 0, t^*) &\approx g\rho_1(h^* + \eta^*) - g\rho_0(0)h^* && (4.1.12)\\ &= g\rho_1\eta^* - g(\rho_0(0) - \rho_1)h^* && (4.1.13)\\ &= g\rho_1\eta^* - g'\rho_* h^*, && (4.1.14) \end{aligned}$$

where we have defined

$$g' := g\frac{\rho_0(0) - \rho_1}{\rho_*} > 0 \quad \text{and} \quad \rho_* := \rho_0(0). \tag{4.1.15}$$

It will be shown, after the derivation is complete, that the error introduced in truncating the above Taylor expansion does not affect the leading-order dynamics.

We introduce generic scalings for length and depth,

$$(x^*, y^*) = L_*(x, y), \qquad z^* = Hz. \tag{4.1.16}$$

We would like the final equations to be identical to continuously-stratified QG theory in the lower layer. This requires that we choose the lengthscale as follows,

$$L_* = \varepsilon_1^{\frac{1}{2}}\frac{\sqrt{g'H}}{f_0}. \tag{4.1.17}$$

This step is equivalent to the assumption made in S93, and is elucidated further in section 5.1 in terms of an appropriate Froude number scaling. Velocities in the upper and lower layer are respectively scaled with the Rossby numbers, ε_1 and ε_2,

$$\mathbf{u}_1^* = \varepsilon_1 f_0 L_* \mathbf{u}_1, \qquad \mathbf{u}_2^* = \varepsilon_2 f_0 L_* \mathbf{u}_2. \tag{4.1.18}$$

As in the derivation of the CS-PG model, the timescale is chosen based on the advective timescale of the ambient layer,

$$t^* = \frac{\kappa t}{\varepsilon_2 f_0}, \tag{4.1.19}$$

where the exact ratio between the temporal and advective Rossby numbers is measured by the O(1) parameter κ. Both the upper layer thickness h^* and topographic height h_B^* are assumed small in comparison with the total fluid depth H,

$$h^* = \delta H h, \qquad h_B^* = \delta H h_B, \tag{4.1.20}$$

where the relation of the small parameter δ to ε_1 and ε_2 is yet to be determined. The pressures η^* and φ^* are scaled so that their non-dimensional analogues will be the geostrophic pressures in layer 1 and 2, respectively,

$$\eta^* = \varepsilon_1 \frac{\rho_1 f_0^2 L_*^2}{g} \eta, \qquad \varphi^* = \varepsilon_2 \rho_* f_0^2 L_*^2 \varphi. \tag{4.1.21}$$

The lower-layer density is scaled so as to be in hydrostatic balance with the lower-layer pressure,

$$\rho^* = \rho_0(z^*) + \varepsilon_2 \frac{\rho_* f_0^2 L_*^2}{gH} \rho, \tag{4.1.22}$$

and the lower-layer vertical velocity is non-dimensionalized with the time rate of change of upper layer thickness,

$$w^* = \delta \varepsilon_2 \frac{f_0 H}{\kappa} w. \tag{4.1.23}$$

The source/sink terms are scaled similarly,

$$(Q_1^*, Q_2^*) = \delta \varepsilon_2 \frac{f_0 H}{\kappa} (Q_1, Q_2), \tag{4.1.24}$$

while for β_0 we use the traditional QG scaling, using the lower-layer Rossby number,

$$\beta_0 = \varepsilon_2 f_0 \beta / L_*. \tag{4.1.25}$$

We substitute the scalings into the primitive equations. In the upper layer mass conservation equation we neglect terms of O(g'/g) as part of the rigid lid approximation. Then the non-dimensional equations are

$$\varepsilon_2 \mathbf{u}_{1t} + \varepsilon_1 \kappa \mathbf{u}_1 \cdot \nabla \mathbf{u}_1 + \kappa (1 + \varepsilon_2 \beta y) \mathbf{e}_3 \times \mathbf{u}_1 = -\kappa \nabla \eta, \tag{4.1.26}$$

$$\varepsilon_2 h_t + \kappa\varepsilon_1 \boldsymbol{\nabla}\cdot(\mathbf{u}_1 h) = \varepsilon_2 Q_1, \tag{4.1.27}$$

$$\varepsilon_2 \mathbf{u}_{2t} + \varepsilon_2 \kappa \mathbf{u}_2\cdot\boldsymbol{\nabla}\mathbf{u}_2 + \delta\varepsilon_2 w \mathbf{u}_{2z} + \kappa(1+\varepsilon_2\beta y)\mathbf{e}_3 \times \mathbf{u}_2 = -\kappa\boldsymbol{\nabla}\varphi, \tag{4.1.28}$$

$$\varphi_z + \rho = -\frac{\delta\varepsilon_2}{\kappa^2}\left(\frac{H}{L}\right)^2 \left(w_t + \kappa\mathbf{u}_2\cdot\boldsymbol{\nabla}w + \delta w w_z\right), \tag{4.1.29}$$

$$\rho_t + \kappa\mathbf{u}_2\cdot\boldsymbol{\nabla}\rho + \delta w\rho_z = \frac{\delta\kappa}{\varepsilon_1\varepsilon_2}\frac{H}{g'}N_*^2(z)w, \tag{4.1.30}$$

$$\kappa(1-\delta h_B - \delta h)(\boldsymbol{\nabla}\cdot\mathbf{u}_2 + \delta w_z) = -\delta Q_2, \tag{4.1.31}$$

where the dimensional buoyancy frequency N_* is defined by

$$N_*^2(z) = \frac{-g}{\rho_*}\left[\frac{\mathrm{d}\rho_0(z^*)}{\mathrm{d}z^*}\right]_{z^*=Hz} > 0. \tag{4.1.32}$$

Pressure continuity then requires

$$\varepsilon_2\varphi = \varepsilon_1(1-\frac{g'}{g})\eta - \frac{\delta}{\varepsilon_1}h \qquad \text{at } z=0. \tag{4.1.33}$$

Using the rigid lid ansatz, we may write

$$\varepsilon_2\varphi = \varepsilon_1\eta - \frac{\delta}{\varepsilon_1}h \qquad z=0. \tag{4.1.34}$$

The vertical boundary conditions become

$$w = -h_t - \kappa\mathbf{u}_2\cdot\boldsymbol{\nabla}h \qquad z = -\delta h, \tag{4.1.35}$$

$$w = \kappa\mathbf{u}_2\cdot\boldsymbol{\nabla}h_B \qquad z = -1+\delta h_B + \delta h. \tag{4.1.36}$$

Taylor expanding (4.1.35) about $z=0$ and (4.1.36) about $z=-1$, to leading order in δ we have

$$w = -h_t - \kappa\mathbf{u}_2\cdot\boldsymbol{\nabla}h \qquad z=0, \tag{4.1.37}$$

$$w = \kappa\mathbf{u}_2\cdot\boldsymbol{\nabla}h_B \qquad z=-1. \tag{4.1.38}$$

In order for the lower layer to be governed by QG theory, we will need that $\varepsilon_2 \approx \delta$. To obtain the FG limit in the upper layer, we require that $\varepsilon_1 \gg \varepsilon_2$. Finally, we would like the leading-order balance in the pressure continuity equation to be between η and h. We therefore define

$$\varepsilon_1 = \varepsilon_2^{\frac{1}{2}}, \qquad \varepsilon_2 = \delta. \tag{4.1.39}$$

We also non-dimensionalize the stratification frequency by

$$N_* = \delta^{\frac{1}{4}} \sqrt{\frac{g'}{H}} N, \qquad N = O(1). \tag{4.1.40}$$

With the above relationship between the Rossby numbers, it is easy to see that the dynamic lengthscale turns out to be the geometric mean of the upper- and lower-layer Rossby radii,

$$L_* = \sqrt{R_1 R_2}, \tag{4.1.41}$$

where, respectively,

$$R_1 = \frac{\sqrt{g' h_*}}{f_0} \qquad \text{and} \qquad R_2 = \frac{\sqrt{g' H}}{f_0}. \tag{4.1.42}$$

4.1.2 Governing Equations

We deal with the lower layer first. Introducing the relative vorticity, $\zeta_2 = \mathbf{e}_3 \cdot \nabla \times \mathbf{u}_2$, the lower-layer equations may be written

$$\delta(\partial_t + \kappa \mathbf{u}_2 \cdot \nabla)\zeta_2 + \delta\kappa\zeta_2 \nabla \cdot \mathbf{u}_2 + \kappa(1 + \delta\beta y)\nabla \cdot \mathbf{u}_2 + \delta\kappa\beta v_2 = O(\delta^2), \tag{4.1.43}$$

$$\varphi_z + \rho = O(\delta^2), \tag{4.1.44}$$

$$w = N^{-2}(\rho_t + \kappa \mathbf{u}_2 \cdot \nabla\rho + \delta w \rho_z), \tag{4.1.45}$$

$$\kappa \nabla \cdot \mathbf{u}_2 = -\delta w_z + \delta\kappa(h_B + h)\nabla \cdot \mathbf{u}_2 - \delta Q_2, \tag{4.1.46}$$

together with pressure continuity,

$$\eta = h + \delta^{\frac{1}{2}}\varphi \qquad z = 0. \tag{4.1.47}$$

All fields are expanded in powers of $\delta^{\frac{1}{2}}$,

$$(\mathbf{u}_1, \mathbf{u}_2, w, \eta, h, \varphi, \rho) = (\mathbf{u}_1, \mathbf{u}_2, w, \eta, h, \varphi, \rho)^{(0)} + \delta^{\frac{1}{2}}(\mathbf{u}_1, \mathbf{u}_2, w, \eta, h, \varphi, \rho)^{(1)} + \ldots \tag{4.1.48}$$

The $O(\delta^{\frac{1}{2}})$ expansion terms are not needed in determining the leading-order behavior of the ambient fluid. To $O(\delta)$ the lower layer will be governed by continuously-stratified QG theory and we form the QGPV equation in the usual fashion (Pedlosky 1987),

$$(\Delta\varphi^{(0)} + (N^{-2}\varphi_z^{(0)})_z)_t + \kappa J(\varphi^{(0)}, \Delta\varphi^{(0)} + (N^{-2}\varphi_z^{(0)})_z + \beta y) = Q_2. \tag{4.1.49}$$

The rest of the lower-layer equations reduce to the relations

$$\rho^{(0)} = -\varphi_z^{(0)}, \qquad \mathbf{u}_2^{(0)} = \mathbf{e}_3 \times \boldsymbol{\nabla}\varphi^{(0)}, \qquad \boldsymbol{\nabla}\cdot\mathbf{u}_2^{(0)} = 0, \tag{4.1.50}$$

with boundary conditions at $z = 0$,

$$w^{(0)} = -N^{-2}(\varphi_{zt}^{(0)} + \kappa J(\varphi^{(0)}, \varphi_z^{(0)})) = -h_t^{(0)} - \kappa J(\varphi^{(0)}, h^{(0)}), \tag{4.1.51}$$

and $z = -1$,

$$w^{(0)} = -N^{-2}(\varphi_{zt}^{(0)} + \kappa J(\varphi^{(0)}, \varphi_z^{(0)})) = \kappa J(\varphi^{(0)}, h_B). \tag{4.1.52}$$

The boundary conditions further simplify to

$$(\varphi_z^{(0)} - N^2 h^{(0)})_t + \kappa J(\varphi^{(0)}, \varphi_z^{(0)} - N^2 h^{(0)}) = 0 \qquad z = 0, \tag{4.1.53}$$

and

$$\varphi_{zt}^{(0)} + \kappa J(\varphi^{(0)}, \varphi_z^{(0)} + N^2 h_B) = 0 \qquad z = -1. \tag{4.1.54}$$

Derivation of the upper layer equation is then analogous to S93. The $O(1)$ problem is given by

$$\mathbf{u}_1^{(0)} = \mathbf{e}_3 \times \boldsymbol{\nabla}\eta^{(0)}, \tag{4.1.55}$$

$$\boldsymbol{\nabla}\cdot(\mathbf{u}_1^{(0)} h^{(0)}) = 0, \tag{4.1.56}$$

$$\eta^{(0)} = h^{(0)}, \tag{4.1.57}$$

where (4.1.56) is trivially satisfied. Since the $O(1)$ fields are not determined, we examine the $O(\delta^{\frac{1}{2}})$ problem,

$$\mathbf{u}_1^{(0)}\cdot\boldsymbol{\nabla}\mathbf{u}_1^{(0)} + \mathbf{e}_3 \times \mathbf{u}_1^{(1)} = -\boldsymbol{\nabla}\eta^{(1)}, \tag{4.1.58}$$

$$\frac{1}{\kappa}h_t^{(0)} + \mathbf{u}_1^{(0)}\cdot\nabla h^{(1)} + \mathbf{u}_1^{(1)}\cdot\nabla h^{(0)} + h^{(0)}\nabla\cdot\mathbf{u}_1^{(1)} = \frac{1}{\kappa}Q_1, \tag{4.1.59}$$

$$\eta^{(1)} = h^{(1)} + \varphi^{(0)}|_{z=0}. \tag{4.1.60}$$

We solve for $\mathbf{u}_1^{(1)}$ in (4.1.58) and simplify using (4.1.55), (4.1.57) and (4.1.60),

$$\mathbf{u}_1^{(1)} = \mathbf{e}_3 \times \nabla(h^{(1)} + \varphi|_{z=0}) + \mathbf{e}_3 \times J(h^{(0)}, \mathbf{e}_3 \times \nabla h^{(0)}). \tag{4.1.61}$$

This expression is substituted into the mass conservation equation (4.1.59),

$$\begin{aligned} &\frac{1}{\kappa}h_t^{(0)} + J(h^{(0)}, h^{(1)}) + \nabla h^{(0)}\cdot[\mathbf{e}_3 \times \nabla(h^{(1)} + \varphi|_{z=0})] \\ &+\nabla h^{(0)}\cdot J(\nabla h^{(0)}, h^{(0)}) + h^{(0)}\nabla\cdot[\mathbf{e}_3 \times \nabla(h^{(1)} + \varphi|_{z=0})] \\ &+h^{(0)}\nabla\cdot J(\nabla h^{(0)}, h^{(0)}) = \frac{1}{\kappa}Q_1. \end{aligned} \tag{4.1.62}$$

The last equation is simplified by employing the following identities,

$$\begin{aligned} \mathbf{A}\cdot J(\mathbf{A}, B) &\equiv \frac{1}{2}J(\mathbf{A}\cdot\mathbf{A}, B), \\ \nabla\cdot J(\nabla A, A) &\equiv J(\Delta A, A), \\ AJ(B, A) &\equiv J(AB, A), \end{aligned} \tag{4.1.63}$$

which yields

$$h_t^{(0)} + \kappa J(\varphi^{(0)}, h^{(0)}) + \kappa J(h^{(0)}\Delta h^{(0)} + \tfrac{1}{2}\nabla h^{(0)}\cdot\nabla h^{(0)}, h^{(0)}) = Q_1, \qquad z = 0. \tag{4.1.64}$$

Before writing down the final form of the model equations, it remains to justify the neglect of higher order terms when Taylor expanding the pressure continuity equation (4.1.11). We expand about $z^* = 0$, retaining the derivative terms,

$$g\rho_0(0)h^* + g\rho_{0z^*}(0)h^{*2} + \varphi^*(x^*, y^*, 0, t^*) + h^*\varphi^*_{z^*}(0) = g\rho_1(h^* + \eta^*). \tag{4.1.65}$$

Substitution of the scalings yields

$$\begin{aligned} \delta\rho_* f_0^2 L^2\varphi(0) &= \delta g\rho_1 Hh + \delta^{\frac{1}{2}}\rho_1 f_0^2 L^2\eta - \delta\rho_* gHh \\ &-\delta^2 gH^2\rho_{0z^*}(0) - \delta\rho_* f_0^2 L^2\varphi_z(0). \end{aligned} \tag{4.1.66}$$

Recall that $\rho_0(0) = \rho_*$, and that

$$\rho_{0z^*} = -\delta^{\frac{1}{2}} \frac{\rho_* g'}{gH} N^2. \tag{4.1.67}$$

Then, neglecting terms of $O(g'/g)$, we obtain

$$\delta^{\frac{3}{2}} \rho_* g' H \varphi(0) = \delta \rho_* g' H(\eta - h) - \delta^{\frac{5}{2}} \rho_* g' H h \varphi_z(0) + \delta^{\frac{5}{2}} \rho_* g' H N^2, \tag{4.1.68}$$

or

$$\delta^{\frac{1}{2}} \varphi(0) = \eta - h - \delta^{\frac{3}{2}} h \varphi_z(0) + \delta^{\frac{3}{2}} N^2. \tag{4.1.69}$$

The last two terms are of higher order in δ and thus do not play a role in our derivation.

We note that $h_t^{(0)}$ may be eliminated from (4.1.53) *via* (4.1.64). Then, dropping the superscripts, the governing equations are

$$h_t + \kappa J(\varphi + h\Delta h + \tfrac{1}{2}\nabla h\cdot\nabla h, h) = Q_1, \qquad z = 0, \tag{4.1.70}$$

$$\varphi_{zt} + \kappa J(\varphi, \varphi_z) + \kappa N^2 J(h\Delta h + \tfrac{1}{2}\nabla h\cdot\nabla h, h) = N^2 Q_1, \qquad z = 0, \tag{4.1.71}$$

$$(\Delta\varphi + (N^{-2}\varphi_z)_z)_t + \kappa J(\varphi, \Delta\varphi + (N^{-2}\varphi_z)_z + \beta y) = Q_2, \tag{4.1.72}$$

$$\varphi_{zt} + \kappa J(\varphi, \varphi_z) + \kappa N^2 J(\varphi, h_B) = 0, \qquad z = -1, \tag{4.1.73}$$

with the auxiliary relations

$$\mathbf{u}_1 = \mathbf{e}_3 \times \nabla h, \qquad \mathbf{u}_2 = \mathbf{e}_3 \times \nabla\varphi,$$

$$w = -N^{-2}[\varphi_{zt} + \kappa J(\varphi, \varphi_z)], \qquad \rho = -\varphi_z. \tag{4.1.74}$$

In what follows, the integral of Q_1 over the horizontal domain will be referred to as $\overline{Q}_1$. Its dimensional counterpart $\overline{Q_1^*}$ will have dimensions of volume/time and will b identified as the "source strength".

4.1.3 Boundary conditions at outcroppings

Following S93, we derive the appropriate condition on h at outcroppings, starting with the dimensional variables. We consider the case without sources or sinks, i.e. $Q_1 \equiv Q_2 \equiv 0$. Assume that the projection onto $z^* = 0$ of an outcropping is given by $y = \xi^*(x^*, t^*)$. Then we must have

$$\left.\begin{aligned} h^* &= 0 \\ \xi^*_{t^*} + \mathbf{u}_1^* \cdot \boldsymbol{\nabla}^*(\xi^* - y^*) &= 0 \end{aligned}\right\} y = \xi^*(x^*, t^*). \tag{4.1.75}$$

Using the non-dimensionalizations given earlier, and $\xi^* = L_* \xi$,

$$\left.\begin{aligned} h &= 0 \\ \frac{\delta^{\frac{1}{2}}}{\kappa}\xi_t + u_1 \xi_x - v_1 &= 0 \end{aligned}\right\} y = \xi(x, t). \tag{4.1.76}$$

We expand h and ξ in $\delta^{\frac{1}{2}}$ (consistently with expansion (4.1.48)). Then the leading-order relations associated with (4.1.76) at $y = \xi^{(0)}(x, t)$ are

$$h^{(0)} = 0, \tag{4.1.77}$$

$$h_x^{(0)} + h_y^{(0)} \xi_x^{(0)} = 0, \tag{4.1.78}$$

where we have already used $\mathbf{u}_1^{(0)} = \mathbf{e}_3 \times \boldsymbol{\nabla} h^{(0)}$ from (4.1.55) and (4.1.57). However, (4.1.78) always holds at an outcropping, because it is simply the statement that the upper layer thickness is invariant along the outcropping, that is,

$$\frac{\partial}{\partial x}[h^{(0)}(x, \xi^{(0)}(x, t), t)] = 0. \tag{4.1.79}$$

Thus, assuming we may differentiate $h^{(0)}$ smoothly as we approach the outcropping, (4.1.77) implies (4.1.78).

Because the upper layer governing equation (4.1.70) resulted from the $O(\delta^{\frac{1}{2}})$ balance, here we must examine the $O(\delta^{\frac{1}{2}})$ problem as well. This is given by

$$h^{(1)} + h_y^{(0)} \xi^{(1)} = 0, \tag{4.1.80}$$

$$\frac{1}{\kappa}\xi_t^{(0)} + u_1^{(0)}\xi_x^{(1)} - v_1^{(1)} + u_1^{(1)}\xi_x^{(0)} + u_{1y}^{(0)}\xi_x^{(0)}\xi^{(1)} - v_{1y}^{(0)}\xi^{(1)} = 0, \tag{4.1.81}$$

which must hold on $y = \xi^{(0)}(x,t)$. The last term in (4.1.80) and the final two terms in (4.1.81) result from linearizing about $y = \xi^{(0)}(x,t)$. The latter of these two boundary conditions may be simplified as follows. First, we note that (4.1.80) implies

$$h_x^{(1)} + h_{xy}^{(0)}\xi_x^{(1)} + h_y^{(0)}\xi_x^{(1)} = 0 \qquad \text{and} \qquad h_y^{(1)} + h_{yy}^{(0)}\xi^{(1)} = 0, \tag{4.1.82}$$

on $y = \xi^{(0)}(x,t)$. Velocities in (4.1.81) are rewritten using (4.1.55), (4.1.57) and (4.1.61), while terms involving $h^{(1)}$ and $\xi^{(1)}$ cancel upon use of (4.1.82),

$$\frac{1}{\kappa}\xi_t^{(0)} - [\varphi_x^{(0)}]_{z=0} - J(h_y^{(0)}, h^{(0)}) - [\varphi_y^{(0)}]_{z=0}\xi_x^{(0)} + J(h_x^{(0)}, h^{(0)})\xi_x^{(0)} = 0. \tag{4.1.83}$$

Multiplying through by $h_y^{(0)}$ we may write

$$\begin{aligned}\frac{1}{\kappa}h_y^{(0)}\xi_t^{(0)} - J(\varphi^{(0)}, h^{(0)}) - \frac{1}{2}J(\nabla h^{(0)}\cdot\nabla h^{(0)}, h^{(0)})&\\ -[\varphi_y^{(0)} + J(h^{(0)}, h_x^{(0)})](h_x^{(0)} + h_y^{(0)}\xi_x^{(0)}) = 0,&\end{aligned} \tag{4.1.84}$$

at $y = \xi^{(0)}(x,t)$, $z = 0$. The last term vanishes due to (4.1.78). If we take the limit of (4.1.64) as $y \to \xi^{(0)}(x,t)$ and substitute into (4.1.84) the result is

$$h_t^{(0)} + h_y^{(0)}\xi_t^{(0)} = 0. \tag{4.1.85}$$

However, this equation always holds at an outcropping, because it is simply the statement that the frontal thickness is time-invariant on $y = \xi^{(0)}(x,t)$, i.e.

$$\frac{\partial}{\partial t}[h^{(0)}(x, \xi^{(0)}(x,t), t)] = 0. \tag{4.1.86}$$

This implies that, if we evolve the governing equation (4.1.64) forward in time, the frontal boundary condition is trivially satisfied. No extra computation is necessary to track the motion of the outcroppings. This is also the result which was obtained by Swaters (1993).

4.1.4 Reduction to FG-SW

Here we show that the FG-CS governing equations include the S93 dynamical limit. First, integrate (4.1.72) in z,

$$\int_{-1}^{0}\left[(\Delta\varphi+(N^{-2}\varphi_z)_z)_t+\kappa J(\varphi,\Delta\varphi+(N^{-2}\varphi_z)_z+\beta y)\right]dz=Q_2. \tag{4.1.87}$$

Simplifying, we obtain

$$\frac{\partial}{\partial t}\Delta\int_{-1}^{0}\varphi dz+N^{-2}\varphi_{zt}|_{z=-1}^{z=0}+J(\varphi,\Delta\varphi)dz$$

$$+\kappa N^{-2}J(\varphi,\varphi_z)|_{z=-1}^{z=0}-\kappa\int_{-1}^{0}N^{-2}J(\varphi_z,\varphi_z)dz+\kappa\beta\int_{-1}^{0}\varphi_x dz=Q_2, \tag{4.1.88}$$

where the fourth and fifth terms are the result of integration by parts. Rearranging, and realizing that $J(A,A)\equiv 0$ for any differentiable function A,

$$\frac{\partial}{\partial t}\Delta\int_{-1}^{0}\varphi dz+\kappa\int_{-1}^{0}J(\varphi,\Delta\varphi)dz+\kappa N^{-2}\left[\varphi_{zt}+J(\varphi,\varphi_z)\right]_{z=0}$$

$$-\kappa N^{-2}\left[\varphi_{zt}+J(\varphi,\varphi_z)\right]_{z=-1}+\kappa\beta\int_{-1}^{0}\varphi_x dz=Q_2. \tag{4.1.89}$$

Substituting in the vertical boundary conditions (4.1.71), (4.1.73), the result is

$$\frac{\partial}{\partial t}\Delta\int_{-1}^{0}\varphi dz+\kappa\int_{-1}^{0}J(\varphi,\Delta\varphi)-\kappa J(h\Delta h+\tfrac{1}{2}\nabla h\cdot\nabla h,h)$$

$$+\kappa J(\varphi|_{z=-1},h_B)+\kappa\beta\int_{-1}^{0}\varphi_x dz=Q_2-Q_1. \tag{4.1.90}$$

Taking the limit as $\frac{\partial\varphi}{\partial z}\to 0$ and using (4.1.70) the upper- and lower-layer equations can be written, respectively,

$$h_t+\kappa J(\varphi+h\Delta h+\tfrac{1}{2}\nabla h\cdot\nabla h,h)=Q_1, \tag{4.1.91}$$

$$(\Delta\varphi+h)_t+\kappa J(\varphi,\Delta\varphi+h+h_B+\beta y)=Q_2, \tag{4.1.92}$$

which will henceforth be called the FG-SW model. It becomes identical to the theory presented in S93 (henceforth the "S93 model") if $\beta=0$, $\kappa=1$, $Q_1\equiv Q_2\equiv 0$ and $h_B=-sy$.

4.1.5 An invariant of the equations

Next, we will define a conserved quantity for the system, when no sources or sinks are present, i.e. $Q_1 \equiv Q_2 \equiv 0$. We assume an x-periodic channel domain, Ω, whose horizontal extent is $\Omega_H = \{(x,y)|0 < x < x_R, 0 < y < L\}$. Thus all flow variables are periodic in x and the velocities satisfy the no-normal flow condition at the channel walls. We will also need to employ conservation of circulation at the rigid boundaries,

$$\frac{\mathrm{d}}{\mathrm{d}t}\int_0^{x_R} \varphi_y|_{y=0}\ dy = \frac{\mathrm{d}}{\mathrm{d}t}\int_0^{x_R} \varphi_y|_{y=L}\ dy = 0. \tag{4.1.93}$$

Next, we establish a facile preliminary result. For differentiable functions A, B we may write

$$\iint_{\Omega_H} J(A,B)\ dxdy = \int_0^{x_R} [A_x B]_{y=0}^{L}\ dx - \int_0^{L} [A_y B]_{x=0}^{x_R}\ dy. \tag{4.1.94}$$

The second integral on the right-hand side vanishes due to x-periodicity of the fields, while the first vanishes if A satisfies no-normal flow at the channel walls. Thus,

$$\iint_{\Omega_H} J(A,B)\ dxdy = 0, \tag{4.1.95}$$

if $A_x = 0$ at the channel boundaries $y = 0, L$.

Now if we define

$$q_1 = h, \qquad q_2 = [\varphi_z - N^2 h]_{z=0},$$

$$q_3 = \Delta\varphi + (N^{-2}\varphi_z)_z + \beta y, \qquad q_4 = [\varphi_z + N^2 h_B]_{z=-1}, \tag{4.1.96}$$

then the governing equations may be written compactly as

$$q_{1t} + \kappa J(\varphi + h\Delta h + \tfrac{1}{2}\nabla h\cdot\nabla h, q_1) = 0, \qquad z = 0, \tag{4.1.97}$$

$$q_{2t} + \kappa J(\varphi, q_2) = 0, \qquad z = 0, \tag{4.1.98}$$

$$q_{3t} + \kappa J(\varphi, q_3) = 0, \tag{4.1.99}$$

$$q_{4t} + \kappa J(\varphi, q_4) = 0, \qquad z = -1. \tag{4.1.100}$$

The invariant, H, is defined by

$$H = \frac{1}{2}\iiint_{\Omega} \nabla\varphi\cdot\nabla\varphi + (\varphi_z/N)^2 \; dxdydz - \frac{1}{2}\iint_{\Omega_H} h\nabla h\cdot\nabla h \; dxdy$$

$$-\int_{-1}^{0}\left[\Gamma_L \int_0^{x_R} \varphi_y|_{y=L} \; dx - \Gamma_0 \int_0^{x_R} \varphi_y|_{y=0} \; dx\right] dz, \tag{4.1.101}$$

where

$$\Gamma_0 = \varphi|_{y=0} \qquad \text{and} \qquad \Gamma_L = \varphi|_{y=L}. \tag{4.1.102}$$

To show that H is conserved, we compute its time derivative,

$$\frac{\mathrm{d}H}{\mathrm{d}t} = \iiint_{\Omega} \nabla\varphi\cdot\nabla\varphi_t + N^{-2}\varphi_z\varphi_{zt} \; dxdydz$$

$$-\iint_{\Omega_H} \tfrac{1}{2}\nabla h\cdot\nabla h h_t + \nabla h\cdot(\nabla h_t)h \; dxdy$$

$$-\frac{\mathrm{d}}{\mathrm{d}t}\int_{-1}^{0}\left[\Gamma_L \int_0^{x_R} \varphi_y|_{y=L} \; dx - \Gamma_0 \int_0^{x_R} \varphi_y|_{y=0} \; dx\right] dz. \tag{4.1.103}$$

The last integral vanishes by (4.1.93). Integrating by parts and using periodicity of φ and h,

$$\frac{\mathrm{d}H}{\mathrm{d}t} = -\iiint_{\Omega} \varphi\Delta\varphi_t + \varphi(\varphi_{zt}/N^2)_z \; dxdydz + \iint_{\Omega_H} N^{-2}\varphi\varphi_{zt}|_{z=-1}^{z=0} \; dxdy$$

$$+\iint_{\Omega_H} [\nabla\cdot(h\nabla h) - \tfrac{1}{2}\nabla h\cdot\nabla h + \varphi|_{z=0} - \varphi|_{z=0}]h_t \; dxdy$$

$$+\int_{-1}^{0}(\Gamma_L \int_0^{x_R} \varphi_{yt}|_{y=L} \; dx)dy - \int_{-1}^{0}(\Gamma_0 \int_0^{x_R} \varphi_{yt}|_{y=0} \; dx)dy, \tag{4.1.104}$$

where we have cleverly added zero in the third integral. The last two integrals vanish by (4.1.93). Recalling that βy and h_B are independent of time and simplifying, we may write

$$\frac{\mathrm{d}H}{\mathrm{d}t} = \iint_{\Omega_H} (h\Delta h + \tfrac{1}{2}\nabla h\cdot\nabla h + \varphi|_{z=0})h_t \; dxdy$$

$$-\iiint_{\Omega} \varphi(\Delta\varphi + (N^{-2}\varphi_z)_z + \beta y)_t \; dxdydz$$

$$+\iint_{\Omega_H} [N^{-2}\varphi(\varphi_{zt} - h)_t]_{z=0} \; dxdy$$

$$-\iint_{\Omega_H} [N^{-2}\varphi(\varphi_{zt} - h)_{Bt}]_{z=-1}\ dxdy. \tag{4.1.105}$$

Substitution of (4.1.96) yields

$$\frac{\mathrm{d}H}{\mathrm{d}t} = \iint_{\Omega_H} (\varphi|_{z=0} + h\Delta h + \tfrac{1}{2}\nabla h\cdot\nabla h)q_{1t}\ dxdy + \iint_{\Omega_H} [N^{-2}\varphi]_{z=0}q_{2t}\ dxdy$$
$$-\iiint_{\Omega} \varphi q_{3t}\ dxdydz - \iint_{\Omega_H} [N^{-2}\varphi]_{z=-1}q_{4t}\ dxdy. \tag{4.1.106}$$

Now the governing equations (4.1.97)–(4.1.100) are used to replace the time derivative terms to obtain

$$\frac{\mathrm{d}H}{\mathrm{d}t} = \frac{\kappa}{2}\iint_{\Omega_H} J(q_1|_{z=0}, (\varphi|_{z=0} + h\Delta h + \frac{1}{2}\nabla h\cdot\nabla h)^2)\ dxdy$$
$$-\frac{\kappa}{2}[N^{-2}]_{z=0}\iint_{\Omega_H} J((\varphi|_{z=0})^2, q_2)\ dxdy + \frac{\kappa}{2}\iiint_{\Omega} J(\varphi^2, q_3)\ dxdydz$$
$$+\frac{\kappa}{2}[N^{-2}]_{z=-1}\iint_{\Omega_H} J((\varphi|_{z=-1})^2, q_4)\ dxdy. \tag{4.1.107}$$

Since q_1 and φ satisfy the no-normal flow condition on the channel walls, all the above integrals vanish by (4.1.95), so that

$$\frac{\mathrm{d}H}{\mathrm{d}t} = 0. \tag{4.1.108}$$

As defined by (4.1.101), H is similar to the Hamiltonian for continuously-stratified QG theory as well as the one derived in Swaters (1993). In order to make the claim that H is the Hamiltonian associated with (4.1.70)–(4.1.73), we would have to define an appropriate Poisson bracket and show that $\frac{\delta \mathbf{q}}{\delta t} = \mathbf{D}\frac{\delta H}{\delta \mathbf{q}}$, where $\mathbf{D}$ is a matrix of differential operators and the elements of $\mathbf{q}$ are given by (4.1.96) (e.g. Swaters 2000). A formal discussion of the Hamiltonian structure associated with this model, however, is beyond the scope of this thesis.

4.1.6 Mass Conservation

As in chapter 2, we should check that mass is conserved in the case of exact exchange of fluid between the layers, i.e. $Q_1 = Q_2$. The dimensional lower-layer continuity equation is integrated in z,

$$\int_{-H+h_B^*}^{-h^*} \nabla^*\cdot\mathbf{u}_2^* + w^*_{z^*}\ dz^* = -Q_2^*. \tag{4.1.109}$$

We employ Leibniz's Theorem, (2.1.79), where $a = -H + h_B^*$, $b = -h^*$ and $\mathbf{F} = \mathbf{u}_2^*$, and integrate the vertical velocity,

$$\nabla^*\cdot \int_{-H+h^*}^{-h^*} \mathbf{u}_2^*\ dz^* + \mathbf{u}_2^*|_{-h^*}\cdot\nabla^* h^* + \mathbf{u}_2^*|_{-H+h_B^*}\cdot\nabla^* h_B^* + w^*|_{-H+h_B^*}^{-h^*} = -Q_2^*. \tag{4.1.110}$$

Substituting the vertical boundary conditions (4.1.7), (4.1.8),

$$\nabla^*\cdot \int_{-H+h_B^*}^{-h^*} \mathbf{u}_2^*\ dz^* - h^*_{t^*} = -Q_2^*. \tag{4.1.111}$$

Eliminating $h^*_{t^*}$ *via* the dimensional analogue of (4.1.27) and using that $Q_1^* = Q_2^*$,

$$\nabla^*\cdot \int_{-H+h_B^*}^{-h^*} \mathbf{u}_2^*\ dz^* + \nabla^*\cdot(\mathbf{u}_1^* h^*) = 0. \tag{4.1.112}$$

Since $\mathbf{u}_1^*$ is z-independent, we may write this as

$$\nabla^*\cdot \left[\int_{-h^*}^{0} \mathbf{u}_1^*\ dz^* + \int_{-H+h_B^*}^{-h^*} \mathbf{u}_2^*\ dz^*\right] = 0. \tag{4.1.113}$$

Thus, if there is a local divergence (convergence) of the vertically averaged horizontal velocity in layer 1, there must be a compensating convergence (divergence) of the vertically averaged horizontal velocity in layer 2, and vice versa. We now show that this balance is satisfied to $O(\delta^{\frac{3}{2}})$ for the leading-order fields under the governing equations (4.1.70)–(4.1.73). We define D^* to be the left-hand side of (4.1.113) and non-dimensionalize through $D^* = \delta f_0 H D$. Then we have

$$D = \nabla\cdot \left[\int_{-1+\delta h_B}^{-\delta h} \mathbf{u}_2\ dz + \delta^{\frac{1}{2}}\mathbf{u}_1 h\right]. \tag{4.1.114}$$

Taylor expanding the integral and truncating the series with error $O(\delta^{\frac{3}{2}})$, we may write

$$D = \nabla\cdot \left[\int_{-1}^{0} \mathbf{u}_2\ dz - \delta\mathbf{u}_2|_{z=0} h - \delta\mathbf{u}_2|_{z=-1} h_B + \delta^{\frac{1}{2}}\mathbf{u}_1 h\right] + O(\delta^{\frac{3}{2}}), \tag{4.1.115}$$

Expanding all fields in powers of $\delta^{\frac{1}{2}}$ and retaining terms up to $O(\delta)$, we have

$$\begin{aligned} D = \boldsymbol{\nabla}\cdot &\left[\int_{-1}^{0} (\mathbf{u}_2^{(0)} + \delta\mathbf{u}_2^{(2)})\ dz - \delta\mathbf{u}_2^{(0)}|_{z=0} h^{(0)} - \delta\mathbf{u}_2^{(0)}|_{z=-1} h_B \right. \\ &\left. + \delta^{\frac{1}{2}}\mathbf{u}_1^{(0)} h^{(0)} + \delta\mathbf{u}_1^{(0)} h^{(1)} + \delta\mathbf{u}_1^{(1)} h^{(0)}\right] + O(\delta^{\frac{3}{2}}) \\ = &\left[\int_{-1}^{0} (\boldsymbol{\nabla}\cdot\mathbf{u}_2^{(0)} + \delta\boldsymbol{\nabla}\cdot\mathbf{u}_2^{(2)})\ dz - \delta\mathbf{u}_2^{(0)}|_{z=0}\cdot\boldsymbol{\nabla} h^{(0)} - \delta\mathbf{u}_2^{(0)}|_{z=-1}\cdot\boldsymbol{\nabla} h_B \right. \\ &\left. + \delta^{\frac{1}{2}}\mathbf{u}_1^{(0)}\cdot\boldsymbol{\nabla} h^{(0)} + \delta\mathbf{u}_1^{(0)}\cdot\boldsymbol{\nabla} h^{(1)} + \delta\mathbf{u}_1^{(1)}\cdot\boldsymbol{\nabla} h^{(0)} + \delta h^{(0)}\boldsymbol{\nabla}\cdot\mathbf{u}_1^{(1)}\right] + O(\delta^{\frac{3}{2}}), \end{aligned} \tag{4.1.116}$$

where $\mathbf{u}_2^{(1)}$ has been absorbed into $\mathbf{u}_2^{(0)}$ as in the derivation of the governing equations.

Using (4.1.46), (4.1.53), (4.1.54) and (4.1.59), it is easy to show that

$$\begin{aligned} \int_{-1}^{0} \boldsymbol{\nabla}\cdot\mathbf{u}_2^{(2)}\ dz = &-\mathbf{u}_1^{(0)}\cdot\boldsymbol{\nabla} h^{(1)} - \mathbf{u}_1^{(1)}\cdot\boldsymbol{\nabla} h^{(0)} - h^{(0)}\boldsymbol{\nabla}\cdot\mathbf{u}_1^{(1)} \\ &+ J(\varphi^{(0)}|_{z=0}, h^{(0)}) + J(\varphi^{(0)}_{z=-1}, h_B). \end{aligned} \tag{4.1.117}$$

Finally, simplifying (4.1.116) we have

$$\begin{aligned} D = \delta &\left[\int_{-1}^{0} \boldsymbol{\nabla}\cdot\mathbf{u}_2^{(2)}\ dz - J(\varphi^{(0)}|_{z=0}, h^{(0)}) - J(\varphi^{(0)}|_{z=-1}, h_B) + J(h^{(0)}, h^{(1)}) \right. \\ &\left. + \mathbf{u}_1\cdot\boldsymbol{\nabla} h^{(0)} + h^{(0)}\boldsymbol{\nabla}\cdot\mathbf{u}_1^{(1)}\right] + O(\delta^{\frac{3}{2}}) \\ = &\ O(\delta^{\frac{3}{2}}), \end{aligned} \tag{4.1.118}$$

where all terms in the square brackets cancel after substitution of (4.1.117).

4.2 Linear Stability Analysis

We analyze the growth of infinitesimal perturbations on a steady mean flow. Here and in the rest of the chapter we assume, for simplicity, that $\kappa = 1$, $N =$ const and $\beta = 0$. Inclusion of the beta term in the linear analysis is possible (see Karsten and Swaters 2000b), but beyond the scope of this work, and not required for the applications we describe in sections 4.3 and 4.4. The domain is an x-periodic channel with $0 < y < L$ and the topography will be a function solely of the cross-channel coordinate, $h_B = h_B(y)$. The governing equations (4.1.70)–(4.1.73) may be written in the following form,

$$h_t + J(\varphi, h) + J(h(h_{xx} + h_{yy}) + \tfrac{1}{2}(h_x^2 + h_y^2), h) = 0 \qquad \text{at} \qquad z = 0, \tag{4.2.1}$$

$$\varphi_{zt} + J(\varphi, \varphi_z) + N^2 J(h(h_{xx} + h_{yy}) + \tfrac{1}{2}(h_x^2 + h_y^2), h) = 0 \qquad \text{at} \qquad z = 0, \tag{4.2.2}$$

$$(\Delta\varphi + N^{-2}\varphi_{zz})_t + J(\varphi, \Delta\varphi + N^{-2}\varphi_{zz}) = 0, \tag{4.2.3}$$

$$\varphi_{zt} + J(\varphi, \varphi_z) + N^2 \varphi_x h_{By} = 0 \qquad \text{at} \qquad z = -1. \tag{4.2.4}$$

The upper layer is assumed to have a time-dependent outcropping given by

$$y = \xi(x, t). \tag{4.2.5}$$

We require the no-normal-flow condition at the channel walls,

$$(v_1, v_2) = 0 \qquad \text{on } y = 0, L, \tag{4.2.6}$$

and that the frontal layer thickness vanishes at the outcropping,

$$h = 0 \qquad \text{on } y = \xi. \tag{4.2.7}$$

The following perturbed flow fields are substituted into the governing equations,

$$\varphi(x, y, z, t) = \varphi_0(y, z) + \varphi'(x, y, z, t),$$

$$h(x, y, t) = h_0(y) + h'(x, y, t),$$

$$\xi = b + \xi'(x, t), \tag{4.2.8}$$

where $y = b \in [0, L)$ is the initial location of the outcropping, and the upper layer thickness is initially nonzero for $b < y \leq L$. If we define $U_0 := -\varphi_{0y}$ to be the mean flow in the lower layer, and immediately drop primes, we obtain the linear instability equations,

$$h_t + U_0 h_x + h_{0y}\varphi_x - [(h_0 h_{0yy})_y h_x - h_0 h_{0y} \Delta h_x - h_{0y}^2 h_{xy}] = 0 \qquad z = 0, \tag{4.2.9}$$

$$\varphi_{zt} + (\varphi_{xz} - \varphi_x \partial_z)U_0 - N^2[(h_0 h_{0yy})_y h_x - h_0 h_{0y} \Delta h_x - h_{0y}^2 h_{xy}] = 0 \qquad z = 0, \quad (4.2.10)$$

$$\Delta\varphi_t + N^{-2}\varphi_{zzt} + [\Delta\varphi_x + N^{-2}\varphi_{xzz} - \varphi_x \partial_{yy} - N^{-2}\varphi_x \partial_{zz}]U_0 = 0, \qquad (4.2.11)$$

$$\varphi_{zt} + (\varphi_{xz} - \varphi_x \partial_z)U_0 + N^2 h_{By}\varphi_x = 0 \qquad z = -1, \qquad (4.2.12)$$

together with linearized boundary conditions,

$$h_x, \varphi_x = 0 \qquad y = 0, L,$$

$$h + h_{0y}\xi = 0 \qquad y = b. \qquad (4.2.13)$$

Here we discuss the energetics of the perturbed system. The growth of upper layer perturbations is governed by

$$\frac{\mathrm{d}}{\mathrm{d}t}\int_0^L \left\langle \tfrac{1}{2}h^2 \right\rangle dy = -\int_0^L \tau h_{0yy} dy - \int_0^L h_{0y} \left\langle h\varphi_x|_{z=0} \right\rangle dy, \qquad (4.2.14)$$

where the angle brackets denote the integral operator (2.3.14) and

$$\tau = h_0 \left\langle h_x h_y \right\rangle \qquad (4.2.15)$$

is the along-channel averaged perturbation Reynolds stress. Equation (4.2.14) becomes identical to the one derived in Swaters (1993) if φ is replaced by a depth-independent streamfunction. The lower-layer energy equation for FG-CS is derived as follows. Multiplying (4.2.11) by φ and integrating over the domain yields

$$\int_{-1}^0 \int_0^L \left\langle \varphi(\Delta\varphi + N^{-2}\varphi_{zz})_t \right\rangle dydz = -\int_{-1}^0 \int_0^L \left\langle \varphi(\Delta\varphi_x U_0 - \varphi_x U_{0yy}) \right\rangle dydz$$

$$-N^{-2}\int_{-1}^0 \int_0^L \left\langle \varphi(\varphi_{xzz} U_0 - \varphi_x U_{0zz}) \right\rangle dydz. \qquad (4.2.16)$$

The second term in the integrand on the left-hand side is integrated by parts with respect to z and the boundary conditions (4.2.10), (4.2.12) are substituted. Defining the lower-layer total energy,

$$E := \frac{1}{2}\int_{-1}^0 \int_0^L \left\langle |\nabla\varphi|^2 + (\varphi_z/N)^2 \right\rangle dydz, \qquad (4.2.17)$$

we obtain

$$\begin{aligned}\frac{\mathrm{d}E}{\mathrm{d}t} &= \frac{1}{2N^2}\int_0^L \left\langle (\varphi^2)_x U_{0z} \right\rangle \Big|_{z=-1}^{z=0} dy + \frac{1}{2}\int_0^L \left\langle (\varphi^2)_x h_{0y} \right\rangle_{z=0} dy \\ &\quad + \int_0^L \langle \varphi(h_t + U_0 h_x)\rangle_{z=0} + \left\langle \tfrac{1}{2}(\varphi^2)_x h_{By}\right\rangle_{z=-1} dy \\ &\quad - \int_{-1}^0\int_0^L \left\langle \tfrac{1}{2}(\varphi_x^2)_x U_0 - (\varphi_y^2)_x U_0 \right\rangle dydz - N^{-2}\int_{-1}^0\int_0^L \left\langle \tfrac{1}{2}(\varphi_z^2)_x U_0 + \varphi\varphi_{xz} U_{0z}\right\rangle dydz.\end{aligned} \tag{4.2.18}$$

Using integration by parts and the fact that all variables are periodic in x gives the result

$$\frac{\mathrm{d}E}{\mathrm{d}t} = \int_0^L \langle \varphi(h_t + U_0 h_x)\rangle_{z=0} dy + \int_{-1}^0\int_0^L \langle \varphi_x\varphi_y U_{0y} + \varphi_x\varphi_z U_{0z}\rangle dydz. \tag{4.2.19}$$

The first and second terms in the second integral represent the barotropic and baroclinic energy terms (LeBlond and Mysak 1978). If we set $U_0 \equiv 0$ then

$$\frac{\mathrm{d}E}{\mathrm{d}t} = \int_0^L \langle \varphi h_t\rangle_{z=0} dy. \tag{4.2.20}$$

Thus, growth of $E(t)$ is directly dependent on the growth of frontal disturbances.

4.2.1 Homogeneous limit

In the limit of no stratification in the lower layer, we expect to recover the S93 linearized perturbation equations. First, the vertical boundary conditions are written in the form

$$\varphi_{zt} = (\varphi_x\partial_z - \varphi_{xz})U_0 + N^2(h_t + U_0 h_x + h_{0y}\varphi_x) \qquad z = 0, \tag{4.2.21}$$

$$\varphi_{zt} = (\varphi_x\partial_z - \varphi_{xz})U_0 - N^2 h_{By}\varphi_x \qquad z = -1. \tag{4.2.22}$$

We integrate (4.2.11) in z,

$$\int_{-1}^0 \Delta\varphi_t + U_0\Delta\varphi_x - U_{0yy}\varphi_x dz + N^{-2}\varphi_{zt}\big|_{-1}^0 + N^{-2}\int_{-1}^0 U_0\varphi_{xzz} - U_{0zz}\varphi_x dz = 0. \tag{4.2.23}$$

Using integration by parts, and substituting in the vertical boundary conditions (4.2.21) and (4.2.22), we have

$$\int_{-1}^{0} \Delta\varphi_t + U_0\Delta\varphi_x - U_{0yy}\varphi_x dz + h_t + U_0|_{z=0}h_x + h_{0y}\varphi_x|_{z=0} + h_{By}\varphi_x|_{z=-1} = 0. \quad (4.2.24)$$

As U_0, φ become z-independent, we recover

$$h_t + U_0 h_x + h_{0y}\varphi_x - (h_0 h_{0yy})_y h_x + h_0 h_{0y}\Delta h_x + h_{0y}^2 h_{xy} = 0, \quad (4.2.25)$$

$$(\partial_t + U_0\partial_x)(\Delta\varphi + h) + (h_{0y} - U_{0yy} + h_{By})\varphi_x = 0, \quad (4.2.26)$$

which are identical to the analogous equations in Swaters (1993), for linearly sloping topography $h_B = -sy$.

4.2.2 Normal modes

Before making the normal mode assumption, we let $U_0 \equiv 0$, i.e. there is no mean flow in the ambient fluid. This allows us to focus on the baroclinic aspect of the instability. The linearized equations become

$$h_t + h_{0y}\varphi_x - [(h_0 h_{0yy})_y\partial_x - h_0 h_{0y}\Delta_x - h_{0y}^2\partial_{xy}]h = 0 \qquad z = 0, \quad (4.2.27)$$

$$\varphi_{zt} - N^2[(h_0 h_{0yy})_y\partial_x - h_0 h_{0y}\Delta_x - h_{0y}^2\partial_{xy}]h = 0 \qquad z = 0, \quad (4.2.28)$$

$$(\Delta\varphi + N^{-2}\varphi_{zz})_t = 0 \quad (4.2.29)$$

$$\varphi_{zt} + N^2 h_{By}\varphi_x = 0 \qquad z = -1. \quad (4.2.30)$$

We assume simple, linearly-sloping topography,

$$h_B = \nu y, \quad (4.2.31)$$

for $\nu =$ const., and make the normal mode approximation,

$$(\varphi, h, \xi) = (\tilde{\varphi}(y,z), \tilde{h}(y), \tilde{\xi})\exp[ik(x - ct)] + \text{c.c.} \quad (4.2.32)$$

where c.c. refers to the complex conjugate, as before. For convenience, we define the operator

$$\mathcal{L}[*] = \left\{(h_0 h_{0yy})_y + h_0 h_{0y}(k^2 - \partial_{yy}) - h_{0y}^2 \partial_y\right\}(*). \tag{4.2.33}$$

At this point we could solve for h in terms of φ, as in chapter 2, however we find it more convenient to retain the original equations. Substituting (4.2.32) and (4.2.33) into (4.2.27)–(4.2.30) and immediately dropping tildes, we obtain

$$\varphi_{yy} + N^{-2}\varphi_{zz} - k^2\varphi = 0, \tag{4.2.34}$$

$$h_{0y}\varphi - \mathcal{L}[h] = ch, \qquad z = 0, \tag{4.2.35}$$

$$-N^2\mathcal{L}[h] = c\varphi_z, \qquad z = 0, \tag{4.2.36}$$

$$\nu N^2\varphi = c\varphi_z, \qquad z = -1, \tag{4.2.37}$$

where the boundary conditions are now given by

$$\begin{aligned} h, \varphi &= 0 \qquad \text{on } y = 0, L, \\ \xi &= -\frac{h}{h_{0y}} \qquad \text{on } y = b. \end{aligned} \tag{4.2.38}$$

Note that ξ, the outcropping perturbation amplitude, is now given diagnostically in terms of the perturbation thickness h.

In the absence of an upper layer (or upper layer cross-channel gradients), the model admits the usual solutions for a continuously-stratified QG fluid. In particular, if $h_0 \equiv 0$ and $h \equiv 0$ then (4.2.35) is trivially satisfied, and the solutions to (4.2.34), (4.2.36), (4.2.37) are channel topographic Rossby waves,

$$\varphi = A\cosh\left(N\sqrt{k^2 + \left(\frac{n\pi}{L}\right)^2}\, z\right)\sin\left(\frac{n\pi y}{L}\right)\exp[ikx - i\omega t] + \text{c.c.}, \tag{4.2.39}$$

where A, k, $\frac{n\pi}{L}$ and ω are the (arbitrary) amplitude, along-channel wavenumber, cross-channel wavenumber and frequency, respectively, for $n = 1, 2, 3 \ldots$ The dispersion relation is given by (Pedlosky 1987)

$$\omega = -\frac{\nu N k}{\sqrt{k^2 + \left(\frac{n\pi}{L}\right)^2}\tanh\left(N\sqrt{k^2 + \left(\frac{n\pi}{L}\right)^2}\right)}. \tag{4.2.40}$$

4.2.3 Necessary Condition for Instability

To derive a necessary condition for instability, we first write (4.2.35)–(4.2.37) as follows

$$h_{0y}\varphi - ch - \mathcal{L}[h] = 0, \qquad z = 0, \tag{4.2.41}$$

$$\varphi_z = N^2\left(h - \frac{h_{0y}}{c}\varphi\right) = 0, \qquad z = 0, \tag{4.2.42}$$

$$\varphi_z = \frac{\nu N^2}{c}\varphi, \qquad z = -1. \tag{4.2.43}$$

Details of the derivation will become easier if we introduce the functional

$$F = \begin{cases} h/h_{0y}, & h_{0y} \neq 0, \\ 0, & h_{0y} = 0. \end{cases} \tag{4.2.44}$$

We will also need an expression for $\int_0^L h_{0y}\varphi^*|_{z=0}F\ dy$ that does not involve the complex conjugate of any variable. Writing (4.2.41) in terms of F and performing the obvious cancellations,

$$h_{0y}\varphi|_{z=0} - (ch_{0y} + k^2h_0h_{0y}^2)F + (2h_0h_{0y}h_{0yy} + h_{0y}^3)F_y + h_0h_{0y}^2F_{yy} = 0. \tag{4.2.45}$$

Next, we take the complex conjugate, multiply through by Fh_{0y} and integrate over the width of the channel,

$$\int_0^L h_{0y}\varphi^*|_0F - (c^*h_{0y} + k^2h_0h_{0y}^2)|F|^2 + (2h_0h_{0y}h_{0yy} + h_{0y}^3)FF_y^* + h_0h_{0y}^2FF_{yy}^*\ dy = 0. \tag{4.2.46}$$

We integrate by parts and exploit the fact that h (and therefore F) vanishes on the boundaries, to obtain

$$\int_0^L h_{0y}\varphi^*|_{z=0}F\ dy = \int_0^L (c^*h_{0y} + k^2h_0h_{0y}^2)|F|^2 + h_0h_{0y}^2|F_y|^2\ dy. \tag{4.2.47}$$

To form the energy equation, multiply (4.2.34) by φ^* and integrate over the domain,

$$\int_{-1}^0\int_0^L \varphi^*\varphi_{yy} + N^{-2}\varphi^*\varphi_{zz} - k^2\varphi^*\varphi\ dydz = 0. \tag{4.2.48}$$

Integrating by parts, we use the boundary conditions (4.2.42), (4.2.43). Noting that φ^* vanishes on the boundaries, we have

$$E = \int_0^L h_{0y}\varphi^*|_{z=0} F \; dy - \frac{1}{c}\int_0^L h_{0y}|\varphi|^2_{z=0} \; dy - \frac{\nu}{c}\int_0^L |\varphi|^2_{z=-1} \; dy, \tag{4.2.49}$$

where $E \in \mathbb{R}$ is defined, in the normal mode context, as

$$E := \int_{-1}^0 \int_0^L k^2|\varphi|^2 + |\varphi_y|^2 + N^{-2}|\varphi_z|^2 \; dy > 0. \tag{4.2.50}$$

Substituting in relation (4.2.47) we obtain

$$\begin{aligned} E = &\int_0^L (c^* h_{0y} + k^2 h_0 h_{0y}^2)|F|^2 + h_0 h_{0y}^2 |F_y|^2 dy \\ &- \frac{c^*}{|c|^2}\int_0^L h_{0y}|\varphi|^2_{z=0} + \nu|\varphi|^2_{z=-1} \; dy. \end{aligned} \tag{4.2.51}$$

Expanding $c^* = c_R - ic_I$ and taking the imaginary part,

$$c_I\left\{\int_0^L h_{0y}|F|^2 dy - \frac{1}{|c|^2}\int_0^L h_{0y}|\varphi|^2_{z=0} + \nu|\varphi|^2_{z=-1} \; dy\right\} = 0. \tag{4.2.52}$$

If $c_I > 0$ (i.e. we have instability) then the terms within the braces must sum to zero,

$$\int_0^L h_{0y}|F|^2 dy - \frac{1}{|c|^2}\int_0^L h_{0y}|\varphi|^2_{z=0} + \nu|\varphi|^2_{z=-1} \; dy = 0. \tag{4.2.53}$$

We consider basic frontal profiles such that $h_{0y} > 0 \; \forall y \in (0, L)$. We may interpret this as, for example, an upwelling front, whose thickness increases away from shore ($y = 0$). For nontrivial perturbations, the first term above will be strictly positive, and thus

$$-\int_0^L \nu|\varphi|^2_{z=-1} \; dy \; < \int_0^L h_{0y}|\varphi|^2_{z=0} \; dy. \tag{4.2.54}$$

For comparison with Swaters (1993), we introduce $s = -\nu$ and define $\alpha = \max[h_{0y}]$ on $y \in (0, L)$. Then a necessary condition for instability is

$$s\int_0^L |\varphi|^2_{z=-1} \; dy \; < \alpha\int_0^L |\varphi|^2_{z=0} \; dy. \tag{4.2.55}$$

Conversely,

$$0 < \alpha \leq s \frac{\displaystyle\int_0^L |\varphi|^2_{z=-1}\, dy}{\displaystyle\int_0^L |\varphi|^2_{z=0}\, dy} \tag{4.2.56}$$

is a sufficient condition for stability, which should be compared with the analogous Swaters (1993) stability condition,

$$0 < \alpha \leq s. \tag{4.2.57}$$

We point out that, if the perturbations are surface-intensified (e.g. due to wind stress, river outflow, etc.), then the right-hand side of (4.2.56) will generally be smaller than s. This implies that the FG-CS model has a smaller region of stability (i.e. is potentially more unstable) than FG-SW.

4.2.4 Gently sloping wedge front

Analytical solutions may be obtained for the special case of a linearly sloping (non-outcropping) frontal profile, if the frontal and topographic slopes are assumed small. Since there is no actual outcropping, we will take $b = 0$. The following basic state is assumed,

$$h_0(y) = 1 + \alpha y, \tag{4.2.58}$$

with $\alpha = O(\nu) \ll 1$. It will also turn out that $c = O(\alpha)$. Keeping only $O(1)$ terms, (4.2.35)–(4.2.37) are modified as follows

$$[k^2 - \partial_{yy}]h + \frac{c}{\alpha}h - \varphi = 0, \qquad z = 0, \tag{4.2.59}$$

$$N^2[k^2 - \partial_{yy}]h + \frac{c}{\alpha}\varphi_z = 0, \qquad z = 0, \tag{4.2.60}$$

$$N^2\varphi - \frac{c}{\nu}\varphi_z = 0, \qquad z = -1. \tag{4.2.61}$$

Separated solutions to (4.2.34), (4.2.59)–(4.2.61) and (4.2.38) may be sought in the form

$$h_n = a_n \sin(l_n y),$$

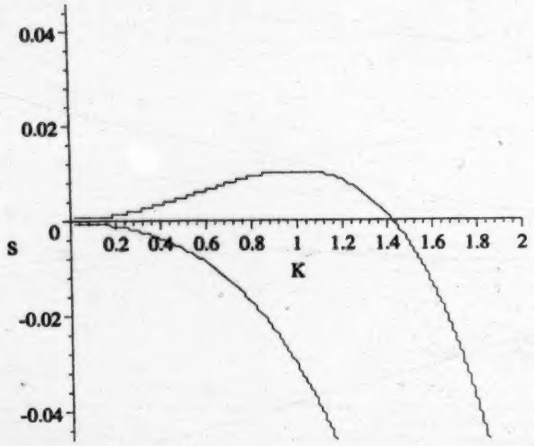

Figure 4.2: Marginal stability curves in the $K-s$ plane for the gently sloping wedge front with $\alpha = 0.01$ and $N = 0$.

$$\varphi_n = \sin(l_n y)[b_n \cosh(\lambda_n(z+1)) + c_n \cosh(\lambda_n z)], \tag{4.2.62}$$

with unknown coefficients a_n, b_n and c_n, where

$$l_n = \frac{n\pi}{L}, \qquad K_n = \sqrt{k^2 + l_n^2} \qquad \text{and} \qquad \lambda_n = NK_n, \tag{4.2.63}$$

for $n = 1, 2, 3, ...$ Substitution into the above equations yields the following system

$$\begin{bmatrix} K_n^2 + \frac{c}{\alpha} & -\cosh(\lambda_n) & -1 \\ \lambda_n & \frac{c}{\alpha}\sinh(\lambda_n) & 0 \\ 0 & N^2 & N^2\cosh(\lambda_n) + \frac{c}{\nu}\lambda_n\sinh(\lambda_n) \end{bmatrix} \begin{bmatrix} a_n \\ b_n \\ c_n \end{bmatrix} = \mathbf{0}. \tag{4.2.64}$$

For nontrivial solutions we require that the determinant of the coefficient matrix vanishes. Introducing the notation $T_n = \tanh(\lambda_n)/\lambda_n$, we thus obtain the dispersion relation,

$$(\lambda_n^2 T_n)c^3 + N^2(\alpha K_n^4 T_n + \nu)c^2 + \alpha\lambda_n^2(\alpha + \nu)c + \alpha^2\nu N^2\lambda_n^2 T_n = 0. \tag{4.2.65}$$

In the limit of a homogeneous lower layer, we should expect this equation to reduce to the analogous dispersion relation for the S93 model. For easier comparison with previous results, in the rest of this section we adopt the notation s in place of $-\nu$, i.e.

the topography is assumed to be of the form $h_B = -sy$. Dividing (4.2.65) through by N^2 yields

$$K_n^2 T_n c^3 + (\alpha K_n^4 T_n - s)c^2 + \alpha K_n^2(\alpha - s)c - \alpha^2 s N^2 K_n^2 T_n = 0. \tag{4.2.66}$$

As $N^2 \longrightarrow 0$, we have $T_n \longrightarrow 1$. In the limit of no stratification, the last term on the left-hand side vanishes, and we may therefore divide through by c (assuming $|c| \neq 0$),

$$K_n^2 c^2 + (\alpha K_n^4 - s)c + \alpha K_n^2(\alpha - s) = 0. \tag{4.2.67}$$

Solving for c we obtain

$$c = \frac{s - \alpha K_n^4 \pm \sqrt{(\alpha K_n^4 - s)^2 - 4\alpha(\alpha - s)K_n^4}}{2K_n^2}, \tag{4.2.68}$$

which agrees with the dispersion relation derived in R97. Setting the discriminant equal to zero yields two marginal stability curves, which are most conveniently written

$$\frac{s}{\alpha} = K^2(2 - K^2) \qquad \text{and} \qquad \frac{s}{\alpha} = -K^2(2 + K^2). \tag{4.2.69}$$

The roots, c, of the cubic equation (4.2.65) may be found analytically by using Cardan's technique. To obtain instability characteristics, in practice it is more convenient to use a numerical implicit plotting package, such as the one provided in Maple. It is of interest to examine the effect of incrementally increasing N on stability in the simple context of the wedge front. Relevant figures in this section were generated using $\alpha = 0.01$. Fig. 4.2 is a $K - s$ marginal stability plot, in the $N = 0$ limit (i.e. relations (4.2.69)). In Fig. 4.3 we plot the marginal stability curves for a) $N = 0.02$, b) $N = 0.08$, c) $N = 0.5$ and d) $N = 1.0$. As N increases, so does the overall extent of the unstable region. For $s < 0$ two robust unstable modes exist for small values of N, which then merge in wavenumber space as N becomes O(1). We will refer to the low- and high-wavenumber mode as the bottom- and surface-intensified mode, respectively.

The wedge front configuration is typically dominated by the gravest (i.e. $n = 1$) mode (see R97, PS99a). In Fig. 4.4 we plot growth rates and phase speeds for the

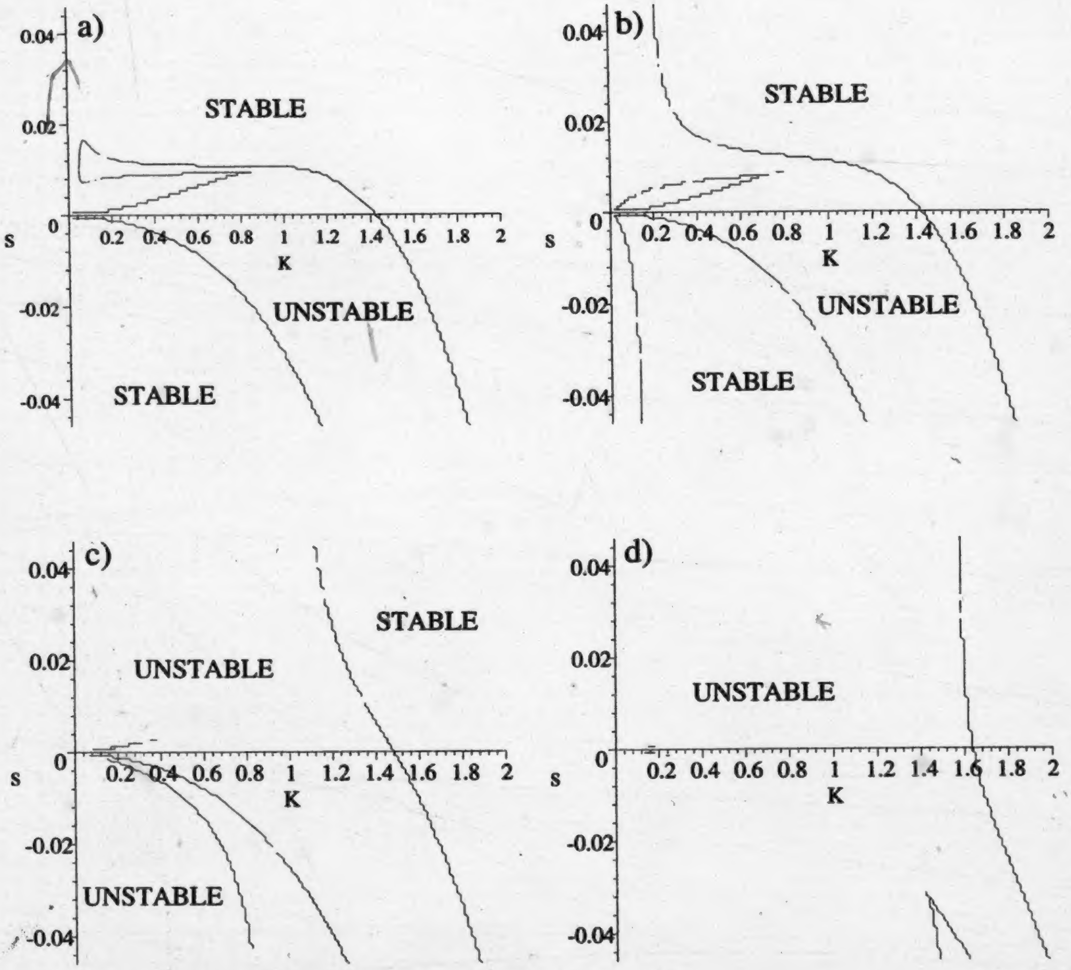

Figure 4.3: Marginal stability curves in the $K - s$ plane for four different values of the non-dimensional buoyancy frequency, $N =$ a) 0.02, b) 0.08, c) 0.5 and d) 1.0.

gravest mode of the perturbation obtained by solving (4.2.65). Here we employed $N^2 = 0.5$ and $L = 10.0$ (so $l_1 = 0.63$). The same plots, but with $N^2 = 1.0$, are shown in Fig. 4.5. The instability characteristics were computed for three different values of the bottom slope, $s = 0.02$, 0.0 and -0.02. With a buoyancy frequency of 0.5 we see that the maximum growth rate of the most unstable mode increases with decreasing s, as does the most unstable along-channel wavenumber. This is consistent with the

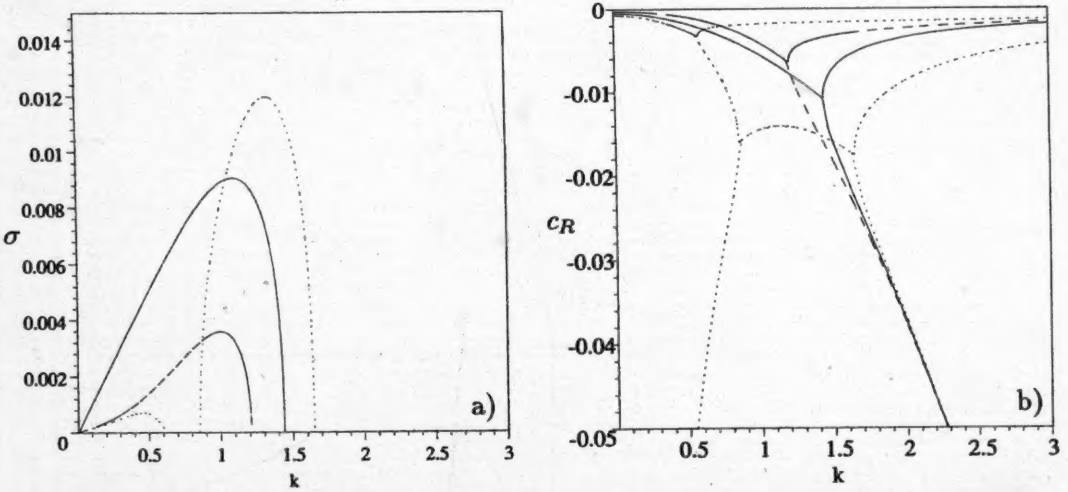

Figure 4.4: a) Growth rate curves and b) phase speed curves for gently-sloping wedge front where $\alpha = -0.01$, $N = 0.5$. Three values for s were employed, 0.2 (dashed line), 0 (continuous line) and -0.02 (dotted line).

idea that topography which slopes in the same sense as the front is a stabilizing influence (see, for example, Orlanski 1969).

In the $s = -0.02$ case (Fig. 4.4, dotted line), the smaller, bottom-intensified mode is also evident at low wavenumbers, as was pointed out in reference to the marginal stability curves, Fig. 4.3c. With $N^2 = 1.0$ and $s = -0.02$ (Fig. 4.5) the bottom- and surface-intensified modes have merged, however the discontinuity in the derivative of the σ curve at $k \approx 1.1$ highlights the distinct nature of these two modes. In Fig. 4.5, of the three growth rates we have computed, the largest occurs at $s = 0$. While the actual maximum may not occur exactly at $s = 0$, it certainly occurs somewhere for $-0.02 < s < 0.02$, in contrast to the case $N^2 = 0.5$. Thus, we can say that topography is predominantly a stabilizing influence in this parameter regime. We elaborate on this observation in the following section. However, a remark is appropriate here. The influence of topography on coastal/upwelling fronts is similar to the effect of β on zonal flows, such that the presence of β is stabilizing for eastward flows. We refer the

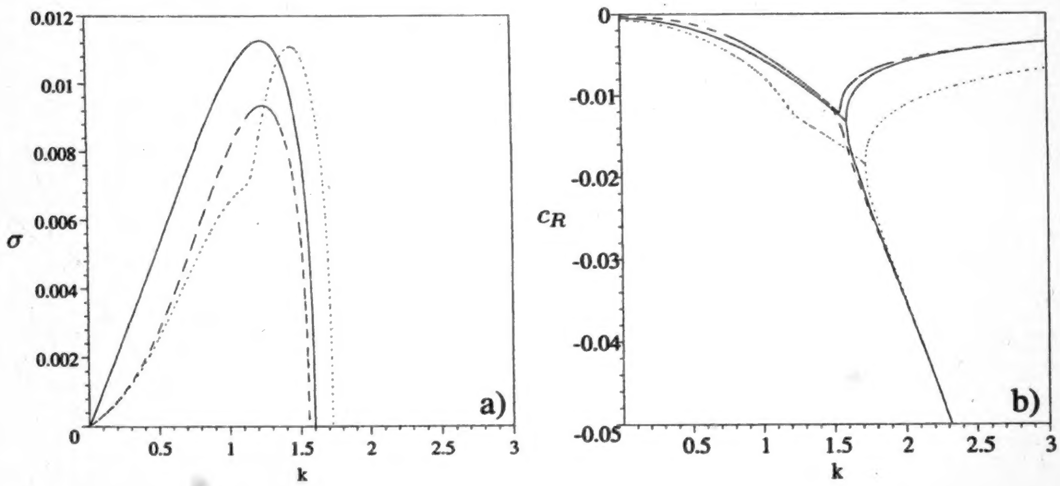

Figure 4.5: a) Growth rate curves and b) phase speed curves for gently-sloping wedge front where $\alpha = -0.01$, $N = 1.0$. Three values for s were employed, 0.2 (dashed line), 0 (continuous line) and -0.02 (dotted line).

reader to Karsten and Swaters (2000b) for a discussion of FG dynamics on a β-plane.

Fig. 4.6 demonstrates the connection between the FG-SW model and the traditional two-layer QG model on an f-plane with bottom topography. In the latter model, linearly sloping topography plays the same role as the beta effect, but the topographic term appears in the lower-layer equation only. The derivation of the marginal stability criterion in this case is similar to the analogous derivation for the Phillips model where β appears in both layers (Pedlosky 1987), and is summarized below.

If the amplitudes of the pressure perturbations in layer 1 and 2 are A_1 and A_2, respectively, then the normal mode linear instability problem may be written

$$\begin{bmatrix} (c - U_2 - U_s)(K^2 + F_1) + F_1 U_s & (U_2 + U_s - c)F_1 \\ (U_2 - c)F_2 & (c - U_2)(K^2 + F_2) - s - F_2 U_s \end{bmatrix} \begin{bmatrix} A_1 \\ A_2 \end{bmatrix} = \mathbf{0}, \tag{4.2.70}$$

where U_2 is the mean flow in the lower layer, U_s is the vertical shear and s is the scaled

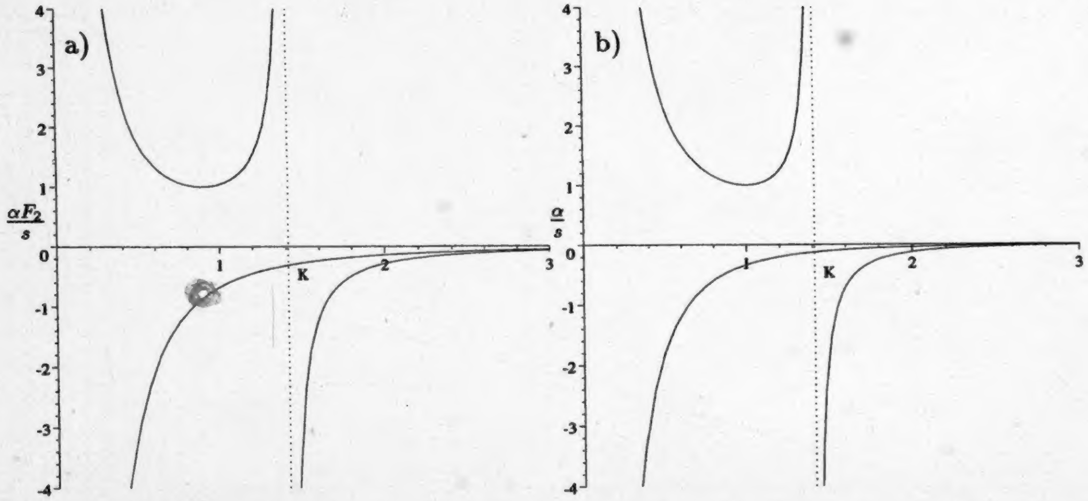

Figure 4.6: Marginal stability curves for a) two-layer QG model on an f-plane with sloping bottom and b) gently sloping wedge front in the FG-SW model. In a) K is rescaled according to $K^2 \rightarrow \sqrt{F_1 F_2} K^2$, making the assumption $F_1 = 5F_2$ (as in Pedlosky 1987).

topographic slope as before. The solvability condition yields a quadratic equation in c, the complex phase speed,

$$\begin{aligned}
&\left\{(K^2+F_1)(K^2+F_2)-F_1F_2\right\}c^2 \\
&+\left\{(K^2+F_1)[-U_2(K^2+F_2)-s-F_2U_s]\right. \\
&\left.+[-(U_s+U_2)(K^2+F_1)+F_1U_s](K^2+F_2)+F_1F_2(U_s+2U_2)\right\}c \\
&+[-(U_s+U_2)(K^2+F_1)+F_1U_s][-U_2(K^2+F_2)-s-F_2U_s] \\
&-(U_s+U_2)U_2F_1F_2=0. \qquad (4.2.71)
\end{aligned}$$

Solving for c, the marginal stability curves are obtained by setting the discriminant equal to zero,

$$K^4(4F_1F_2-K^4)\left(\frac{U_s}{s}\right)^2+2K^2(K^4+K^2F_1-2F_1F_2)\frac{U_s}{s}-(K^2+F_1)^2=0. \quad (4.2.72)$$

If we set $U_2 = 0$, i.e. no mean flow in the lower layer, then $U_s = U_1 = -\alpha$, and the condition for marginal stability takes the form

$$\frac{\alpha}{s} = \frac{K^4 + K^2F_1 - 2F_1F_2 \pm 2F_1\sqrt{K^2F_2 + F_2^2 + F_1F_2}}{K^2(4F_1F_2 - K^4)}. \qquad (4.2.73)$$

At this point if we write $F_1 = \gamma F_2$, for some constant γ, and rescale K by $(F_1F_2)^{\frac{1}{4}}K$, then (4.2.73) simplifies to

$$\frac{\alpha F_2}{s} = \frac{K^4 + \sqrt{\gamma}K^2 - 1 \pm 2\sqrt{\sqrt{\gamma}K^2 + 1 + \gamma}}{\sqrt{\gamma}K^2(4 - K^4)}, \qquad (4.2.74)$$

where the right-hand side no longer depends on either Froude number. We choose $\gamma = 5$, which implies a lower layer 5 times deeper than the surface flow. This choice is consistent with our assumption of a thin upper layer and also allows direct comparison with Pedlosky (1987).

We plot $\alpha F_2/s$ versus K in Fig. 4.6a. In contrast with the Phillips model, the sloping-bottom QG model extends the region of instability in K, when $\alpha F_2/s < 0$. Indeed, the high wavenumber cutoff grows without bound as $\alpha/s \to 0^-$. In Fig. 4.6b we plot α/s for the wedge front case of FG-SW. Here the total wavenumber was not rescaled and the ratio of the Froude numbers was not assigned a numerical value.

We remind the reader that the FG theory derived in this chapter is a leading-order balance in δ, where we made the *a priori* assumptions $F_1 = O(\delta^{-\frac{1}{2}})$ and $F_2 = O(\delta^{\frac{1}{2}})$ (see (4.1.17) and (4.1.39)). Thus, the dispersion relationships (4.2.69) and (4.2.73) are not mathematically equivalent. However the instability regions are quite similar qualitatively. This demonstrates that FG-SW behaves much like traditional QG theory in the limit of a gently-sloping, non-outcropping frontal profiles. More generally however, the FG scaling is appropriate for outcropping fronts and allows the description of coherent, isolated vortex features, while the QG approximation is better suited to the description of small interfacial anomalies.

4.3 The nonseparable problem

For more realistic frontal profiles, in particular ones that allow an outcropping, the problem becomes nonseparable, and we use the Galerkin technique introduced in chapter 2. We expand the streamfunctions on an orthonormal basis,

$$h = \sqrt{\frac{2}{L}} \sum_{n=1}^{\infty} a_n \sin(l_n y), \tag{4.3.1}$$

$$\varphi = \sqrt{\frac{2}{L}} \sum_{n=1}^{\infty} \sin(l_n y)[b_n \cosh(\lambda_n(z+1)) + c_n \cosh(\lambda_n z)], \tag{4.3.2}$$

such that each expansion mode satisfies (4.2.34) and (4.2.38). We then obtain

$$\begin{gathered}
\sum_n \{\sin(l_n y)[b_n \cosh(\lambda_n) + c_n] h_{0y} - a_n \mathcal{L}[\sin(l_n y)]\} = c \sum_n a_n \sin(l_n y), \\
-\sum_n a_n N^2 \mathcal{L}[\sin(l_n y)] = c \sum_n b_n \lambda_n \sin(l_n y) \sinh(\lambda_n), \\
-\sum_n \nu N^2 \sin(l_n y)[b_n + c_n \cosh(\lambda_n)] = c \sum_n c_n \lambda_n \sin(l_n y) \sinh(\lambda_n).
\end{gathered} \tag{4.3.3}$$

For convenience, define the integral operators,

$$\begin{aligned}
\mathcal{J}_1^{mn}[*] &:= \int_b^L * \sin(l_m y) \sin(l_n y) \; dy, \\
\mathcal{J}_2^{mn}[*] &:= \int_b^L * \sin(l_m y) \cos(l_n y) \; dy,
\end{aligned} \tag{4.3.4}$$

where $b > 0$ for outcropping fronts. We will also need the following integrals,

$$\begin{aligned}
I_1^{mn} &:= \mathcal{J}_1^{mn}[h_{0y}], \qquad & I_2^{mn} &:= \mathcal{J}_1^{mn}[(h_0 h_{0yy})_y], \\
I_3^{mn} &:= \mathcal{J}_1^{mn}[h_0 h_{0y}], \qquad & I_4^{mn} &:= \mathcal{J}_2^{mn}[h_{0y}^2].
\end{aligned} \tag{4.3.5}$$

Multiplying (4.3.3) by $\sin(l_m y)$ and integrating over $y \in (0, L)$ yields

$$\sum_n \frac{2}{L}\{(b_n \cosh(\lambda_n) + c_n) I_1^{mn} - a_n (I_2^{mn} + K_n^2 I_3^{mn} - l_n I_4^{mn})\} = c\delta_{mn} a_m,$$

$$-\sum_n \frac{2}{L} N^2 a_n (I_2^{mn} + K_n^2 I_3^{mn} - l_n I_4^{mn}) = c\delta_{mn} b_m \lambda_m \sinh(\lambda_m),$$

$$-\sum_n \delta_{mn}\nu N^2(b_n + c_n\cosh(\lambda_n)) = c\delta_{mn}c_m\lambda_m\sinh(\lambda_m), \tag{4.3.6}$$

for $m = 1, 2, 3, ...$, where we have used the orthonormal property of the cross-channel expansion functions,

$$\frac{2}{L}\int_0^L \sin(l_m y)\sin(l_n y)dy = \delta_{mn}. \tag{4.3.7}$$

Rearranging, we obtain

$$\sum_n\{-a_n\frac{2}{L}(I_2^{mn} + K_n^2 I_3^{mn} - l_n I_4^{mn}) + \frac{2}{L}(b_n\cosh(\lambda_n) + c_n)I_1^{mn}\} = c\delta_{mn}a_m,$$

$$-\sum_n a_n\frac{2N^2}{L\lambda_m\sinh(\lambda_m)}(I_2^{mn} + K_n^2 I_3^{mn} - l_n I_4^{mn}) = c\delta_{mn}b_m,$$

$$-\sum_n \delta_{mn}\frac{\nu N^2}{\lambda_m\sinh(\lambda_m)}(b_n + c_n\cosh(\lambda_n)) = c\delta_{mn}c_m, \tag{4.3.8}$$

for $m = 1, 2, 3, ...$

More compactly, the eigenproblem is written as

$$\mathbf{PV} = c\mathbf{V}, \tag{4.3.9}$$

where

$$\mathbf{P} = \begin{bmatrix} \mathbf{P}_{11} & \mathbf{P}_{12} & \mathbf{P}_{13} \\ \mathbf{P}_{21} & \mathbf{O} & \mathbf{O} \\ \mathbf{O} & \mathbf{P}_{32} & \mathbf{P}_{33} \end{bmatrix} \quad \text{and} \quad \mathbf{V} = \begin{bmatrix} \mathbf{a} \\ \mathbf{b} \\ \mathbf{c} \end{bmatrix}. \tag{4.3.10}$$

Here the elements of the vectors **a**, **b** and **c** are the coefficients a_m, b_m and c_m, respectively, and the coefficient submatrices have the form

$$\mathbf{P}_{11}^{mn} = -\frac{2}{L}(I_2^{mn} + K_n^2 I_3^{mn} - l_n I_4^{mn}), \qquad \mathbf{P}_{12}^{mn} = \frac{2}{L}\cosh(\lambda_n)I_1^{mn}$$

$$\mathbf{P}_{13}^{mn} = \frac{2}{L}I_1^{mn}, \qquad \mathbf{P}_{21}^{mn} = -\frac{2N^2}{L\lambda_m\sinh(\lambda_m)}(I_2^{mn} + K_n^2 I_3^{mn} - l_n I_4^{mn}),$$

$$\mathbf{P}_{32}^{mn} = -\delta_{mn}\frac{\nu N^2}{\lambda_m\sinh(\lambda_m)}, \qquad \mathbf{P}_{33}^{mn} = -\delta_{mn}\frac{\nu N^2}{\lambda_m}\coth(\lambda_m). \tag{4.3.11}$$

Equation (4.3.9) is a standard eigenvalue problem, which, after truncation at a finite number of expansion modes, M, we solve numerically using the DEIGV routine as in chapter 2.

We have not been able to derive a semicircle theorem for FG-CS or FG-SW. However, the energy equation (4.2.51) provides two integral constraints. The real part of (4.2.51) is

$$E = \int_0^L (c_R h_{0y} + k^2 h_0 h_{0y}^2)|F|^2 + h_0 h_{0y}^2 |F_y|^2 \; dy$$
$$- \frac{c_R}{|c|^2} \int_0^L h_{0y} |\varphi|^2_{z=0} + \nu |\varphi|^2_{z=-1} \; dy. \tag{4.3.12}$$

Assuming instability, we add this to $c_R \times$(4.2.53). The first constraint can then be written

$$E = \int_b^L h_0 \left(k^2 |h|^2 + \frac{|h_{0yy} h - h_{0y} h_y|^2}{h_{0y}^2} \right) \; dy, \tag{4.3.13}$$

where E is given by (4.2.50). Equation (4.2.53) itself provides the second constraint, which upon rearrangement becomes

$$\int_b^L \frac{|ch|^2}{h_{0y}} - h_{0y} |\varphi|^2_{z=0} \; dy \;\; = \;\; \nu \int_0^L |\varphi|^2_{z=-1} \; dy, \tag{4.3.14}$$

where the right-hand side vanishes for flat topography. In practice, however, we find that significant error is introduced wherever h_{0y} becomes small and the above integrals are not useful indicators of the accuracy of solutions found with the spectral technique.

4.3.1 General wedge front

Here we consider a more general front-topography configuration, such that both the frontal and topographic slope are allowed to be O(1). Although this wedge front profile is non-outcropping, its properties will be intermediate between the gently sloping wedge and the outcropping exponential profile (next subsection). For $b = 0$

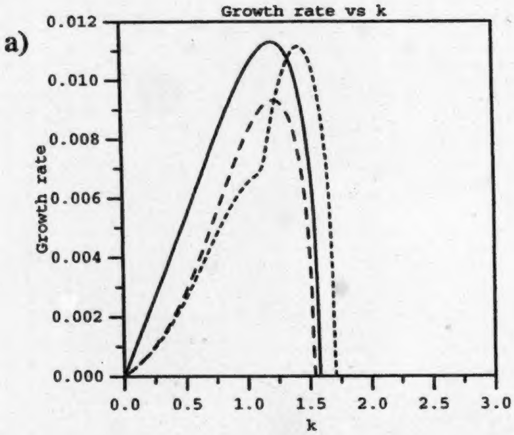

Figure 4.7: a) Growth rate curves and b) phase speed curves for the gently sloping wedge front with $\alpha = 0.01$ and $N = 1.0$, obtained with the spectral technique, using 120 expansion modes. Here $\nu = -0.02$ (dashed lines), 0.0 (solid lines) and 0.02 (dotted lines), however we solve the nonseparable eigenproblem (4.3.9), without the simplifying assumption $\alpha \sim \nu \ll 1$. These plots should be compared with Fig. 4.5.

and $\alpha, \nu = O(1)$, the integrals (4.3.5) simplify to

$$I_1^{mn} = \delta_{mn}\frac{\alpha L}{2}, \tag{4.3.15}$$

$$I_2^{mn} = 0, \tag{4.3.16}$$

$$I_3^{mn} = \delta_{mn}\frac{\alpha L}{2} + \alpha^2 \mathcal{J}_1^{mn}[y], \tag{4.3.17}$$

$$I_4^{mn} = \alpha^2 \mathcal{J}_2^{mn}[1], \tag{4.3.18}$$

where

$$\mathcal{J}_1^{mn}[y] = \begin{cases} L^2/4 & m = n \\ 2mnL^2\dfrac{(-1)^{m+n} - 1}{\pi^2(m+n)^2(m-n)^2} & m \neq n \end{cases} \tag{4.3.19}$$

and

$$\mathcal{J}_2^{mn}[1] = \begin{cases} 0 & m = n \\ mL\dfrac{(-1)^{m+n} - 1}{\pi(m+n)(m-n)} & m \neq n \end{cases} \tag{4.3.20}$$

In order to lend credibility to the Galerkin technique in the context of the FG-CS/FG-SW linearized equations, we first examine the instability characteristics for a

	theory			simulation		
ν	$\hat{k}$	$\sigma_{\max}$	c_R	$\hat{k}$	$\sigma_{\max}$	c_R
-1.0	0.74	0.299	-0.528	0.79	0.318	-0.526
0.0	0.77	0.418	-0.600	0.79	0.431	-0.588
1.0	0.93	0.489	-1.074	1.05	0.507	-1.091
2.0	1.15	0.484	-1.641	1.31	0.461	-1.442
3.0	1.33	0.405	-2.131	1.31	0.419	-1.923

Table 4.1: Most unstable wavenumber $\hat{k}$, maximum growth rate $\sigma_{\max}$ and corresponding phase speed c_R, for the O(1) wedge profile. Characteristics obtained with the spectral technique, and those resulting from direct numerical simulations are recorded. Here $\alpha = 0.5$ and $L = 4.0$.

gently sloping wedge. These are plotted in Fig. 4.7 for the same parameter values as in Fig. 4.5. No assumptions are made here as to the separability of the eigenproblem, or the smallness of α and s (even though both parameters happen to be small, for the purposes of comparison). Agreement between Figs. 4.5 and 4.7 is excellent, even for the case $s = -0.02$, in which the growth rate and phase speed curves both exhibit a kink at $k \approx 1.1$. As in chapter 2, secondary modes appear as part of the analysis. However, they are not discussed here, and we focus on the primary (i.e. fastest growing) mode in the rest of the chapter.

Next, we considered the O(1) wedge profile, for which the dispersion relation cannot be written down in closed form. Setting the frontal slope α equal to 0.5 and the channel width L equal to 4.0, we computed the instability characteristics, listed in Table 4.1, for 5 different values of the bottom slope. Table 4.1 also records the characteristics that emerged during numerical simulations of the governing equations for the same frontal and topographic profiles, starting with a small random perturbation. Agreement between theory and simulation is relatively good, however we had to utilize 320 expansion modes, and convergence was rather slow with respect to M.

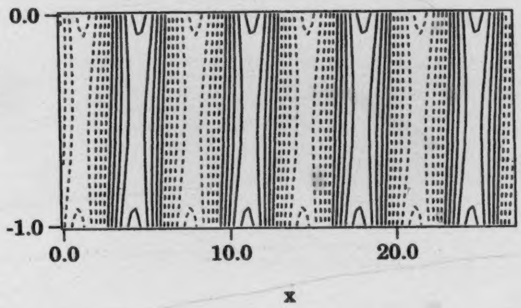

Figure 4.8: Lower layer perturbation at $y = 2.0$ obtained with the spectral technique for the $O(1)$ wedge front. Here $L = 4.0$ and $\nu = 1.0$. The contour extrema and intervals are, respectively, -0.9, 0.9, 0.2. Dashed lines correspond to negative values. The solution is both surface- and bottom-intensified. The corresponding plot from a numerical simulation during the linear stage of growth shows virtually the same vertical structure of the growing anomaly.

For example, with $\nu = -1.0$, σ_{max} showed a change of 7% when M was increased from 160 to 320, and a change of 2% when M was increased from 320 to 480.

On the other hand, the spatial structure of the perturbations is captured quite well by the Galerkin technique, even with modest values of M. In particular, for $\nu = 1.0$ (topography slopes in the opposite sense to the front), the solutions exhibit both surface and bottom intensification. A vertical cross-section of the lower-layer streamfunction at $y = 2.0$ is shown in Fig. 4.8. The corresponding plot from a numerical simulation (not shown) is virtually identical. Amplitudes at the surface are slightly larger than at the bottom, and the smallest amplitudes clearly occur at mid-depth. Phase lines also lean slightly backward with respect to the mean flow, which is in the negative x direction. This phase tilt is consistent with the process of baroclinic energy release (Pedlosky 1987).

Table 4.1 shows the following trends. The wavenumber $\hat{k}$ of the instability increases with ν, as does the absolute value of the phase speed, c_R. We note that the wavelength of the instability in the simulations was constrained by the length of the channel. The domain always accommodated at least 4 waves of the most unstable mode, however we did not finetune the channel length to obtain more precise values for $\hat{k}$.

For the range of topographic slopes we have considered, growth rates first increase with ν, then decrease. We believe that this behavior may be explained as follows. Upper layer disturbances tend to propagate in the direction of the mean flow (determined by the front). If the frontal and topographic slopes have the same sign, then lower-layer disturbances (i.e. topographic Rossby waves) and upper-layer disturbances travel in opposite directions. Coupling between the layers is inhibited, and so is the release of potential energy (Cushman-Roisin 1994). As the topography decreases toward zero this effect diminishes. When the topographic gradient switches sign, upper- and lower-layer perturbations propagate in the same direction, thus enhancing coupling and growth. However, as the bottom becomes even more steep, the speed of ambient Rossby waves becomes much greater than that of upper-layer perturbations, which again hinders coupling between the layers.

4.3.2 Exponential front

Upwelling fronts are often approximated by an exponential profile, with a distinct offshore outcropping (Barth 1989a). Here we present a sample of the linear instability characteristics associated with this frontal profile and compare our results with those of Barth (1989b) and Barth (1994). We assume the basic state

$$h_0(y) = \alpha \max\{1 - \exp(\gamma(b - y)), 0\}, \tag{4.3.21}$$

where $\alpha > 0$, γ and $b > 0$ are constants. Here α controls the maximum layer thickness, γ is a measure of the front steepness, and b gives the initial y coordinate of the outcropping. This profile has the advantage that its y derivatives are simply multiples of $\exp(\gamma(b-y))$, which makes the mathematical details more tractable. The necessary integrals may then be written

$$I_1^{mn} = \alpha\gamma\mathcal{J}_1^{mn}[\exp(\gamma(b - y))], \tag{4.3.22}$$

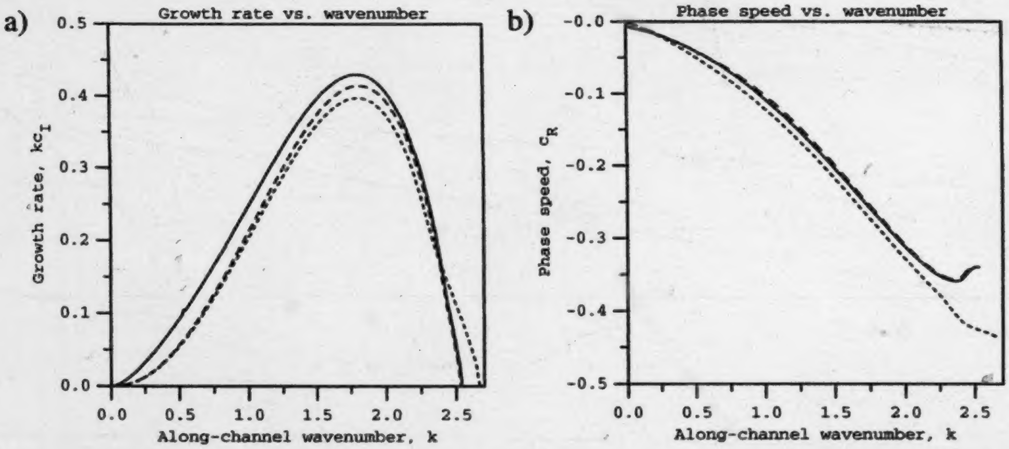

Figure 4.9: a) Growth rates and b) phase speeds for the exponential front, computed with the spectral technique for $\nu = -1.0$ (dashed lines), $\nu = 0$ (solid lines) and $\nu = 1.0$ (dotted lines). Here $L = 20.0$, $b = 10.0$, and $\alpha = \gamma = N = 1.0$. Phase speeds are only plotted for nonzero growth rates.

$$I_2^{mn} = \alpha^2\gamma^3(\mathcal{J}_1^{mn}[\exp(\gamma(b-y))] - 2\mathcal{J}_1^{mn}[\exp(2\gamma(b-y)))], \qquad (4.3.23)$$

$$I_3^{mn} = \alpha^2\gamma(\mathcal{J}_1^{mn}[\exp(\gamma(b-y))] - \mathcal{J}_1^{mn}[\exp(2\gamma(b-y)))], \qquad (4.3.24)$$

$$I_4^{mn} = \alpha^2\gamma^2\mathcal{J}_2^{mn}[\exp(2\gamma(b-y))]. \qquad (4.3.25)$$

The integrations were performed symbolically in Maple, and the resulting expressions evaluated for all necessary pairs m, n. The matrix of interaction coefficients thus computed then served as input for our eigenproblem solver. In the case of the exponential front a number of aphysical modes appeared, whose growth rates were not necessarily smaller than those of the physical modes. Without the advantage of a semicircle theorem, these spurious modes had to be eliminated by examining their spatial structure. For relatively small topographic slopes (i.e. absolute value no larger than the maximum frontal slope) we were also guided by the notion, discussed in Barth (1989b), that the phase speed of the most unstable mode should lie within the range of mean flow speeds. Typically the expansion (4.3.1), (4.3.2) was truncated at 160 modes.

In this section we adopt the following parameters, $L = 20.0$, $b = 10.0$, and

ν	$\hat{k}$	$\sigma_{\max}$	c_R	λ^* (km)	T_e^* (h)	c_R^* (cm/s)
-1.0	1.82	0.41	-0.27	66.6	18	10.5
0.0	1.80	0.43	-0.27	67.3	18	10.5
1.0	1.81	0.40	-0.29	67.0	19	11.3

Table 4.2: Instability characteristics for the exponential profile, predicted by linear theory.

ν	$\hat{k}$	$\sigma_{\max}$	c_R	λ^* (km)	T_e^* (h)	c_R^* (cm/s)
-1.0	1.26	0.23	-0.34	96.2	33	13.3
0.0	1.26	0.28	-0.38	96.2	28	14.8
1.0	1.57	0.17	-0.61	77.2	45	23.8

Table 4.3: Instability characteristics for the exponential profile, resulting from direct numerical simulation of the governing equations.

$\alpha = \gamma = N = 1.0$. In Fig. 4.9 we plot growth rates and phase speeds for the exponential front, obtained with the Galerkin technique. The effect of linearly sloping topography is shown by setting $\nu = -1.0$, 0.0 and 1.0. Growth rate curves are very similar for all three values of the bottom slope. While surface- and bottom-intensified modes can be identified in vertical sections of the perturbation (not shown), they are not distinct in wavenumber space as was the case with the wedge front. Table 4.2 lists the most unstable wavenumber $\hat{k}$, the associated growth rate $\sigma_{\max}$ and phase speed c_R, as well as the dimensional wavelength λ^* and e-folding time T_e^*. Instability characteristics for the same parameter values obtained from direct numerical simulation are given in Table 4.3. Simulations were performed employing the fully nonlinear governing equations, where the lower layer was initially quiescent except for a small, random perturbation. Dimensional quantities are based on scalings appropriate for the California Current, discussed below.

Both the spectral technique and direct simulation predict that the maximum

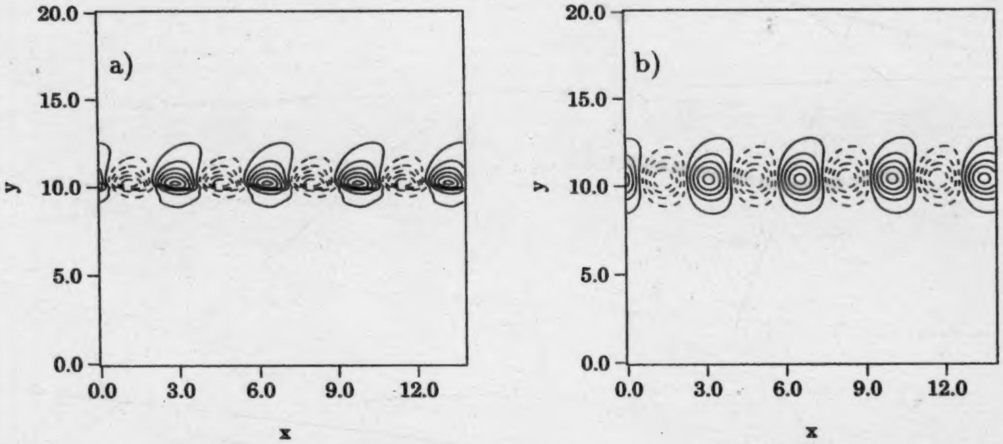

Figure 4.10: Lower layer pressure perturbation associated with the exponential front at a) $z = 0$ and b) $z = -1$ obtained with the spectral technique. Here $L = 20.0$, $b = 10.0$, $\alpha = \gamma = 1.0$ and $\nu = -1.0$. The solution is plotted at the most unstable wavenumber, $k = 1.82$ using 160 expansion modes. The contour extrema and intervals are a) -5.4×10^{-2}, 5.4×10^{-2}, 9.0×10^{-3} and b) -4.7×10^{-3}, 4.7×10^{-3}, 9.4×10^{-4}, respectively. Four along-channel wavelengths are shown. Dashed lines correspond to negative values.

growth rate occurs for $\nu = 0$. However the trend is much more pronounced in the simulations. Quantitatively, agreement with respect to growth rates and phase speeds is less than satisfactory. The simulations also show a significant increase in $\hat{k}$ for $\nu = 1.0$, although this effect could have been exaggerated by our particular choice of channel length. The reason for the discrepancy could be very slow convergence, as discussed in the previous section. This would indicate that a more suitable set of basis functions should be adopted. The source of the error could also lie in non-differentiability of h_0 across the outcropping and the higher derivatives involved in the eigenproblem, compared with the CS-PG model. Difficulty in dealing with the frontal outcropping was also noted by Paldor and Ghil (1991) in a linear instability calculation applicable to coastal currents.

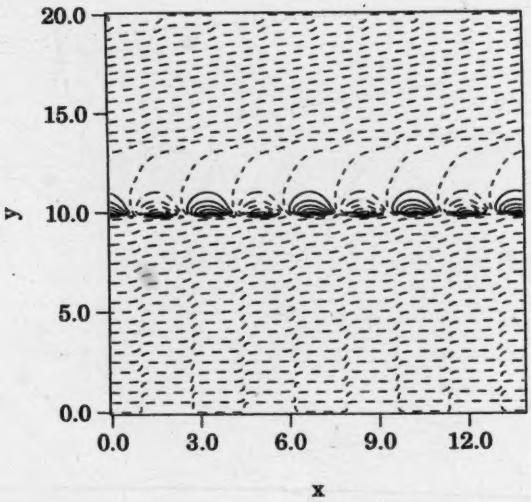

Figure 4.11: Upper layer thickness perturbation obtained with the spectral technique, corresponding to Fig. 4.10. The contour extrema and intervals are -0.51, 0.51, 8.5×10^{-2}, respectively. Four along-channel wavelengths are shown. Dashed lines correspond to negative values.

At this point we discuss the perturbation spatial structure for $\nu = -1.0$, which corresponds to the configuration of an upwelling current over a sloping continental shelf. Solutions obtained with the Galerkin method are depicted in Figs. 4.10 and 4.11 at $k = 1.82$. The structure of the anomalies that emerged during the course of a numerical simulation is shown in Figs. 4.12 and 4.13. While instability characteristics between the two solution techniques deviate somewhat, agreement with respect to spatial distribution seems quite good. The perturbation is strongly surface-intensified, increasing in amplitude by a factor of over 10 from $z = -1$ to $z = 0$. The upper-layer perturbation also has a much greater amplitude than lower-layer anomalies. In analogy with the CS-PG/SW-PG models, the highest amplitudes and cross-channel gradients occur near the outcropping. The crescent shape of the anomalies, and their orientation with respect to the direction of mean flow, are consistent with the solutions obtained by Barth (1989b) and Barth (1994).

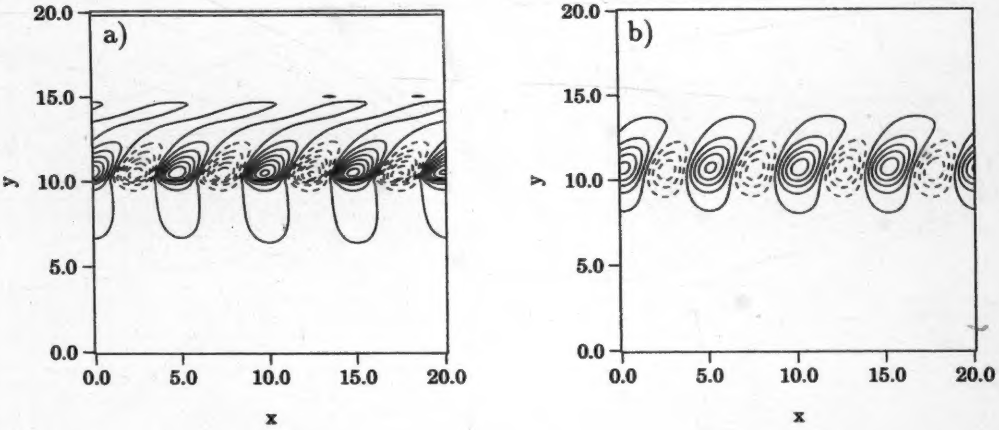

Figure 4.12: Lower layer pressure perturbation at a) $z = 0$ and b) $z = -1$ at $t = 80$ in a direct numerical simulation. These plots should be compared with Fig. 4.10. The contour extrema and intervals are a) -6.2×10^{-2}, 6.4×10^{-2}, 9.0×10^{-3} and b) -7.7×10^{-3}, 9.4×10^{-3}, 1.9×10^{-3}, respectively. Dashed lines correspond to negative values.

To allow discussion of the instability in dimensional terms, we apply the model to the unstable upwelling current described in Barth (1994). Although the author employed the Boussinesq equations with a variable buoyancy frequency, the surface-intensified jet comprised a small fraction of the total depth, and was separated from the ambient fluid by a sharp density front. In accordance with Barth (1994), we adopt the following scalings, $h_* = 90$ m, $H = 250$ m, $f_0 = 10^{-4}$ s^{-1} and $g' = 0.025$ m/s^2. This determines the depth ratio, upper-layer Rossby radius and dynamic lengthscale, respectively, $\delta = 0.36$, $R_1 = 15$ km and $L_* = 19.3$ km. If we examine the $\nu = -1.0$ case described above, then the dimensional buoyancy frequency and bottom slope are $N_* \approx 0.01$ s^{-1} and $\dfrac{\mathrm{d}h_B^*}{\mathrm{d}y^*} \approx -5 \times 10^{-3}$, respectively, both estimates reasonably consistent with Barth (1994).

The dominant wavelength λ^*, e-folding time T_e^* and phase speed c_R^* are thus computed for the linear theory predictions and simulation results in Tables 4.2 and

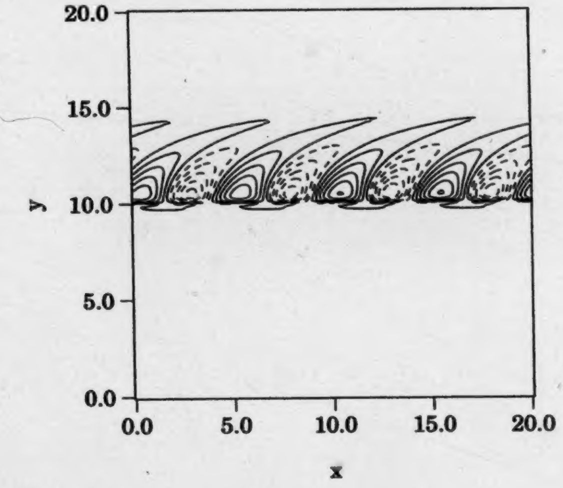

Figure 4.13: Upper layer thickness perturbation at $t = 80$ in a direct numerical simulation. This plot corresponds to Fig. 4.12 and should be compared with the theoretical prediction, Fig. 4.11. The contour extrema and intervals are -6.0×10^{-2}, 5.1×10^{-2} and 9.2×10^{-3}, respectively. Dashed lines correspond to negative values.

4.3, respectively. Barth (1994) reports a fastest-growing wavelength of 92.4 km and a relatively slow propagation speed of 10 cm/s. These values were in agreement with observed instabilities off the coast of Oregon. Our simulation results suggest $\lambda^* =$ 96.2 km, very close to Barth's estimate, and significantly better than our theoretical prediction of 66.6 km. With regard to the phase speed of the perturbation, the Galerkin technique yields $c_R^* = 10.5$ cm, while direct simulation gives 13.3 cm/s. The e-folding period determined by Barth (1994) was about 3.5 days, considerably higher than either of the T_e^* values we have listed. The reason for this departure requires further investigation.

Further evolution of an unstable current is similar to the homogeneous case, as described in R97, RS99a and RS99b. Growth rates tend to be higher and lengthscales smaller, however, than those associated with the FG-SW model. As in chapter 2, the reason is the increased baroclinicity of the two-layer system resulting from continuous stratification of the ambient fluid. Frontal deformation typically leads to development

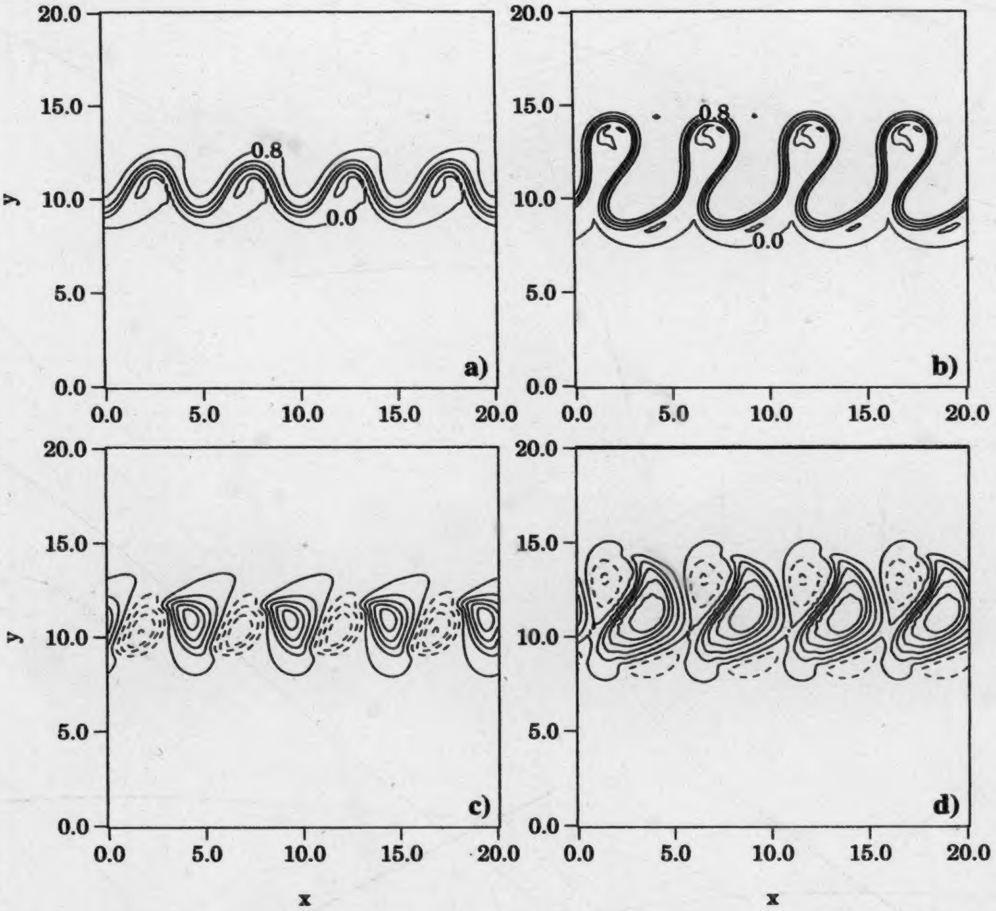

Figure 4.14: Total upper-layer thickness at a) $t = 100$ and b) $t = 110$ and lower-layer pressure at $z = 0$ at c) $t = 100$ and d) $t = 110$ of the numerical simulation. These plots show the initial stages of nonlinear growth. The contour extrema and intervals are a) 0, 1.0, 0.2, b) 0, 1.0, 0.2 c) -0.4, 0.4, 0.1 and d) -0.4, 1.2, 0.2, respectively. Dashed lines correspond to negative values.

of isolated patches of upper-layer fluid (anticyclonic eddies) or voids in the upper layer (interpreted as cyclonic eddies). Evolution of unstable axisymmetric currents in the FG-SW limit is also described in the next section.

Here we would like to provide an interpretation of early nonlinear development, in particular the dynamics of eddy formation. During the linear stage of growth, positive and negative anomalies are identical, except for their sign. This is evident in Fig. 4.12a, at $t = 80$ of the numerical simulation. Any given pair of lower-layer pressure cells is a dipole, whose tendency is to self-advect in the cross front direction. However, since each cell belongs to two dipoles with opposite orientation, the net effect is zero cross front motion. In Fig. 4.14 we plot the upper- and lower-layer streamfunctions at $t = 100$ and 110, representing the earliest nonlinear behavior. As the instability ensues, lower-layer pressure cells deform and elongate to allow dipole motion away from the front (Figs. 4.14c and d). Advection by these local dipole structures deforms the front into a meandering pattern (Figs. 4.14a and b). Within each positive upper-layer anomaly, shear instability causes rapid pinch-off, thus forming eddies (Pavía 1992; Reszka and Swaters 1999a). At this point the dipole character of lower-layer anomalies is lost and upper-layer eddies begin to interact with each other.

As a final note, we point out that Barth (1994) found two distinct modes of instability. The first, discussed above, was identified as the traditional baroclinic instability present in QG dynamics. The second mode, called the frontal mode, had considerably smaller lengthscales and higher growth rates than the first mode. It was argued that the usual baroclinic mode still emerged after a period of time because the frontal mode did not alter the frontal structure significantly enough. Nevertheless, the frontal mode was identified in both numerical simulations and satellite observations of the California Current, and is likely to provide additional cross-front mixing. We have not detected this second mode of instability, in our linear analysis or simulation using the governing equations. It is likely that this mode was filtered out by our assumption of leading-order geostrophy. Barth (1994) noted that the frontal mode is typically eliminated in shallow water models if velocity in the momentum equations is replaced by its geostrophic counterpart, as was done in Barth (1989b).

4.4 Axisymmetric currents

We employed the FG-SW model in a series of numerical simulations in order to explore the instability of a buoyant axisymmetric current, in a configuration similar to the laboratory experiments of CL (see section 1.3).

4.4.1 Linear Stability

The linear stability problem in polar coordinates is briefly examined. With $\kappa = 1$, $\beta = 0$, equations (4.1.91), (4.1.92) are written in terms of polar coordinates (r, θ), where $r = \sqrt{x^2 + y^2}$ and $\tan(\theta) = y/x$. The domain will be the annulus $\Omega = \{(r,\theta) | r_I \le r \le r_O\}$, where r_I^*, r_O^* and Ω^* will be the dimensional analogues of r_I, r_O and Ω, respectively. Previous numerical studies involving (4.1.91), (4.1.92) have shown that along-front topographic variations are not necessary for the destabilization of a steady flow (Reszka and Swaters 1999a).

Assuming topography of the form $h_B = h_B(r)$, the governing equations may be written as

$$h_t = J(h, \varphi + h\Delta h + \tfrac{1}{2}\nabla h \cdot \nabla h) + Q_1, \tag{4.4.1}$$

$$(\Delta\varphi + h)_t = J(\Delta\varphi + h, \varphi) + \frac{1}{r}\frac{\mathrm{d}h_B}{\mathrm{d}r}\varphi_\theta + Q_2, \tag{4.4.2}$$

where $\nabla = (\partial_r, \partial_\theta / r)$, $\Delta = \partial_r(r\partial_r)/r + \partial_\theta^2/r^2$, and $J(A, B) = (A_r B_\theta - A_\theta B_r)/r$. Radial velocities in the upper- and lower-layer are now defined in terms of the streamfunctions as

$$u_{1r} = -\frac{1}{r}\frac{\partial h}{\partial \theta} \quad \text{and} \quad u_{2r} = -\frac{1}{r}\frac{\partial \varphi}{\partial \theta}, \tag{4.4.3}$$

respectively. Upper- and lower-layer azimuthal velocities (positive in the counter-clockwise direction) are given by

$$u_{1\theta} = \frac{\partial h}{\partial r} \quad \text{and} \quad u_{2\theta} = \frac{\partial \varphi}{\partial r}. \tag{4.4.4}$$

In the absence of sources and sinks, $h = h_0(r)$, $\varphi = \varphi_0(r)$ comprise an exact steady solution to (4.1.91)–(4.1.92), for sufficiently smooth functions h_0, φ_0. We consider a perturbed steady state, by making the substitution

$$(h,\varphi) = (h_0(r),0) + (h',\varphi')(r,\theta,t), \tag{4.4.5}$$

where $|h'|, |\varphi'| \ll 1$. In order to focus on the baroclinic aspect of the problem, there is no imposed mean flow in the lower layer, i.e. $\varphi_0 \equiv 0$.

The interface does not have to outcrop, however if it does, we will assume the outcropping is located at $r = b \in (r_I, r_O)$. If $h > 0$ for $r \in [r_I, b)$, then we shall consider h to be defined but zero for $r \in [b, r_O]$. If $h > 0$ for $r \in (b, r_O]$, then we shall consider h to be defined but zero for $r \in [r_I, b]$. Thus, h is defined and continuous on the entire domain, although its radial derivative may be discontinuous at the outcropping. Then, dropping the primes, the linearized stability equations become

$$\begin{aligned} rh_t - \frac{\mathrm{d}h_0}{\mathrm{d}r}\varphi_\theta + \Bigg[\frac{\mathrm{d}}{\mathrm{d}r}\left(h_0\frac{\mathrm{d}^2h_0}{\mathrm{d}r^2}\right) &+ h_0\frac{\mathrm{d}}{\mathrm{d}r}\left(\frac{1}{r}\frac{\mathrm{d}h_0}{\mathrm{d}r}\right) \\ &- h_0\frac{\mathrm{d}h_0}{\mathrm{d}r}\Delta - \left(\frac{\mathrm{d}h_0}{\mathrm{d}r}\right)^2\partial_r\Bigg] h_\theta = 0, \end{aligned} \tag{4.4.6}$$

$$r(\Delta\varphi + h)_t - \frac{\mathrm{d}}{\mathrm{d}r}(h_B + h_0)\varphi_\theta = 0. \tag{4.4.7}$$

The upper-layer perturbation energy equation is formed as follows. Equation (4.4.6) is multiplied by h/r and integrated over the domain. Employing integration by parts, the result may be written

$$\iint_\Omega rhh_t dr d\theta = \iint_\Omega \frac{\mathrm{d}h_0}{\mathrm{d}r}\varphi_\theta h dr d\theta + \iint_\Omega h_0\left(\frac{\mathrm{d}^2h_0}{\mathrm{d}r^2} - \frac{1}{r}\frac{\mathrm{d}h_0}{\mathrm{d}r}\right)h_r h_\theta dr d\theta, \tag{4.4.8}$$

where we have used the azimuthal periodicity of all fields and the fact that the perturbation vanishes on the radial boundaries.

Redefining the integral operator

$$\langle(*)\rangle = \int_0^{2\pi} (*) r d\theta, \tag{4.4.9}$$

and using (4.4.3) and (4.4.4), we obtain

$$\frac{\mathrm{d}}{\mathrm{d}t}\int_{r_I}^{r_O} \tfrac{1}{2}\langle h^2\rangle dr = -\int_{r_I}^{r_O} r\frac{\mathrm{d}}{\mathrm{d}r}\left(\frac{1}{r}\frac{\mathrm{d}h_0}{\mathrm{d}r}\right)\langle h_0 u_{1r} u_{1\theta}\rangle dr - \int_{r_I}^{r_O} \frac{\mathrm{d}h_0}{\mathrm{d}r}\langle u_{2r} h\rangle dr, \tag{4.4.10}$$

where $\langle h_0 u_{1\theta} u_{1r} \rangle$ represents the along-coast perturbation Reynolds stress. Our interpretation of this equation is similar to that of Swaters (1993) for the analogous result in rectangular coordinates. Assume that baroclinic processes dominate (the first term on the right-hand side is small) and that the current thickness decreases offshore, i.e. $\mathrm{d}h_0/\mathrm{d}r < 0$. Growth of perturbations (positive left-hand side) requires that, on average, $\langle u_{2r} h \rangle$ and $\mathrm{d}h_0/\mathrm{d}r$ are negatively correlated. Therefore, there must be a net offshore flux of warm anomalies ($h > 0$) by the geostrophic velocity u_{2r}.

A necessary condition for instability may be derived by first making the normal mode assumption with respect to azimuthal flow,

$$(h, \varphi) = (\tilde{h}, \tilde{\varphi})(r) \exp[in(\theta - ct)] + \text{c.c.}, \tag{4.4.11}$$

where n is the (integer) azimuthal wavenumber. Then, dropping the tildes, we have

$$\begin{aligned} crh + \frac{\mathrm{d}h_0}{\mathrm{d}r}\varphi \; - \; & \frac{\mathrm{d}}{\mathrm{d}r}\left(h_0 \frac{\mathrm{d}^2 h_0}{\mathrm{d}r^2}\right) h - h_0 \frac{\mathrm{d}}{\mathrm{d}r}\left(\frac{1}{r}\frac{\mathrm{d}h_0}{\mathrm{d}r}\right) h \\ + \; & h_0 \frac{\mathrm{d}h_0}{\mathrm{d}r}\left[h_{rr} + \frac{1}{r}h_r - \frac{n^2}{r^2}h\right] + \left(\frac{\mathrm{d}h_0}{\mathrm{d}r}\right)^2 h_r = 0, \end{aligned} \tag{4.4.12}$$

$$c\left(r\varphi_{rr} + \varphi_r + \frac{1}{r}\varphi_{\theta\theta} + rh\right) + \frac{\mathrm{d}}{\mathrm{d}r}(h_B + h_0)\varphi = 0. \tag{4.4.13}$$

Similarly to Swaters (1993), we define a function $\widehat{h}(r)$ by

$$h(r) = \frac{\mathrm{d}h_0}{\mathrm{d}r}\widehat{h}(r), \tag{4.4.14}$$

substitution of which will simplify the algebraic expressions below. We multiply the complex conjugate of (4.4.12) by $r\widehat{h}$ and integrate over $r_I < r < r_O$. After integration by parts, using the fact that the perturbation (and therefore $\widehat{h}$) vanishes on the boundaries, the result is

$$\begin{aligned} & \int_{r_I}^{r_O} h_0 \left(\frac{\mathrm{d}h_0}{\mathrm{d}r}\right)^2 \left(\frac{n^2}{r}|\widehat{h}|^2 + r|\widehat{h}_r|^2\right) dr \\ - & \int_{r_I}^{r_O} \left(c^* r^2 \frac{\mathrm{d}h_0}{\mathrm{d}r} + \frac{1}{r}h_0\left(\frac{\mathrm{d}h_0}{\mathrm{d}r}\right)^2\right)|\widehat{h}|^2 dr = \int_{r_I}^{r_O} r\frac{\mathrm{d}h_0}{\mathrm{d}r}\varphi^* \widehat{h} dr. \end{aligned} \tag{4.4.15}$$

Similarly, multiplying (4.4.13) by φ^*/c (assuming $|c|^2 > 0$), integrating with respect to r, and using integration by parts, we obtain

$$\int_{r_I}^{r_O} \left(r|\varphi_r|^2 + \frac{1}{r}|\varphi_\theta|^2 \right) dr - \frac{1}{c} \int_{r_I}^{r_O} \frac{\mathrm{d}}{\mathrm{d}r}(h_B + h_0)|p|^2 dr = \int_{r_I}^{r_O} r \frac{\mathrm{d}h_0}{\mathrm{d}r} \varphi^* \widehat{h} dr. \quad (4.4.16)$$

If we subtract (4.4.16) from (4.4.15), substitute in $c = c_R + ic_I$, and take the imaginary part of the resulting equation, then

$$c_I \int_{r_I}^{r_O} \left(r^2 \frac{\mathrm{d}h_0}{\mathrm{d}r} |\widehat{h}|^2 - \frac{1}{|c|^2} \frac{\mathrm{d}}{\mathrm{d}r}(h_B + h_0)|\varphi|^2 \right) dr = 0. \quad (4.4.17)$$

Let us assume that we are dealing with a coastally-trapped current, such that the frontal thickness decays away from the shore, $\mathrm{d}h_0/\mathrm{d}r < 0$. Then

$$\frac{\mathrm{d}h_B}{\mathrm{d}r} > -\frac{\mathrm{d}h_0}{\mathrm{d}r} \text{ for all } r \in (r_I, r_O) \quad (4.4.18)$$

is a sufficient condition for stability. Conversely, a necessary condition for instability is that

$$\frac{\mathrm{d}h_B}{\mathrm{d}r} \leq -\frac{\mathrm{d}h_0}{\mathrm{d}r}, \quad (4.4.19)$$

for at least one $r \in (r_I, r_O)$. This result is analogous to the one derived in Swaters (1993) (i.e. (4.2.57)), and as we discuss in section 4.4.7 it is consistent with the QG necessary condition for instability (Pedlosky 1964) that the PV gradients be of opposite sign in the two layers.

4.4.2 Numerical details

The governing equations (4.1.91)–(4.1.92) with $\kappa = 1$ and $\beta = 0$ were solved in Cartesian coordinates, using the finite difference scheme described in Appendix B. The annular domain was centered at the origin, with inner and outer radii, respectively, $r_I = 13$ cm and $r_O = 45$ cm, as in CL. Since the domain was not simply-connected, we utilized a Conjugate Gradient elliptic solver (Kincaid and Cheney 1996), instead of one of the MUDPACK routines as in other simulations. Two sets of simulations were performed, one that did not include an upper-layer source (SERIES 1), and one where the source strength was $\overline{Q_1^*} = 10\ \mathrm{cm^3/s}$ (SERIES 2). In both cases, a sink was not prescribed in the lower layer (i.e. $Q_2 \equiv 0$).

In all our simulations we assume $h_* = 3.5$ cm, $H = 13.0$ cm, $g' = 2.2\ \mathrm{cm/s^2}$ and $f_0 = 3.0$ rad/s, which are mid-range parameter values in the experiments of CL. The depth fraction, upper-layer Rossby radius and dynamic lengthscale are then $\delta = 0.27$, $R_1 = 0.93$ cm and $L_* = 1.28$ cm, respectively. The upper layer streamfunction was held fixed at the inner boundary throughout each simulation. Despite the fact that the domain is not simply-connected, explicit use of a circulation integral is not required for consistent boundary conditions, since the upper-layer evolution equation is itself a statement of mass conservation, while the lower layer streamfunction was held fixed (at zero) at both lateral boundaries.

Some of our modelling assumptions are violated in the CL experiments, and consequently, direct comparisons should be made with caution. In particular, since we assume that the velocity is geostrophic, an imposed source does not induce spreading of the surface layer. As we can only simulate lateral growth after instability has occurred, we impose a current profile as an initial condition, such that the current width is consistent with experimental values at the onset of instability. A source of upper-layer fluid does, however, allow us to explore the transition to instability while the fluid depth (and therefore Rossby radius) is increasing. Therefore in SERIES 2 a source of buoyant fluid is introduced, with the same strength as in CL.

Another point to remember is that, in the experiments of CL, the inteface often touches the shallow part of the topography before instability occurs, which undoubtedly affects the ensuing dynamics. Contact with a bottom boundary induces drag and Ekman draining, both processes being absent in the FG-SW model. Our derivation also assumes that the lower layer is everywhere thicker than the upper layer, which is clearly not the case when the upper layer and topography meet. Our results are therefore most relevant to the laboratory trials in which the buoyant fluid did not touch the bottom. However, it should be stressed that the results of CL do not show

simulation	$\overline{Q_1^*}$ (cm^3/s)	r_S (cm)	λ^* (cm)
flat1	0	N/A	7.2
step1-I	0	20.0	4.5
step1-O	0	22.9	3.6
slope1-I	0	20.0	6.0
slope1-O	0	22.9	6.5
flat2	10.0	N/A	7.2
step2-I	10.0	20.0	5.1
step2-O	10.0	22.9	3.6
slope2-I	10.0	20.0	6.5
slope2-O	10.0	22.9	7.2

Table 4.4: Configuration of numerical simulations and observed dominant wavelength, pertaining to axisymmetric currents in an annulus domain. For simulations designated "step" or "slope", r_S is the radius at which the topography deepens abruptly or becomes linearly sloping, respectively. The step has a depth of 13.0 cm while the sloping topography has a radial gradient of 0.5. Other symbols are defined in the text.

a marked difference between these two dynamical regimes.

Where it is convenient, our discussion will be in terms of polar coordinates (r, θ). The initial, non-dimensional frontal profile is similar to (4.3.21) and is given by

$$h_0(r) = \alpha \max\{1 - \exp(\gamma(r - b)), 0\}, \tag{4.4.20}$$

We choose the parameter values $\gamma = 0.5$, $\alpha = 1.021$ and $b = 17.891$. The maximum depth of the upper-layer jet is then 3.5 cm, and occurs at the coast. The jet width is about 10 cm and its maximum azimuthal speed is approximately -1 cm/s. Our simulations are designated with the names "flat", "step" and "slope", which refer to the three kinds of topography we consider. The names and their corresponding configurations are given in Table 4.4. The number within each name refers to the absence (1) or presence (2) of the source term. Finally, there are two possible locations, $r = r_S$, of the step or top of the slope. These are on the inner side (designated "I") of the front, about two Rossby radii away from the outcropping, or on the outer side (designated "O") of the front, exactly at the outcropping. The step will also be referred to as a ridge, or shelf break, while the region interior of the step (or slope) will be identified as the continental shelf.

4.4.3 Description of the instability

Here we give a detailed description of simulation step1-I, which was typical, and which will serve as the standard case for later comparisons. In Fig. 4.15 we plot the dimensional upper-layer thickness, at (dimensional) times 0, 50, 75 and 100 s, while the corresponding contour plots of non-dimensional upper-layer pressure are displayed in Fig. 4.16. We note that one rotation period corresponds to 4.2 s in all the simulations described here. Initially, a steady axisymmetric current profile is imposed on the upper-layer streamfunction (Fig. 4.15a). There is no mean flow in the lower layer, however we seed its pressure field with a small-amplitude random perturbation (Fig. 4.16a). The initial perturbation amplitude is scaled so that its area-integrated kinetic energy is 4 orders of magnitude smaller than the area-integrated kinetic energy of the current, i.e.

$$\iint_\Omega |\nabla\varphi|^2 r dr d\theta = 10^{-4} \iint_\Omega h|\nabla h|^2 r dr d\theta. \tag{4.4.21}$$

This allows the most unstable mode to develop before nonlinear effects become important.

After 50 s, the dominant mode has emerged and the outcropping is deformed by a wavelike disturbance. Wave crests are seen to break backwards in relation to the mean flow of the jet, behaviour consistent with the findings of CL and (Griffiths and Linden 1981) (Fig. 4.15b). The lower layer exhibits a regular pattern of high- and low-pressure anomalies along the shoreward side of the outcropping (Fig. 4.16b). Each pair of pressure cells is a dipole, whose natural tendency is to self-advect in a

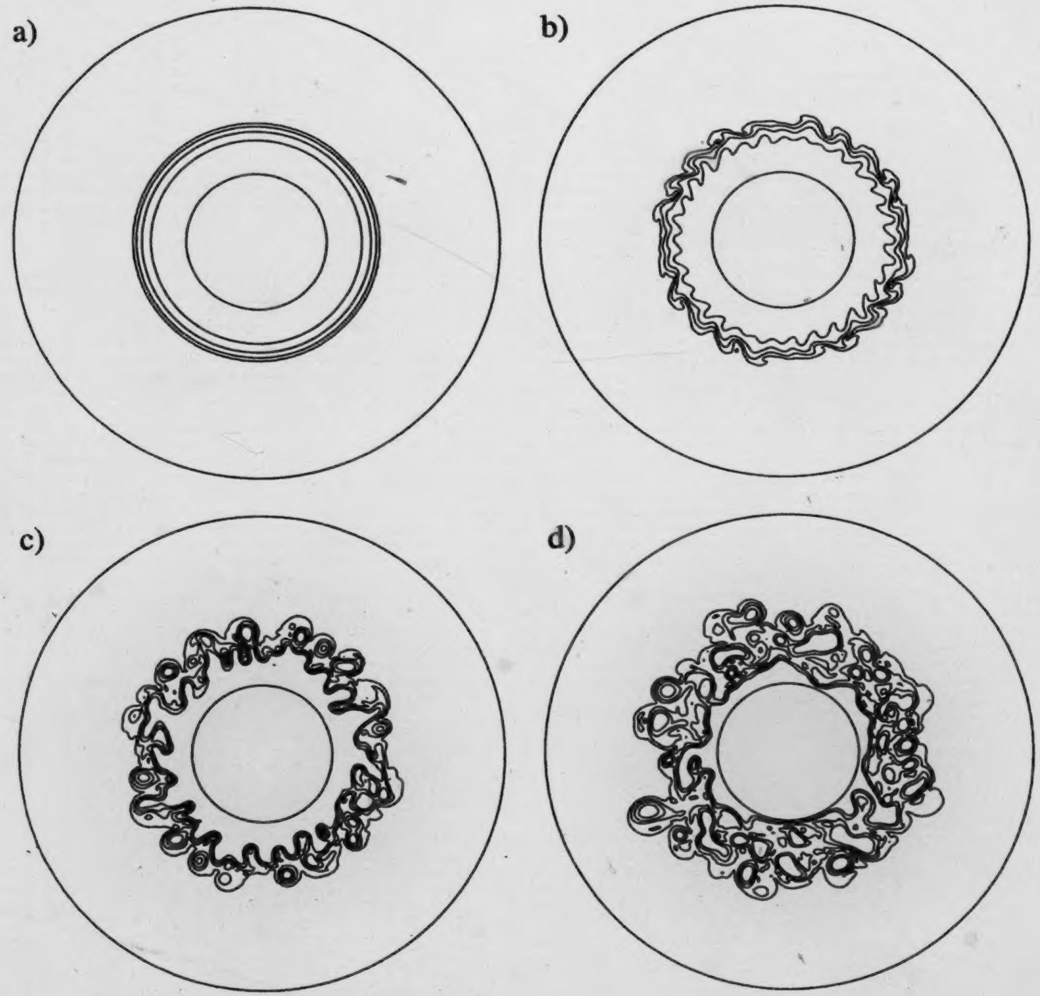

Figure 4.15: Dimensional upper-layer thickness in simulation step1-I at a) 0, b) 50, c) 75 and d) 100 s. The contour range is 0 to 3.5 cm and the contour interval is 0.875 cm. The location of the topographic step is along the outcropping (i.e. outer edge of the current) in (a).

cross-front direction. Growth of the upper-layer meanders continues and some of the waves merge with their neighbors.

The first eddies appear at $t \approx 62$ s, however these are quickly reabsorbed by the current. Numerous coherent upper-layer eddies appear in Fig. 4.15b, as they begin

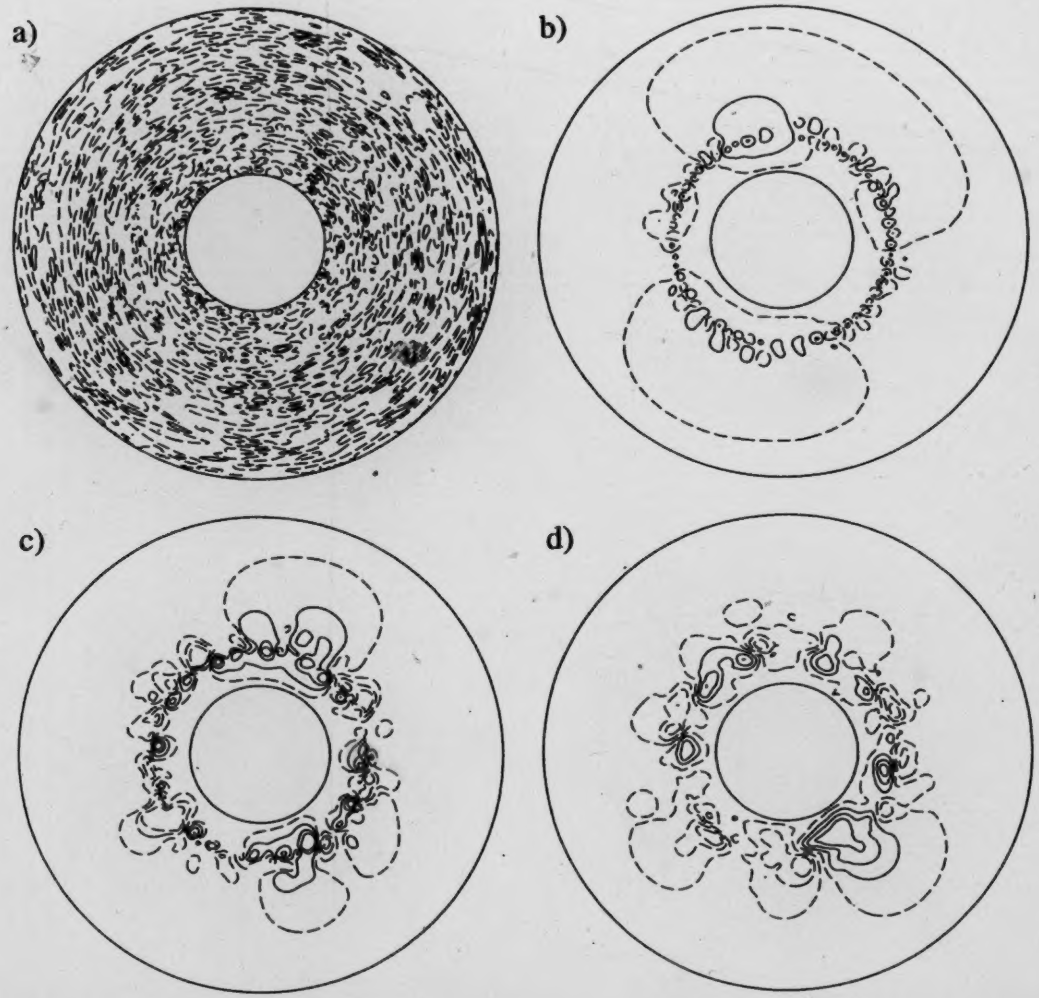

Figure 4.16: non-dimensional lower-layer pressure in simulation step1-I at a) 0, b) 50, c) 75 and d) 100 s. The contour extrema and intervals are, respectively, a) -1.3×10^{-3}, 1.4×10^{-3}, 4.5×10^{-4}, b) -0.43, 0.44, 0.145, c) -0.96, 0.96, 0.32, d) -2.0, 2.8, 0.8. The radial perturbation maximum in (b) marks the location of the topographic step, $r = r_S$.

to move away from the current. By this time the lower layer is showing signs of the upscale energy cascade, with many adjacent pressure anomalies merging together. Upper layer lenses continue to pinch off, and are often observed to merge together or split apart. Elongated eddies that merge with protrusions of the main body of the current appear as filaments (Fig. 4.15d).

At $t \approx 100$ s the buoyant flow may best be described as a turbulent eddy field, whose individual features are advected around by large, prominent gyres which now dominate the ambient fluid. Eddy generation slows down as the current becomes very narrow, however instabilities of the frontal region still occur near the end of the simulation, at $t = 125$ s. CL observed that buoyant fluid reached the outer tank wall faster with ridge topography (on the interior side of the front) than with a flat bottom. However, we did not find the rate of spreading to differ significantly in these two cases. At late times the flow is reminiscent of geostrophic turbulence. A discussion of geostrophic turbulence in the two-layer FG limit may be found in Tang and Cushman-Roisin (1992).

The behavior of the evolving current is markedly different when the ridge lies at the same radius as the outcropping. The upper- and lower-layer streamfunctions for simulation step1-O at $t = 86$ s are plotted in Fig. 4.17. The instability seems confined to the shelf region, and upper-layer meanders do not protrude as far in the radial distance as they do in step1-I at the same stage of instability. The same phenomenon was observed by CL, and was attributed to the greater energy requirement associated with motion across the ridge. Crossing the shelf break induces a significant spin up (spin down) of the ambient fluid due to the stretching (compression) of vortex tubes. We believe this is the mechanism that traps fluid on the shelf in our simulations, until the current has released enough potential energy to allow robust radial motions across the high topographic PV gradient. We note that, on a finite discretization grid, the topographic step is not a true discontinuity, and appears as a very steep slope of width Δx. Eventually, meanders pinch off forming eddies, and the spreading of the buoyant fluid progresses similarly to step1-I.

All of our SERIES 1 simulations show eddy detachment following the initial growth of meanders, with the exception of simulation step1-O where a noticeable delay occurs (as described above). In the case of flat topography, however, CL found that

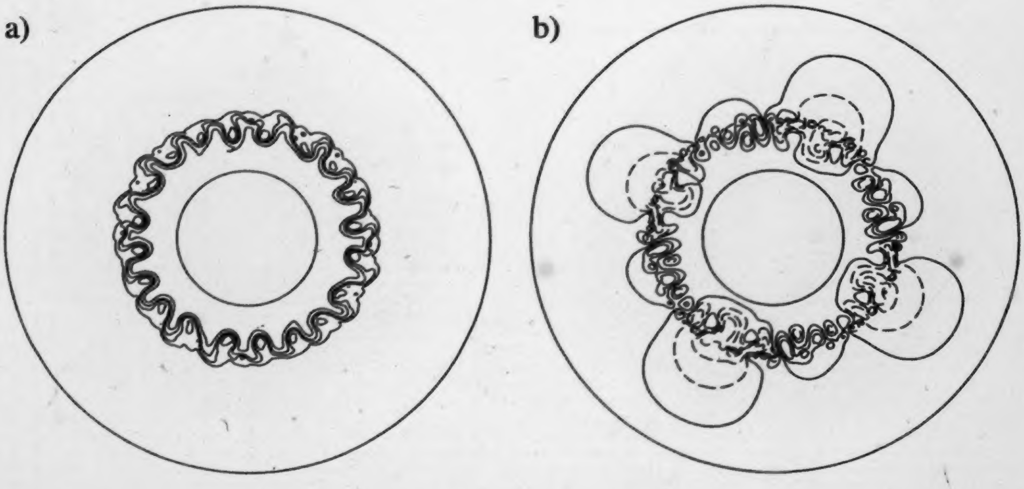

Figure 4.17: a) Dimensional upper-layer thickness and b) non-dimensional lower-layer pressure in simulation step1-O at 86 s. The contour extrema and intervals are, respectively, a) 0.0 cm, 3.5 cm, 0.875 cm, and b) -0.45, 0.45, 0.15.

eddies generated by the instability did not detach and move away from the current. A possible explanation for this discrepancy is that the source flux in CL's experiments induced a continual spreading of the current, thus making it more likely that developing eddies remain attached. The turbulence caused by this constant injection of fluid may also have contributed to an abrupt saturation of the instability, which suppressed eddy pinch-off. On the other hand, we find that growing eddy features remain attached and are subsequently reabsorbed in some of our source flow simulations (SERIES 2, described below). It is possible, therefore, that deepening of the upper layer plays a key role in this process.

4.4.4 Some diagnostics

In order to quantify the amount of offshore spreading due to the instability, we have computed the average radial moment of the buoyant fluid, defined by

$$\overline{R}(t) = \frac{1}{V} \iint_{\Omega} r^2 h \, dr \, d\theta, \tag{4.4.22}$$

where $h(r,\theta,t)$ is the total upper-layer thickness and V is the (constant) volume of the upper layer,

$$V = \iint_{\Omega} rh\,dr\,d\theta. \tag{4.4.23}$$

The integral in (4.4.22) is essentially the average radius over the volume of the buoyant fluid, and thus can account for an offshore mass transport whether or not the average position of the outcropping shifts. We note that $2(\overline{R} - r_I)$ is a measure of the (non-dimensional) width of the current, taking its thickness into account.

In Fig. 4.18a we plot $\overline{R}^*(t^*)$, the dimensional version of $\overline{R}(t)$, for the five simulations in SERIES 1. Lateral growth of the jet is similar for simulations step1-I and flat1, suggesting that step topography plays a minor role if it is located shoreward of the outcropping. Simulations slope1-I and slope1-O demonstrate a somewhat more vigorous instability and faster spreading of buoyant fluid. The most dramatic response however, is seen for simulation step1-O, in which radial spreading as measured by $\overline{R}^*$ is significantly delayed.

A similar trend is visible in Fig. 4.18b, a plot of the volume-integrated upper-layer perturbation kinetic energy,

$$\widetilde{KE}(t) = \frac{1}{V}\iint_{\Omega} h|\nabla h'|^2 r\,dr\,d\theta, \tag{4.4.24}$$

where $h(r,\theta,t) = h_0(r) + h'(r,\theta,t)$, using notation introduced in (4.4.5). Since the frontal profile and lower-layer perturbation were the same in all simulations, we may compare the kinetic energies quantitatively. Simulation flat1 exhibits lower levels of $\widetilde{KE}$ than step1-I, slope1-I and slope1-O. Trial step1-O is associated with a drastic reduction in kinetic energy for the majority of the simulation, compared to the other trials. Again, this trend is consistent with the trend in $\overline{R}^*$, as discussed above. Because the instability in simulation flat1 is free from the complex influence of topographic variations, the corresponding $\widetilde{KE}$ curve in Fig. 4.18 clearly shows a quasi-periodic cycle of growth and saturation. CL also observed distinct subsequent instability events in some of their experiments, before the buoyant fluid reached the outer boundary.

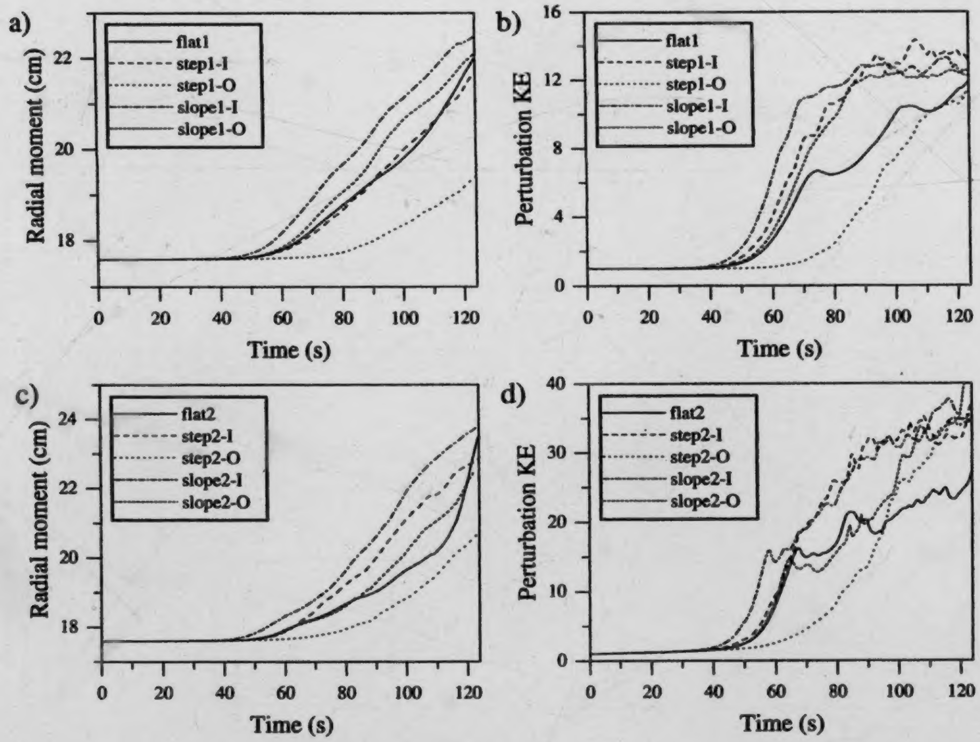

Figure 4.18: a) Dimensional upper-layer radial moment, b) non-dimensional upper-layer kinetic energy for simulation SERIES 1, c) dimensional upper-layer radial moment, d) non-dimensional upper-layer kinetic energy for simulation SERIES 2.

If we identify the annulus domain with a straight, x-periodic channel and the axisymmetric current profile (4.3.21) with an x-invariant jet of the same exponential form, then we may compare the dominant wavelength of the instability with that predicted by linear theory of section 4.3.2. The instability is always focussed near the sharpest frontal gradients, therefore we take the length of the periodic channel to be the initial circumference of the outside edge of the jet (i.e. the length of the outcropping). With our chosen values for α, γ and b, the outcropping has a dimensional length of 144 cm. Using a flat bottom the spectral technique gives a characteristic wavelength λ^* of approximately 6 cm.

Regarding the simulations, Table 4.4 records the values of λ^*, which were obtained by dividing 144 cm by the number of waves observed in the lower layer at the initial stages of instability (as in Fig. 4.16b). We found that dipoles developing in the lower layer were significantly easier to identify than deformations of the outcropping. The observed wavelength for flat1 is 7.2 cm, which is not far from the linear prediction. Some error is to be expected, given the different geometries employed in the theory and simulations. Also, as noted in section 4.3.2, our solution method seems to overestimate wavenumbers somewhat. Since the assumed eigenproblem can only account for linearly sloping (or flat) topography we are only able to predict the wavelength for simulation flat1.

As Table 4.4 indicates, the dominant wavelength in our simulations was 4–8 times the Rossby radius. Here we use $R_1 = 0.93$ cm for all simulations, even though in practice R_1 increased with time in SERIES 2 simulations, due to deepening of the upper layer. On the other hand, CL found that the wavelength of the instability was, on average, 13 times the upper-layer Rossby radius. Even if we include only the first instability event from each experiment in CL (which is most relevant to our chosen configuration), their data suggest $\lambda^* \approx 10$ cm. CL observed that buoyant fluid reached the outer tank wall faster with ridge topography (on the interior side of the front) than with a flat bottom. However, we did not find the rate of spreading to differ significantly in these two cases. Such discrepancies may be due to flow features not accounted for in our theory, such as a large depth fraction, $\delta \approx 1$ or a non-negligible ambient mean flow (see section 4.4.1).

We also feel that the presence of a source could modify the observed instability characteristics to some degree. CL argue that lateral spreading does not affect the instability due to a timescale separation between the two processes. In the theory of Griffiths and Linden (1981), the growing current is stable until a critical value of the Froude number is reached. The authors define a Froude number $\widehat{F}$ based on the current width W at the onset of instability, which we will write as

$$\widehat{F} = \frac{f_0^2 W^2}{g' h_*}, \tag{4.4.25}$$

for future reference. It seems that if the current is stable for a period of time, after which it is unstable, then it would have passed through a regime where growth rates are non-zero but small. In such a regime, the timescale of the instability would be similar to that of the spreading, thus allowing the two processes to interact. However, the results of CL are in good agreement with previous laboratory and numerical studies (e.g. Griffiths and Linden 1981; Barth 1989b; Verzicco, Lalli, and Campana 1997).

4.4.5 Source flow simulations

In SERIES 2, the initial condition for the upper layer was the same as in SERIES 1, however the introduction of a source term caused the current to deepen over time, so that its thickness increased to 5.25 cm by $t = 125$ s. The source term $Q_1(x, y)$ was proportional to the initial isopycnal profile $h(x, y, 0)$, with its amplitude adjusted to give a total flux 10 cm^3/s. The resulting compression of vortex tubes in the lower layer induced an anticyclonic azimuthal current in the ambient fluid. In this regard, SERIES 2 simulations are more in keeping with the configuration of CL's experiments.

As Table 4.4 shows, the azimuthal wavenumber of the instability was modified in only two simulations, and only by a small amount. Diagnostic quantities, plotted in Figs. 4.18c and d, evolved similarly to those in SERIES 1. As exemplified by the radial moment $\overline{R}$, spreading of the current was enhanced for sloping topography (also the step topography, step2-I), but was impeded for a ridge located at the outcropping (step2-O). The upper-layer perturbation kinetic energy clearly reflects a delay in lateral penetration in the early stages of instability, as was the case in SERIES 1.

On the other hand, some qualitative differences in behavior did arise in SERIES 2. These were most pronounced in the flat bottom simulation, flat2, and we plot two

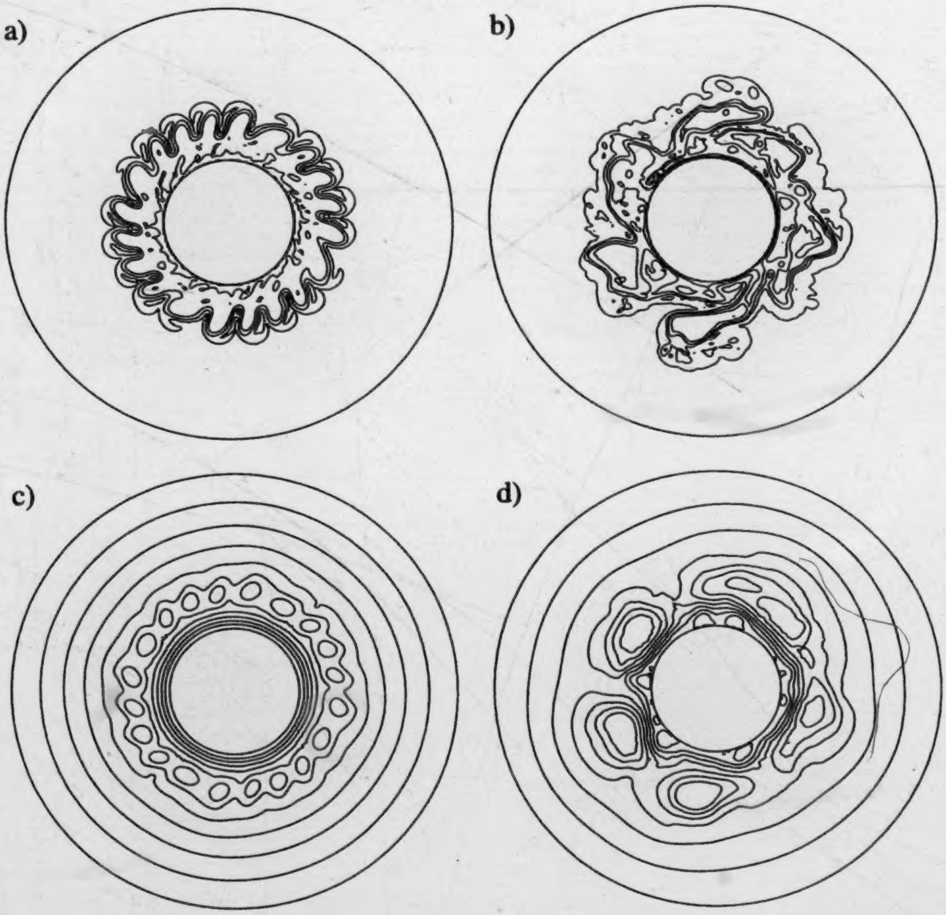

Figure 4.19: Dimensional upper-layer thickness at a) 62 s and b) 99 s, non-dimensional lower-layer pressure at c) 62 s and d) 99 s in simulation flat2. The contour extrema and intervals are, respectively, a) 0, 4.2 and 1.4 cm, b) 0, 4.8 and 1.2 cm, c) 0, 3.6 and 0.6, d) 0, 7.2 and 1.2.

snapshots of the streamfunctions for this case in Fig. 4.19. Initially the upper-layer thickness looked the same as in Fig. 4.15a, while the lower-layer pressure field was zero everywhere. A growing, wavelike deformation of the outcropping was observed as in SERIES 1, however the associated pressure anomalies in the lower layer did not have a cyclonic component. Gradually, additional horizontal shear developed in

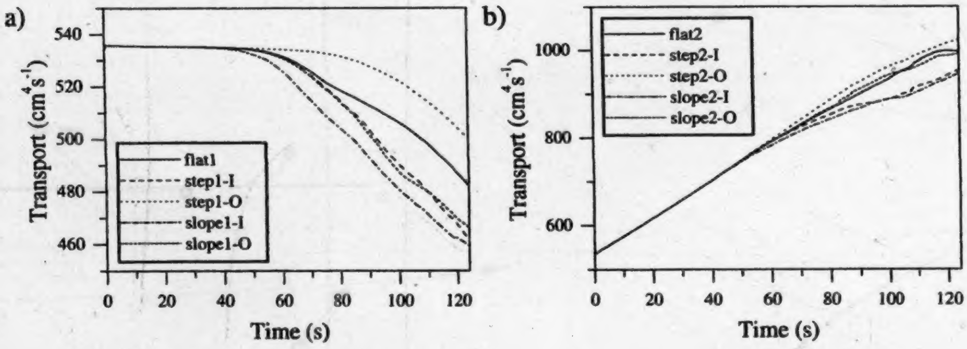

Figure 4.20: Total dimensional upper-layer azimuthal flux for a) SERIES 1 and b) SERIES 2.

the radial direction due to the imposed flux. In fact, velocities at the outer edge of the current were high enough to cause the growing meanders to break forward and merge together. In Fig. 4.19a waves that break backward are visible at the extreme edge of the current, however the main body of each emerging anticyclonic eddy leans forward.

The corresponding lower-layer streamfunction (Fig. 4.19b) exhibits high pressure cells exclusively. No eddies pinch off at this stage, in agreement with observations of CL. Increased anticyclonic vorticity results in continued merging of adjacent features, as well as a more turbulent flow than in SERIES 1. This is evident in Figs. 4.19b and d. At late times, the upper layer is dominated by a few large, irregular blobs, which circulate around the inner wall. Some of these detach by the end of the simulation, at $t = 125$ s.

4.4.6 Eddy transports

The instability we have described leads to a general outward spreading of the buoyant fluid, as discussed in section 4.4.2. However, we have not found a preferred direction of azimuthal motion for isolated eddies in either series of simulations. Frequent collisions between the vortices and interactions with the jet typically obscure any overall drift.

Eddies that manage to remain isolated usually maintain a stationary position with respect to the rotating coordinate frame, or are advected in curved paths by cyclonic recirculations between meander crests. In the oceanographic context, this raises the possibility that, in the long term, detached lenses may affect the total along-coast mass flux.

We define the total non-dimensional upper-layer azimuthal transport $T_\theta(t)$ as

$$T_\theta(t) = -\iint_\Omega r h u_{1\theta} dr d\theta, \tag{4.4.26}$$

where the minus sign in front of the integral simply ensures that the transport will be positive for frontal profiles with $\mathrm{d}h_0/\mathrm{d}r < 0$. In Fig. 4.20 we plot $T_\theta^*(t^*)$, the dimensional counterpart of (4.4.26). For SERIES 1, the magnitude of the average transport diminishes over time by as much as 16% (Fig. 4.20a). Thus the eddies have a small, but non-negligible effect on T_θ^*. We note that the transport diminishes the least for simulation step1-O, which is consistent with the delay in destabilization (and subsequent eddy formation) discussed above.

In SERIES 2, the source flux induces an increasingly strong clockwise flow, which dominates over eddy fluxes. In this case the total transport increases for all simulations by a factor of approximately 2, over the course of the simulation (Fig. 4.20b). As noted before, simulations involving a source are relevant to the experiments of CL and Griffiths and Linden (1981). Anticyclonic vorticity induced by the injection, as well as the increase in the effective deformation radius due to deepening of the buoyant layer, seem to inhibit eddy pinch-off, corroborating CL's findings. The effect is even more pronounced than it would be in the laboratory setting since, in the present model, there is no lateral spreading associated with the source. Actual coastal currents whose depth remains quasi-steady are likely to spawn vortices more readily than SERIES 2 suggests. However, judging from Fig. 4.20a, the associated along-shore transport is unlikely to be affected by eddy shedding to a significant degree.

4.4.7 Discussion of topographic effects

The QG formalism makes several simplifying assumptions, such as those of small interfacial displacements and topographic gradients, which are often too restrictive to be applied in actual laboratory or oceanographic settings associated with coastally-trapped currents. Nevertheless, it does offer a useful theoretical framework for understanding many of the physical processes involved in baroclinic dynamics. Indeed, Griffiths and Linden (1981) used a modified version of the Phillips model (Pedlosky 1987) to explain the instability they observed, and CL reported general agreement between their results and those of the Griffiths and Linden (1981).

Let us consider the traditional inviscid two-layer QG channel model that includes topography and the β-plane, where y is the cross-channel coordinate. The cross-channel PV gradients in the upper and lower layer are, respectively,

$$\frac{\partial q_1}{\partial y} = F_1(u_1 - u_2) - u_{1yy} + \beta, \tag{4.4.27}$$

$$\frac{\partial q_2}{\partial y} = F_2(u_2 - u_1) - u_{2yy} + \beta + h_{By}, \tag{4.4.28}$$

where, for $i = 1, 2$, q_i, F_i, u_i are the potential vorticities, Froude numbers and along-channel velocities, respectively. Here β is the usual beta parameter and $h_B(y)$ is a scaled topography term. If the flow in the upper layer is y-independent and is zero in the lower layer, then we may write

$$\frac{\partial q_1}{\partial y} = F_1 u_1 + \beta, \tag{4.4.29}$$

$$\frac{\partial q_2}{\partial y} = -F_2 u_1 + \beta + h_B y. \tag{4.4.30}$$

The necessary condition for instability is that the PV gradient be somewhere positive and somewhere negative (Pedlosky 1964). It is not necessary that either PV gradient vanish somewhere, only that the gradients be of opposite sign.

It is well-known that increasing β stabilizes the system to infinitesimal perturbations (Orlanski 1969). It is easy to see from (4.4.29), (4.4.30) that as β increases, eventually both gradients become positive everywhere, thus meeting the sufficient criterion for stability. The influence of the topographic term, however, is not unambiguous, since this term occurs only in q_2, and its gradient may be positive or negative. Presently, let us make the f-plane approximation ($\beta = 0$), and assume that $u_1 > 0$. The latter condition corresponds to an interface that rises in the offshore direction and a positive q_{1y}. In this case, sufficiently large h_{By} will force $q_{2y} > 0$, thus stabilizing the fluid. Conversely, for h_{By} small enough, q_{2y} becomes negative, thus meeting the necessary condition for instability. These conditions are exactly analogous to the ones derived in section 4.4.1.

Experience shows that the above system is unstable in some parameter regimes where the instability condition is met. Assuming that the dependence of the instability characteristics on the topographic gradient is continuous, one may suppose, for $u_1 > 0$, that growth rates will increase with decreasing h_{By}. Indeed, this is the general trend we observe in our simulations, comparing the flat and sloping topography cases (see also Reszka and Swaters 1999a). However, as CL point out, a necessary condition for instability does not ensure instability, and other criteria may come into effect depending on the details of the flow. Additional criteria were found in the two-layer shallow water context by Barth (1989a), although his study only considered upwelling fronts. The investigations of (Flagg and Beardsley 1978), Mechoso and Sinton (1981) and Gawarkiewicz (1991) clearly demonstrate that factors such as mean flows, large-amplitude topography, and the shape of the topography all compete in determining the growth rate.

Almost certainly, fluid evolution in a laboratory environment will be much more complex than the simple arguments above suggest. In particular, our discussion with respect to QG dynamics and the governing equations (4.1.91), (4.1.92) has neglected the existence of lateral shear in the mean flow, friction at the bottom boundary and sidewalls, as well as Ekman draining. As we pointed out in section 4.4.2 a constant source of buoyant fluid and a non-negligible outward pressure gradient may also affect the instability. It is perhaps not surprising then, that CL found sloping topography to be generally a stabilizing, rather than a destabilizing, influence.

On the other hand, our simulations corroborate the observation of CL that step topography inhibits vortex growth and pinch-off, at least when the step is located on the offshore side of the front. The buoyant fluid is then trapped, at least temporarily, on the shoreward side of the ridge. A likely reason for this behaviour is that motion across the ridge (or any steep topography) would require significant changes in the relative vorticity of the fluid, due to conservation of PV (CL). Such drastic increases/decreases in relative vorticity were not observed by CL, and they concluded that lower-layer fluid must be draining radially outward through an Ekman-like layer along the topography. This mechanism is clearly absent in our model. In our simulations motion across the ridge was delayed until the front had released enough potential energy. In a real oceanographic setting, tidal and wind forcings are likely to interrupt the instability, therefore this mechanism may be partly responsible for the persistence of shelf-break fronts.

We end the discussion with a simple scaling argument. Griffiths and Linden (1981) and CL determined that the dominant wavelength of the instability was inversely proportional to the Froude number. Treating f_0, L, g' and H as external parameters that do not depend on δ, definition (4.4.25) implies that $\widehat{F} = (f_0 W)^2/(\delta g' H) \sim \delta^{-1}$. Thus, our assumption of small δ implies that the present model is applicable in the large Froude number regime. Furthermore, we obtain from (4.1.17) that $L_* = \delta^{\frac{1}{4}} R_2 \sim \delta^{\frac{1}{4}}$ where again R_2 is independent of δ. Thus, heuristically, we would expect $L_* \sim F^{-\frac{1}{4}}$ in the present theory, i.e. an inverse relationship between the model lengthscale and Froude number. We have not tested this argument numerically, however it may be of interest to do so in the future.

Chapter 5

CS-FG-CS Model

5.1 Model Equations

A new, three-layer model is developed in which the middle layer is frontal geostrophic, while the outer layers are governed by QG dynamics. We include the beta effect, and a parameter for controlling the density contrast across the layers. Source and sink terms, although not present, could easily be introduced in the same way as in chapter 4. Continuous stratification is allowed in the QG layers, however a reduced set of equations in the limit of homogeneous QG theory is also presented. The homogeneous variant of the model has the property that it can be further reduced to the familiar Phillips model (Pedlosky 1987), in the absence of the middle layer.

The CS-FG-CS and SW-FG-SW models may be used to study aspects of instability in intermediate depth flows, as well as propagation and eventual destruction of intermediate depth lenses, such as Meddies. The scalings employed in the derivation follow S93 and chapter 4, however we emphasize differences where they arise. A single simulation is presented, which describes the long-term evolution of an isolated Meddy-like feature. Preliminary numerical integrations (not shown) indicate that the qualitative (but not quantitative) characteristics of instability associated with an IDBC would be similar to those discussed in chapter 4 and Reszka and Swaters (1999a). On the other hand, the stability and propagation properties of isolated oceanic lenses are of intrinsic interest, and have been the focus of several studies, including Killworth (1983), Cushman-Roisin *et al.* (1990), and Chassignet and Cushman-Roisin (1991).

We utilize the SW-FG-SW model in this numerical study, instead of CS-FG-CS, for two reasons. We believe it is instructive to consider the simpler case (3 homogeneous layers) first, so that differences arising from the introduction of stratification may be examined at a later date. Also, the CS-FG-CS model is somewhat more costly to run due to the three-dimensional structure of the QG layers, and we felt the additional computational resources were not justified given the simple, idealized nature of the initial and boundary conditions.

5.1.1 Model Derivation

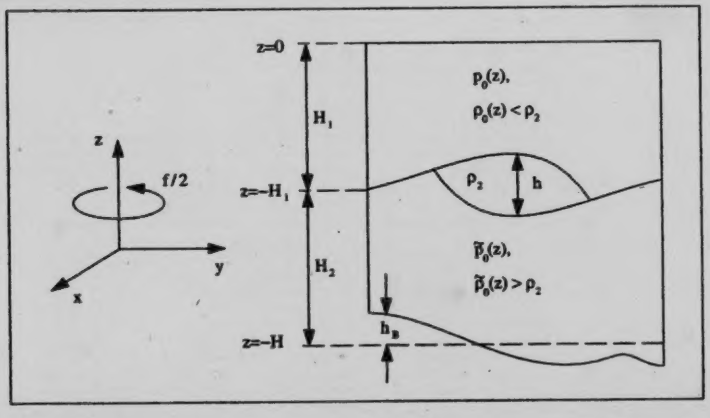

Figure 5.1: CS-FG-CS model geometry. A thin, homogeneous layer lies between two continuously-stratified layers that are relatively deep, but finite. The upper and lower surfaces bounding the middle layer are allowed to intersect each other. This permits fronts with finite spatial extent, or isolated lenses of intermediate water. Spatially varying topography is also allowed.

Using notation similar to the previous derivations, we begin with the Boussinesq equations for top and bottom layers (layers 1 and 3, respectively),

$$\left.\begin{aligned} \mathbf{u}^*_{it^*} + (\mathbf{u}^*_i\cdot\nabla^*)\mathbf{u}^*_i + w^*_i\mathbf{u}^*_{iz^*} + (f_0+\beta_0 y^*)\mathbf{e}_3\times\mathbf{u}^*_i &= -\frac{1}{\rho_*}\nabla^* p^*_i, \\ \rho_*(w^*_{it^*} + (\mathbf{u}^*_i\cdot\nabla^*)w^*_i + w^*_i w^*_{iz^*}) &= -p^*_{iz^*} - g\rho^*_i, \\ \rho^*_{it^*} + (\mathbf{u}^*_i\cdot\nabla^*)\rho^*_i + w^*_i\rho^*_{iz^*} &= 0, \\ \nabla^*\cdot\mathbf{u}^*_i + w^*_{iz^*} &= 0, \end{aligned}\right\} i = 1,3. \quad (5.1.1)$$

The equations for the middle layer (layer 2) are based on Shallow Water theory,

$$\mathbf{u}^*_{2t^*} + (\mathbf{u}^*_2\cdot\nabla^*)\mathbf{u}^*_2 + (f_0+\beta_0 y^*)\mathbf{e}_3\times\mathbf{u}^*_2 = -\frac{1}{\rho_*}\nabla^* p^*_2, \qquad (5.1.2)$$

$$h^*_{t^*} + \nabla^*\cdot(\mathbf{u}^*_2 h^*) = 0. \qquad (5.1.3)$$

Numerical subscripts refer to the layer.

We define $H = H_1 + H_2$ as the constant reference depth of the entire fluid column, where H_1 and H_2 are (constant) reference thicknesses of the upper and lower layers, respectively. Boundary conditions on the vertical velocities w^*_1, w^*_3 in the outer layers may be stated as follows,

$$w^*_1 = 0, \qquad z^* = 0, \qquad (5.1.4)$$

$$w^*_1 = \eta^*_{t^*} + \mathbf{u}^*_1\cdot\nabla^*\eta^*, \qquad z^* = -H_1 + \eta^*, \qquad (5.1.5)$$

$$w^*_3 = (\eta^* - h^*)_{t^*} + \mathbf{u}^*_3\cdot\nabla^*(\eta^* - h^*), \qquad z^* = -H_1 + \eta^* - h^*, \qquad (5.1.6)$$

$$w^*_3 = \mathbf{u}^*_3\cdot\nabla^* h^*_B, \qquad z^* = -H + h^*_B, \qquad (5.1.7)$$

where η^* is identified with the lower boundary of the upper layer, measured as the distance above $z^* = -H_1$, h^* is the thickness of the middle layer and h^*_B is the height of the bottom topography above $z^* = -H$.

We define the total pressures for the system,

$$p_1^*(x^*,y^*,z^*,t^*) = g\int_{z^*}^{0}\rho_0(\xi)d\xi + \varphi^*(x^*,y^*,z^*,t^*), \tag{5.1.8}$$

$$p_2^*(x^*,y^*,z^*,t^*) = g\int_{-H_1}^{0}\rho_0(\xi)d\xi - \rho_2 g(H_1+z^*) + p^*(x^*,y^*,t^*), \tag{5.1.9}$$

$$p_3^*(x^*,y^*,z^*,t^*) = g\int_{-H_1}^{0}\rho_0(\xi)d\xi + g\int_{z^*}^{0}\widetilde{\rho}_0(\xi)d\xi - g\int_{-H_1}^{0}\widetilde{\rho}_0(\xi)d\xi + \psi^*(x^*,y^*,z^*,t^*), \tag{5.1.10}$$

where the reduced pressure in layers 1, 2 and 3 is denoted by φ^*, p^* and ψ^*, respectively. Pressure continuity at the interfaces requires

$$\begin{aligned} & g\int_{-H_1+\eta^*}^{0}\rho_0(\xi)d\xi + \varphi^*(x^*,y^*,-H_1+\eta^*,t^*) \\ &= g\int_{-H_1}^{0}\rho_0(\xi)d\xi - g\rho_2\eta^* + p^* \qquad \text{at } z^* = -H_1+\eta^*, \end{aligned} \tag{5.1.11}$$

and

$$\begin{aligned} g\int_{-H_1}^{0}\rho_0(\xi)d\xi - g\rho_2(\eta^*-h^*) + p^* &= g\int_{-H_1}^{0}\rho_0(\xi)d\xi + g\int_{-H_1+\eta^*-h^*}^{0}\widetilde{\rho}_0(\xi)d\xi \\ -g\int_{-H_1}^{0}\widetilde{\rho}_0(\xi)d\xi + \psi^*(x^*,y^*,-H_1+\eta^*-h^*,t^*) & \qquad \text{at } z^* = -H_1+\eta^*-h^*. \end{aligned} \tag{5.1.12}$$

Taylor expanding both equations about $z^* = -H_1$, we obtain

$$-g\rho_0(-H_1)\eta^* + \varphi^*(x,y,-H_1,t) \approx -g\rho_2\eta^* + p^*, \tag{5.1.13}$$

$$-g\rho_2(\eta^*-h^*) + p^* \approx -g\widetilde{\rho}_0(-H_1)(\eta^*-h^*) + \psi^*(x,y,-H_1,t). \tag{5.1.14}$$

The reference density is taken to be that of the middle layer,

$$\rho_* = \rho_2, \tag{5.1.15}$$

and the reduced gravity is based on the density difference between the outer layers,

$$g' = g\frac{\Delta\rho}{\rho_*}, \qquad \Delta\rho = \widetilde{\rho}_0(-H_1) - \rho_0(-H_1). \tag{5.1.16}$$

Density differences between layers 1 and 2 and between layers 2 and 3 are taken to be fractions, r_1 and r_2, of $\Delta\rho$,

$$\rho_2 - \rho_0(-H_1) = r_1\Delta\rho, \qquad \widetilde{\rho}_0(-H_1) - \rho_2 = r_2\Delta\rho, \tag{5.1.17}$$

where $r_1 + r_2 = 1$. Simplifying, pressure continuity becomes

$$\left.\begin{aligned} r_1 g' \rho_2 \eta^* &= p^* - \varphi^* \\ r_2 g' \rho_2 (\eta^* - h^*) &= \psi^* - p^* \end{aligned}\right\} \quad z^* = -H_1. \tag{5.1.18}$$

Generic scalings for the spatial coordinates are introduced,

$$(x^*, y^*) = L_*(x, y), \qquad z^* = Hz, \tag{5.1.19}$$

and the velocities are scaled using the Rossby numbers ε_1 and ε_2,

$$\mathbf{u}_1^* = \varepsilon_1 f_0 L_* \mathbf{u}_1, \qquad \mathbf{u}_2^* = \varepsilon_2 f_0 L_* \mathbf{u}_2, \qquad \mathbf{u}_3^* = \varepsilon_1 f_0 L_* \mathbf{u}_3. \tag{5.1.20}$$

Although the Rossby numbers are free parameters at this point, we have already assumed that the outermost layers will behave similarly, and thus can be described by the same Rossby number, ε_1. The middle layer thickness, h^*, is scaled with the parameter $\delta \ll 1$, as are the interface deformation η^* and the bottom topography h_B^*,

$$h^* = \delta H h, \qquad \eta^* = \delta H \eta, \qquad h_B^* = \delta H h_B. \tag{5.1.21}$$

Dynamic pressure in all 3 layers is scaled geostrophically with the velocities,

$$\varphi^* = \varepsilon_1 \rho_* f_0^2 L_*^2 \varphi, \qquad p^* = \varepsilon_2 \rho_* f_0^2 L_*^2 p, \qquad \psi^* = \varepsilon_1 \rho_* f_0^2 L_*^2 \psi. \tag{5.1.22}$$

Density in each of the outer layers is composed of a background, z-dependent density plus a density fluctuation which is in hydrostatic balance with the dynamic pressure in that layer,

$$\rho_1^* = \rho_0(z^*) + \varepsilon_1 \frac{\rho_* f_0^2 L_*^2}{gH} \rho_1, \qquad \rho_3^* = \widetilde{\rho}_0(z^*) + \varepsilon_1 \frac{\rho_* f_0^2 L_*^2}{gH} \rho_3. \tag{5.1.23}$$

Vertical velocities are scaled with the time rate of change of the interface,

$$w_1^* = \delta\varepsilon_1 f_0 H w_1, \qquad w_3^* = \delta\varepsilon_1 f_0 H w_3, \tag{5.1.24}$$

while the β-plane scaling uses the ambient fluid Rossby number,

$$\beta_0 = \varepsilon_1 f_0 \beta / L_*. \tag{5.1.25}$$

Substituting the scalings into the primitive equations yields

$$\varepsilon_1(\mathbf{u}_{1t} + \mathbf{u}_1\cdot\nabla\mathbf{u}_1 + \delta w_1 \mathbf{u}_{1z}) + (1+\varepsilon_1\beta y)\mathbf{e}_3 \times \mathbf{u}_1 = -\nabla\varphi, \tag{5.1.26}$$

$$\varphi_z + \rho_1 = -\varepsilon_1\delta\left(\frac{H}{L}\right)^2 (w_{1t} + \mathbf{u}_1\cdot\nabla w_1 + \delta w_1 w_{1z}), \tag{5.1.27}$$

$$\rho_{1t} + \mathbf{u}_1\cdot\nabla\rho_1 + \delta w_1\rho_{1z} = \frac{\delta}{\varepsilon_1 F}\left(\frac{H}{g'}\right) N_*^2(z) w_1, \tag{5.1.28}$$

$$\mathbf{u}_1 + \delta w_{1z} = 0, \tag{5.1.29}$$

$$\varepsilon_1\mathbf{u}_{2t} + \varepsilon_2\mathbf{u}_2\cdot\nabla\mathbf{u}_2 + (1+\varepsilon_1\beta y)\mathbf{e}_3 \times \mathbf{u}_2 = -\nabla p, \tag{5.1.30}$$

$$\varepsilon_1 h_t + \varepsilon_2\nabla\cdot(\mathbf{u}_2 h) = 0, \tag{5.1.31}$$

$$\varepsilon_1(\mathbf{u}_{3t} + \mathbf{u}_3\cdot\nabla\mathbf{u}_3 + \delta w_3 \mathbf{u}_{3z}) + (1+\varepsilon_1\beta y)\mathbf{e}_3 \times \mathbf{u}_3 = -\nabla\psi, \tag{5.1.32}$$

$$\psi_z + \rho_3 = -\varepsilon_1\delta\left(\frac{H}{L}\right)^2 (w_{3t} + \mathbf{u}_3\cdot\nabla w_3 + \delta w_3 w_{3z}), \tag{5.1.33}$$

$$\rho_{3t} + \mathbf{u}_3\cdot\nabla\rho_3 + \delta w_3\rho_{3z} = \frac{\delta}{\varepsilon_1 F}\left(\frac{H}{g'}\right) \widetilde{N}_*^2(z) w_3, \tag{5.1.34}$$

$$\mathbf{u}_3 + \delta w_{3z} = 0, \tag{5.1.35}$$

where buoyancy frequencies for the top and bottom layers are given by, respectively,

$$N_*^2(z) = \frac{-g}{\rho_*}\left[\frac{\mathrm{d}\rho_0(z^*)}{\mathrm{d}z^*}\right]_{z^*=Hz} > 0 \quad \text{and} \quad \widetilde{N}_*^2(z) = \frac{-g}{\rho_*}\left[\frac{\mathrm{d}\widetilde{\rho}_0(z^*)}{\mathrm{d}z^*}\right]_{z^*=Hz} > 0. \tag{5.1.36}$$

and the Froude number is defined in terms of the total fluid thickness,

$$F = \frac{f_0^2 L_*^2}{g' H}. \tag{5.1.37}$$

Defining the depth fractions

$$\lambda_1 = \frac{H_1}{H}, \qquad \lambda_2 = \frac{H_2}{H}, \tag{5.1.38}$$

pressure continuity is then applied at $z = -\lambda_1$,

$$r_1\eta = \frac{\varepsilon_2}{\delta}Fp - \frac{\varepsilon_1}{\delta}F\rho_2\varphi|_{z=-\lambda_1}, \tag{5.1.39}$$

$$r_2(\eta - h) = \frac{\varepsilon_1}{\delta}F\psi|_{z=-\lambda_1} - \frac{\varepsilon_1}{\delta}Fp, \tag{5.1.40}$$

or, solving for η and p,

$$\eta = r_2h + \frac{\varepsilon_1}{\delta}F(\psi - \varphi), \qquad z = -\lambda_1, \tag{5.1.41}$$

$$p = \frac{\delta}{\varepsilon_2F}r_1r_2h + \frac{\varepsilon_1}{\varepsilon_2}(r_2\varphi + r_1\psi), \qquad z = -\lambda_1. \tag{5.1.42}$$

We consider the case where $\varepsilon_1 \approx \delta$ so that the outer layers are governed by QG theory. It is also assumed that $\varepsilon_2F \approx \delta$ and $\varepsilon_1 \ll \varepsilon_2$ so that p and h balance at leading order in (5.1.42). Accordingly, we define

$$\varepsilon_1 = \delta, \qquad \varepsilon_2 = F = \delta^{\frac{1}{2}}. \tag{5.1.43}$$

We note that the latter assumption determines the length scaling,

$$L_* = \delta^{\frac{1}{4}}\frac{\sqrt{g'H}}{f_0}, \tag{5.1.44}$$

similarly to (4.1.17) in the previous chapter. This is an intermediate lengthscale, between the internal Rossby radii of the frontal and ambient layers (e.g. RS99a). In order to obtain a uniformly valid model in the limit of a vanishing middle layer, we retain F in (5.1.41) and formally treat it as an O(1) quantity.

Nondimensional buoyancy frequencies, N and $\widetilde{N}$, are introduced as follows,

$$N_* = \delta^{\frac{1}{4}}\sqrt{\frac{g'}{H}}N, \qquad \widetilde{N}_* = \delta^{\frac{1}{4}}\sqrt{\frac{g'}{H}}\widetilde{N}. \tag{5.1.45}$$

Simplifying the governing equations we obtain,

$$\delta(\mathbf{u}_{1t} + \mathbf{u}_1\cdot\nabla\mathbf{u}_1) + (1 + \delta\beta y)\mathbf{e}_3 \times \mathbf{u}_1 = -\nabla\varphi + O(\delta^2), \tag{5.1.46}$$

$$\varphi_z + \rho_1 = O(\delta^2), \tag{5.1.47}$$

$$\rho_{1t} + \mathbf{u}_1 \cdot \boldsymbol{\nabla} \rho_1 + \delta w_1 \rho_{1z} = N^2(z) w_1, \tag{5.1.48}$$

$$\boldsymbol{\nabla} \cdot \mathbf{u}_1 = -\delta w_{1z}, \tag{5.1.49}$$

$$\delta \mathbf{u}_{2t} + \delta^{\frac{1}{2}} \mathbf{u}_2 \cdot \nabla \mathbf{u}_2 + (1 + \delta\beta y)\mathbf{e}_3 \times \mathbf{u}_2 = -\boldsymbol{\nabla} p, \tag{5.1.50}$$

$$\delta^{\frac{1}{2}} h_t + \boldsymbol{\nabla} \cdot (\mathbf{u}_2 h) = 0, \tag{5.1.51}$$

$$\delta(\mathbf{u}_{3t} + \mathbf{u}_3 \cdot \boldsymbol{\nabla} \mathbf{u}_3) + (1 + \delta\beta y)\mathbf{e}_3 \times \mathbf{u}_3 = -\boldsymbol{\nabla}\varphi + O(\delta^2), \tag{5.1.52}$$

$$\psi_z + \rho_3 = O(\delta^2), \tag{5.1.53}$$

$$\rho_{3t} + \mathbf{u}_3 \cdot \boldsymbol{\nabla} \rho_3 + \delta w_3 \rho_{3z} = \widetilde{N}^2(z) w_3, \tag{5.1.54}$$

$$\boldsymbol{\nabla} \cdot \mathbf{u}_3 = -\delta w_{3z}. \tag{5.1.55}$$

Pressure continuity is then written

$$\left.\begin{aligned} \eta &= r_2 h + F(\psi - \varphi) \\ p &= r_1 r_2 h + \delta^{\frac{1}{2}}(r_1 \psi + r_2 \varphi) \end{aligned}\right\} z = -\lambda_1, \tag{5.1.56}$$

and the vertical boundary conditions have the form

$$w_1 = 0, \qquad z = 0, \tag{5.1.57}$$

$$w_1 = \eta_t + \mathbf{u}_1 \cdot \boldsymbol{\nabla}\eta, \qquad z = -\lambda_1 + \delta\eta, \tag{5.1.58}$$

$$w_3 = (\eta - h)_t + \mathbf{u}_3 \cdot \boldsymbol{\nabla}(\eta - h), \qquad z = -\lambda_1 + \delta\eta - \delta h, \tag{5.1.59}$$

$$w_3 = \mathbf{u}_3 \cdot \boldsymbol{\nabla} h_B \qquad z = -1. \tag{5.1.60}$$

Boundary conditions at the interfaces must be Taylor expanded about $z = -\lambda_1$,

$$w_1 = \eta_t + \mathbf{u}_1 \cdot \boldsymbol{\nabla}\eta, \qquad z = -\lambda_1, \tag{5.1.61}$$

$$w_3 = (\eta - h)_t + \mathbf{u}_3 \cdot \boldsymbol{\nabla}(\eta - h), \qquad z = -\lambda_1, \tag{5.1.62}$$

which is valid to O(δ). As will become apparent, the O(δ) corrections will not be needed (this was also the case in the FG-CS model).

5.1.2 Governing Equations

To obtain a leading order balance in the (small) Rossby number of the frontal layer, we proceed by expanding all flow variables in $\delta^{\frac{1}{2}}$,

$$(\varphi, p, h, \psi, \eta, \mathbf{u}_1, \mathbf{u}_2, \mathbf{u}_3, w_1, w_3, \rho_1, \rho_3) = (\varphi, p, h, \psi, \eta, \mathbf{u}_1, \mathbf{u}_2, \mathbf{u}_3, w_1, w_3, \rho_1, \rho_3)^{(0)}$$

$$+\delta^{\frac{1}{2}}(\varphi, p, h, \psi, \eta, \mathbf{u}_1, \mathbf{u}_2, \mathbf{u}_3, w_1, w_3, \rho_1, \rho_3)^{(1)} + \ldots \tag{5.1.63}$$

To O(δ) the outer layers will be governed by continuously stratified QG theory. We form the QGPV equations by taking the curl of the momentum equations in the traditional manner (Pedlosky 1987),

$$(\Delta\varphi^{(0)} + (N^{-2}\varphi_z^{(0)})_z)_t + J(\varphi^{(0)}, \Delta\varphi^{(0)} + (N^{-2}\varphi_z^{(0)})_z + \beta y) = 0, \tag{5.1.64}$$

$$(\Delta\psi^{(0)} + (N^{-2}\psi_z^{(0)})_z)_t + J(\psi^{(0)}, \Delta\psi^{(0)} + (N^{-2}\psi_z^{(0)})_z + \beta y) = 0. \tag{5.1.65}$$

The leading order fields must then satisfy the following boundary conditions,

$$\varphi_{zt}^{(0)} + J(\varphi^{(0)}, \varphi_z^{(0)}) = 0, \qquad z = 0, \tag{5.1.66}$$

$$\varphi_{zt}^{(0)} + J(\varphi^{(0)}, \varphi_z^{(0)}) = -N^2[\partial_t + J(\varphi^{(0)}, *)][r_2 h^{(0)} + F(\psi^{(0)} - \varphi^{(0)}], \qquad z = -\lambda_1, \tag{5.1.67}$$

$$\psi_{zt}^{(0)} + J(\psi^{(0)}, \psi_z^{(0)}) =$$

$$-\widetilde{N}^2[\partial_t + J(\psi^{(0)}, *)][-r_1 h^{(0)} + F(\psi^{(0)} - \varphi^{(0)})], \qquad z = -\lambda_1, \tag{5.1.68}$$

$$\psi_{zt}^{(0)} + J(\psi^{(0)}, \psi_z^{(0)}) = -\widetilde{N}^2 J(\psi^{(0)}, h_B), \qquad z = -1. \tag{5.1.69}$$

The following auxiliary relations also hold at leading order,

$$\mathbf{u}_1^{(0)} = \mathbf{e}_3 \times \boldsymbol{\nabla}\varphi^{(0)}, \qquad \mathbf{u}_3^{(0)} = \mathbf{e}_3 \times \boldsymbol{\nabla}\psi^{(0)},$$

$$w_1^{(0)} = -N^{-2}[\varphi_{zt}^{(0)} + J(\varphi^{(0)}, \varphi_z^{(0)})], \qquad w_3^{(0)} = -\widetilde{N}^{-2}[\psi_{zt}^{(0)} + J(\psi^{(0)}, \psi_z^{(0)})],$$

$$\rho_1 = -\varphi_z^{(0)}, \qquad \rho_3 = -\psi_z^{(0)}, \qquad \eta^{(0)} = r_2 h^{(0)} + F[\psi^{(0)} - \varphi^{(0)}]_{z=-\lambda_1}. \tag{5.1.70}$$

Derivation of the governing equation for the middle layer is similar to that in the previous chapter. We need to consider the O(1) problem,

$$\mathbf{u}_2^{(0)} = \mathbf{e}_3 \times \boldsymbol{\nabla} p^{(0)}, \tag{5.1.71}$$

$$\nabla\cdot(\mathbf{u}_2^{(0)}h^{(0)}) = 0, \tag{5.1.72}$$

$$p^{(0)} = r_1r_2h^{(0)}, \tag{5.1.73}$$

and the $O(\delta^{\frac{1}{2}})$ problem,

$$\mathbf{u}_2^{(0)}\cdot\nabla\mathbf{u}_2^{(0)} + \mathbf{e}_3 \times \mathbf{u}_2^{(1)} = -\nabla p^{(1)}, \tag{5.1.74}$$

$$h_t^{(0)} + \mathbf{u}_2^{(0)}\cdot\nabla h^{(1)} + \mathbf{u}_2^{(1)}\cdot\nabla h^{(0)} + h^{(0)}\nabla\cdot\mathbf{u}_2^{(1)} = 0, \tag{5.1.75}$$

$$p^{(1)} = r_1r_2h^{(1)} + [r_1\psi^{(0)} + r_2\varphi^{(0)}]_{z=\lambda_1}. \tag{5.1.76}$$

Solving for $\mathbf{u}_2^{(1)}$,

$$\mathbf{u}_2^{(1)} = \mathbf{e}_3 \times \nabla(r_1r_2h^{(1)} + [r_1\psi + r_2\varphi]_{z=\lambda_1}) + (r_1r_2)^2\mathbf{e}_3 \times J(h^{(0)}, \mathbf{e}_3 \times \nabla h^{(0)}). \tag{5.1.77}$$

Substitution of the velocity correction into the mass conservation equation yields

$$\begin{aligned} &h_t^{(0)} + r_1r_2J(h^{(0)}, h^{(1)}) + \nabla h^{(0)}\cdot(\mathbf{e}_3 \times \nabla(r_1r_2h^{(1)} + [r_1\psi + r_2\varphi]_{z=-\lambda_1}) \\ &+(r_1r_2)^2\nabla h^{(0)}\cdot J(\nabla h^{(0)}, h^{(0)}) + h^{(0)}\nabla\cdot(\mathbf{e}_3 \times \nabla(r_1r_2h^{(1)} + [r_1\psi + r_2\varphi]_{z=-\lambda_1}) \\ &+(r_1r_2)^2h^{(0)}\nabla\cdot J(\nabla h^{(0)}, h^{(0)}) = 0. \end{aligned} \tag{5.1.78}$$

Finally, we simplify the above equation,

$$\begin{aligned} &h_t^{(0)} + J(r_1\psi^{(0)} + r_2\varphi^{(0)}, h^{(0)}) \\ &+(r_1r_2)^2J(\frac{1}{2}\nabla h^{(0)}\cdot\nabla h^{(0)} + h^{(0)}\Delta h^{(0)}, h^{(0)}) = 0, \qquad z = -\lambda_1, \end{aligned} \tag{5.1.79}$$

where we have again used the identities (4.1.63).

Dropping superscripts, the leading order balance can be written as

$$[\partial_t + J(\varphi, *)]\varphi_z = 0, \qquad z = 0, \tag{5.1.80}$$

$$[\partial_t + J(\varphi, *)][\Delta\varphi + (N^{-2}\varphi_z)_z + \beta y] = 0, \tag{5.1.81}$$

$$[\partial_t + J(\varphi, *)][\varphi_z + N^2(r_2h + F(\psi - \varphi))] = 0, \qquad z = -\lambda_1, \tag{5.1.82}$$

$$h_t + J(r_1\psi + r_2\varphi, h) + (r_1r_2)^2(h\Delta h + \frac{1}{2}\nabla h\cdot\nabla h, h) = 0, \qquad z = -\lambda_1, \tag{5.1.83}$$

$$[\partial_t + J(\psi, *)][\psi_z - \widetilde{N}^2(r_1 h - F(\psi - \varphi))] = 0, \qquad z = -\lambda_1, \tag{5.1.84}$$

$$[\partial_t + J(\psi, *)][\Delta\psi + (\widetilde{N}^{-2}\varphi_z)_z + \beta y] = 0, \tag{5.1.85}$$

$$[\partial_t + J(\psi, *)][\psi_z + \widetilde{N}^2 h_B] = 0, \qquad z = -1, \tag{5.1.86}$$

with the auxiliary relations

$$\mathbf{u}_1 = \mathbf{e}_3 \times \boldsymbol{\nabla}\varphi, \qquad \mathbf{u}_2 = \mathbf{e}_3 \times \boldsymbol{\nabla}h, \qquad \mathbf{u}_3 = \mathbf{e}_3 \times \boldsymbol{\nabla}\psi,$$

$$w_1 = -N^{-2}[\varphi_{zt} + J(\varphi, \varphi_z)], \qquad w_3 = -\widetilde{N}^{-2}[\psi_{zt} + J(\psi, \psi_z)],$$

$$\rho_1 = -\varphi_z, \qquad \rho_3 = -\psi_z, \qquad r_1 + r_2 = 1. \tag{5.1.87}$$

5.1.3 Boundary conditions at incroppings

In this model, curves that separate regions where $h > 0$ from regions where $h = 0$ will be called incroppings. Derivation of the boundary conditions at an incropping is similar to that in the last chapter and will not be reproduced here. We simply state that the leading order nondimensional fields must satisfy

$$h^{(0)} = 0, \tag{5.1.88}$$

$$h_x^{(0)} + h_y^{(0)}\xi_x^{(0)} = 0, \tag{5.1.89}$$

$$h_t^{(0)} + h_y^{(0)}\xi_t^{(0)} = 0, \tag{5.1.90}$$

at an incropping given by $y = \xi^{(0)}(x, t)$. Again, assuming we may formally differentiate $h^{(0)}$ near an incropping, both (5.1.89) and (5.1.90) follow from (5.1.88). Since $h = 0$ at an incropping by definition, no additional computation is required to track the free boundary other than the evolution of the governing equations (5.1.80)–(5.1.86).

5.1.4 Reduction to SW-FG-SW

In the limit of no stratification in the ambient layers, a simpler theory results, which we call SW-FG-SW. The governing equations may be obtained from the CS-FG-CS model as follows. Integrating (5.1.81) in z we write

$$\int_{-\lambda_1}^{0} \left[(\Delta\varphi + (N^{-2}\varphi_z)_z)_t + J(\varphi, \Delta\varphi + (N^{-2}\varphi_z)_z + \beta y)\right] dz = 0. \qquad (5.1.91)$$

Simplification as in sections (2.1.5) and (4.1.4) leads to

$$\int_{-\lambda_1}^{0} \Delta\varphi_t + J(\varphi, \Delta\varphi) + \beta\varphi_x dz$$
$$+N^{-2}\left[\varphi_{zt} + J(\varphi, \varphi_z)\right]_{z=0} - N^{-2}\left[\varphi_{zt} + J(\varphi, \varphi_z)\right]_{z=-\lambda_1} = 0. \qquad (5.1.92)$$

Substituting in the vertical boundary conditions (5.1.80), (5.1.82), the result is

$$\int_{-\lambda_1}^{0} \Delta\varphi_t + J(\varphi, \Delta\varphi) + \beta\varphi_x dz + \left[(\partial_t + J(\varphi, *)(r_2 h + F(\psi - \varphi))\right]_{z=-\lambda_1} = 0. \quad (5.1.93)$$

At this point we introduce the top and bottom layer Froude numbers, respectively,

$$F_1 = \frac{F}{\lambda_1}, \qquad F_2 = \frac{F}{\lambda_2}. \qquad (5.1.94)$$

Taking the limit as $\dfrac{\partial\varphi}{\partial z} \to 0$ and using (5.1.81) yields

$$(\partial_t + J(\varphi, *))(\Delta\varphi + \frac{r_2}{\lambda_1}h + F_1(\psi - \varphi) + \beta y) = 0, \qquad (5.1.95)$$

where now $\varphi = \varphi(x, y, t)$. Similarly, integrating (5.1.85) over $-1 < z < -\lambda_1$, substituting in (5.1.84) and (5.1.86) and taking the limit $\partial_z \to 0$ yields

$$(\partial_t + J(\psi, *))(\Delta\psi + \frac{r_1}{\lambda_2}h - F_2(\psi - \varphi) + \beta y + \frac{1}{\lambda_2}h_B) = 0, \qquad (5.1.96)$$

where now $\psi = \psi(x, y, t)$. The middle layer equation is unaffected, except for the loss of z-dependence in the streamfunctions φ and ψ. The SW-FG-SW model equations may then be written

$$(\partial_t + J(\varphi, *))(\Delta\varphi + \frac{r_2}{\lambda_1}h + F_1(\psi - \varphi) + \beta y) = 0, \qquad (5.1.97)$$

$$h_t + J(r_1\psi + r_2\varphi, h) + (r_1r_2)^2 J(h\Delta h + \frac{1}{2}\nabla h\cdot\nabla h, h) = 0, \qquad z = -\lambda_1, \tag{5.1.98}$$

$$(\partial_t + J(\psi, *))(\Delta\psi + \frac{r_1}{\lambda_2}h - F_2(\psi - \varphi) + \beta y + \frac{1}{\lambda_2}h_B) = 0. \tag{5.1.99}$$

This model may also be derived by making the initial ansatz of 3 homogeneous layers (see appendix A).

In the limit of a vanishing middle layer ($h \to 0$), the above governing equations reduce to the Phillips model (Pedlosky 1987) with bottom topography,

$$(\partial_t + J(\varphi, *))(\Delta\varphi + F_1(\psi - \varphi) + \beta y) = 0, \tag{5.1.100}$$

$$(\partial_t + J(\psi, *))(\Delta\psi - F_2(\psi - \varphi) + \beta y + \frac{1}{\lambda_2}h_B) = 0. \tag{5.1.101}$$

This simplified dynamics will take effect whenever the middle layer thickness becomes small enough that it no longer makes the leading order contribution to the right hand sides of (5.1.41) and (5.1.42). We speculate that lengthscales in this new regime will increase concurrently, making the Froude number an O(1) quantity.

5.2 Meddy Simulation

Meddies are coherent lenses of warm, salty Mediterranean water, which typically form along the coast of Portugal and later travel south-west. They range in diameter from 40 to 150 km, and may last for several years (Richardson *et al.* 2000). Baey *et al.* (1995) and Sadoux *et al.* (2000) performed laboratory experiments at Grenoble, France, in which an intermediate-depth boundary current (henceforth IDBC) became unstable and shed coherent lenses of intermediate fluid. All three layers were homogeneous in their trials. Different behaviors were observed for different values of the Burger and Ekman numbers. In particular, "meddy" detachment occurred for small Burger number. In terms of our notation, their expression for the Burger number reduces to $\delta^{\frac{1}{2}}$, which we have assumed to be small *a priori.*

Application of the SW-FG-SW model to the Baey *et al.* (1995) set of experiments would be entirely appropriate, however, below we report on the evolution of a single

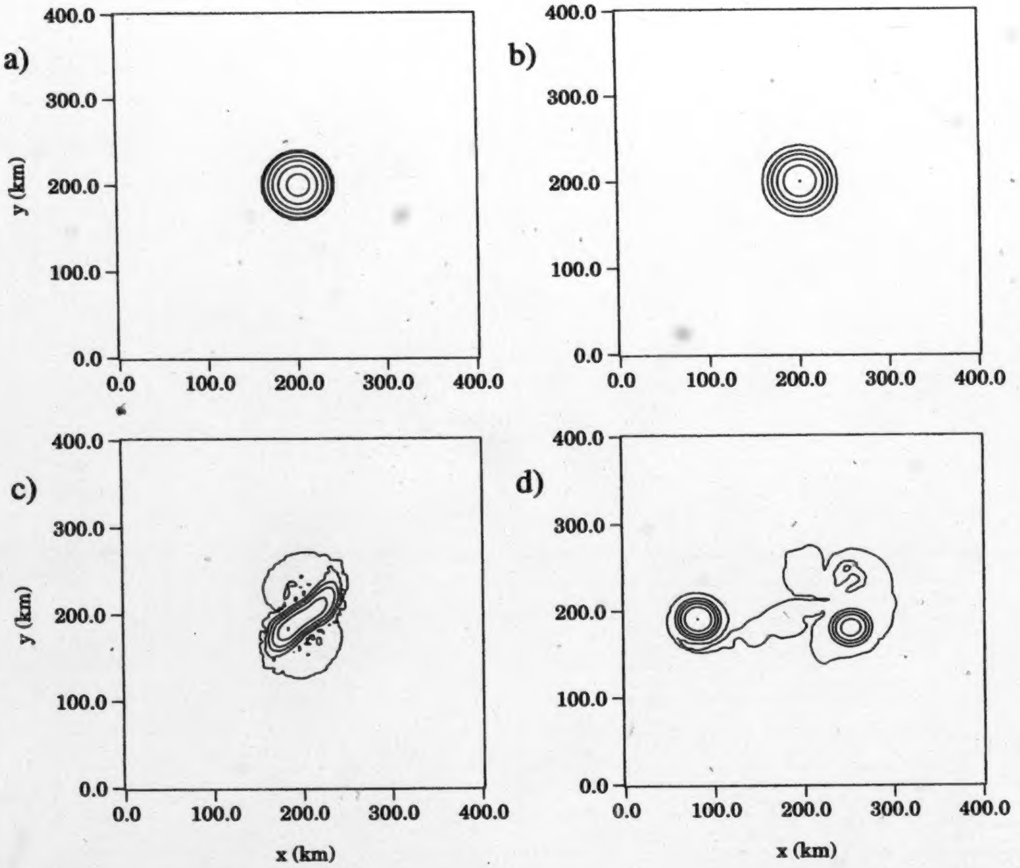

Figure 5.2: Dimensional middle layer thickness at a) 0, b) 22, c) 61 and d) 99 days. The contour extrema and intervals are, respectively, 0, 500, 100 m.

coherent lens in the presence of the beta effect. As it turns out, the meddy profile we prescribe as an initial condition is itself unstable, and the lens quickly splits into two separate meddies. Gradual migration to the south-west is then observed. The simulation is performed in a periodic channel. We emphasize that such a domain is a poor approximation of the real ocean for long-term studies, however it does allow us to observe the southwestward drift associated with mesoscale oceanic eddies.

Following Richardson *et al.* (2000), we focus on a typical meddy spawned in the eastern North Atlantic at a latitude of 30°N. In the parlance of section 5.1, the following scalings are adopted: $f_0 = 7.3 \times 10^{-5}$, $\beta_0 = 2.0 \times 10^{-11}$, $H = 4000$ m, $h_* = 500$ m, $\lambda_1 = \lambda_2 = r_1 = r_2 = 0.5$ and $g' = 5.5 \times 10^{-3}$ m/s^2. The depth ratio, upper layer Rossby deformation radius and dynamic lengthscale are then $\delta = 0.125$, $R_1 = 65$ km and $L_* = 40$ km, respectively. The initial nondimensional thickness profile for the middle layer is given by

$$h(x, y, 0) = \max\{1 - (x - x_0)^2 - (y - y_0)^2, 0\}, \tag{5.2.1}$$

where (x_0, y_0) gives the initial location of the meddy. The above profile represents the meddy core, with a dimensional width of 80 km, and thickness of 500 m.

The lens is assumed to be located in the open ocean (the topography is flat), exactly at mid-depth in the water column for simplicity. The simulation domain has dimensions 400 by 400 km, with a resolution of 3 km. With the above scalings we also obtain $F_1 = F_2 = 0.7$ and $\beta = 0.08$. In this configuration, north is in the positive y direction. We expect that dynamics associated with this model will be qualitatively similar to those of FG-SW, and therefore the exact shape of the initial meddy is not significant. In particular, vanishing thickness at the edge of the vortex is not crucial, but supported by observational evidence (Richardson *et al.* 2000). It is important to realize, however, that our model stipulates a relatively thin middle layer, an assumption which is not always satisfied for meddies, especially near coastlines. We are not concerned here with processes by that gave rise to the meddy, although the rapid descent of Mediterranean water from the sill at Gibraltar may have important consequences for meddy properties (Jungclaus 1999).

Plots of the upper layer streamfunction at 0, 22, 61 and 99 days are given in Fig. 5.2. In this particular simulation, the outermost layers behave almost identically, therefore we only present the streamfunction for the upper layer, shown in Fig. 5.3 for the same times as Fig. 5.2. Initially the eddy is located in the middle of the domain, and streamfunctions in the ambient layers are identically zero. At this stage, the maximum velocity in the middle layer is 1 m/s. At 22 days the eddy is relatively unaltered, however an adjustment begins to take place, due to the presence of the β-

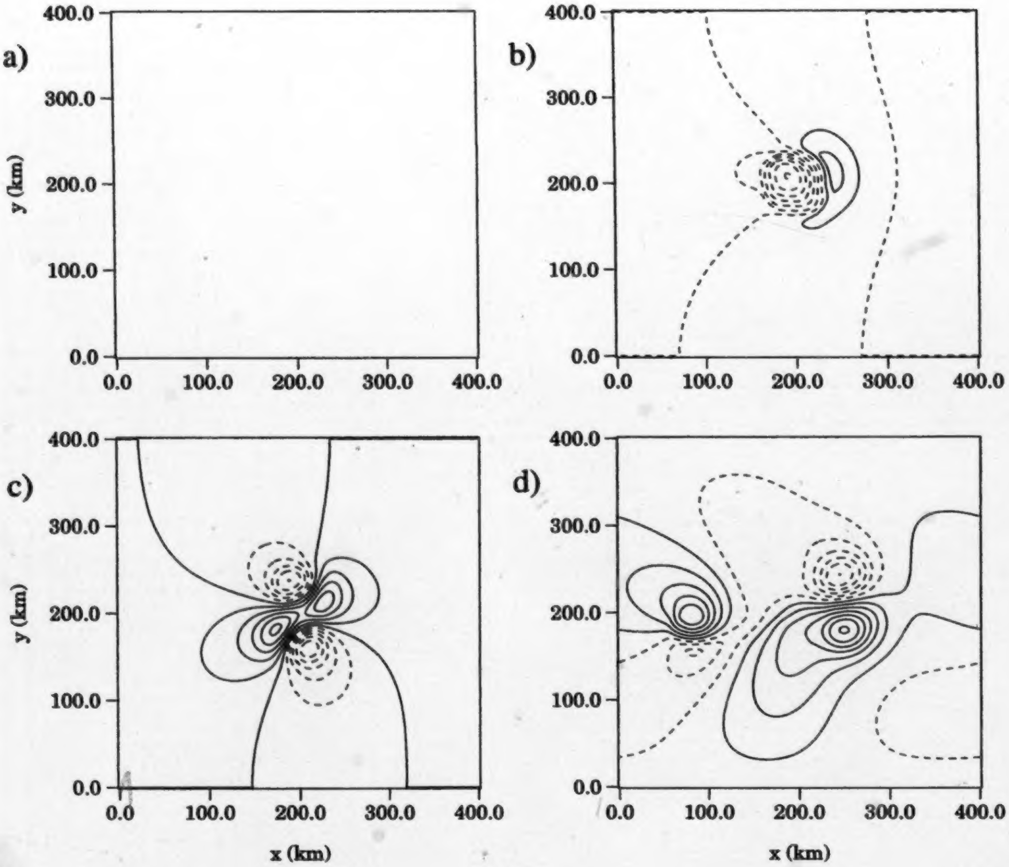

Figure 5.3: Nondimensional upper layer pressure at a) 0, b) 22, c) 61 and d) 99 days. Initially the streamfunction is zero everywhere. In the other plots, the contour extrema and intervals are, respectively, b) −0.3, 0.1, 0.05, c) 0.5, 0.5, 0.1 and d) −2.6, 2.2, 0.4. Dashed lines correspond to negative values.

plane. A cyclonic circulation develops in the upper layer immediately above the lens, and a Rossby wave wake begins to emerge on the eastern side of the eddy (Fig. 5.3b).

By 61 days, a quadrupolar structure has formed in the ambient layers, rotating anticyclonically (Fig. 5.3c). Concurrently, the lens has become elliptical, and is rotating in unison with the quadrupole anomaly (Fig. 5.2c). At this point the elongated eddy is similar to a shear flow, or coupled front. The breakup of such a filament was shown to be predominantly a barotropic process, by Pavía (1992) and R97. The lens splits into two smaller lenses, which then drift apart. The original meddy became unstable due to its lateral size; the resulting smaller meddies were stable for the rest of the simulation.

Given that the diameter of the original lens corresponded to a typical oceanic meddy, stability was expected; therefore the reason for instability requires further investigation. The stability of circular eddies in the generalized geostrophic regime (which includes FG) was studied by Tang (1989). They showed that stability depends on a subtle balance between the strength of β and the depth ratio. The reader is referred to that work for details. It seems plausible that real oceanic lenses also become unstable and split on occasion. If the separation takes only a few eddy turnaround times, as in this simulation, then the process could be missed by longterm observational programs.

Each daughter is associated with a pressure dipole in the ambient fluid, which determines its motion to leading order. A dipole self-propels such that the anticyclonic component is on its right and the cyclonic component on its left. The meddies and the corresponding upper layer dipole anomalies are shown in Figs. 5.2d and 5.3d. The orientation of the dipoles immediately after breakup was such that one dipole began to propagate to the east, and the other, to the west. However, the instability gave rise to Rossby waves, which propagated westward under the influence of the β-plane. Given the relatively short length of the channel, these waves reentered at the eastern boundary several times during the course of the simulation, and interacted with the meddies and dipoles. The net effect was gradual dissipation of the dipoles and translation of the meddies in the southwestward direction.

Trajectories of the two meddies and the center of mass for the middle layer are plotted in Fig. 5.4. The simulation lasted 500 days. Since the domain was periodic, and the meddies themselves eventually reentered at the eastern boundary, the domain in Fig. 5.4 was extended by an additional 400 km in the negative x direction. The

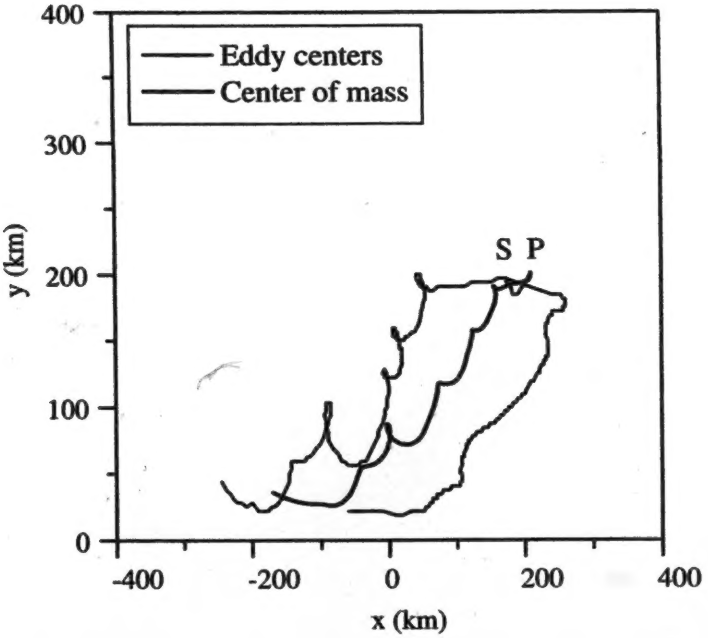

Figure 5.4: Meddy trajectories (thin lines) and trajectory of the center of mass (solid line) over the course of the simulation (500 days).

initial meddy was located at the point P, and separation occurred near the point S, after which the original trajectory diverges into three separate ones. The "western" meddy clearly exhibits a southwestward trajectory, on which are superimposed some oscillations caused by Rossby waves as they move past. The "eastern" eddy propagates to the east somewhat before its dipole counterpart is eroded. Subsequently it too travels to the southwest, as does the centroid of the system. For a discussion of baroclinic riders advected by barotropic dipoles, the reader is referred to Feliks and Ghil (1996) and references therein.

The primary contribution of this chapter has been to derive the CS-FG-CS and SW-FG-SW models and to establish incropping boundary conditions. These three-layer models have the advantage that they retain frontal terms in the middle layer, but reduce to two-layer QG theory as a limiting case. Two-layer QG models have been studied for a long time; therefore many characteristics of the models presented here can be easily predicted. However the addition of a third layer with O(1) thickness variations provides an interesting yet nontrivial extension. The above simulation demonstrates that the description of long-lived, isolated, mid-depth oceanic lenses is feasible with the SW-FG-SW model. Furthermore, it is known that in the primitive equations cyclones and anticyclones behave differently in terms of their growth and stability (Cushman-Roisin and Tang 1989; Boss, Paldor, and Thompson 1996). If advective velocity corrections (i.e. the frontal terms) are incorporated in the final balance, this asymmetry is retained, whereas it is lost in QG models (Cushman-Roisin and Tang 1990).

Chapter 6

Conclusions

6.1 Summary

In this thesis we have derived three new models for the description of mesoscale phenomena, and we demonstrated how to reduce continuously-stratified theories to their homogeneous variants. We have also generalized three previously derived theories by introducing the β-plane approximation, source/sink terms and, in two cases, a simple bottom drag parameterization. Frontal boundary conditions and some basic analytical results were also established. Our goal was to extend and generalize the family of layered frontal models. Such models have been employed successfully by previous authors in studies of instability processes and eddy dynamics (e.g. Flierl 1984; Cushman-Roisin and Tang 1989; Cushman-Roisin *et al.* 1990).

We have solved the linear instability problem for an abyssal current with a parabolic cross-section in the context of the CS-PG model. The resulting solutions and instability characteristics are in excellent agreement with direct numerical simulations employing the original governing equations. Increasing the relative thickness of the abyssal current or the ambient stratification serves to increase growth rates and decrease lengthscales. In the limit of no stratification in the ambient layer, the linear results of Swaters (1991) are recovered. Application to the dense overflow south of

Denmark Strait yields dominant wavelengths and e-folding times which are reasonably close to those observed. However, there are also differences due to the simplifications we have made, as outlined in chapter 3.

The spectral technique used to solve the CS-PG linearized equations was applied to the FG-CS model, for non-outcropping wedge fronts and a more realistic, exponential front. For a gently sloping wedge front, the computed instability characteristics matched analytical solutions, which were available due to a simplification in the linear stability problem. The spatial structure of the solutions and trends with respect to parameters seemed to be captured quite well for all frontal profiles. However, quantitative predictions as to growth rates and phase speeds were not completely satisfying in some cases.

For the O(1) wedge front reasonably accurate values of instability characteristics could be obtained, but only using a large number of expansion functions. Convergence was slow, suggesting that a better choice of basis functions could be made. With regard to the exponential front, comparison with direct numerical simulation showed some discrepancy. For this reason we have not pursued detailed parameter studies with this model, as we did with CS-PG. Phase speeds and dominant wavelengths obtained through numerical simulation were in relatively good agreement with results presented in Barth (1994), who employed the Boussinesq system in an investigation of the California Current. However, e-folding periods were significantly underestimated. A possible reason for the discrepancy is that the layer depth ratio was not very small, although this was a model assumption.

An important aspect of instability in bottom-dwelling and coastally-trapped currents is the effect of topography. It was found that perturbation growth rates for a wedge-shaped abyssal current increase with the bottom slope if the frontal and topographic gradients are of the same sign. For a front bounded by two incroppings and symmetric about its axis, topography was always a destabilizing influence. In the case of surface currents, we found that the situation is more complicated. If the bottom slopes in the same sense as the front then steeper topography is, unambiguously, a stabilizing influence. If the slopes have opposite signs, then growth rates increase with steeper topography, then decrease.

We argued that growth rates are highest when the surface- and bottom-intensified modes of instability have similar phase speeds, and are thus able to couple. An abrupt change in topography close to an outcropping was found to decrease growth rates, even if the topography became deeper as the front became shallow. Thus, a shelf break may also inhibit destabilization, as demonstrated experimentally by Cenedese and Linden (2002). Introduction of stratification in the ambient fluid generally cushions the frontal layer from topographic effects. Growth rates are typically higher and lengthscales smaller than in the homogeneous case. Also, the range of topographic slopes that meet the necessary condition for instability is larger than in the unstratified limit.

Nonlinear flow evolution was studied numerically, and compared with oceanographic and laboratory observations. An application of the CS-PG model to deep water dynamics in the Strait of Georgia, Canada, showed the development of highly-localized, bottom-intensified vortical anomalies along the down-slope incropping of an unstable current. Source flow simulations with the same equations were aimed at modelling instability of the Denmark Strait Overflow. It was found that our linear theory predicts the dominant wavelength fairly accurately in this case. A dense water plume broke up into smaller subplumes, which descended down-slope, releasing their gravitational potential energy. This lead to the development of anticyclones close to shore and strong cyclones farther offshore in the ambient layer, in good agreement some observations (there is debate as to the consistency of different observations). Finally, curved topography induced the formation of baroclinic vortex pairs, which remained coherent for long times. It may be of value to determine whether convex topography south of Denmark Strait, where it exists, has any influence on observed vortex development.

The FG-CS model was applied to the California Current, as discussed above. We employed the FG-SW model in simulations of axisymmetric currents in an annular domain, similar to the laboratory experiments of Cenedese and Linden (2002). A buoyant current was located adjacent to the inner wall, which served as an idealized coastline. Our tests, with and without a source of buoyant fluid, seemed to corroborate several of the findings of Cenedese and Linden (2002). In particular, step topography on the offshore side of the outcropping trapped vortical features on the inner part of the topography, delaying eddy pinch-off. Introduction of a source of upper layer fluid increased the dominant lengthscales at late times, and prevented eddy separation.

Evolution of an idealized meddy was investigated using the SW-FG-SW model in the presence of the β-effect. The mid-depth lens was found to undergo instability, separating into two separate meddies, which then migrated to the southwest. For a significant period of time the meddy trajectories were influenced by coherent dipole anomalies in the ambient layers. The dipoles self-propelled, advecting the meddies. However the dipole features were eventually eroded by β-induced Rossby waves and southwestward motion of the meddies was accelerated.

It must be remembered that all of our theoretical and numerical configurations are idealized to some extent. For example, we have neglected processes such as wind stress, eddy-induced viscosity and high Rossby number flows. However, in general, it seems that layered models such as the ones we have described are useful in characterizing various instability processes. Reduced models help to improve our understanding of underlying mechanisms and general principles. Moreover, the nonlinear frontal terms associated with the FG approximation suppress growth at very small scales and are conducive to the development of large, coherent features, as seen in chapter 4 (see also Karsten and Swaters 2000b). Finally, the FG dynamical limit retains the asymmetry with respect to stability of cyclones versus anticyclones that is characteristic of the primitive equations, but is absent in QG theory.

Isopycnic models formulated in terms of a streamfunction and vorticity have the potential to efficiently describe flows with sharp density gradients. Frontal theories can and should be used in process studies to determine statistical transport properties. Potentially, they could also be incorporated into general circulation models, at specific sites in the computational domain where spatial resolution is inadequate. Due to their simpler dynamics such nested models could be executed at higher resolution with smaller computational resources.

We have endeavored to draw analogies between frontal models and QG theory where possible. A number of stability results and instability mechanisms are common to both classes of models. However, as exemplified by the analyses and applications we have presented, frontal models are appropriate and useful in describing many features of unstable currents and isolated eddy features. As noted by Flierl (1984) and Cushman-Roisin *et al.* (1992), applicability of QG layer models is restricted by the requirement of small interfacial displacements. QG theory also describes dynamics on spatial scales comparable to the Rossby radius, while frontal models are suited for the description of larger-scale phenomena, which is particularly relevant for baroclinic instability studies Karsten and Swaters (2000b). Finally, frontal geostrophic models are more accurate in the description of eddy dynamics than QG models in that they allow completely isolated patches of fluid.

As we have tried to demonstrate, the advantage of these reduced theories is that they not only illustrate key processes, but also reproduce gross and fine-scale flow structures as simulated using more elaborate numerical models. Clearly there are differences between some of our results and oceanographic observations. However this too is instructive, because the physical processes that were neglected are likely to be the ones associated with the discrepancies. There are numerous mesoscale phenomena (a few are outlined below) which are still not adequately understood and deserve closer examination. It is our hope that the governing equations and supporting analyses presented here will be useful in such investigation.

6.2 Avenues for further research

Several observational studies have noted frequent meandering and formation of energetic, anticyclonic eddies associated with the Alaska Current and Alaska Stream, which flow along the coast of mainland Alaska and the Aleutian Islands. Recently, results of a long-term observational study elucidated the complete life cycle of several such eddies (Crawford and Whitney 1999; Crawford, Cherniawsky, and Foreman 2000). Baroclinic instability is thought to be the main contributor although barotropic instability may also play a role (Melsom, Meyers, Hurlburt, Metzger, and O'Brien 1999). The FG-CS model seems suited to a modelling effort of these boundary currents.

On a β-plane, the model could also be used to study heat fluxes due to baroclinic eddies along the poleward edge of the Antarctic Circumpolar Current (R. Karsten, personal communication). However, since the ACC exists at high latitudes, correction terms due to the Veronis effect (Karsten and Swaters 1999) would have to be included in the model. Here, the Veronis effect refers to the geometric distortion that results from the coordinate transformation between spherical and Cartesian coordinates. In FG models, these metric terms should not be neglected on meridional scales where the beta effect is important (Karsten and Swaters 1999).

It would also be interesting to employ the SW-FG-SW model in a similar configuration as the laboratory experiments of Baey *et al.* (1995), in order to investigate instabilities on an intermediate depth boundary current. Ultimately, the goal would be to understand Meddy generation from the salinity tongue along the Iberian coast. Previous studies suggested that coastline irregularities may serve as triggers for meddy separation (Sadoux *et al.* 2000). In this setting, the ambient fluid itself is typically stratified, so that the CS-FG-CS model should be utilized.

Results could be compared in a quantitative way with the laboratory investigation of Folkard and Davies (2001). In their experiments, the ambient fluid was linearly stratified and a thin, well-mixed intermediate depth current was formed by oscillating a grid at one end of the tank. The mixed fluid was of an intermediate density, and after geostrophic adjustment traveled along one of the walls, later becoming unstable. This scenario exactly corresponds to the assumptions we made in chapter 5. Additional experiments on intermediate flows were performed by Davies *et al.* (1991).

The theoretical work presented here lends itself to several natural extensions, such as weakly nonlinear analyses of unstable mean flows. Such analyses for frontal models without continuous stratification may be found in Reszka and Swaters (1999a), Karsten and Swaters (2000b) and elsewhere. The feedback of perturbations on the mean flow could also be investigated using the quasi-linear approach, as was done in the QG context by Phillips (1954) and for the two-layer shallow water system by Boss and Thompson (1999). In the latter study, particular attention was paid to the applicability of QG theory beyond the small Rossby number regime. Similar comparisons between the predictions of frontal models and those of primitive equation models would be valuable. We leave these considerations for future studies.

Appendix A

SW-FG-SW Model

This derivation simply serves to demonstrate how to obtain the SW-FG-SW governing equations by making the assumption of three homogeneous layers at the start, rather than as a reduction of the CS-FG-CS model (subsection 5.1.4). Here, the middle layer will be FG, while the outer layers will be governed by Shallow Water QG dynamics. The resulting system should be useful in studying the dynamics of intermediate depth boundary currents and isolated mid-depth lenses, such as those described in Baey *et al.* (1995). We present a numerical simulation that employs this model in section 5.2.

The model geometry is sketched in Fig. A.1. The ambient layers (subscripts 1 and 3) are homogeneous, hydrostatic and incompressible. For the middle layer (subscript 2), the Shallow Water approximation is made,

$$\left.\begin{aligned} \mathbf{u}^*_{it^*} + \mathbf{u}^*_i\cdot\boldsymbol{\nabla}^*\mathbf{u}^*_i + w^*_i\mathbf{u}^*_{iz^*} + (f_0+\beta_0 y^*)\mathbf{e}_3\times\mathbf{u}^*_i &= -\frac{1}{\rho_*}\boldsymbol{\nabla}^* p^*_i, \\ p^*_{iz^*} &= -g\rho_i, \\ \boldsymbol{\nabla}^*\cdot\mathbf{u}^*_i + w^*_{iz^*} &= 0, \end{aligned}\right\} i = 1,3 \qquad \text{(A.1)}$$

$$\mathbf{u}^*_{2t^*} + \mathbf{u}^*_2\cdot\boldsymbol{\nabla}^*\mathbf{u}^*_2 + (f_0+\beta_0 y^*)\mathbf{e}_3\times\mathbf{u}^*_2 = -\frac{1}{\rho_*}\boldsymbol{\nabla}^* p^*, \qquad \text{(A.2)}$$

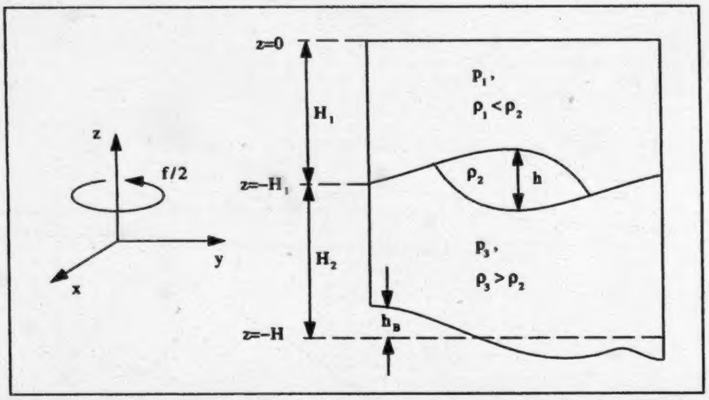

Figure A.1: SW-FG-SW model geometry. A thin, homogeneous layer lies between two homogeneous layers that are relatively deep, but finite. The upper and lower surfaces bounding the middle layer are allowed to intersect each other. This permits fronts with finite spatial extent, or isolated lenses of intermediate water. Spatially varying topography is also allowed.

$$h^*_{t^*} + \boldsymbol{\nabla}^*\cdot(\mathbf{u}^*_2 h^*) = 0. \tag{A.3}$$

The notation is similar to that in chapter 5, except that the velocities and dynamic pressures are z-independent. We state the boundary conditions as follows,

$$w^*_1 = 0, \qquad z^* = 0, \tag{A.4}$$

$$w^*_1 = \eta^*_{t^*} + \mathbf{u}^*_1\cdot\boldsymbol{\nabla}^*\eta^*, \qquad z^* = -H_1 + \eta^*, \tag{A.5}$$

$$w^*_3 = (\eta^* - h^*)_{t^*} + \mathbf{u}^*_3\cdot\boldsymbol{\nabla}^*(\eta^* - h^*), \qquad z^* = -H_1 + \eta^* - h^*, \tag{A.6}$$

$$w^*_3 = \mathbf{u}^*_3\cdot\boldsymbol{\nabla}^* h^*_B, \qquad z^* = -H_1 - H_2 + h^*_B, \tag{A.7}$$

where H_1 and H_2 are the constant reference depths of the upper and lower layers, respectively. The lower boundary of the upper layer is at $z^* = -H_1 + \eta^*$ while the upper boundary of the lower layer is at $z^* = -H_1 + \eta^* - h^*$, where h^* is the thickness of the middle layer. The two boundaries are coincident wherever h^* vanishes. The total pressure in each of the three layers is given by

$$p^*_1(x^*, y^*, z^*, t^*) = -g\rho_1 z^* + \varphi^*(x^*, y^*, t^*), \tag{A.8}$$

$$p_2^*(x^*,y^*,z^*,t^*) = -g\rho_2 z^* - g(\rho_2-\rho_1)H_1 + p^*(x^*,y^*,t^*), \tag{A.9}$$

$$p_3^*(x^*,y^*,z^*,t^*) = -g\rho_3 z^* + g(\rho_3-\rho_1)H_1 + \psi^*(x^*,y^*,t^*). \tag{A.10}$$

Pressure is required to be continuous at the fluid interfaces,

$$\begin{aligned} -g\rho_1(-H_1+\eta^*) + \varphi^* &= -g\rho_2(-H_1+\eta^*) \\ &+ g(\rho_1-\rho_2)H_1 + p^* \qquad \text{at } z^* = -H_1+\eta^*, \end{aligned} \tag{A.11}$$

and

$$\begin{aligned} &-g\rho_2(-H_1+\eta^*-h^*) - g(\rho_2-\rho_1)H_1 + p^* \\ &= -g\rho_3(-H_1+\eta^*-h^*) + g(\rho_1-\rho_3)H_1 + \psi^* \qquad \text{at } z^* = -H_1+\eta^*-h^*. \end{aligned} \tag{A.12}$$

Simplifying, we obtain

$$g(\rho_2-\rho_1)\eta^* = p^* - \varphi^*, \tag{A.13}$$

$$g(\rho_3-\rho_2)(\eta^*-h^*) = \psi^* - p^*. \tag{A.14}$$

Scalings are based on the "intermediate lengthscale" ansatz (see S93 or section 5.1.1),

$$\begin{gathered} g' = g\frac{\Delta\rho}{\rho_*}, \qquad \rho_* = \rho_2, \qquad \Delta\rho = \rho_3-\rho_1, \\ \rho_2-\rho_1 = r_1\Delta\rho, \qquad \rho_3-\rho_2 = r_2\Delta\rho, \qquad r_1+r_2=1, \\ (x^*,y^*) = L_*(x,y), \qquad z^* = Hz, \qquad t^* = \frac{t}{\varepsilon_1 f_0}, \\ \mathbf{u}_1^* = \varepsilon_1 f_0 L_* \mathbf{u}_1, \qquad \mathbf{u}_2^* = \varepsilon_2 f_0 L_* \mathbf{u}_2, \qquad \mathbf{u}_3^* = \varepsilon_1 f_0 L_* \mathbf{u}_3, \\ h^* = \delta H h, \qquad \eta^* = \delta H\eta, \qquad h_B^* = \delta H h_B, \\ \varphi^* = \varepsilon_1\rho_* f_0^2 L_*^2 \varphi, \qquad p^* = \varepsilon_2 \rho_* f_0^2 L_*^2 p, \qquad \psi^* = \varepsilon_1 \rho_* f_0^2 L_*^2 \psi, \\ w_1^* = \delta\varepsilon_1 f_0 H w_1, \qquad w_3^* = \delta\varepsilon_1 f_0 H w_3, \qquad \beta_0 = \varepsilon_1 f_0 \beta / L_*. \end{gathered} \tag{A.15}$$

Substitution of the scalings into the primitive equations yields

$$\varepsilon_1(\mathbf{u}_{1t} + \mathbf{u}_1\cdot\nabla\mathbf{u}_1 + \delta w_1 \mathbf{u}_{1z}) + (1+\varepsilon_1\beta y)\mathbf{e}_3 \times \mathbf{u}_1 = -\nabla\varphi, \tag{A.16}$$

$$\nabla\cdot\mathbf{u}_1 + \delta w_{1z} = 0, \tag{A.17}$$

$$\varepsilon_1 \mathbf{u}_{2t} + \varepsilon_2 \mathbf{u}_2 \cdot \nabla \mathbf{u}_2 + (1 + \varepsilon_1 \beta y)\mathbf{e}_3 \times \mathbf{u}_2 = -\nabla p, \tag{A.18}$$

$$\varepsilon_1 h_t + \varepsilon_2 \nabla \cdot (\mathbf{u}_2 h) = 0, \tag{A.19}$$

$$\varepsilon_1(\mathbf{u}_{3t} + \mathbf{u}_3 \cdot \nabla \mathbf{u}_3 + \delta w_3 \mathbf{u}_{3z}) + (1 + \varepsilon_1 \beta y)\mathbf{e}_3 \times \mathbf{u}_3 = -\nabla \psi, \tag{A.20}$$

$$\nabla \cdot \mathbf{u}_3 + \delta w_{3z} = 0, \tag{A.21}$$

together with the boundary conditions,

$$w_1 = 0, \qquad z = 0, \tag{A.22}$$

$$w_1 = \eta_t + \mathbf{u}_1 \cdot \nabla \eta, \qquad z = -\lambda_1 + \delta\eta, \tag{A.23}$$

$$w_3 = (\eta - h)_t + \mathbf{u}_3 \cdot \nabla(\eta - h), \qquad z = -\lambda_1 + \delta\eta - \delta h, \tag{A.24}$$

$$w_3 = \mathbf{u}_3 \cdot \nabla h_B, \qquad z = -1 + \delta h_B, \tag{A.25}$$

where λ_1 is defined by (5.1.38).

Pressure continuity can now be stated as

$$r_1 \eta = \frac{\varepsilon_2}{\delta} F p - \frac{\varepsilon_1}{\delta} F \rho_2 \varphi, \tag{A.26}$$

$$r_2(\eta - h) = \frac{\varepsilon_1}{\delta} F \psi - \frac{\varepsilon_1}{\delta} F p, \tag{A.27}$$

or, solving for η and p,

$$\eta = r_2 h + \frac{\varepsilon_1}{\delta} F(\psi - \varphi), \tag{A.28}$$

$$p = \frac{\delta}{\varepsilon_2 F} r_1 r_2 h + \frac{\varepsilon_1}{\varepsilon_2}(r_2 \varphi + r_1 \psi). \tag{A.29}$$

As in chapter 5, we want to focus on the following case,

$$\varepsilon_1 = \delta \qquad \text{(outer layers QG)}, \tag{A.30}$$

$$\varepsilon_2 = \delta^{\frac{1}{2}} \qquad (p \sim h). \tag{A.31}$$

Vertically integrating the mass conservation equations for the outer layers, we obtain the nondimensional equations,

$$\delta(\mathbf{u}_{1t} + \mathbf{u}_1 \cdot \nabla \mathbf{u}_1 + \delta w_1 \mathbf{u}_{1z}) + (1 + \delta \beta y)\mathbf{e}_3 \times \mathbf{u}_1 = -\nabla \varphi, \tag{A.32}$$

$$(\lambda_1 - \delta\eta)\boldsymbol{\nabla}\cdot\mathbf{u}_1 = \delta(\eta_t + \mathbf{u}_1\cdot\boldsymbol{\nabla}\eta), \tag{A.33}$$

$$\delta\mathbf{u}_{2t} + \delta^{\frac{1}{2}}\mathbf{u}_2\cdot\boldsymbol{\nabla}\mathbf{u}_2 + (1+\delta\beta y)\mathbf{e}_3\times\mathbf{u}_2 = -\boldsymbol{\nabla}p, \tag{A.34}$$

$$\delta^{\frac{1}{2}}h_t + \boldsymbol{\nabla}\cdot(\mathbf{u}_2 h) = 0, \tag{A.35}$$

$$\delta(\mathbf{u}_{3t} + \mathbf{u}_3\cdot\boldsymbol{\nabla}\mathbf{u}_3 + \delta w_3\mathbf{u}_{3z}) + (1+\delta\beta y)\mathbf{e}_3\times\mathbf{u}_3 = -\boldsymbol{\nabla}\psi, \tag{A.36}$$

$$(\lambda_2 + \delta\eta - \delta h)\boldsymbol{\nabla}\cdot\mathbf{u}_3 = -\delta((\eta - h)_t + \mathbf{u}_3\cdot\boldsymbol{\nabla}(\eta - h - h_B)), \tag{A.37}$$

with pressure continuity,

$$\eta = r_2 h + F(\psi - \varphi), \tag{A.38}$$

$$p = r_1 r_2 h + \delta^{\frac{1}{2}}(r_1\psi + r_2\varphi), \tag{A.39}$$

where the Froude number is given by (5.1.37).

We take the curl of outer layer momentum equations to obtain vorticity equations. Defining $\zeta_i = \mathbf{e}_3\cdot\boldsymbol{\nabla}\times\mathbf{u}_i$ for $i = 1, 3$,

$$\delta(\partial_t + \mathbf{u}_1)\zeta_1 + \delta\zeta_1\boldsymbol{\nabla}\cdot\mathbf{u}_1 + (1+\delta\beta y)\boldsymbol{\nabla}\cdot\mathbf{u}_1 + \delta\beta v_1 = O(\delta^2), \tag{A.40}$$

where

$$\begin{aligned}\boldsymbol{\nabla}\cdot\mathbf{u}_1 &= \frac{\delta}{\lambda_1}(\eta_t + \mathbf{u}_1\cdot\boldsymbol{\nabla}\eta + \eta\boldsymbol{\nabla}\cdot\mathbf{u}_1),\\ \eta &= r_2 h + F(\psi - \varphi).\end{aligned} \tag{A.41}$$

Similarly for layer 3,

$$\delta(\partial_t + \mathbf{u}_3)\zeta_3 + \delta\zeta_3\boldsymbol{\nabla}\cdot\mathbf{u}_3 + (1+\delta\beta y)\boldsymbol{\nabla}\cdot\mathbf{u}_3 + \delta\beta v_3 = O(\delta^2), \tag{A.42}$$

where

$$\begin{aligned}\boldsymbol{\nabla}\cdot\mathbf{u}_3 &= \frac{\delta}{\lambda_2}((\eta - h)_t + \mathbf{u}_3\cdot\boldsymbol{\nabla}(\eta - h - h_B) + (\eta - h)\boldsymbol{\nabla}\cdot\mathbf{u}_3),\\ \eta - h &= -r_1 h + F(\psi - \varphi).\end{aligned} \tag{A.43}$$

All variables are expanded in $\delta^{\frac{1}{2}}$,

$$(\varphi, \mathbf{u}_1, \eta, h, p, \mathbf{u}_2, \psi, \mathbf{u}_3) = (\varphi, \mathbf{u}_1, \eta, h, p, \mathbf{u}_2, \psi, \mathbf{u}_3)^{(0)}$$

$$+\delta^{\frac{1}{2}}(\varphi, \mathbf{u}_1, \eta, h, p, \mathbf{u}_2, \psi, \mathbf{u}_3)^{(1)} + \ldots \tag{A.44}$$

To $O(\delta)$ the outer layers are governed by QG theory, i.e. the $O(\delta^{\frac{1}{2}})$ corrections do not play a role and may be absorbed into the leading order flow fields. Then, we may write

$$[\partial_t + J(\varphi^{(0)}, *)][\Delta\varphi^{(0)} + \frac{1}{\lambda_1}(r_2 h^{(0)} + F(\psi^{(0)} - \varphi^{(0)})) + \beta y] = 0, \tag{A.45}$$

$$[\partial_t + J(\psi^{(0)}, *)][\Delta\psi^{(0)} - \frac{1}{\lambda_2}(-r_1 h^{(0)} + F(\psi^{(0)} - \varphi^{(0)}) - h_B) + \beta y] = 0, \tag{A.46}$$

where

$$\mathbf{u}_1^{(0)} = \mathbf{e}_3 \times \nabla\varphi^{(0)}, \qquad \mathbf{u}_3^{(0)} = \mathbf{e}_3 \times \nabla\psi^{(0)},$$

$$\eta^{(0)} = r_2 h^{(0)} + F(\psi^{(0)} - \varphi^{(0)}). \tag{A.47}$$

Details of the derivation for the middle layer are the same as in chapter 5, with $\varphi^{(0)}(x,y,t)$ and $\psi^{(0)}(x,y,t)$ playing the role of $\varphi^{(0)}(x,y,-\lambda_1,t)$ and $\psi(x,y,-\lambda_1,t)$. We obtain

$$h_t^{(0)} + J(r_2\varphi^{(0)} + r_1\psi^{(0)}, h^{(0)}) + (r_1 r_2)^2 J(\frac{1}{2}\nabla h^{(0)} \cdot \nabla h^{(0)} + h^{(0)}\Delta h^{(0)}, h^{(0)}) = 0. \tag{A.48}$$

Dropping the superscript (0), the SW-FG-SW governing equations are

$$(\partial_t + J(\varphi, *))(\Delta\varphi + \frac{r_2}{\lambda_1}h + F_1(\psi - \varphi) + \beta y) = 0, \tag{A.49}$$

$$h_t + J(r_1\psi + r_2\varphi, h) + (r_1 r_2)^2 J(h\Delta h + \frac{1}{2}\nabla h \cdot \nabla h, h) = 0, \qquad z = -\lambda_1, \tag{A.50}$$

$$(\partial_t + J(\psi, *))(\Delta\psi + \frac{r_1}{\lambda_2}h - F_2(\psi - \varphi) + \beta y + \frac{1}{\lambda_2}h_B) = 0. \tag{A.51}$$

where $r_1 + r_2 = 1$, $F_i = F/\lambda_i$, $i = 1, 2$, and the leading order velocities are given by

$$\mathbf{u}_1 = \mathbf{e}_3 \times \nabla\varphi, \qquad \mathbf{u}_2 = \mathbf{e}_3 \times \nabla h, \qquad \mathbf{u}_3 = \mathbf{e}_3 \times \nabla\psi. \tag{A.52}$$

Appendix B

Numerical Scheme

Direct numerical simulation of the governing equations described in this thesis is based on finite differences in space, with explicit time-stepping. While details of the numerical scheme differ for each model, there are many common features, which we describe here. For the purposes of numerical integration, all variables for a given model are discretized on a regular, rectangular grid in a rectangular or annular domain. For 2-dimensional models (SW-PG, FG-SW and SW-FG-SW) the nondimensional domain is Ω_H, while for 3-dimensional models (CS-PG, FG-CS and CS-FG-CS) the nondimensional domain is $\Omega = \Omega_H \times [-1, 0]$. If a time-derivative term is the sum of two or more quantities, then it is denoted as a single auxiliary variable. At each time step, the auxiliary variable is evolved forward in time, after which the original variables are recovered.

The procedure for all the models is similar. As an example, the CS-PG governing equations are reformulated as follows,

$$q_t = \mu J(q, \varphi) + Q_1, \tag{B.1}$$

$$\rho_t = \mu J(\rho, \varphi), \qquad z = 0, \tag{B.2}$$

$$\chi_t = \mu J(\chi, \varphi) + N^2 J(h_B, \varphi), \qquad z = -1, \tag{B.3}$$

$$h_t = \frac{1}{C_d^2 + 1} J(h, p) + \frac{C_d}{C_d^2 + 1} \nabla \cdot (h \nabla p) + Q_2 + F, \qquad z = -1, \tag{B.4}$$

where $q = \Delta\varphi + (N^{-2}\varphi_z)_z$ is the potential vorticity, $\rho = -\varphi_z$ and $\chi = \varphi_z + N^2h$. Numerical friction, F, is introduced into the evolution equation for h, in order to damp small scale noise.

The friction term F has the form $k_1\Delta h + k_2(-1)^{n-1}\Delta^n h$ where coefficients k_1 and k_2 are chosen empirically so that grid-scale noise is minimized, without significantly affecting the long-term evolution of the flow. Numerical friction $k_2(-1)^{n-1}\Delta^n h$ for PG models is always biharmonic ($n = 2$). For FG models, we have found that the presence of higher derivatives in the governing equation for the FG layer requires a higher order friction operator ($n = 4$) with an appropriately decreased k_2. Typical values for k_1, k_2 are 5×10^{-4}, 5×10^{-5} respectively for the PG family of models, and 10^{-4}, 10^{-8} for the FG models. Negative values of h are clearly unphysical, however they still arise due to error associated with the finite discretization. These are eliminated at each time step, and the associated volume is subtracted uniformly over the frontal layer, so that overall volume of the layer is exactly conserved. A possible improvement would be the implementation of a flux-corrected transport scheme (e.g. Durran 1998).

Our numerical experiments were performed in an x-periodic channel or a closed domain. In cases where Ω_H was closed, its shape was either a rectangle (chapters 2, 3 and 4) or an annulus (section 4.4). No-normal flow conditions were applied on all rigid walls, i.e. the appropriate derivative of each streamfunction was zero. In practice, the values of the streamfunction along a rigid wall were held constant throughout the simulation. The size of the domain was chosen empirically, such that it allowed at least two (and usually more) wavelengths of the most unstable along-front mode. Cross-front profiles for the initial thickness of the frontal layer are described for each simulation separately.

All the models except FG-SW and SW-FG-SW are integrated forward in time using the Leapfrog scheme, with Robert smoothing (coefficient of 5×10^{-3}) applied at every time step to filter out the computational mode (Asselin 1972). For FG-SW and SW-FG-SW we employ the 3rd order Adams–Bashforth method (Durran

1998). Jacobian terms are discretized using the (Arakawa 1966) formula and 2$^{\text{nd}}$ order accurate central differences are employed for all necessary spatial derivatives. At each iteration, the streamfunction for the ambient layer is recovered using an elliptic solver. In (B.1)–(B.4), φ is recovered from q *via* the MUDPACK routine, mud3sp. Vertical Neumann boundary conditions are provided by $\varphi_z(z = 0)$ and $\varphi_z(z = -1)$, which are easily computed from ρ and χ, respectively.

For the 2-dimensional models, the elliptic problem does not involve vertical boundary conditions, and we use the variant mud2sp. MUDPACK is a library of elliptic solvers based on the Multigrid method with Gauss-Seidel relaxation and red-black ordering (Adams 1989; Kincaid and Cheney 1996). For simulations of buoyant axisymmetric currents (FG-SW model, chapter 4) we use a straightforward Conjugate-Gradient solver (Reszka 1997; Kincaid and Cheney 1996) because the domain is non-simply-connected. However, the discretization grid is still rectangular in that case, and both the x- and y-velocities are held constant on the inner annulus boundary. Thus the boundary conditions are no-normal flow as well as no-slip.

To focus on the baroclinic aspects of the instabilities, the mean flow in the QG layer(s) was initially set to zero. In simulations without a source, the pressure in each QG layer was seeded with a superposition of waves with random amplitudes and phase shifts, in order to excite the instability. The amplitude of this initial perturbation was small, typically between 10^2 and 10^{18} times smaller than the initial mean velocity of the frontal layer, depending on the model and the type of simulation. The perturbation amplitude was chosen such that the dominant along-front wavelength emerged before nonlinear effects became significant. In the case of the annulus simulations, the initial perturbation consisted of radial and azimuthal modes. For simulations involving a source, where no steady-state solution exists, no perturbation was required for the development of the instability.

The horizontal resolution varied between experiments, and is described for each simulation separately. A typical horizontal resolution, however, was 128×128 nodes.

For 3-dimensional models, the vertical resolution of the QG layer was maintained at 16 levels, which adequately captured the evolution of the vertical structure in all cases considered. We endeavored to use grids such that the resolution in each spatial direction contained a high power of 2, which increased the efficiency of the MUDPACK routines. The time step used was the highest possible which still ensured numerical stability. For the PG models, Δt was usually 10^{-2} nondimensional times units. For the FG models, Δt was typically around 10^{-3} because of the cubic nonlinearity, and often had to be decreased further by a factor of 10 during the fully nonlinear stages of instability. Finally, the introduction of a source is discussed for each model individually. Numerical investigations of mesoscale gravity currents employing the SW-PG model can be found in (Karsten *et al.* 1995; Swaters 1998) as well as (Choboter and Swaters 2000). Karsten and Swaters (2000a) and Karsten and Swaters (2000b) describe simulations of wedge fronts and parabolic fronts for the FG-SW model and related models.

References

Adams, J. 1989. Mudpack: Multigrid Fortran Software for the Efficient Solution of Linear Elliptic Partial Differential Equations. *Applied Math. and Comput.*, **34**, 113–146.

Arakawa, A. 1966. Computational design for long term numerical integration of the equations of fluid motion: Two-dimensional incompressible flow. *J. Comput. Phys.*, **1**, 119–143.

Asselin, R. A. 1972. Frequency filter for time integrations. *Mon. Weather Rev.*, **100**, 487–490.

Baey, J. M., Renouard, D., and D'Hieres, G. C. 1995. Preliminary results about the stability of an intermediate water current. *Deep-Sea Res.*, **42**, 2063–2073.

Barth, J. A. 1989a. Stability of a coastal upwelling front. 1. Model development and a stability theorem. *J. Geophys. Res.*, **94**, 10844–10856.

Barth, J. A. 1989b. Stability of a coastal upwelling front. 2. Model results and comparison with observations. *J. Geophys. Res.*, **94**, 10857–10883.

Barth, J. A. 1994. Short-wavelength instabilities on coastal jets and fronts. *J. Geophys. Res.*, **99**, 16095–16115.

Blumsack, S. L., and Gierasch, P. J. 1972. Mars: The effects of topography on baroclinic instability. *J. Atmos. Sci.*, **29**, 1081–1089.

Boss, E., Paldor, N., and Thompson, L. 1996. Stability of a potential vorticity front from quasigeostrophy to shallow water. *J. Fluid. Mech.*, **315**, 65–84.

Boss, E., and Thompson, L. 1999. Mean flow evolution of a baroclinically unstable potential vorticity front. *J. Phys. Oceanogr.*, **29**, 273–287.

Bruce, J. G. 1995. Eddies southwest of the Denmark Strait. *Deep-Sea Res.*, **42**, 13–29.

Cenedese, C., and Linden, P. F. 2002. Stability of a buoyancy-driven coastal current at the shelf break. *J. Fluid Mech.*, **452**, 97–121.

Chassignet, E. P., and Cushman-Roisin, B. 1991. On the influence of a lower layer on the propagation of nonlinear oceanic eddies. *J. Phys. Oceanogr.*, **21**, 939–957.

Choboter, P. F., and Swaters, G. E. 2000. On the baroclinic instability of axisymmetric rotating gravity currents with bottom slope. *J. Fluid Mech.*, **408**, 149–177.

Choboter, P. F., and Swaters, G. E. 2002. Shallow-Water modeling of Antarctic Bottom Water crossing the equator. *J. Phys. Oceanogr.*, submitted.

Cooper, L. H. N. 1955. Deep water movements in the North Atlantic as a link between climatic changes around Iceland and biological productivity of the English Channel and Celtic Sea. *J. Mar. Res.*, **14**, 347–362.

Crawford, W. R., Cherniawsky, J. Y., and Foreman, M. G. G. 2000. Multi-year meanders and eddies in the Alaskan Stream as observed by TOPEX/Poseidon altimeter. *Geophys. Res. Lett.*, **27**, 1025–1028.

Crawford, W. R., and Whitney, F. 1999. Mesoscale eddy aswirl with data in Gulf of Alaska. *Eos. Trans. AGU*, **80**, 365.

Cushman-Roisin, B. 1986. Frontal Ggeostrophic Dynamics. *J. Phys. Oceanogr.*, **22**, 117–127.

Cushman-Roisin, B. 1994. *Introduction to Geophysical Fluid Dynamics.* New Jersey: Prentice Hall.

Cushman-Roisin, B., Chassignet, E. P., and Tang, B. 1990. Westward Motion of Mesoscale Eddies. *J. Phys. Oceanogr.*, **20**, 758–768.

Cushman-Roisin, B., Sutyrin, G. G., and Tang, B. 1992. Two-Layer Geostrophic Dynamics. Part I: Governing Equations. *J. Phys. Oceanogr.*, **20**, 758–768.

Cushman-Roisin, B., and Tang, B. 1989. Geostrophic regimes and geostrophic turbulence beyond the radius of deformation. In J. C. J. Nihoul and B. M. Jamart (Eds.), *Mesoscale/Synoptic Structures in Geophysical Turbulence* (pp. 51–74). Elsevier.

Cushman-Roisin, B., and Tang, B. 1990. Geostrophic turbulence and the emergence of eddies beyond the radius of deformation. *J. Phys. Oceanogr.*, **20**, 97–113.

Davies, P. A., Fernando, H. J. S., Besley, P., and Simpson, R. J. 1991. Generation and Spreading of a Turbulent Mixed Layer in a Rotating, Stratified Fluid. *J. Geophys. Res.*, **96**, 12567–12585.

Dickson, R. R., and Brown, J. 1994. The production of North Atlantic Deep Water: Sources, rates, and pathways. *Dyn. Atmos. Oceans*, **31**, 139–164.

Durran, D. R. 1998. *Numerical Methods for Wave Equations in Geophysical Fluid Dynamics.* New York: Springer-Verlag.

Etling, D., Gelhardt, F., Schrader, U., Brennecke, F., Kuhn, G., d'Hieres, G. C., and Didelle, H. 2000. Experiments with density currents on a sloping bottom in a rotating fluid. *Dyn. Atmos. Oceans*, **31**, 139–164.

Feliks, Y., and Ghil, M. 1996. Mixed barotropic-baroclinic eddies growing on an eastward mid-latitude jet. *Geophys. Astrophys. Fluid Dynamics*, **82**, 137–171.

Flagg, C. N., and Beardsley, R. C. 1978. On the stability of the shelf water/slope water front south of New England. *J. Geophys. Res.*, **83**, 4623–4631.

Flierl, G. R. 1984. Rossby wave radiation form a strongly nonlinear warm eddy. *J. Phys. Oceanogr.*, **14**, 47–58.

Folkard, A. M., and Davies, P. A. 2001. Laboratory studies of the effects of interrupted, sloping topography on intermediate depth boundary currents in linearly stratified fluids. *Dyn. Atmos. Oceans*, **33**, 239–261.

Gawarkiewicz, G. 1991. Linear stability models of shelfbreak fronts. *J. Phys. Oceanogr.*, **21**, 471–488.

Gawarkiewicz, G. 2000. Effects of ambient stratification and shelfbreak topography on offshore transport of dense water on continental shelves. *J. Geophys. Res.*, **105**, 3307–3324.

Gawarkiewicz, G., and Chapman, D. C. 1995. A numerical study of dense water formation and transport on a shallow, sloping continental shelf. *J. Geophys. Res.*, **100**, 4489–4507.

Gill, A. E. 1982. *Atmosphere-Ocean Dynamics.* New Jersey: Academic Press.

Griffies, S. M., Böning, C., Bryan, F. O., Chassignet, E. P., Gerdes, R., Hasumi, H., Hirst, A., Treguier, A.-M., and Webb, D. 2000. Developments in ocean climate modelling. *Ocean Modelling*, **2**, 123-192.

Griffiths, R. W., Killworth, P. D., and Stern, M. E. 1982. Ageostrophic instability of ocean currents. *J. Fluid. Mech.*, **117**, 343–377.

Griffiths, R. W., and Linden, P. F. 1981. The stability of buoyancy-driven coastal currents. *Dyn. Atmos. Oceans*, **5**, 281–306.

Haidvogel, D. B., Beckmann, A., and Hedström, K. S. 1991. Dynamical simulations of filament formation and evolution in the coastal transition zone. *J. Geophys. Res.*, **96**, 15017–15040.

Hogg, N. G. 1976. On spatially growing baroclinic waves in the ocean. *J. Fluid Mech.*, **78**, 217–235.

Ikeda, M., and Emery, W. J. 1984. Satellite observations and modeling of meanders in the california current system off oregon and northern california. *J. Phys. Oceanogr.*, **14**, 31434–1450.

Ikeda, M., Emery, W. J., and Mysak, L. A. 1984. Seasonal variability in meanders of the California Current system off Vancouver Island. *J. Geophys. Res.*, **89**, 3487–3505.

Jiang, L., and Garwood Jr., R. W. 1995. A numerical study of three-dimensional dense bottom plumes on a Southern Ocean continental shelf. *J. Geophys. Res.*, **100**, 18471–18488.

Jiang, L., and Garwood Jr., R. W. 1996. Three-Dimensional Simulations of Overflows on Continental Slopes. *J. Phys. Oceanogr.*, **26**, 1214–1233.

Jungclaus, J. H. 1999. A three-dimensional simulation of the formation of anticyclonic lenses (Meddies) by the instability of an intermediate depth boundary current. *J. Phys. Oceanogr.*, **29**, 1579–1598.

Jungclaus, J. H., Hauser, J., and Käse, R. H. 2001. Cyclogenesis in the Denmark Strait Overflow Plume. *J. Phys. Oceanogr.*, **31**, 3214–3229.

Karsten, R. H., and Swaters, G. E. 1999. A unified asymptotic derivation of two-layer frontal geostrophic models including planetary sphericity and variable topography. *Phys. Fluids*, **11**, 2583–2597.

Karsten, R. H., and Swaters, G. E. 2000a. Nonlinear effects in two-layer, large-amplitude, geostrophic dynamics: Part 1. The strong-beta case. *J. Fluid Mech*, **412**, 125–160.

Karsten, R. H., and Swaters, G. E. 2000b. Nonlinear effects in two-layer, large-amplitude, geostrophic dynamics: Part 2. The weak-beta case. *J. Fluid Mech*, **412**, 161–196.

Karsten, R. H., Swaters, G. E., and Thomson, R. E. 1995. Stability Characteristics of Deep-Water Replacement in the Strait of Georgia. *J. Phys. Oceanogr.*, **25**, 2391–2403.

Kikuchi, T., Wakatsuchi, M., and Ikeda, M. 1999. A numerical investigation of the transport process of dense shelf water from a continental shelf to a slope. *J. Geophys. Res.*, **104**, 1197–1210.

Killworth, P. D. 1983. On the Motion of Isolated Lenses on a Beta-Plane. *J. Phys. Oceanogr.*, **13**, 368–376.

Kincaid, D., and Cheney, W. 1996. *Numerical analysis.* Pacific Grove: Brooks/Cole.

Krauss, W., and Käse, R. 1998. Eddy formation in the Denmark Strait Overflow. *J. Geophys. Res.*, **103**, 15525–15538.

Kundu, P. K. 1990. *Fluid mechanics.* San Diego: Academic Press.

Lane-Serff, G. F., and Baines, P. G. 1998. Eddy formation by dense flows on slopes in a rotating fluid. *J. Fluid Mech.*, **363**, 229–252.

Lane-Serff, G. F., and Baines, P. G. 2000. Eddy Formation by Overflows in Stratified Water. *J. Phys. Oceanogr.*, **30**, 327–337.

LeBlond, P. H., Ma, H., Doherty, F., and Pond, S. 1991. Deep and Intermediate Water Replacement in the Strait of Georgia. *Atmos.-Ocean*, **29**, 288–312.

LeBlond, P. H., and Mysak, L. A. 1978. *Waves in the ocean.* New York: Elsevier.

McDowell, S. E., and Rossby, H. T. 1978. Mediterranean water: an intense mesoscale eddy off the Bahamas. *Science*, **202**, 1085–1087.

Meacham, S. P., and Stephens, J. C. 2001. Instabilities of Gravity Currents along a Slope. *J. Phys. Oceanogr.*, **31**, 30–53.

Mechoso, C. R., and Sinton, D. M. 1981. Instability of baroclinic flows with horizontal shear along topography. *J. Phys. Oceanogr.*, **11**, 813–821.

Melsom, A., Meyers, S. D., Hurlburt, H. E., Metzger, E. J., and O'Brien, J. J. 1999. ENSO effects on Gulf of Alaska eddies. *Earth. Inter.*, **3**, pap. 001 (Available at http://EarthInteractions.org).

Mooney, C. J., and Swaters, G. E. 1996. Finite-amplitude baroclinic instability of a mesoscale gravity current in a channel. *Geophys. Astrophys. Fluid Dynamics*, **82**, 173–205.

Morris, A. H. 1993. *NSWC Library of Mathematics Subroutines.* Nswcdd/tr-92/425, Naval Surface Warfare Center, Dahlgren Division: Dahlgren, VA 22448, USA.

Nof, D. 1983. The translation of isolated cold eddies on a sloping bottom. *Deep-Sea Res.*, **30**, 171–182.

Orlanski, I. 1969. The influence of bottom topography on the stability of jets in a baroclinic fluid. *J. Atmos. Sci.*, **26**, 1216–1232.

Paldor, N., and Ghil, M. 1990. Finite-wavelength instabilities of a coupled density front. *J. Phys. Oceanogr.*, **20**, 114–123.

Paldor, N., and Ghil, M. 1991. Shortwave instabilities of coastal currents. *Geophys. Astrophys. Fluid Dynamics*, **58**, 225–241.

Paldor, N., and Killworth, P. D. 1987. Instabilities of a two-layer coupled front. *Deep-Sea Res.*, **34**, 1525–1539.

Pavía, E. G. 1992. The Breakup of Frontal Filaments. *J. Phys. Oceanogr.*, **22**, 399–403.

Pedlosky, J. 1964. The stability of currents in the atmosphere and the ocean: Part I. *J. Atmos. Sci.*, **21**, 210–219.

Pedlosky, J. 1987. *Geophysical Fluid Dynamics* (2nd ed.). New York: Springer Verlag.

Pedlosky, J. 1996. *Ocean Circulation Theory*. Berlin: Springer-Verlag.

Phillips, N. A. 1954. Energy transformations and meridional circulations associated with simple baroclinic waves in a two-level quasigeostrophic model. *Tellus*, **6**, 273–286.

Poulin, F. J. 1997. *Buoyancy currents and cold-pools overlying gently sloping topography*. M. Sc. Thesis: University of Alberta. 191 p.

Poulin, F. J., and Swaters, G. E. 1999a. Sub-inertial dynamics of density-driven flows in a continuously stratified fluid on a sloping bottom. I. Model derivation and stability characteristics. *Proc. R. Soc. Lond. A*, **455**, 2281–2304.

Poulin, F. J., and Swaters, G. E. 1999b. Sub-inertial dynamics of density-driven flows in a continuously stratified fluid on a sloping bottom. II. Isolated eddies and radiating cold domes. *Proc. R. Soc. Lond. A*, **455**, 2305–2329.

Prater, M. D., and Rossby, T. 1999. An alternative hypothesis for the origin of the Mediterranean salt lens observed off the Bahamas in the fall of 1946. *J. Phys. Oceanogr.*, **29**, 2103–2109.

Price, J. F., and Baringer, M. O. 1994. Outflows and deep water production by marginal seas. *Prog. Oceanog.*, **33**, 161–200.

Reszka, M. K. 1997. ***Finite amplitude waves and eddy development on a baroclinically unstable front over a sloping bottom.*** M. Sc. Thesis: University of Alberta. 189 p.

Reszka, M. K., and Swaters, G. E. 1999a. Eddy formation and interaction in a frontal geostrophic model. *J. Phys. Oceanogr.*, **29**, 3025–3042.

Reszka, M. K., and Swaters, G. E. 1999b. Numerical investigation of baroclinic instability in the Gaspé current using a frontal geostrophic model. *J. Geophys. Res.*, **104**, 25685–25696.

Reszka, M. K., and Swaters, G. E. 2001. Dynamics of bottom-trapped currents with application to the Strait of Georgia. *Can. Appl. Math. Quart.*, **9**, 127–158.

Reszka, M. K., Swaters, G. E., and Sutherland, B. R. 2002. Instability of abyssal currents in a continuously stratified ocean with bottom topography. *J. Phys. Oceanogr.*, **32**, 3528–3550.

Rhines, P. B. 1977. The dynamics of unsteady currents. In J. J. O. E. D. Goldberg, I. N. McCave and J. H. Steele (Eds.), *Vol.* (pp. 189–318). Wiley.

Richardson, P. L., Bower, A. S., and Zenk, W. 2000. A census of Meddies tracked by floats. *Prog. Oceanog.*, **45**, 209–250.

Sadoux, S., Baey, J. M., Fincham, A., and Renouard, D. 2000. Experimental study of the stability of an intermediate current and its interaction with a cape. *Dyn. Atmos. Oceans*, **31**, 165–192.

Samelson, R. M. 1998. Large-scale circulation with locally enhanced vertical mixing. *J. Phys. Oceanogr.*, **28**, 712–726.

Samelson, R. M., and Chapman, D. C. 1995. Evolution of the instability of a mixed-layer front. *J. Geophys. Res.*, **100**, 6743–6759.

Samelson, R. M., and Vallis, G. K. 1997. A simple friction and diffusion scheme for planetary geostrophic basin models. *J. Phys. Oceanogr.*, **27**, 186–194.

Sandoval, F. J., and Weatherly, G. L. 2001. Evolution of the deep western boundary current of Antarctic Bottom Water in the Brazil Basin. *J. Phys. Oceanogr.*, **31**, 1440–1460.

Shi, X. B., and Røed, L. P. 1999. Frontal instabilities in a two-layer, primitive equation ocean model. *J. Phys. Oceanogr.*, **29**, 948–968.

Shi, X. B., Røed, L. P., and Hackett, B. 2001. Variability of the Denmark Strait Overflow: A numerical study. *J. Geophys. Res.*, **106**, 22277–22294.

Smith, P. C. 1976. Baroclinic instability in the denmark strait overflow. *J. Phys. Oceanogr.*, **6**, 355–371.

Spall, M. A., and Price, J. F. 1998. Mesoscale Variability in Denmark Strait: The PV Outflow Hypothesis. *J. Phys. Oceanogr.*, **28**, 1598–1623.

Stacey, J. W., Pond, S., and LeBlond, P. H. 1988. An objective analysis of the low-frequency currents in the Strait of Georgia. *Atmos.-Ocean*, **26**, 1–15.

Stacey, J. W., Pond, S., and LeBlond, P. H. 1991. Flow dynamics in the Strait of Georgia, British Columbia. *Atmos.-Ocean*, **29**, 1–13.

Stacey, J. W., Pond, S., LeBlond, P. H., Freeland, H. J., and Farmer, D. M. 1987. An analysis of the low-frequency fluctuations in the Strait of Georgia, from June 1984 until January 1985. *J. Phys. Oceanogr.*, **17**, 326–342.

Sutherland, B. R., and Peltier, W. R. 1992. The stability of stratified jets. *Geophys. Astrophys. Fluid Dynamics*, **66**, 101–131.

Sutherland, B. R., and Peltier, W. R. 1994. Turbulence transition and internal wave generation in density stratified jets. *Phys. Fluids*, **6**, 1267–1284.

Swaters, G. E. 1991. On the baroclinic instability of cold-core coupled density fronts on a sloping continental shelf. *J. Fluid Mech.*, **224**, 361–382.

Swaters, G. E. 1993. On the baroclinic dynamics, hamiltonian formulation and general stability characteristics of density-driven currents and fronts over a sloping continental shelf. *Phil. Trans. R. Soc. Lond. A*, **345**, 295–325.

Swaters, G. E. 1998. Numerical simulations of the baroclinic dynamics of density-driven coupled fronts and eddies on a sloping bottom. *J. Geophys. Res.*, **103**, 2945–2961.

Swaters, G. E. 2000. *Introduction to Hamiltonian Fluid dynamics and Stability Theory*. Chapman & Hall/CRC.

Swaters, G. E., and Flierl, G. R. 1991. Dynamics of ventilated coherent cold eddies on a sloping bottom. *J. Fluid Mech.*, **223**, 565–587.

Tanaka, K., and Akitomo, K. 2001. Baroclinic instability of density current along a sloping bottom and the associated transport process. *J. Geophys. Res.*, **106**, 2621–2638.

Tang, B. 1989. *Numerical modeling of geostrophic turbulence and eddy evolution using generalized geostrophic equations*. Ph.D. Thesis: Florida State University. 189 p.

Tang, B., and Cushman-Roisin, B. 1992. Two-Layer Geostrophic Dynamics. Part II: Geostrophic Turbulence. *J. Phys. Oceanogr.*, **22**, 128–138.

Tisseur, F., and Meerbergen, K. 2001. The Quadratic Eigenvalue Problem. *SIAM Review*, **43**, 235–286.

Trenberth, K. E., and Caron, J. M. 2001. Estimates of meridional atmosphere and ocean heat transports. *J. Climate*, **14**, 3433–3443.

Verzicco, R., Lalli, F., and Campana, E. 1997. Dynamics of baroclinic vortices in a rotating, stratified fluid: A numerical study. *Phys. Fluids*, **9**, 419–431.

Whitehead, J. A., Stern, M. E., Flierl, G. R., and Klinger, B. A. 1990. Experimental Observations of Baroclinic Eddies on a Sloping Bottom. *J. Geophys. Res.*, **95**, 9585–9610.

Wilkinson, J. H. 1965. *The Algebraic Eigenvalue Problem.* Oxford: Clarendon Press.